Long Path Fourier Transform Absorption Spectroscopy for Investigating Pollution in the Urban Boundary Layer

Pauline Anne Sinclair

Merton College, Oxford

November 2000
Thesis submitted for the degree of Doctor of Philosophy

Abstract

Long Path Fourier Transform Absorption Spectroscopy for Investigating Pollution in the Urban Boundary Layer

Pauline Anne Sinclair
Merton College
Atmospheric, Oceanic and Planetary Physics

Thesis submitted for the degree of Doctor of Philosophy in the University of Oxford.
Michaelmas Term, 2000

The control of atmospheric pollution in the urban environment has, in recent years, taken on important local, national and international significance. Legislation has been introduced in many countries to improve air quality in urban areas. Monitoring air pollution is an important part of understanding and improving air quality. Current standard methods of measuring air pollution only monitor at a single point in space which can lead to ambiguities when assessing air quality over an extended region, such as a city centre or a road intersection. Optical remote sensing techniques, such as long path Fourier transform absorption spectroscopy, overcome the limitations of point measurements by integrating over long paths and thus measuring the average ambient pollutant concentrations.

A commercially available Fourier transform infrared (FTIR) spectrometer, together with custom built external optics has been used to make measurements of air pollution in Oxford city centre. It has been shown that it is possible to measure the concentrations of several pollutants simultaneously and in short measurement times. Issues relating to the performance of the spectrometer have been studied, their effects quantified and solutions proposed.

Optimal estimation techniques have been applied to the analysis of the single beam spectra recorded by the FTIR spectrometer. This technique has previously only been applied to radiance and transmission spectra and so extensions were necessary.

High resolution laboratory measurements of the absorption cross-sections of benzene and 1,3-butadiene have been made and the potential for detecting them in ambient urban air determined.

Acknowledgements

This DPhil was made possible by a tied studentship and CONNECT grant from the Natural Environment Research Council. Co-funding for the research project has come from our industrial sponsor, Perkin-Elmer, who provided a cost-subsidized FTIR instrument.

Heartfelt thanks must go to my two supervisors Dr John Barnett and Dr Paul Morris for all their help and advice and for reading drafts of this thesis. John must be particularly thanked for his ability to build equipment for me on a shoestring, having scavenged many of the parts from skips or the backs of cupboards and his assistance with my field measurements - I couldn't have managed without him. I must also thank Paul for his endless patience in answering all my questions and for continuing to supervise me after he had left the department.

I am grateful for technical assistance regarding the working of my spectrometer from my contacts at Perkin-Elmer; Dr Catherine Deeley, Dr Richard Spragg, and Dr Dave Cutler.

Thanks also must go to Dr David Newnham at the Rutherford Appleton Lab for his advice, assistance and instruction in using the Bruker IFS120 HR spectrometer in the Molecular Spectroscopy Facility there. Thanks also to Dr Kevin Smith at the Rutherford Appleton Lab for his IDL program to convert interferograms to spectra, which has been of use.

I am particularly grateful to Peter Stott at Blackwell's Book Services for allowing me to make pollution measurements on their land on Hythe Bridge Street, and to Erwin Becke, the area business manager for Thames Trains, for allowing me to make pollution measurements on land at Oxford railway station.

My thanks go to Merton College for accommodation and meals and for supporting me through my time in Oxford. I am grateful to all my friends and colleagues in Oxford for their friendship and advice, and especially to Robin for all his computing help, including the LaTeX style file used to create this thesis.

Finally a big thank you to my family, for everything they've done for me.

Conventions and common abbreviations

Throughout this thesis, unless otherwise stated, all spectra referred to were recorded at a resolution of 0.2 cm^{-1}, using the MCT detector, with Norton-Beer apodization. The conversion from the recorded interferogram was carried out by the Perkin-Elmer 'Spectrum for Windows' software.

It should be noted that the arbitrary units for signal, which are used as the ordinate axis on all plots of spectra, are different for spectra created from interferograms by an IDL program written by Dr Kevin Smith of Rutherford Appleton Laboratory, and for those spectra created by the Perkin-Elmer Spectrum for Windows software. However, they are comparable within each set.

Abbreviations will be defined where introduced in the text. However, for convenience, commonly-used abbreviations are listed in the following table.

APPIS	Air Pollution Public Information System
ARN	Automated Rural Network
AUN	Automated Urban Network
DETR	Department of the Environment, Transport and the Regions
DTGS	Deuterated TriGlycine Sulphate
EPA	Environmental Protection Agency
FFT	Fast Fourier Transform
FTS	Fourier Transform Spectrometer
FTIR	Fourier Transform Infrared
FWHH	Full Width at Half Height
FWHM	Full Width at Half Maximum
ILS	Instrument Line Shape
MCT	Mercury Cadmium Telluride
MSF	Molecular Spectroscopy Facility, RAL
NAQS	National Air Quality Strategy
NETCEN	National Environmental Technology Centre, AEA Technology
NPL	National Physical Laboratory
OPD	Optical Path Difference
OTS	Oxford Transport Strategy
ppbv	parts per billion by volume
ppmv	parts per million by volume
RAL	Rutherford Appleton Laboratory
RFM	Reference Forward Model
SNR	Signal to Noise Ratio
VMR	Volume Mixing Ratio
VOC	Volatile Organic Compound
ZPD	Zero Path Difference

Contents

Chapter 1

Introduction

1.1 Air Pollution

The control of atmospheric pollution in the urban environment has, in recent years, taken on important local, national and international significance. Legislation has been introduced in many countries to improve air quality in urban areas. In March 1997 the UK Government published the National Air Quality Strategy (NAQS) (Department of the Environment, Welsh Office & Scottish Office 1997). This sets out objectives, to be achieved by the year 2005, for the allowable atmospheric concentrations of eight pollutants (see figure **??**[1]) which are believed to pose a significant danger to health. The eight pollutants concerned are carbon monoxide (CO), nitrogen dioxide (NO_2), ozone (O_3), sulphur dioxide (SO_2), benzene (C_6H_6), 1,3-butadiene (C_4H_6), lead (Pb) and PM_{10} (Particulate Matter less than 10 micrometres in diameter). The strategy was updated in January 2000 (Department of the Environment, Transport and the Regions et al. 2000), leading to more stringent (see table 1.1[2]) targets for five of the eight pollutants. Targets for ozone and sulphur dioxide remain unchanged, but that for particles (PM_{10}) has been relaxed.

In addition to the NAQS, the Department of the Environment, Transport and the Regions (DETR) has established an Air Pollution Public Information System (Department of the Environment Transport and the Regions 1997) which is based upon three air pollution thresholds (Standard, Information and Alert) and four bands (Low, Moderate, High and

[1] Table extracted from (Department of the Environment, Welsh Office & Scottish Office 1997)
[2] Tables extracted from (Department of the Environment, Transport and the Regions et al. 2000).

Table 1.1: Updated objectives set by the UK government in January 2000 for the 8 pollutants included in the National Air Quality Strategy.

Objectives to be included in Regulations for the purpose of Local Air Quality.

Pollutant	**Objective**		**Date to be achieved by**
	Concentration†	Measured as‡	
Benzene	16.25 μg/m^3 (5ppb)	running annual mean	31 December 2003
1,3-Butadiene	2.25 μg/m^3 (1ppb)	running annual mean	31 December 2003
Carbon monoxide	11.6 mg/m^3 (10ppm)	running 8 hour mean	31 December 2003
Lead	0.5 μg/m^3 0.25 μg/m^3	annual mean annual mean	31 December 2004 31 December 2008
Nitrogen dioxide*	200 μg/m^3 (105ppb) not to be exceeded more than 18 times a year 40 μg/m^3 (21ppb)	1 hour mean annual mean	31 December 2005 31 December 2005
Particles (PM_{10})	50 μg/m^3 not to be exceeded more than 35 times a year 40 μg/m^3	24 hour mean annual mean	31 December 2004 31 December 2004
Sulphur dioxide	350 μg/m^3 (132ppb) not to be exceeded more than 24 times a year 125 μg/m^3 (47ppb) not to be exceeded more than 3 times a year 266 μg/m^3 (100ppb) not to be exceeded more than 35 times a year	1 hour mean 24 hour mean 15 minute mean	31 December 2004 31 December 2004 31 December 2005

† Conversions of ppb and ppm to μg/m^3 and mg/m^3 at 20°C and 1013 mb.

‡ How the objectives are to be measured is set out in Regulations.

* The objectives for nitrogen dioxide are provisional.

National objectives not to be included in Regulations for the purpose of Local Air Quality.

Pollutant	**Objective**		**Date to be achieved by**
	Concentration†	Measured as‡	
Objectives for the protection of human health			
Ozone*	100 μg/m^3 (50ppb) not to be exceeded more than 10 times a year	daily maximum of running 8 hour mean	31 December 2005
Objectives for the protection of vegetation and ecosystems			
Nitrogen oxides**	30 μg/m^3 (16ppb)	annual mean	31 December 2000
Sulphur dioxide	20 μg/m^3 (8ppb) 20 μg/m^3 (8ppb)	annual mean winter average (1 October to 31 March)	31 December 2000 31 December 2000

† Conversions of ppb and ppm to μg/m^3 and mg/m^3 at 20°C and 1013 mb.

‡ How the objectives are to be measured is set out in Regulations.

* The objective for ozone is provisional.

** Assuming NO_x is taken as NO_2.

Very High). The bands are determined by the health effects of the individual pollutants at different concentrations and are detailed in table 1.2. The Standard threshold is defined by the National Air Quality Strategy and the Information and Alert thresholds are in line with EC directives on Air Quality.

Table 1.2: UK Air Quality Bandings

	Carbon Monoxide	**Nitrogen Dioxide**	**Ozone**	**PM_{10}**	**Sulphur Dioxide**
Time averaging period	8 hour running mean	1 hour mean	1 hour mean	24 hour running mean	15 minute mean
Unit	ppmv	ppbv	ppbv	μg m^{-3}	ppbv
Low Pollution	< 10	< 150	< 50 †	< 50	< 100
Standard Threshold	**10**	**150**	**50**	**50**	**100**
Moderate Pollution	10 - 14	150 - 299	50 - 89 ‡	50 - 74	100 - 199
Information Threshold	**15**	**300**	**90**	**75**	**200**
High Pollution	15 - 19	300 - 399	90 - 179	75 - 99	200 - 399
Alert Threshold	**20**	**400**	**180**	**100**	**400**
Very High Pollution	> 20	> 400	> 180	> 100	> 400

†running 8 hour mean
‡running 8 hour mean or 1 hour mean

The pollutants included in the Air Pollution Public Information System (APPIS) are those for which there are potentially acute health effects. The three pollutants included in the National Air Quality Strategy for which only chronic health effects are known, benzene, 1,3-butadiene and lead, are therefore excluded from the APPIS.

Inhalation of the pollutants included in the APPIS can be fatal, for healthy adults, at very high concentrations - far higher than those measured in polluted air. At concentrations found in ambient air, the main effects will be to susceptible individuals such as those with cardiovascular and/or pulmonary illness, including asthma. A recent study published in the Lancet (Knzli et al. 2000) found that 6% of deaths in France, Switzerland and Austria were triggered by air pollution. The study also found that air pollution accounted for increased levels of bronchitis in children and adults and triggered more than half a million asthma attacks in the three countries. The individual effects of the five pollutants included in APPIS as noted by the DETR's Expert Panel on Air Quality Standards are detailed in

the next paragraph.

Carbon monoxide reduces the oxygen-carrying capacity of the blood by binding preferentially to hæmoglobin. In extreme cases this can lead to loss of consciousness and death. Nitrogen dioxide is an irritant gas which causes serious and sometimes fatal lung damage at very high concentrations. At lower concentrations it causes inflammation of the lungs and may increase the sensitivity of individuals to allergens. Ozone is another irritant gas, which at high concentrations can lead to irritation of the eyes and nose and inflammation of the airways. Particulates (PM_{10}) have been shown to cause inflammation of the lungs thus provoking asthma attacks and precipitating episodes, which could be fatal, of cardiovascular and pulmonary illness in susceptible individuals. Sulphur dioxide is an irritant gas which stimulates the nerves in the nose, throat, and airways of the lung leading to a reflex cough, irritation, the chest feeling tight and possibly a narrowing of the airways. At very high concentrations this can lead to breathing difficulties and even death.

1.2 Air Pollution in Oxford

Traffic-related air pollution in Oxford is fairly high. Estimates of Oxford air quality in the middle 1990s are comparable to values recorded in much larger cities (Mr. R Pittman, Oxford City Council, private communication). Figure 1.1[3] shows concentrations of various pollutants measured in the centre of Oxford[4] in January 1997. The high levels of air pollution and congestion in the centre of the city led to the introduction of the Oxford Transport Strategy (OTS) by the City and County Councils in June 1999. This aimed to improve the general environment in the centre of the city by pedestrianising the main shopping street (Cornmarket) and restricting traffic on the surrounding streets. It also aimed to dissuade people from driving into Oxford by improving the park and ride schemes on the outskirts of the city, improving bus services by giving buses priority and providing bus lanes, and improving facilities for cyclists, with both dedicated cycle lanes and convenient

[3]Data for graph is from AEA Technology's National Environmental Technology Centre (NETCEN) - see http://www.aeat.co.uk/netcen/airqual/data/auto/ox.html

[4]The monitoring station is located in the Town Hall on St. Aldates.

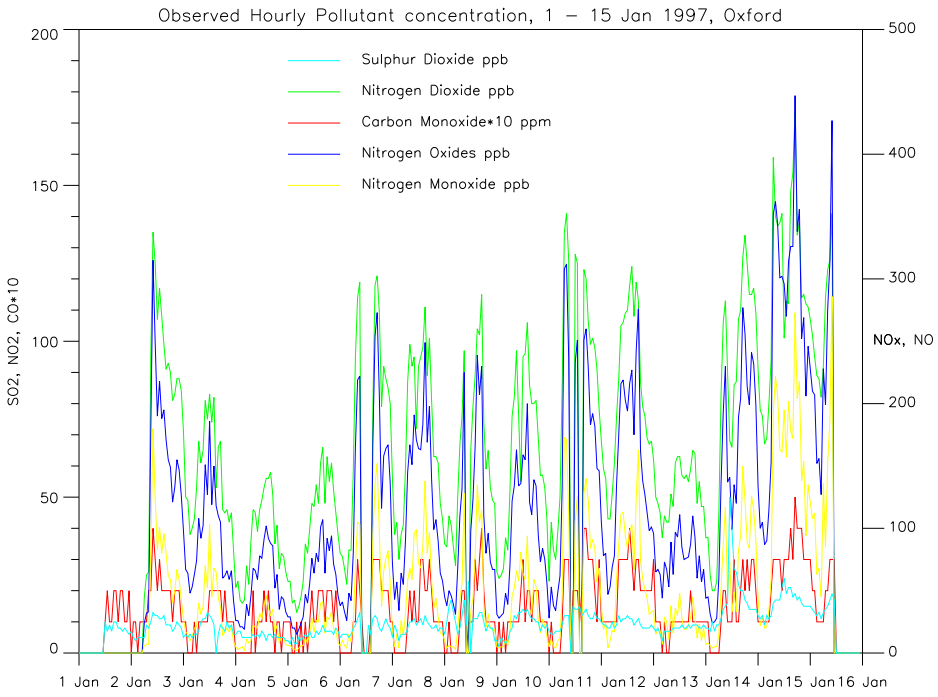

Figure 1.1: Pollution levels (averaged hourly) in Oxford, January 1997

secure parking.

In order to monitor the effect of implementing the OTS, the City and County Councils have initiated a partnership project with groups from Oxford and London Universities. This project, called EMITS (Environmental Monitoring of Integrated Transport Strategies), will assess the effects of the transport, environmental, public health and economic effects of the OTS. EMITS is a five year project which commenced in March 1996.[7]

In April 1998 Oxford was selected as one of 6 European cities to take the lead in an initiative aimed at tackling air pollution in cities by only allowing 'green' vehicles access to city centres. The project, ALTER (Alternative Traffic in Towns), aims to promote the use of zero or low emission vehicles both in the public and private sectors.[8] As part of the project electric buses and gas powered buses, both compressed natural gas and liquefied

[6]Map copied from Oxfordshire County Council's leaflet about the Oxford Transport Strategy.

[7]Further details of EMITS can be found at http://www.oxfordshire.gov.uk/emitsidx.htm

[8]See press release from the Department of the Environment, Transport and the Regions at http://www.coi.gov.uk/coi/depts/GTE/coi0748e.ok

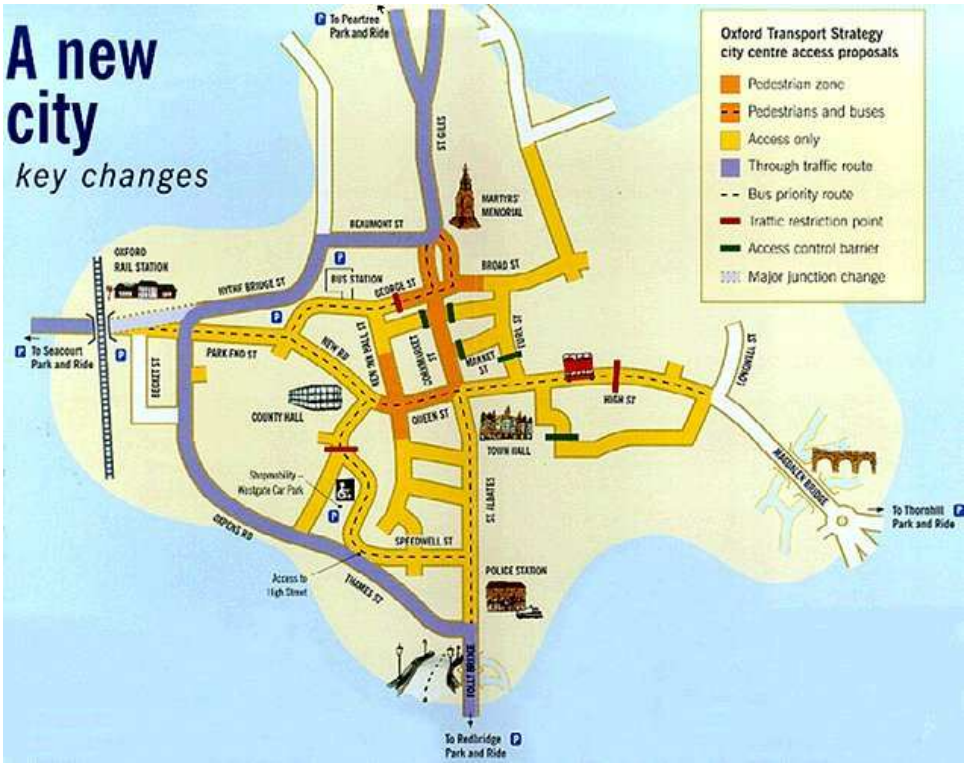

Figure 1.2: A map showing the changes that were implemented as part of the Oxford Transport Strategy.[6]

petroleum gas, have undergone trials in Oxford. Also, buses in Oxford have been fitted with efficient particle traps and catalysts to reduce pollution and many now run on ultra low sulphur diesel.

1.3 Sources of Urban Air Pollution

Urban air pollutants arise from a wide range of sources, although the majority are released from combustion processes. In the UK the source of a sizeable fraction of primary pollutants, those emitted directly into the atmosphere rather than formed in the atmosphere by chemical reactions, is from motor vehicles. 90% of CO emissions come from motor vehicles, as does 50% of all NO and NO_2 emissions in urban areas. Traffic is also a source of hydrocarbons and particulates. The level of emissions from vehicles depends on many factors, such as the type of fuel used, the fuel to air ratio, the type of vehicle, the size

of engine, the age of the vehicle, how well maintained it is, whether it is accelerating or not, which leads to difficulties in predicting the total pollution output from motor vehicles. Emissions of hydrocarbons, and in particular volatile organic compounds (VOCs), are even more difficult to estimate since they originate from a wide range of sources including incomplete combustion of fossil fuels and leakage and evaporative losses from engines and storage areas.

Traffic is not the main source for all pollutants and is often only one of many sources. In the UK the main source of SO_2 is the burning of fossil fuels, mainly coal and heavy fuel oil, in industry and power stations (such as the one at Didcot, which is predominantly coal fired[9]). Emissions of SO_2 from transport, mainly from diesel vehicles, account for just 2% of total emissions in the UK. However, power stations are usually located in rural areas and have high chimneys for dispersal of pollutants, and so unless a city or town is downwind of such a power station at the point where its plume reaches ground level, other sources of SO_2, such as industry, commerce and even domestic use of coal and oil, and to some extent transport, dominate in urban areas.

Ozone and other photochemical oxidants, such as peroxyacetyl nitrate (PAN), are generated by chemical reactions between major and minor primary pollutants. Many of these reactions, in particular those between oxides of nitrogen and hydrocarbons which form O_3, are driven by sunlight. These reactions take place on a range of timescales from minutes to hours, which cause difficulties in predicting the concentrations of pollutants in urban, and rural, air.

1.4 Current Monitoring Techniques

Air pollution monitoring in the UK is undertaken by the National Environmental Technology Centre (NETCEN), which is part of AEA Technology, on behalf of the DETR. NETCEN runs three automated monitoring networks - the Automatic Urban Network (AUN),

[9] SO_2 emissions from Didcot power station were 26,000 tonnes in 1999. Source is the Environment Agency's pollution inventory.

the Automated Rural Network (ARN) and the Hydrocarbon Network. The AUN monitors SO_2, NO_x, CO, O_3 and PM_{10} using a variety of techniques. SO_2 is measured using UV fluorescence, NO_x (NO_2 + NO) and NO_2 are measured by ozone chemiluminescence (which is the reference method specified by the EC NO_2 Directive), CO is measured by IR absorption (gas filter correlation), O_3 is measured by UV absorption spectrophotometry and PM_{10}s by a tapered element oscillating microbalance. The ARN mainly measures O_3, but also NO_x and SO_2, with a few sites also measuring PM_{10}. Concentrations of these pollutants are measured by the same techniques as are used in the AUN. The Hydrocarbon Network measures 26 hydrocarbon species, including benzene and 1,3-butadiene, using continuous gas chromatography.

NETCEN provide hourly, and in some cases 15 minute, averages of the concentrations of the measured pollutants. The sampling time for the gas chromatographs is 30 minutes in each hour. For the other measurements the instantaneous data from the instruments is logged every 10 seconds, from which 15 minute and hourly averages are derived.

In addition to these techniques, simple 'wet-chemical' analysis techniques are still used for some measurements. Two examples of this type of measurement are SO_2 acidmetric bubblers and NO_2 diffusion tubes. In the former ambient air is drawn through a bubbler containing a dilute hydrogen peroxide solution and samples are measured, using ion chromatography, on a weekly basis. In the latter air diffuses along a 10 mm diameter, 70 mm long tube and is absorbed onto stainless steel mesh disks coated in triethanolamine at the far end. Samples are collected over periods of a week to a month and then analysed colourimetrically.

All of these in-situ methods can only monitor polluted air at one point in space, which can lead to ambiguities when assessing air quality over an extended region, such as a city centre or road intersection. The location of the monitoring device then becomes a critical factor as a sensor mounted high on a building will give a very different result to that placed at the kerb-side. The sites used for the automated monitoring networks are classified as one of six types depending on their location. The six types are 'Urban Background', 'Urban

Centre', 'Roadside', 'Urban Industrial', 'Suburban' and 'Rural'. However, the problem remains that point measurements may still be unrepresentative, particularly when the results are used to determine health risks through exposure.

To some extent diffusion tube measurements can be used to overcome these limitations, since their very low cost means that many tubes can be placed around an area of interest. However, each tube is specific to only one pollutant and they are less sensitive than the techniques used for the automated networks. Another disadvantage is that they can only provide long-term, a week to a month, averages which can make the results difficult to interpret.

A disadvantage of the ozone chemiluminescence method used to measure NO_x, which uses molybdenum NO_2 to NO converters, is that NO_y species, such as N_2O_5 or NO_3, can register as NO_2, thus leading to false detection.

1.5 Optical Remote Sensing Techniques

Optical absorption techniques overcome the problems associated with point measurements by integrating over long paths (anywhere from 5 m to 20 km depending on the particular technique and location) in order to measure average ambient pollution concentrations along the length of the optical beam. These path-averaged measurements allow more accurate exposure levels to be determined.

Optical remote sensing techniques also have the advantage that the pollutants being measured do not react with the sampling system, a beam of light, and so highly reactive gases can be measured by these techniques. Also, no errors due to chemical interactions of the measured pollutants with the monitoring apparatus are introduced. All these techniques have short measurement times ranging from a second to a few minutes.

There are several different optical remote sensing techniques in use. The common ones are diode laser remote sensing, LIDAR (LIght Detection And Ranging), DIAL (DIfferential Absorption LIDAR), DOAS (Differential Optical Absorption Spectroscopy) and FTIR (Fourier Transform InfraRed) spectroscopy. There are also a few instruments that

have been used to measure air pollution which use other optical techniques. Three of these, PerspectUV, FEAT and FTUV will be described in this section.

Diode laser remote sensing (Hardin 1998b) measures the amount of laser light absorbed over an atmospheric path, in order to calculate the average concentration of a gas along the optical path. It uses a low power (approximately 100 mW) diode laser as the source, which is expanded and collimated by a telescope and directed over an optical path of up to 1 km in length (which may include being reflected off a plane mirror or retroreflector) to a telescope which condenses the beam and directs it onto a photodiode detector. The system has short, 1 second, response times and is highly sensitive; it has a detection limit of an absorptance of 10^{-5}, which corresponds to detection limits of less than 1 ppmv for most gases. This technique can only measure one gas at a time, and a different laser must be used for each gas, although advances in laser technology mean that diode lasers able to scan across a range of wavelengths and thus detect several species with the same laser, though not simultaneously, may soon be available. Diode lasers are available in the visible and near-infrared (600 nm-2 μm or 16700 cm^{-1} to 5000 cm^{-1}) and can detect a range of gases such as CO_2, NO, NO_2, CO, CH_4, NH_3, HF, and HCN.

Lidar (Leonelli 1995) uses the atmospheric backscattering of pulsed laser beams to determine, by using the time delays of the return pulses, variations in gas concentrations along a line of sight. By making measurements along several sight lines a 3-D map of pollutants can be assembled. Lidar is less sensitive and uses higher power (several kilowatts) lasers, which are large and expensive, than the diode laser method. Lidar is mainly used to measure aerosols and particulates in the atmosphere, along with physical parameters such as turbulence, however by using a UV light source and detecting Raman-shifted return light both water vapour and ozone can be detected by this technique.

The dial technique (Moody 1999) extends the usefulness of lidar by enabling the measurement of pollutants such as NO, NO_2, SO_2, O_3, benzene and toluene. In dial, laser pulses are transmitted at two wavelengths; one is tuned to the centre of an absorption line of the gas of interest and the second is tuned to a nearby wavelength where the target gas

has little absorption. By measuring the ratio of the backscatter at the two wavelengths as a function of distance, the concentration of the target gas along the line of sight can be calculated. 3-D maps of pollutants, over ranges of up to 10 km, can be created in the same manner as for lidar. This technique provides high sensitivity (in the ppbv range) measurements of the limited range of pollutants it can detect. Dial has been mainly used in the ultraviolet, however the development of tunable optical parametric oscillator (OPO) laser technology is allowing access to the infrared where measurements of CO, CO_2, and hydrocarbons can be made. The technique, however, can only measure one gas at a time.

Doas operates in the ultraviolet (UV) and visible wavelengths over pathlengths of 100 m to 20 km. A broadband of UV and visible light, from a xenon arc lamp for example, is collimated and expanded before passing through the atmosphere to a telescope which collects the light and feeds it into a grating spectrometer. Either software (Becker 1996) or hardware (Reisinger et al. 1998) is used to separate the spectrum into low and high frequency signals. Ratioing the two signals removes all low resolution features and produces a spectrum which only contains the differential absorptions from trace gases and xenon emission lines. The differential absorption of a molecule is defined as the part of the total absorption of that molecule which varies 'rapidly'[10] with wavelength. This technique enables the simultaneous measurement of a range of gases, including NO, NO_2, SO_2, O_3, NH_3, benzene, toluene and halogen oxides.

Open path FTIR spectroscopy operates in the infrared (IR) over pathlengths of 5 m to 2 km. A collimated, broadband IR light beam is directed through the volume of the atmosphere that is to be sampled into a telescope which feeds it into a FTIR spectrometer which disperses and detects the different IR wavelengths. This technique enables the simultaneous measurement of a range of gases, including CO, CH_4, NO, NO_2, SO_2, O_3, NH_3, benzene and other organic molecules. All gases included in the NAQS are detectable with open path FTIR spectroscopy.

[10]The meaning of 'rapid' depends on the observed wavelength interval and the width of the absorption bands to be detected.

PerspectUV (Hardin 1998a) is an all-solid-state correlation interferometer. It operates in the UV over a path of 10 m to 1 km. It can make simultaneous measurements of up to 16 gases by using 4 co-located receivers and a dedicated sensing channel for each gas. The detectable gases include NO, NO_2, SO_2, O_3, formaldehyde and chlorine.

FEAT (Bishop & Stedman 1996), which stands for Fuel Efficiency Automobile Test, is an instrument based on NDIR (non-dispersive infrared) spectroscopy. It measures the ratios of CO:CO_2, hydrocarbons:CO_2 and, by using NDUV spectroscpy, NO:CO_2 in vehicle exhausts. The beam is setup across a single lane of traffic and the breaking of the beam by individual vehicles causes it to make a measurement. The system can only measure the gas concentration ratios, and smoke opacity, and not the actual concentrations of the gases. However, these data can be used to determine whether a vehicle is operating efficiently or not.

The FTUV instrument (Hirst et al. 1998) is an open path Fourier transform ultraviolet spectrometer which was developed between 1995 and 1998 inclusive by a collaboration between Siemens, Shell Research, St. Andrews University, BG Technology, Dräger and Halbo Optics. However, it is not based on a Michelson interferometer and has no moving parts. Instead it uses two Wollaston prisms to form an interferogram on a camera. The interferogram is a set of interference fringes as a function of space, not time (as for a Michelson interferometer). It uses a deuterium bulb at the focus of an off-axis parabolic mirror as a UV source, which is then expanded with an afocal telescope. The UV beam is collected at the other end of the open path with an identical telescope and fed into the spectrometer. The instrument is capable of detecting H_2S, SO_2, NH_3, benzene and vehicle exhaust gases.

The technique of FTIR spectroscopy was chosen for this study because it enables the simultaneous measurement of all the pollutant gases included in the NAQS, as well as a wide range of other gases.

1.6 Fourier Transform Spectroscopy

Fourier transform spectrometers (FTS) can operate in the infrared, visible or ultraviolet depending on the optics used. The infrared region, and specifically the mid-infrared region of 4 μm to 16 μm or 625 cm^{-1} to 2500 cm^{-1}, was chosen for this study because many molecules[11] have an infrared spectrum and so can be detected by FTIR spectroscopy. Infrared spectral lines are due to vibration and rotation of the atoms in a molecule. Atomic species, such as helium, and homonuclear diatomic species (e.g. O_2, N_2, Cl_2) have no infrared absorption lines and so cannot be detected by this technique. Since N_2, O_2, and argon are the three most abundant species in the atmosphere, it is convenient that they do not absorb in the infrared and so do not interfere with measurements of the species of interest.

Most FTSs, including the one used in this study, are based on the Michelson interferometer (see figure 1.3). A brief outline of how such instruments operate is included in this section. The design of FTIR spectrometers is discussed in greater detail in chapter 2 and extensively in e.g. (Beer 1992) and (Griffiths & de Haseth 1986).

Infrared light from a broadband continuum source (such as a Nernst Globar or lamp) is collimated before it impinges on a beamsplitter. The beamsplitter is a plate which has approximately equal transmittance and reflectance (essentially a half-silvered mirror). It splits the incoming radiation into two beams of approximately equal intensity, each of which is reflected off a plane mirror and recombined at the beamsplitter. One of these mirrors is fixed, the other moveable, and so an optical path difference (OPD) between the two beams can be introduced by changing the separation of the beamsplitter and moveable mirror. When the beams recombine at the beamsplitter, they interfere constructively or destructively depending on the OPD and the wavelength of the light. Changing the OPD, by moving one of the mirrors, causes the recombined beams to periodically interfere constructively and destructively, where the period depends on the wavelength of the light. The

[11] e.g. CO_2, CO, NO_2, NO, O_3, SO_2, H_2O, CH_4, benzene, 1,3-butadiene etc.

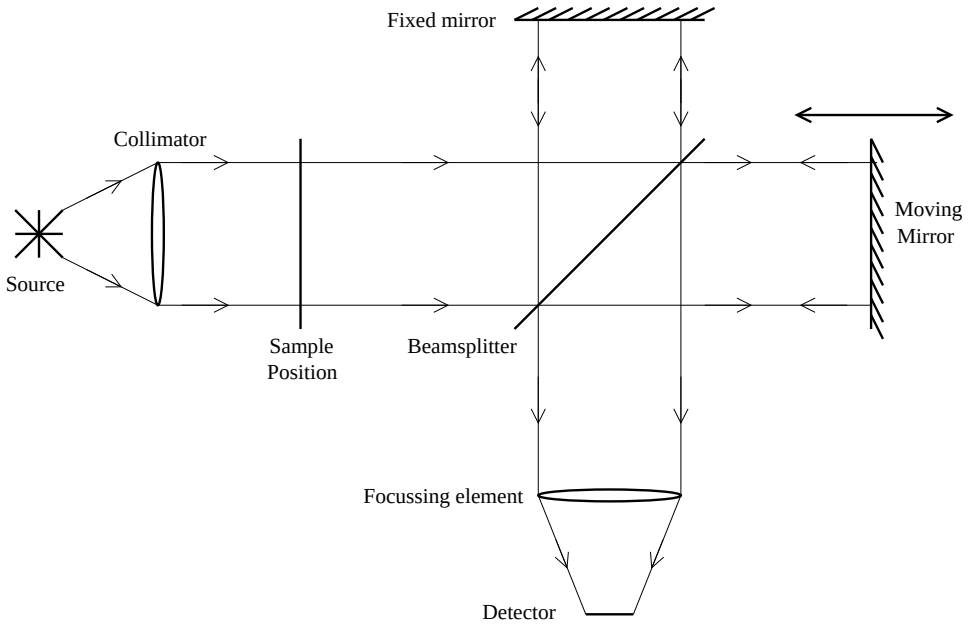

Figure 1.3: Layout of a Michelson Interferometer

point where all wavelengths interfere constructively is called the *zero path difference*. The interference pattern thus created consists of a superposition of sine waves, each of which corresponds to a wavelength in the incoming beam. If the intensity of light is measured as a function of the OPD, the result is the Fourier transform of the intensity of light as a function of wavenumber (cm^{-1}); a conventional spectrum.

The intensity modulated signal, or *interferogram*, produced by the beamsplitter is recorded by a detector and a computer is used to perform the Fourier transform and display the result as a spectrum of intensity versus wavenumber or wavelength (wavenumber = $wavelength^{-1}$).

1.6.1 Advantages of FTIR Spectroscopy

Open path FTIR spectroscopy has the advantages shared by other remote sensing techniques, namely path-averaged measurements, no chemical reactions between the monitoring apparatus and the gases being measured and short measurement times. It also has the advantage of being able to measure the concentrations of a wide range of gaseous pollutants

simultaneously. The use of mirrors, which can bend light round corners and change the height levels of the measurement, in the optical path enables a wide range of different paths to be covered (Sandridge & Peterson 1995) and increases the versatility of the technique over current methods.

Fourier transform spectrometers have a number of advantages over dispersive spectrometers. These are

- Multiplex, or Fellgett, advantage - All wavelengths are measured simultaneously using frequency-division multiplexing in which the signals are impressed on carriers of different frequencies. In dispersive spectrometers the wavelengths are measured successively.

  The introduction of digital detector arrays has allowed 'polychromators' to measure multiple spectral lines simultaneously. This is a *multichannel* advantage, rather than a multiplex advantage, and can also be achieved by FTSs with detector arrays.

- Throughput, or Jacquinot, advantage - For the same resolution FTSs (and Fabry-Perot interferometers) have a higher throughput, or *étendue*, than dispersive spectrometers.

- Connes advantage - the instrument lineshape (ILS), and resolution, of an ideal FTS is constant on a frequency scale (beam divergence in real FTSs causes the ILS to have a weak dependence on frequency see section 2.1.3). The ILS of a dispersive spectrometer has a strong frequency dependence.

- Frequency accuracy - Very accurate calibration of wavenumber scale. The wavenumber scale of a FTS is derived from HeNe laser reference beam. This is very stable and its wavelength is known very accurately, hence the very accurate wavenumber calibration. Dispersive spectrometers make relative measurements and must therefore be provided with a set of wavelength calibration sources.

- Negligible stray light - Stray light can be a problem in dispersive spectrometers.

1.7 Applications of Long Path Fourier Transform Spectroscopy

The technique of long path FTIR spectroscopy has been under development for over twenty five years. Following earlier work using dispersive infrared spectrophotometers and multipass, long, gas cells to measure trace atmospheric pollutants, long path FTIR spectroscopy was first used for these measurements in the early 1970s (Hanst, Lefohn & Gay, Jr 1973). The early work on long path FTIR spectroscopy (Tuazon et al. 1978) (Hanst, Wong & Bragin 1982) used multipass gas cells, for example White cells (White 1942), and extractive gas sampling to monitor polluted air.

Open path FTIR systems, where the sample of air to be measured is not enclosed in a cell, were first used in 1977 (Herget & Brasher 1979). These early measurements included HF and SiF_4 over gypsum ponds, CO and total hydrocarbons from jet engines and SO_2, CO, CH_4 and total hydrocarbons from an oil refinery, which illustrates some of the wide range of uses that open path FTIR systems are put to. Although open path FTIR was first demonstrated in 1977, extractive long path FTIR was more common until the early 1990s and it is still used today for some measurements, such as process monitoring in industry (Spellicy et al. 1995).

The development of open path FTIR spectroscopy has continued apace with improvements in the technology, in particular computing technology, and techniques, which have led to improved detection sensitivities and a wider range of detectable gases. Most of the development work has been carried out in the United States of America. The main impetus behind this has been the implementation of the 1990 Clean Air Act Amendments (CAAA) by the EPA. The act increased the number of hazardous air pollutants (HAPs) for which reporting is mandatory from 7 to 189 and has increased industry's needs for ambient air monitoring. Open path FTIR spectroscopy has the potential to detect those pollutants which are gaseous, or are volatile under typical emission conditions, which includes a large fraction of the listed HAPs.

Long path FTIR techniques are now frequently employed alongside gas chromatog-

raphy systems to monitor emissions from industrial sites in the United States (Marshall et al. 1994). Indeed in January 1997 the United States Environmental Protection Agency (EPA) published a reference method for monitoring atmospheric gases by FTIR; Compendium Method TO-16: Long-Path Open-Path FTIR Monitoring of Atmospheric Gases (Russwurm 1997). However, long path FTIR techniques can still be improved further.

Open path FTIR techniques have been used to investigate the composition of volcanic plumes (Chaffin et al. 1995), biomass fires (Yokelson, Griffith & Ward 1996), vehicle emissions (Bradley et al. 2000) and jet engines (Lindermeir, Haschberger & Geatches 1998) as well as a wide range of industrial sites. All these measurements use active FTIR spectroscopy, where an infrared source is placed at one end of the path and the gases being monitored absorb some of the infrared light and transmit the rest. However, measurements can also be made using passive FTIR spectroscopy, where the infrared emissions come from the gases being analysed and can be detected if they are at a different temperature to the background. This technique has been used to investigate volcanic emissions (Chaffin et al. 1995) and the gases emitted from industrial smokestacks (Herget 1982) (Carlson, Hayden & Telfair 1988).

Although most of the development work on open path and long path FTIR techniques has taken place in the United States, some work has been carried out in Europe (Haus et al. 1994) (Schäfer et al. 1995) and long path FTIR techniques are used in several research projects. However, use of long path FTIR techniques in the UK is very limited. It has been used to measure volcanic plumes by a collaboration between Cambridge University and the Open University (Horrocks et al. 1999) and for ground based atmospheric remote sounding, mainly of the stratosphere, by groups at the National Physical Laboratory (NPL) (Goldman et al. 1999) and the Rutherford Appleton Laboratory (RAL). The group at NPL have also carried out stack gas measurements and open path measurements with a view to validating the techniques through calibration and traceability. A group at Reading University have utilized the method to investigate the composition of exhaust fumes from aircraft gas turbine engines (Hilton & Lettington 1997). A student, Nick Davies, in the group carried out

measurements of carbon monoxide, methane and ethyne in car exhausts (Davies, Hilton & Lettington 1997), carbon monoxide during rush hour (at a busy roundabout), ammonia and methane in a cow shed on a dairy farm and methane from an industrial smokestack (Davies, Lettington & Hilton 1997). BOC use an FTIR spectrometer to continuously monitor gases flowing through a gas cell for impurities.

1.8 Analysis of Spectra

Analysing the spectra recorded by long path FTIR spectroscopy is as important as measuring the spectra. In order to understand how the concentration of an absorbing gaseous species in the optical path can be calculated from the recorded spectrum, it is necessary to know some basic radiative transfer theory.

Assuming scattering and atmospheric emission is negligible, the transmission of light along an atmospheric path is given by

$$I(\tilde{\nu}) = I_0(\tilde{\nu}) \exp\left(-\int k(\tilde{\nu})\rho \, dl\right) \tag{1.1}$$

where $I(\tilde{\nu})$ is the intensity of radiation at wavenumber $\tilde{\nu}$ detected by the spectrometer, $I_0(\tilde{\nu})$ is the intensity incident on the atmospheric path, $k(\tilde{\nu})$ is the absorption coefficient of the gaseous species, of density ρ, present in the atmospheric path of length l. Equation 1.1 encapsulates the law of absorption, also known as *Lambert's law* or *Bouguet's law*. For a homogeneous path, such as can be assumed[12] is the case for long path FTIR measurements, this equation can be approximated by

$$\tau(\tilde{\nu}) = e^{-k(\tilde{\nu})\rho l} \tag{1.2}$$

where $\tau(\tilde{\nu}) = I(\tilde{\nu})/I_0(\tilde{\nu})$ is the transmission through the atmosphere. This is true for a single absorber in the path; for multiple absorbing species the individual transmittances are multiplied together.

[12]The path may not actually be a homogeneous path, it may have a plume of pollution passing through a small segment of its length, however, it is assumed to be homogeneous and concentrations of the pollutant are averaged over the whole pathlength.

Most of the analysis techniques used to determine the concentration of absorbing gaseous species in the measured optical path do so by applying *Beer's law*. This is based on equation 1.2 and can be stated as follows:

$$A(\tilde{\nu}) = -ln[\tau(\tilde{\nu})] = k(\tilde{\nu})Cl \tag{1.3}$$

where $A(\tilde{\nu})$ is the absorbance, and C is the concentration of the absorber in the atmospheric path. The concentration, in ppmv, is related to the density, in kgm^{-3}, by

$$C = \left(\frac{273}{T}\right)\left(\frac{p}{101.33}\right)\left(\frac{22.4}{M_r}\right)10^6\rho \tag{1.4}$$

where T is the temperature in K, p is the pressure in kPa, and M_r is the relative molecular mass in $\mathrm{kg{\cdot}kmol}^{-1}$.[13] Therefore equations 1.2 and 1.3 are equivalent.

Several analysis techniques have been used, the most common of which is classical least squares (CLS). This technique is the one described in the EPA's Compendium Method TO-16 (Russwurm 1997). Other techniques used include partial least squares, principle component analysis, spectral subtraction, peak height calculations and peak area calculations.

CLS analysis works by fitting a linear combination of calibration spectra to the measured spectrum using the statistical least squares technique. The calibration spectra are generated either by measuring known concentrations of each gaseous species over a known pathlength in the laboratory, or by calculation from a spectral line database such as HITRAN (Rothman et al. 1992). In the latter case the form of the instrument lineshape (ILS) of the spectrometer, a function that describes the effect the instrument has on the spectrum, must be known. In the former case, the spectra should be recorded with the field instrument if possible. In either case the set of calibration spectra should contain spectra for each gaseous species present in the measured spectrum at a range of temperatures, pressures and concentrations corresponding to the conditions likely to be encountered in the field. All the absorbing species in the chosen spectra range are fitted simultaneously.

[13] N.B. The standard molecular volume at 273 K and 1 atmosphere, or 101.33 kPa, is 22.4 $\mathrm{m}^3\mathrm{kmol}$.

In spectral subtraction an operator interactively subtracts a calibration spectrum for each absorbing species from the measured spectrum, scaling it as necessary in order to completely remove the associated spectral feature in the measured spectrum. Since the concentration and pathlength at which the calibration spectrum was recorded and the pathlength over which the measured spectrum was recorded are known, the scaling factor can be used to calculate the concentration of each gaseous species present.

In peak height calculations the absorption coefficient for the peak frequency of each gaseous species present are calculated from the slope of the best fit line through a Beer's law plot of absorbance versus the product of concentration and pathlength, which is created from a set of calibration spectra. The coefficients are then applied to the peak heights in the measured spectrum and the concentration of each gaseous species calculated using Beer's law.

All these techniques must be applied to absorbance spectra. These can be calculated from the measured single beam spectra as follows.

$$A(\tilde{\nu}) = -ln[\tau(\tilde{\nu})] = -ln[I(\tilde{\nu})/I_0(\tilde{\nu})] \tag{1.5}$$

where $A(\tilde{\nu})$ is the absorbance spectrum, $\tau(\tilde{\nu})$ is a transmission spectrum, $I(\tilde{\nu})$ is the single beam spectrum and $I_0(\tilde{\nu})$ is a background spectrum. It is therefore necessary to generate a background spectrum for each single beam spectrum (the same background spectrum may be used for several single beam spectra where the atmospheric conditions have not changed between measurements).

The EPA's Compendium Method TO-16 lists four different methods for acquiring a background spectrum;

- the upwind background
- the cross-path background
- the zero target gas background
- the synthetic background

each of which have their own problems.

The upwind background can be used where the gases of interest are the emissions from a particular site. In this case a spectrum is taken upwind of the site, and so should not contain any emissions from the site. However, it will contain the absorptions of other gases whose concentrations may vary during the measurement period, in particular water vapour, and thus introduce ratioing errors into the absorption spectra created with it, as well as erroneous variations in any gases which are emitted both at the site and upwind of the site.

The cross-path background is recorded along a boundary of the site from which emissions are being measured, with the wind blowing parallel to the optical path. It suffers from similar problems to the upwind background. Also, if the wind speed is low, then emissions from the site may diffuse into the optical path.

The zero target gas background is only possible to record if the gases of interest are transient. It is mainly used where emissions from a site are measured over several hours. If one of these recorded spectra contains no absorption by the target gas, then this spectrum can be used as a background for the other spectra. This technique suffers from the problem that absorptions from water vapour and other gases that are present in the atmosphere may vary and thus ratioing errors may be introduced into the absorption spectra thus created. Also it cannot be used for gaseous species which are always present in the atmosphere, such as CO.

The synthetic background can be created in two ways. The first is to take one of the measurement spectra which includes some absorption by the target gas, or gases. The absorption features of the target gas(es) are removed by interpolating between points on the baseline where there is no absorption by the target gas(es). This may be difficult when absorption between a target gas and another gas overlap. The second way is to generate the spectrum from a spectral line database, such as HITRAN. The main difficulty with this method is matching the intensity and shape of the single beam spectrum, the form of the ILS, and the absorbance of the non-target absorbant species in the single beam spectrum.

1.9 Aim of this Study

The aim of this study is to investigate the potential for making high-sensitivity simultaneous measurements of a number of gaseous pollutants with a portable FTIR spectrometer. As such it combines the acquisition of novel field measurements of atmospheric pollution with the development of enhanced data analysis methods.

Optimal estimation retrieval techniques (Rodgers 1976) have been developed in the Department of Atmospheric Physics for over twenty years. Together with an advanced radiative transfer model (Dudhia 1997) they provide an enhanced ability to obtain gas concentrations even in the presence of overlapping absorptions from contaminants such as water vapour and carbon dioxide. The innovative use of optimal estimation to retrieve the intensity and shape of the single beam spectrum together with the concentrations of the target species has removed the need for background spectra to be acquired. An additional advantage of this analysis technique is that the integration of the radiative transfer model with the retrieval obviates the requirement to have a database of calibration spectra available. Instead the spectra are calculated as they are required by the retrieval process and for the specific conditions of the measurement.

Early open path FTIR studies operated at a high spectral resolution of up to 0.06 cm^{-1} (Herget & Brasher 1979). More recent studies have used lower resolutions of 0.5 cm^{-1} to 2.0 cm^{-1} (Yokelson et al. 1997) (Bradley et al. 2000) in order to use smaller, more portable spectrometers. This has led to an inevitable loss of sensitivity in the measurements. It is therefore intended to operate this study's commercial lab spectrometer at its highest resolution; 0.2 cm^{-1}.

It should be noted that the urban boundary layer to which the title of this work refers and in which the measurements described herein were made can be defined as the portion of the atmosphere whose climate characteristics are modified by the presence of a city at the surface.

1.10 Thesis Outline

This thesis presents in chapter 1 a brief introduction to air pollution in the United Kingdom and Oxford in particular, together with a description of the current monitoring techniques used in the UK and an outline of optical remote sensing techniques. A brief description of Fourier transform spectroscopy and its use in remote sensing together with a short discussion of common techniques for the interpretation of spectra is also included.

The operation of the Fourier transform spectrometer used in this study is discussed more extensively in chapter 2. Descriptions of the other items of equipment used in this study and the experimental arrangements used are provided.

Three issues relating to the performance of the spectrometer, which were encountered during the initial performance testing, are described in chapter 3. Their origins and possible solutions are discussed.

An outline of retrieval theory together with a discussion of its implementation in this study are covered in chapter 4.

Laboratory measurements of the absorption cross-sections of two hydrocarbons, benzene and 1,3-butadiene, and the potential for detecting them are set out in chapter 5.

Chapter 6 contains the results and main findings of this study. The detection limits of various pollutants are determined using simulated data. Typical retrievals for five pollutants are described and the results of the work carried out reported. An intercomparison of the methods and equipment used in this study with those used by the National Physical Laboratory are detailed.

The conclusions of this study are summarized and suggestions for further work put forward in chapter 7.

Chapter 2

Equipment

2.1 Spectrometer

The Fourier transform infrared spectrometer used in this study was a Perkin-Elmer Spectrum 2000. This is a standard lab spectrometer, which can be used in several different configurations due to the flexible design and range of accessories available. The range of beamsplitters, sources and detectors available for the spectrometer enables it to be operated over the spectral range of 30 cm^{-1} to 15,000 cm^{-1}. It has four possible sample station positions, and can also be used with an external source. The specification of this spectrometer, as used in this study, is as follows:

Resolution	0.2 cm^{-1} to 64 cm^{-1}.
Spectral range	Limited to 370 cm^{-1} to 7,800 cm^{-1} by the beamsplitter used in this study.
Beamsplitter	Optimised KBr (Potassium bromide) beamsplitter, with a spectral range of 370 cm^{-1} to 7,800 cm^{-1}.
Source	A voltage stabilized, air-cooled wire coil which is temperature stabilized to 1350 K provides broadband radiation in the mid to far infrared spectral region.
Detectors	A mid infrared (15,600 cm^{-1} to 370 cm^{-1}) FR-DTGS (Deuterated TriGlycine Sulphate) detector. A liquid nitrogen cooled (to 77 K) narrow band (10,000 cm^{-1} to 700 cm^{-1}) MCT (Mercury Cadmimum Telluride) detector.
Scan speed	The optical path difference (OPD) velocity is variable between 0.05 $cm{\cdot}s^{-1}$ and 5.0 $cm{\cdot}s^{-1}$.
Filterwheel	8 position software controlled filterwheel.
Emission port	Back left position. Has KBr window.
Sample station	Front left position. Has KBr window and dual detector station.

Size and weight	The optical module is 50.0 cm long, 42.0 cm high, 63.0 cm deep, and weighs 62.5–71.5 kg. The sample compartment module (which includes the detectors) is 41.0 cm long, 32.0 cm high, 63.0 cm deep, and weighs 34.0 kg.

The spectrometer is controlled by a proprietary computer program, Spectrum for Windows, which runs in the Windows environment on a PC. The Fourier transforms are performed on a transputer (parallel processors) card in the PC. The spectra are saved in Perkin-Elmer's own file format and converted to ASCII format for use with the retrieval algorithm.

2.1.1 Perkin-Elmer Spectrum 2000 Optics

The Perkin-Elmer Spectrum 2000 optics are housed in a sealed and desiccated module, which is at atmospheric temperature and pressure. It is possible to purge the optical module with dry, oil-free nitrogen or air, but this is not necessary for the long path measurements carried out in this study. Two KBr windows, which are 47.5 mm in diameter and 5.0 mm thick and are angled at 3° to the infrared beam in order to reduce channelling, seal the optical module. One allows infrared light from an external source to enter the optical module, and the other allows light that has been modulated by the interferometer to exit the optical module into the sample compartment.

The optical layout is shown schematically in figure 2.1, and the optical path through the spectrometer is as follows: broadband infrared radiation from either the internal source or external source is brought to a focus between the B-stop and the J-stop. If an optical filter is required, it can be placed in the filter wheel which is located between the focus of the beam and the J-stop. The diverging infrared beam is then collimated before passing through the interferometer[1]. The modulated beam is directed to the lower, detector, level by two flat periscope mirrors, where further mirrors direct the beam to the appropriate sample station. The beam then passes through a 200 mm sample compartment, where it has a focus, before it is imaged onto one of two detectors.

[1]The interferometer consists of the beamsplitter, fixed and moving mirrors. It modulates the infrared beam.

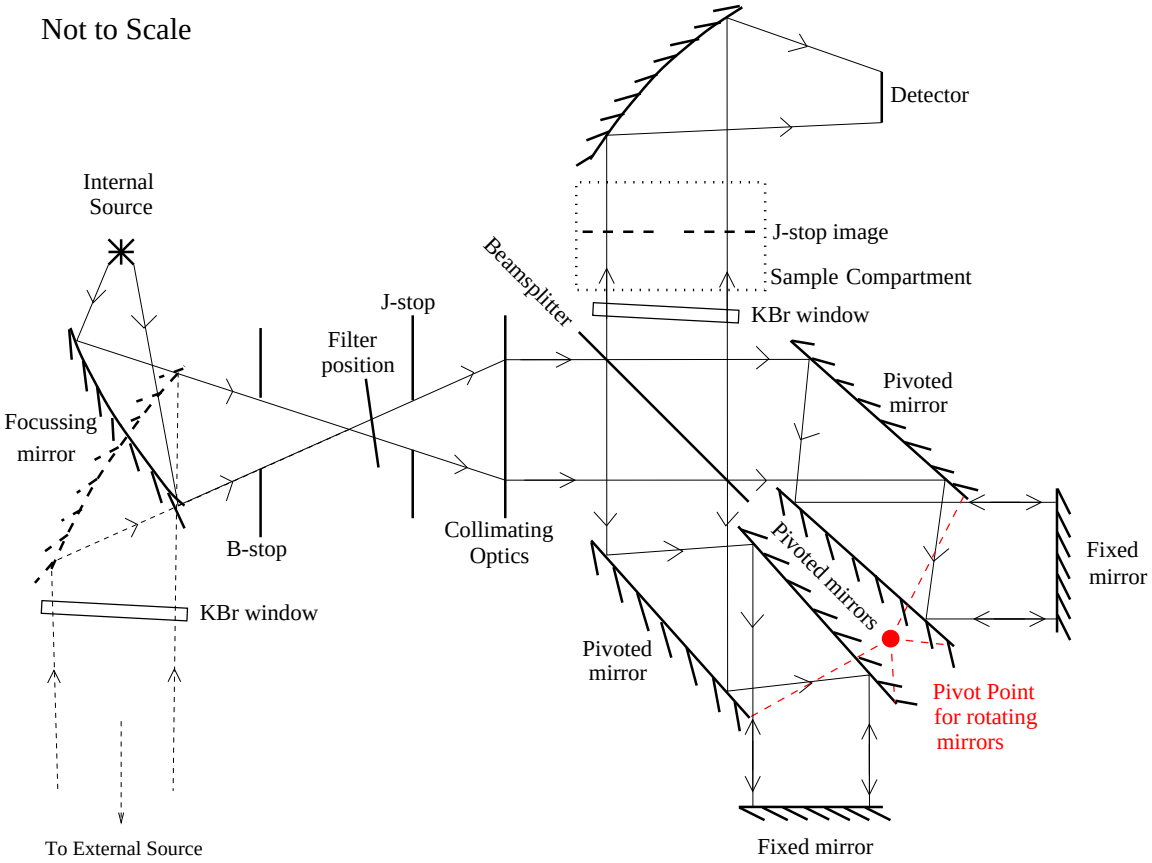

Figure 2.1: Schematic diagram of the optical layout of the Perkin Elmer Spectrum 2000

Internal Source

The internal source supplied with the spectrometer, and used in this study, is a voltage stabilized, air-cooled wire coil which operates at 1350 K and provides broadband radiation in the mid to far infrared spectral region. Light from the internal source is brought to a focus, between the B-stop and J-stop, by an ellipsoidal mirror. If the spectrometer is configured for use with the external source, which is described in section 2.2, then the ellipsoidal mirror is replaced by an off-axis parabolic mirror which brings to a focus parallel, collimated light from the external source, at the same point as light from the internal source is brought to a focus. The two mirrors are mounted vertically above one another on a motor-driven mount. Which source, and consequently which mirror, is in use is controlled by the Perkin-Elmer Spectrum for Windows software.

B-Stop

The B-stop, or Beamsplitter stop, is the aperture stop in the system. It is positioned at an image of the beamsplitter between the source and interferometer. It has a variable circular aperture with a maximum diameter of 11.2 mm. The B-stop size can be reduced in order to attenuate the beam. This may be necessary in order to avoid overloading highly sensitive detectors. It also restricts the angle of the cone of radiation at the J-stop image in the sample compartment, where a sample can be positioned. For all measurements made in the course of this study, the B-stop was maintained at its maximum diameter.

Filter Wheel

A filter wheel is positioned in the optical path between the B-stop and J-stop. It can accommodate up to seven filters, the eighth position being empty, with selection controlled by the Spectrum for Windows software. Filters with a diameter up to 25.4 mm and a thickness up to 5 mm can be accommodated. No filters have been used in the recording of the measurements made in the course of this study.

J-Stop

The J-stop, or Jaquinot stop, is the field stop in the system. It defines the maximum angle at which rays can travel through the spectrometer, and thus restricts the beam divergence to the maximum allowable for the given resolution and spectral range (for more details see section 2.1.3). It is imaged onto the internal source, the detector and also in the sample compartment, where a second aperture can be placed (referred to in this document as an 'external J-stop'). The J-stop has a circular aperture, which ranges in diameter from 1.2 mm to 12.5 mm. For 0.2 cm^{-1} resolution the smallest diameter, of 1.2 mm, is required. A diameter of 8 mm gives the best quality imaging, and throughput through the spectrometer is increased up to the maximum diameter of 12.5 mm. For all measurements made in the course of this study, except those made to investigate spectrometer self-emission, no external J-stop was used, and the internal J-stop diameter was set to its smallest size.

Interferometer

The design of the interferometer in the Perkin-Elmer Spectrum 2000, although based on that of a Michelson interferometer, is novel. The interferometer of a standard Michelson interferometer consists of a beamsplitter, plus compensator plate[2], a fixed and a moving mirror (see figure 1.3). In the Spectrum 2000 interferometer the fixed and moving mirrors are replaced by two pivoted and one fixed mirror in each arm of the interferometer (see figure 2.1). All four of the pivoted mirrors are attached to a tilt table which is rotated about a pivot point by a magnetic drive, thus creating the necessary optical path difference. The advantage of this system over a standard Michelson interferometer is that the moving mirrors cannot twist or tilt relative to the fixed mirrors thus introducing an optical path difference between the two extreme rays of the beam and degrading the resolution of the spectrometer in a manner analogous to that of beam divergence, as discussed in section 2.1.3. Tilt can also be compensated for by using retroreflectors, either cat's-eye or corner-cube retroreflectors, or by continuously monitoring and adjusting the alignment of the moving mirror throughout the scan. However, the solution implemented by Perkin-Elmer is both cheaper and easier to engineer.

There are disadvantages to the Perkin-Elmer design. The infrared beam will move across the surface of the plane mirrors on the tilt table during each scan, and so any variation in reflectivity across the mirror surface will affect the signal reaching the detector. Also, the angle at which the infrared beam reflects off the plane mirrors on the tilt table will change throughout the scan, and since the reflectivity of a mirror varies slightly with angle the signal reaching the detector will also vary with angle. However, the disadvantages

[2]Assuming that the front surface of the beamsplitter is the coated (reflecting) surface, then the reflected beam only passes through the beamsplitter once, whereas the transmitted beam passes through the beamsplitter three times. Thus the transmitted beam travels further in an optically dense medium, which introduces an extra wavelength dependent optical path difference between the two beams (and zero path difference is no longer when the moving mirror is at the same distance from the beamsplitter as the fixed mirror). In order to compensate for this, a compensator plate, which in all respects, except that it does not have the semi-reflective coating of the beamsplitter, is identical to the beamsplitter (same refractive index and thickness), is placed in the optical path of the reflected beam at such an angle that the pathlength of the reflected beam through the compensator plate and beamsplitter is identical to the pathlength of the transmitted beam through the beamsplitter. In practice, this means that the reflective coating is sandwiched between the beamsplitter and compensator plate.

are outweighed by the advantages.

The beamsplitter used in this study is an optimised KBr (Potassium bromide) beamsplitter, with a spectral range of 370 cm^{-1} to 7,800 cm^{-1}. Potassium bromide is hygroscopic and the beamsplitter should not be exposed to a relative humidity greater than 75%. Therefore, the Spectrum 2000 optics are housed in a sealed and desiccated module.

Sample Compartment

The Perkin-Elmer Spectrum 2000 spectrometer is a lab instrument, and as such has a compartment where samples to be analysed can be placed. This compartment is located between the interferometer and detectors. It is 200 mm long, 291 mm wide and 225 mm high. An image of the J-stop is located in the sample compartment, and an external J-stop could be located at that point, if required. For the long path measurements carried out in the course of this study, the sample compartment was left empty. The KBr window which seals the optical module from the sample compartment was removed for the duration of these measurements in order to reduce channelling (see section 3.3).

Detectors

The spectrometer as utilised in this study is equipped with two infrared detectors. Detector selection, including the re-alignment of the plane mirror which directs the modulated infrared beam to the appropriate detector, is controlled by the Spectrum for Windows software.

The two detectors are a DTGS (Deuterated TriGlycine Sulphate) detector, which operates in the mid infra-red (15,600 cm^{-1} to 370 cm^{-1}) region, and a liquid nitrogen cooled (to 77 K), narrow band (10,000 cm^{-1} to 700 cm^{-1}) MCT (Mercury Cadmium Telluride) detector. The former is a pyroelectric bolometer, which detects infrared radiation via the change in polarisation with temperature of a ferroelectric material. The latter is a photoconductive detector, in which infrared radiation is detected via photons exciting the electrons in a semiconductor[3] from one state to another in which their electrical properties

[3]MCT detectors are a mixture of two semiconductors; mercury-telluride and cadmium-telluride, but the

are different. The narrow band MCT detector used in this study has a signal-to-noise ratio approximately five times greater than that of the DTGS detector and therefore the MCT detector is used to record all Spectrum 2000 spectra in this study, except those where the 370 cm^{-1} to 700 cm^{-1} region is required.

He-Ne Laser

A helium-neon (He-Ne) laser beam (wavelength 632.99 nm, i.e. a wavenumber of 15798 cm^{-1}) is introduced to the optical path through the spectrometer at the beamsplitter, and thereafter follows the same optical path as the infrared beam from the source. The beam passes through a notch in the top of the beamsplitter which has a coating which transmits in the visible region. The interferogram of the He-Ne laser is a very nearly perfect cosine oscillation at 15798 cycles per cm of optical path difference. This provides an excellent measure of the optical path difference, and thus of creating the wavenumber scale of the spectrum. The He-Ne laser is also used to control the sampling of the interferogram. If sampling is triggered at each zero crossing of the laser, then from the Nyquist sampling theorem[4], the shortest wavelength allowed in the spectrum allowed is 15798 cm^{-1}. If samples are recorded at every second crossing, then the shortest wavelength allowed is 7899 cm^{-1}.

2.1.2 FTIR Data Processing

In section 1.6 it was stated that the intensity of light measured by the detector, as a function of the optical path difference, was equal to the Fourier transform of the intensity spectrum of the source. This is now discussed more fully and an expression relating the measured interferogram to the intensity spectrum of the source is derived.

For the following discussion, assume that the spectrometer is an ideal instrument with a monochromatic, point source, for which all rays of light passing through the interferometer are parallel (and therefore subject to the same optical path difference, OPD), and for which

same principle applies.

[4]The Nyquist sampling theorem can be used to determine either the maximum wavenumber, the *Nyquist wavenumber* that can be sampled unambiguously, given a particular sampling frequency, or the minimum frequency required to sample unambiguously any waveform that is sinusoidal in time or distance. The Nyquist wavenumber, $\tilde{\nu}_N = (2\delta)^{-1}$, where δ is the sample spacing.

the beamsplitter is perfect; i.e. it has transmittance of 0.5 and reflectance of 0.5. Also, assume that the moving and fixed mirrors of the interferometer remain perfectly aligned throughout a scan. The intensity of the light beam impinging on the detector is then:

$$I_f(x) = \frac{S_0}{2}\left[1 + \cos(2\pi\tilde{\nu}x)\right] \tag{2.1}$$

where S_0 = the intensity of the source

$\tilde{\nu}$ = the wavenumber, in cm^{-1}, of the source

x = the optical path difference (or retardation) in cm (= twice the mirror travel).

For a broadband source, the intensity of the light beam impinging on the detector becomes:

$$I_f(x) = \int_{-\infty}^{\infty} \frac{S(\tilde{\nu})}{2}\, d\tilde{\nu} + \int_{-\infty}^{\infty} \frac{S(\tilde{\nu})}{2}\cos(2\pi\tilde{\nu}x)\, d\tilde{\nu} \tag{2.2}$$

where $S(\tilde{\nu})$ = the intensity spectrum of the broadband source. $I_f(x)$ is known as the interference function. The first term in equation 2.2 is the total energy incident on the detector, which is a constant. The second term in equation 2.2 is the recorded interferogram, I_D, which is the cosine Fourier transform of $S(\tilde{\nu})$. Therefore, $S(\tilde{\nu})$ can be obtained by applying an inverse cosine Fourier transform to the interferogram, i.e.

$$S(\tilde{\nu}) = 2\int_{-\infty}^{\infty} I_D(x)\cos(2\pi\tilde{\nu}x)\, dx \tag{2.3}$$

This can be re-written as

$$S(\tilde{\nu}) = 4\int_{0}^{\infty} I_D(x)\cos(2\pi\tilde{\nu}x)\, dx \tag{2.4}$$

because of the symmetry of the interferogram about the point of zero path difference (ZPD). Such an interferogram, where information is only recorded for mirror travel on the positive side of ZPD, is called a *single-sided* interferogram, as opposed to a *double-sided* interferogram when the moving mirror is scanned equally either side of ZPD.

Since $I_D(x)$ is real, the cosine Fourier transform can be replaced by the full complex Fourier transform, and the spectrum implicitly taken to be the real part of the transform. Therefore, $I_D(x)$ and $S(\tilde{\nu})$ can be written as a Fourier transform pair:

$$I_D(x) = \int_{-\infty}^{\infty} S(\tilde{\nu})e^{2\pi i\tilde{\nu}x}\, d\tilde{\nu} \tag{2.5}$$

$$S(\tilde{\nu}) = \int_{-\infty}^{\infty} I_D(x) e^{-2\pi i \tilde{\nu} x}\, dx \tag{2.6}$$

where the multiplicative constant which appeared before the integral sign in equation 2.4 has been dropped, since the computed spectrum is usually normalised. For a real instrument, the constant would depend on instrumental factors such as the beamsplitter efficiency and detector response, and as such may well be a wavenumber dependent function, rather than a constant. In this case they would modify the source spectrum, $S(\tilde{\nu})$. Other instrumental effects, such as finite mirror travel, and the effect of beam divergence, modify the expressions given above and these effects will be discussed in section 2.1.3.

Process to Convert an Interferogram to a Spectrum

Equation 2.6 shows that, in theory, the intensity spectrum of a broadband source can be determined by measuring the interferogram as a function of the OPD. In practice the limitations of real instruments mean a number of steps are required to do so. Since it is only possible to measure the analogue interferogram that impinges on the detector at discrete intervals, the integral in equation 2.6 must be replaced by a summation and a discrete, rather than continuous, Fourier transform performed.

The discrete Fourier transform that is used is the fast Fourier transform (FFT) (see, for example, (Griffiths & de Haseth 1986) or (Bingham 1974)) which, as its name implies, is much faster than the general discrete Fourier transform because it drastically reduces the number of computations required. The FFT requires that the number of data points in the interferogram is an integer power of 2. If this is not the case, then the interferogram must be *zero filled* in order to meet this requirement. Zero filling is the process whereby zeros are added to the end of the interferogram, thus increasing the number of data points it contains. This has the effect of increasing the number of points per wavenumber in the spectrum, which interpolates between the data points and results in a smoother spectrum. Zero filling does not introduce any errors because the instrument line shape (see section 2.1.3) has not been changed. As well as being used to satisfy the FFT requirement of the number of data points in an interferogram, zero filling is also used to interpolate the spectrum in order to

reduce clipping of spectral lines and increase precision. It has been suggested (Gronholz & Herres) that a zero filling factor of at least 2 should be used on all spectra, and up to 8 in the case where the expected line width of the sample being measured is similar to the spacing of independent (as opposed to interpolated) data points in the spectrum. Perkin-Elmer use a zero-filling factor of 4. To avoid changing the resolution and instrument lineshape of the spectrum to be computed, any apodization function (see section 2.1.3) selected by the user must only be applied to the measured data and not to the zero filled data points.

After apodization and zero filling, the FFT can be applied to the interferogram (in the case of the Perkin-Elmer spectrometer used in this study, this operation is carried out on a transputer card installed in the PC which controls the spectrometer) and phase correction applied to the FFT of the interferogram. Phase correction is necessary because phase errors arising from optical, electronic or sampling effects result in an asymmetric interferogram, and therefore a complex spectrum, $C(\tilde{\nu})$, rather than a real spectrum, $S(\tilde{\nu})$. The three main causes of phase errors are the point of zero optical path difference not coinciding with a sampling point, the beamsplitter introducing a wavelength-dependent phase change[5], and electronic filters, employed in the amplification of the detected signal, introducing a wavelength-dependent phase lag. The form of phase correction which is most commonly used, and which is used for the Perkin-Elmer Spectrum 2000, is *Mertz* phase correction or 'multiplicative phase correction'. Mertz phase correction calculates the phase of the spectrum

$$\phi(\tilde{\nu}) = \arctan\left[\frac{\mathrm{Im}(C(\tilde{\nu}))}{\mathrm{Re}(C(\tilde{\nu}))}\right] \tag{2.7}$$

from a short double-sided portion of the interferogram[6] on either side of ZPD, and then

[5]This could be because the beamsplitter coating introduces a wavelength-dependent phase change, or because the optical thickness of the beamsplitter and compensator are not identical or the compensator is misaligned.

[6]Although the Spectrum 2000 only records single-sided interferograms when the resolution is higher than 0.5 cm^{-1}, all single-sided interferograms include a short double-sided section in order that phase correction can be implemented.

calculates the true phase-corrected spectrum, $S(\tilde{\nu})$, from the complex spectrum

$$C(\tilde{\nu}) = S(\tilde{\nu}) \exp(i\phi(\tilde{\nu}))$$

as follows

$$S(\tilde{\nu}) = C(\tilde{\nu}) \exp(-i\phi(\tilde{\nu}))$$

where $\phi(\tilde{\nu})$ is calculated according to equation 2.7. The phase-corrected spectrum can then be displayed on a VDU, or stored in the format required by the user.

2.1.3 Instrument Line Shape and Resolution

The interferogram described by equation 2.5 is that produced by an ideal spectrometer of infinite resolution. In practice, the resolution is limited by the finite distance travelled by the mirror. If the moving mirror is scanned between 0 and D, then the range of optical path differences (OPDs) that are sampled lies between $x = 0$ and $x = L$, where $L = 2\mathrm{D}$. This has the effect of truncating the complete interferogram (from $x = -\infty$ to $x = +\infty$), or multiplying it by a function which takes the value of 1 for $0 \leq x \leq L$ and is zero at all other points. Due to its shape, this function is often called a *boxcar* function. The spectrum is therefore given by the equation:

$$S(\tilde{\nu}) = \int_{-\infty}^{\infty} I(x) \cdot B(x) e^{-2\pi i \tilde{\nu} x} \, dx \tag{2.8}$$

where $B(x) = 1$ for $0 \leq x \leq L$

$B(x) = 0$ otherwise

It can be shown that the Fourier transform of the product of 2 functions is the *convolution* of the Fourier transform of each function (see any undergraduate mathematics textbook e.g. (Boas 1983)). Therefore, the effect of only scanning the moving mirror over a finite distance is to convolve the true spectrum (that calculated from an interferogram measured over an infinitely long OPD) with the Fourier transform of a boxcar function of width equal to twice the distance scanned by the moving mirror. The Fourier transform of

$B(x)$, $b(\tilde{\nu})$, is given by:

$$\begin{aligned} b(\tilde{\nu}) &= \frac{\sin(2\pi\tilde{\nu}L)}{2\pi\tilde{\nu}L} \\ &= \text{sinc}(2\pi\tilde{\nu}L) \end{aligned} \tag{2.9}$$

This function, called a *sinc function*, is centered about $\tilde{\nu} = 0$ and intersects the $\tilde{\nu}$ axis at $\tilde{\nu} = n/2L$, where $n = 1,\ 2,\ 3,\ ...$ and is shown in figure 2.2. Note that the first sidelobes, which are minima, have an amplitude equal to 22% of the amplitude of the central maximum.

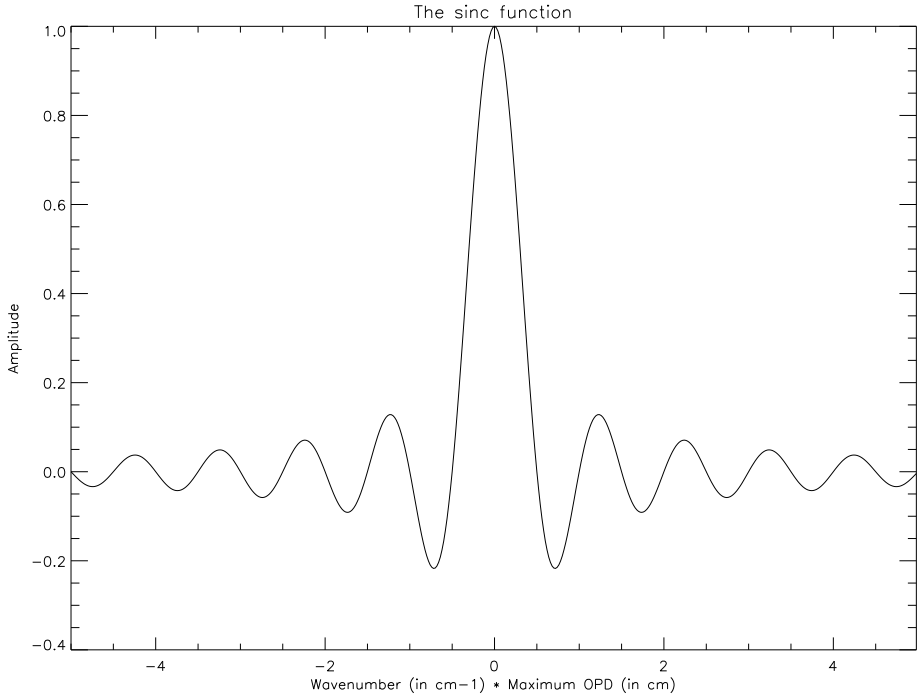

Figure 2.2: The Sinc Function

The spectrum of a monochromatic line of wavenumber $\tilde{\nu} = \tilde{\nu}_0$, whose true spectrum is a Dirac delta function (which is unity at $\tilde{\nu}_0$ and zero at all other points), recorded by an instrument with a maximum OPD of L is therefore

$$S(\tilde{\nu}) = L\text{sinc}[2\pi(\tilde{\nu} - \tilde{\nu}_0)L]$$

which is the sinc function scaled by a factor of L. Since $b(\tilde{\nu})$ modifies the line shape of any spectral line measured, it is often called the *Instrument Line Shape* (ILS). Other factors influence the ILS and these will be discussed in the following sections.

The spectral resolution of a Fourier transform spectrometer is usually defined as being the full width at half height (FWHH) of the main peak, i.e. the resolution = $0.603/L$. Other definitions that are in use include the full width at half maximum (FWHM) and the Rayleigh criterion. The FWHM differs from the FWHH because the first sidelobes of the sinc function are minima, therefore the maximum amplitude of the function is the difference between the central maximum and the first minimum, whereas the height of the function is the difference between zero and the central maximum. Therefore the FWHM = $0.683/L$. Under the Rayleigh criterion two lines are considered to be just resolved when the central maximum of one is at the same frequency as the first zero of the lineshape of the other. This criterion was originally developed to define the resolution for diffraction-limited grating spectrometers, which have a sinc^2 ILS. This leads to a dip in the combined profile of the 2 lines of approximately 20% of the maximum intensity. However, for Fourier transform spectrometers, which have a sinc ILS, where the criterion is satisfied by a separation of the 2 lines of $0.5/L$, there is no dip in the combined profile and the 2 lines cannot be resolved. Perkin-Elmer have adopted the definition of $1.0/L$ for the Spectrum 2000 and this is the definition used in this work.

The Effect of Beam Divergence

In the previous sections it has been assumed that the source is a point source, and therefore that all rays of light passing through the interferometer are parallel. In practice, all sources have a finite size, and therefore light with a finite range of angles traverses the interferometer. For light passing through a circular field stop of radius r and collimated by a collimator of focal length f, the range of angles traversing the interferometer is r/f radians. This has an effect on the resolution of the spectrometer and its ILS which will be described in this section. For more details see (Bell 1972), (Chamberlain 1979) and (Steel 1964).

Consider figure 2.3 which is a simplified diagram of the interferometer with the beamsplitter omitted and the image of the fixed mirror created by the beamsplitter superimposed on the arm of the interferometer containing the moving mirror. The two mirrors are separated by a distance d, which corresponds to an on-axis optical path difference (OPD) of $x = 2d$. An off-axis ray entering at an angle θ will be reflected at each mirror as shown in

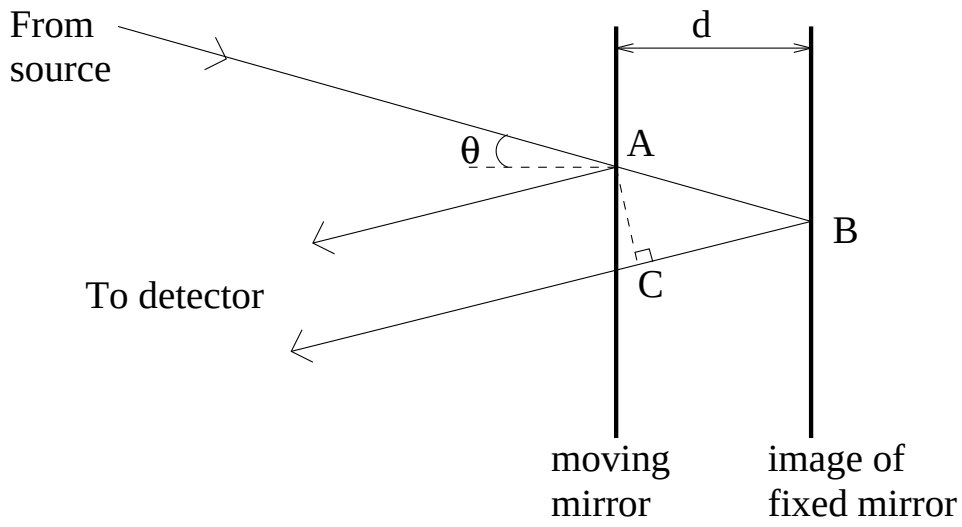

Figure 2.3: Geometric equivalent of a Michelson interferometer

the figure. The path difference between the two rays is the distance $AB + BC$, which by trigonometry is

$$\begin{aligned} x_\theta &= AB + BC \\ &= \frac{d}{\cos(\theta)} + \cos(2\theta)\frac{d}{\cos\theta} \\ &= 2d\cos\theta \\ &= x\cos\theta \end{aligned} \tag{2.10}$$

since $x = 2d$. The off-axis path difference is *less* than the on-axis path difference, x.

The off-axis ray will be out of phase with the on-axis ray for the first time when the difference between their OPDs is half a wavelength

$$x - x_\theta = \frac{\lambda}{2} = \frac{1}{2\tilde{\nu}}$$

$$\begin{aligned} x(1-\cos\theta) &= \frac{1}{2\tilde{\nu}} \\ \cos\theta &= 1-\frac{1}{2x\tilde{\nu}} \end{aligned} \tag{2.11}$$

which defines the maximum beam divergence that can be tolerated. Assuming θ is small, then $\cos\theta \approx 1-\theta^2/2$ and

$$\theta_{max} = \sqrt{\frac{\delta\tilde{\nu}}{\tilde{\nu}_{max}}} \tag{2.12}$$

since x defines the maximum OPD allowed and the resolution, $\delta\tilde{\nu}$ is 1/(max. OPD). $\tilde{\nu}_{max}$ is the highest wavenumber in the recorded spectrum. The maximum solid angle allowed is therefore

$$\Omega_{max} = 2\pi\theta^2 = 2\pi\frac{\delta\tilde{\nu}}{\tilde{\nu}_{max}} \qquad \text{steradians(sr)} \tag{2.13}$$

Assuming an isotropic source, that is, that the intensity of the source is constant with unit solid angle, area and wavelength, then the effect of the off-axis rays on the interferogram is given by

$$I(x) = \int_0^\infty S(\tilde{\nu}) \int_0^\infty \frac{1}{\Omega}\cos(2\pi\tilde{\nu}x\cos\theta)\,d\Omega\,d\tilde{\nu} \tag{2.14}$$

Now, the solid angle, Ω, is given by

$$\Omega = \int_0^{2\pi} d\phi \int_0^\theta sin\theta\,d\theta = 2\pi(1-\cos\theta) \tag{2.15}$$

therefore, for small angles $\cos\theta = 1-\Omega/2\pi$, and the equation for the interferogram becomes

$$\begin{aligned} I(x) &= \int_0^\infty S(\tilde{\nu}) \int_0^\infty \frac{1}{\Omega}\cos\left[2\pi\tilde{\nu}x\left(1-\frac{\Omega}{2\pi}\right)\right] d\Omega\,d\tilde{\nu} \\ &= \int_{-\infty}^\infty S(\tilde{\nu})\mathrm{sinc}\left(\frac{\tilde{\nu}x\Omega_L}{2}\right)\cos\left[2\pi\tilde{\nu}x\left(1-\frac{\Omega_L}{4\pi}\right)\right] d\tilde{\nu} \end{aligned} \tag{2.16}$$

where Ω_L is the limiting solid angle. In general Ω_L is defined either by the field stop, or by the detector size.

The instrument lineshape, which is given by the spectrum recorded for a monochromatic line, $\tilde{\nu}_0$, is for an infinitely long interferogram

$$S_{ILS}(\tilde{\nu}) = \int_{-\infty}^\infty \mathrm{sinc}\left(\frac{\tilde{\nu}_0 x\Omega_L}{2}\right)\exp\left[2i\pi\tilde{\nu}_0 x\left(1-\frac{\Omega_L}{4\pi}\right)\right] e^{-2\pi i\tilde{\nu}_0 x}\,dx$$

$$= \int_{-\infty}^{\infty} \text{sinc}\left(\frac{\tilde{\nu}_0 x \Omega_L}{2}\right) \exp\left(\frac{-i\tilde{\nu}_0 x \Omega_L}{2}\right) dx \tag{2.17}$$

therefore

$$S_{ILS}(\tilde{\nu}) = \frac{\pi}{\tilde{\nu}_0 \Omega_L} \qquad \text{for} \qquad \tilde{\nu}_0 - \left(\frac{\tilde{\nu}_0 \Omega_L}{2\pi}\right) \leq \tilde{\nu} \leq \tilde{\nu}_0 \tag{2.18}$$

The result of the beam divergence allowed by a finite field stop is to impose a rectangular lineshape of height $\pi/\tilde{\nu}_0\Omega_L$ and width (the FWHH and the FWHM are the same and equal to the width of the rectangular lineshape) $\tilde{\nu}_0\Omega_L/2\pi$. It also imposes a lineshift of the spectral line to lower wavenumbers, the centre of the line being shifted to $\tilde{\nu}_0\Omega_L/4\pi$.

For the Perkin-Elmer Spectrum 2000, when operated at a resolution of 0.2 cm^{-1}, the limiting solid angle is determined by the field stop (the J-stop). For small angles $\Omega = \pi\theta^2$ and $\theta \approx h/2f$ where h is the diameter of the source or field stop and f is the focal length of the collimating mirror. Therefore $\Omega \approx \pi h^2/4f^2$. The diameter of the J-stop at 0.2 cm^{-1} resolution (i.e. an OPD of 5 cm) is 1.2 mm, and the focal length of the collimating mirror is 130 mm, which gives a value of the limiting solid angle of $\Omega_L = 6.69\times10^{-5}$ steradians. The resolution due to beam divergence at an OPD of 5 cm and a wavenumber of 2000 cm^{-1} is 0.021 cm^{-1}.

Apodisation

The third factor that affects resolution and instrument lineshape (ILS) is apodisation. It has already been shown (see section 2.1.3) that the truncation of the interferogram due to finite mirror travel imposes a sinc function on all spectral lines. Figure 2.2 shows that the sinc lineshape produces large sidelobes which can cause considerable error in the measurement of neighbouring spectral lines. The sidelobes, or feet[7], are spectral artifacts arising from the abrupt termination of the interferogram. If instead the data are gradually attenuated, or *apodised*, then the amplitude of the sidelobes may be reduced at the expense of broadening the central maximum of the lineshape and thus decreasing the resolution.

Any function which is real, has a value of 1 at $x = 0$, and decreases with increasing

[7] Apodisation comes from the Greek word $\alpha\pi o\delta$ which means 'feet removal'.

optical path difference can be used as an apodisation function. Since it is applied symmetrically about the point of zero path difference, the resulting ILS is symmetrical, and no frequency shifts occur. The amount by which any individual apodising function attenuates the sidelobes and decreases the resolution depends on the precise form of the function. Norton and Beer (Norton & Beer 1976) tested over a thousand functions and recommended three which provided a given level of sidelobe suppression with a minimum reduction in resolution. These are:

Name	Function in interferogram space	FWHH
weak:	$A(x) = 0.348093 - 0.087577(1-u^2) + 0.703484(1-u^2)^2$	$0.724/L$
medium:	$A(x) = 0.152442 - 0.136176(1-u^2) + 0.983734(1-u^2)^2$	$0.844/L$
strong:	$A(x) = 0.045335 + 0.554883(1-u^2)^2 + 0.399782(1-u^2)^4$	$0.965/L$

where $u = x/L$

The amplitudes of the largest sidelobes (all of which are minima) as a percentage of the height of the central peak for each function is 5.8% for the weak apodising function, 1.4% for the medium apodising function, and 0.3% for the strong apodising function, which are greatly reduced from the 22% of the boxcar apodising function.

All three Norton and Beer apodising functions are provided with the Spectrum 2000, along with the triangular apodising function (which is a sinc^2 function in spectral space), the raised cosine apodising function, the Kaiser-Bessel apodising function and the filler apodising function. Their full widths at half height (FWHH) and the amplitudes of their largest sidelobes as a percentage of the height of the central maximum are given in the following table.

Name	Amplitude of largest sidelobe	FWHH
triangular	4.5%	$0.885/L$
raised cosine	0.7%	$0.907/L$
Kaiser-Bessel	0.05%	$1.19/L$
filler	0.09%	$1.16/L$

The Norton and Beer strong apodising function was applied to all spectra recorded with the Spectrum 2000 in this study. It is used extensively in atmospheric spectroscopy and provides a good compromise between sidelobe suppression and reduction in resolution.

Instrument Lineshape

Combining the effects of finite mirror travel, beam divergence and any applied apodising function, the instrument lineshape in interferogram space is then

$$B(x)A(x)\text{sinc}\left(\frac{\tilde{\nu}_0 x\Omega_L}{2}\right)\exp\left(\frac{-i\tilde{\nu}_0 x\Omega_L}{2}\right) \tag{2.19}$$

where $B(x)$ is the boxcar function due to finite mirror travel

and $A(x)$ is the apodisation function selected by the user.

The spectrum measured by the spectrometer is therefore

$$S(\tilde{\nu}) = \int_{-\infty}^{\infty} I(x)B(x)A(x)\text{sinc}\left(\frac{\tilde{\nu}_0 x\Omega_L}{2}\right)\exp\left(\frac{-i\tilde{\nu}_0 x\Omega_L}{2}\right)e^{-2\pi i\tilde{\nu}_0 x}\,dx \tag{2.20}$$

where $I(x)$ is the interferogram recorded by an ideal instrument with an infinitely long OPD.

Choice of Resolution

The choice of resolution affects both the signal to noise ratio (SNR) and the measurement time, t. It can be shown (see for example (Griffiths & de Haseth 1986)) that

- SNR $\propto t^{1/2}$
- SNR $\propto$ resolution ($\delta\tilde{\nu}$)
- SNR $\propto$ 'optical throughput' or 'etendue' ($A\Omega$)

If the scan speed is held constant then since SNR $\propto t^{1/2}$, SNR $\propto \sqrt{\text{no.scans}}$. Therefore, to achieve a doubling of the SNR the number of scans, and the measurement time needed to acquire them, must be quadrupled and to achieve an order of magnitude increase in the SNR, the number of scans, and the measurement time needed to acquire them, must be increased a hundred fold.

If the resolution is halved, by doubling the maximum OPD (L), then the SNR is also halved, assuming that the measurement time, the scan speed and etendue are kept constant. In order to maintain the same SNR when doubling L, the measurement time, and the number of scans (if the scan speed is kept constant), must be quadrupled as long as the etendue is kept constant. If the optimum etendue is used for each resolution, then from equation 2.13 if the maximum OPD is doubled, thus halving the resolution, the etendue is halved and so is the SNR. Thus doubling the maximum OPD, when the optimum etendue is used, reduces the SNR to a quarter overall. In this case, in order to maintain the SNR at the same level as for $L/2$, the measurement time, and thus the number of scans (if the scan speed is kept constant), must be multiplied by a factor of sixteen.

The above arguments just considered the effects on the noise level. For spectra the signal is the absorbance (or transmittance) at the centre of a spectral feature. For a weak, narrow (FWHH of the line $\ll$ resolution) line, the apparent absorbance of the feature in the spectrum will approximately double when the maximum OPD is doubled (i.e. the resolution is halved). Thus, as long as the etendue is kept constant, the SNR will remain the same for the two resolutions. However, the degree of separation between adjacent spectral lines will be greater at the higher resolution, and so the use of the higher resolution is preferable. For weak, broad spectral features, where the apparent absorbance of the feature does not change when the maximum OPD is doubled, the increase in the noise level at the higher resolution, means that the lower resolution is preferable.

The apparent absorbance of strongly absorbing spectral features, whether broad or narrow, depends on their true absorbance and the relative widths of the resolution and the FWHH of the spectral feature. However, a higher resolution is normally used to separate

the spectral feature of interest from adjacent overlapping lines. In this case, the resolution which should be used is that which just adequately resolves the spectral feature of interest, since using a higher resolution would decrease the SNR.

The spectra recorded in this study are of gases under ambient atmospheric conditions at ground level. The spectral line widths of these gases are typically 0.1 cm^{-1}. Therefore, the maximum resolution of the spectrometer, of 0.2 cm^{-1}, was used for all spectra recorded with the Spectrum 2000 in this study.

2.2 External Source

The external source used for long path measurements in this study is a diesel engine glow-plug (Lucas HDS274, see figure 2.4) which is mounted at the focus of a 450 mm (18") diameter, gold plated, aluminium paraboloid (see figure 2.5), with a focal length of 115 mm (4.5") and a centre hole of diameter 29 mm. A Manson EP-920 DC power supply, fed off an uninterruptible power supply (APC Smart-UPS 1400), supplies the glowplug with 13.8 Volts at 11 Amps. The glowplug operates at a temperature of approximately 850°C

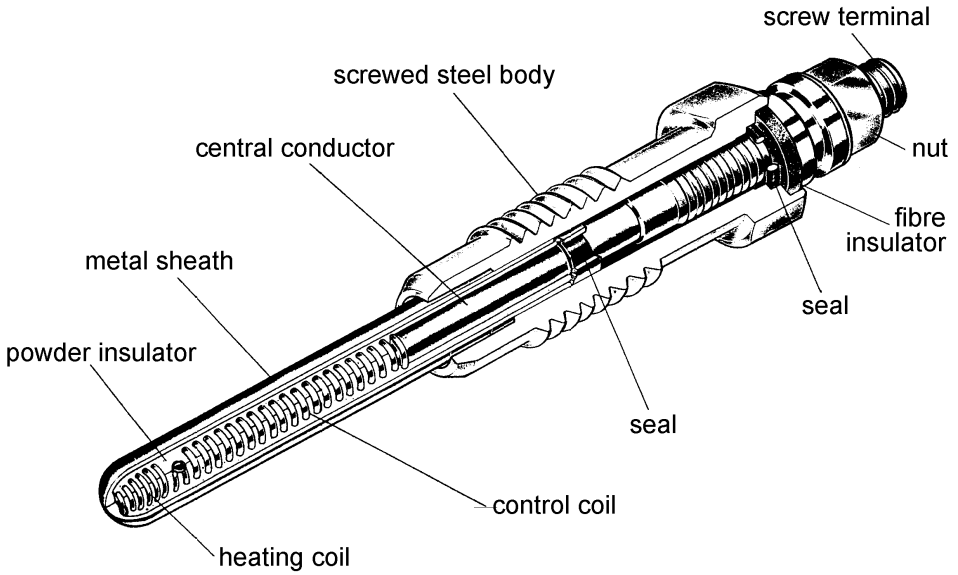

Figure 2.4: Glowplug used in external source (taken from a Lucas catalogue).

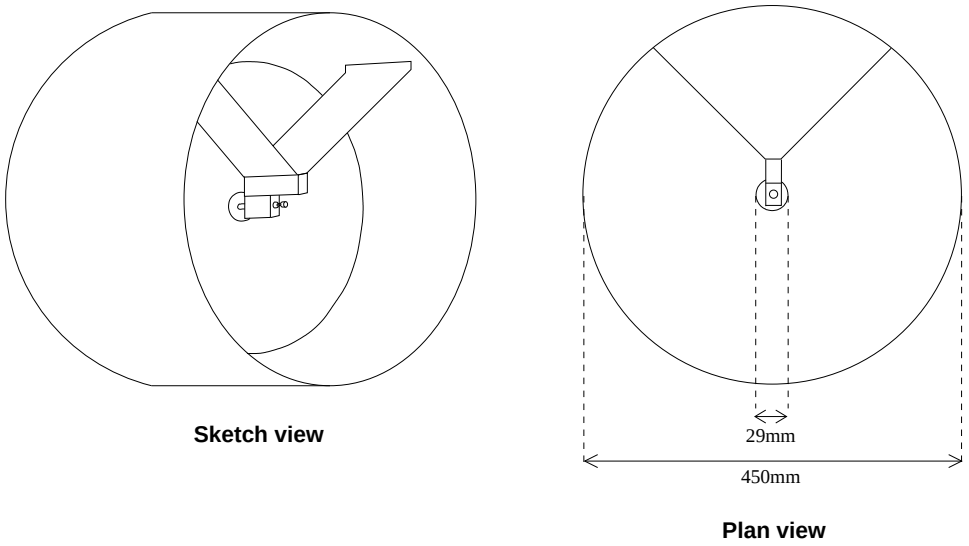

Figure 2.5: External Source

(1123K), but this temperature is known to fluctuate over a range of 675°C (948K) to 950°C (1223K) due to the wind. The temperature is measured by a K-type thermocouple attached to the glowplug the output from which is fed into a Metex M-3850D multimeter where it can be monitored. The multimeter readings can also be fed into a PC and written to file.

The extended nature of the source (the glowplug has a diameter of approximately 5 mm) and the short focal length of the parabola used in the source combine to give the source a beam divergence of approximately 43 milliradians. Of more relevance is the fact that the usable[8] width of the beam at the entrance to the periscope on the roof of the Atmospheric Physics building when reflected off the plane mirror mounted on the Clarendon physics building (for more details see section 2.5.1) is approximately 1 m (over a pathlength of approximately 155 m, giving a beam divergence for the usable region of 6.5 milliradians). The entirety of the collimator (see section 2.3) must be within this usable region of the infrared beam.

The source is larger than strictly necessary, which is due to the fact that a cheap 18" diameter parabola was readily available. However, the large diameter of the beam,

[8]Where the whole source is seen, by eye, as having an uniform orange glow, with no dark areas.

due to the width of the parabola and large beam divergence, aids alignment, and reduces susceptibility to movement of the source, for example due to vibration of its support, or wind.

2.3 Collimator

The beam divergence of the input beam of the spectrometer, as defined by the J-stop (at 0.2 cm^{-1} resolution) and B-stop (when fully open) is 0.12 radians (the extreme rays through the J-stop and B-stop have a beam divergence of 0.15 radians). If the off-axis parabolic mirror which collects light from an external source and directs it into the spectrometer optics is included, then the beam divergence is reduced to 10 milliradians. This is larger than the beam divergence of the external source and it was decided that a collimator, or telescope, was required to match the external source to the spectrometer. Such an instrument should be usable over a range of source spectrometer separations (optical pathlengths were expected to be in the range 40 m to 1 km) and should match the input optics of the spectrometer.

Only reflective optics were considered, due to their chromatic independence. The main disadvantage of reflective optical systems is the obscuration of part of the primary mirror by the secondary mirror, and the consequent loss of optical throughput. Off-axis parabolic systems can be used to place the secondary mirror outside the incoming beam, whilst still retaining an on-axis image, however the cost of such a system was prohibitive for this study. Of the possible arrangements for a folded system the concentrically folded systems, where the focal plane is located on the axis of the primary mirror, were considered preferable to folding the infrared beam off to one side of the collimator or telescope. Both the Gregorian, where the secondary mirror is concave, and Cassegrain, where the secondary mirror is convex, systems were considered.

It was decided that the telescope or collimator field of view should either be undersized, or oversized, but not matched to the external source. That is, the field of view of the instrument should either be filled by a part of the external source, or it should include some of the background as well the entire source, but it should not be completely filled by

the entirety of the external source. This requirement results from the fact that the source, or any distant plane mirror it is reflected off, is likely to be moved in the wind or suffer vibrations from traffic or other sources. Such vibrations (or indeed any relative movement between the instrument and the source), when combined with a field of view sized so that the external source just fills it, would cause noticeable fluctuations in the radiance from the source reaching the detector, and thus increase the noise in the spectra. If the source is only a part of the field of view, or if the field of view only encompasses part of the source, then as long as the vibrations do not move, either part of the source out of the field of view in the former case, or include part of the background in the field of view in the latter case, then for a uniform source the radiation reaching the detector from the source will not fluctuate[9].

Initially it was thought that the undersized case, where the field of view of the instrument is filled by a part of the external source, was preferable, and the design of the instrument proceeded on this basis. However, it was realised that for a real, non-uniform source, relative movements of the source and instrument due to vibrations would cause fluctuations in the radiation reaching the detector from the source, and thus increase the noise in recorded spectra. For an oversized instrument, provided that the source was centered in the field of view, and the vibrations were relatively small (so the source stayed within the field of view), the apparent source as seen by the detector would remain stable.

Three designs of telescope were considered. In the first design it was decided to minimise the diameter of the input beam of the spectrometer on the parabolic mirror of the external source. This criterion is fulfilled when the J-stop is imaged on the parabolic mirror of the external source. The main disadvantage of this design is that it needs refocussing for each value of the separation between the external source and spectrometer.

[9]This decision was vindicated on the first day of field measurements at Oxford railway station. The plane mirrors used to reflect the light from NPL's and this study's infrared sources onto their respective collimators were affixed to the railings of a pedestrian bridge. The movement of pedestrians on the bridge vibrated both mirrors. In the case of NPL, where their source, mirror and collimator were sized to their spectrometer optics, the vibrations caused increased noise in their spectra. For the setup used in this study, in which the collimator was oversized and thus only partly filled by the source, there was no extra noise recorded in the spectra.

In the second design, the effect of imaging the J-stop (the input plane for the telescope) to infinity was considered. This produces an optical system that meets the requirements of being matched to the spectrometer optics and being usable over a range of source spectrometer separations. The required focal length of the telescope is dependent upon the acceptable divergence of the input beam of the spectrometer. For a beam divergence of 1 milliradian, a focal length of 1.2 m is required. For the minimum diameter of the input beam of the spectrometer at the parabolic mirror of the external source, a focal length of 3 m is required, giving a beam divergence of 0.4 milliradians.

The third design which was considered was that of an afocal telescope, or collimator, in which the separation of the primary and secondary mirrors was such that they were confocal[10]. Such a system is sometimes referred to as a beam expander, its magnification being the ratio of the focal length of the primary mirror to the focal length of the secondary mirror. This also produces an optical system that meets the requirements of being matched to the spectrometer optics and being usable over a range of source spectrometer separations. It has the advantage of it being easier to adjust the secondary mirror to the correct separation from the primary mirror than for the second design. For this design, the divergence of the input beam beyond the collimator is the beam divergence before the collimator divided by the magnification of the collimator. For a magnification of 10 times, the beam divergence is then 1 milliradian, and for a magnification of 8 times, the beam divergence is 1.25 milliradians.

The third design was that chosen. It was implemented as a modified Cassegrain optical system, rather than a Gregorian one, because the Cassegrain layout leads to a more physically compact design. For an afocal system, parabolic mirrors are required for the concave primary and convex secondary mirrors. A magnification of between 8 times and 10 times was considered acceptable. The other constraint on the system was that the emission port of the spectrometer, where light from an external source can enter the spectrometer through a 5.0 mm thick KBr window which is angled at 3° to the optical axis of the internal

[10] i.e. their focal points coincided

optics, is 47.5 mm in diameter.

Cost considerations led to an 8 times magnification system being chosen. The primary mirror is a concave parabola with a 350 mm clear aperture, a 200 mm focal length and a 42 mm diameter centre hole. The secondary mirror is a convex parabola with a clear aperture of 42 mm and a focal length of 24 mm. Both mirrors are made of aluminium, which has a 90%, or greater, reflectivity at infrared wavelengths. The secondary mirror is mounted in such a way that its separation from the primary mirror can be adjusted in order to focus the collimator. The focus of the collimator was set to infinity with the use of a single lens reflex (SLR) camera focussed at infinity viewing through the hole in the primary mirror via two 45° plane mirrors (described below).

The collimator is mounted such that its optical axis is at 90° to that of the emission port of the spectrometer. A gold coated plane mirror, mounted at 45° to the optical axis of the collimator, and placed in the compressed, infrared beam at a point just beyond the hole in the primary mirror, directs the beam along the optical axis of the emission port of the spectrometer (see figure 2.6). The collimator can be rotated about the optical axis of the emission port of the spectrometer and locked in place at the required polar angle. Variation in the polar angle is required to accommodate the range of possible relative heights of the source and spectrometer necessary for measuring air pollution at different sites. Variation of the azimuthal angle is achieved by physically rotating the collimator and spectrometer system as a whole.

A 45° plane mirror can be inserted between the entrance port of the spectrometer and the 45° collimator plane mirror to provide a view of the scene in the field of view of the collimator, thus enabling the operator to adjust the collimator focus and alignment of the collimator and source. This mirror is only in place during alignment and is removed for the normal operation of the spectrometer.

For the external source described in section 2.2, which has a beam divergence of 6.5 milliradians, the divergence of the beam entering the spectrometer, having passed through the collimator, is 52 milliradians. This is greater than the divergence allowed

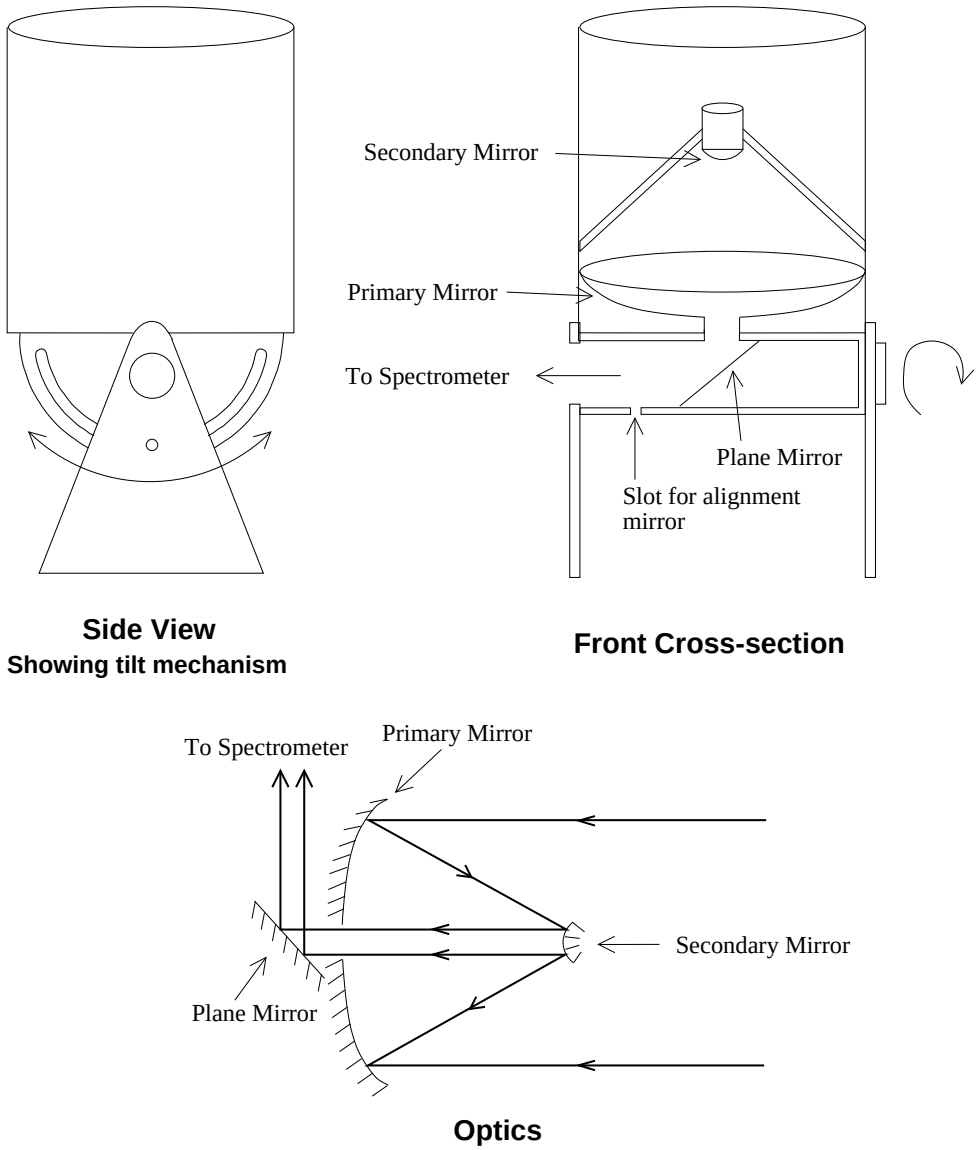

Figure 2.6: Collimator

by the J-stop, and so the optical throughput will be reduced. The diameter of the beam entering the spectrometer is limited to 38.5 mm by the cowling round the KBr window. The etendue of the beam entering the spectrometer is therefore 1.98 $\times 10^{-5}$ m^2 sr. The etendue of the spectrometer, as defined by the diameter of the J-stop and the limiting solid angle (see section 2.1.3), is 3.03 $\times 10^{-10}$ m^2 sr. Thus the beam from the external source and collimator system overfills the spectrometer.

2.4 Trolley

It was necessary to improve the portability of the spectrometer for field measurements, and to this end a custom made trolley (see figure 2.7) was purchased. The varnished $\frac{3}{4}$" (19 mm) exterior grade plywood top is 1.26 m by 0.61 m, thus the spectrometer slightly overhangs it

Figure 2.7: Spectrometer, trolley and PC in the lab on the third floor of the atmospheric physics building.

(by 20 mm) widthwise, but fits easily within its length. The top is supported on a powder coated, hollow box, steel frame and four 8" (203 mm) diameter pneumatic wheels, the front pair of which are steerable. The height of the wooden top is adjustable over a range of approximately 0.4 m to 0.9 m by means of a 2 ton hydraulic trolley jack. The jack adjusts the angle to the horizontal of the struts supporting the wooden top, in order to adjust the height of the wooden top. The base, which is 0.77 m at its widest point, is wider than the top in order to accommodate this motion. The trolley is 1.60 m long at its lowest height and 1.53 m long at its full height. Its minimum length, of 1.26 m, is at an intermediate height. The dimensions of the trolley were dictated by the interior dimensions of the goods

lift, from the ground floor to the second floor, in the atmospheric physics building. The trolley weighs 90 kg, and the recommended safe working load is 500 kg, which is much greater than the combined weight of the spectrometer and collimator.

2.5 Experimental Setup

The possible spatial arrangements of the spectrometer, external source and other auxilary optical components used for long path FTIR spectroscopy can be divided into two main categories; those where the spectrometer and source are physically separated by the length of the optical path (arrangement (a) in figure 2.8), often referred to as a bistatic configuration, and those where they are adjacent (arrangement (b) in figure 2.8), often referred to as a monostatic configuration. Spatial arrangements belonging to the former category

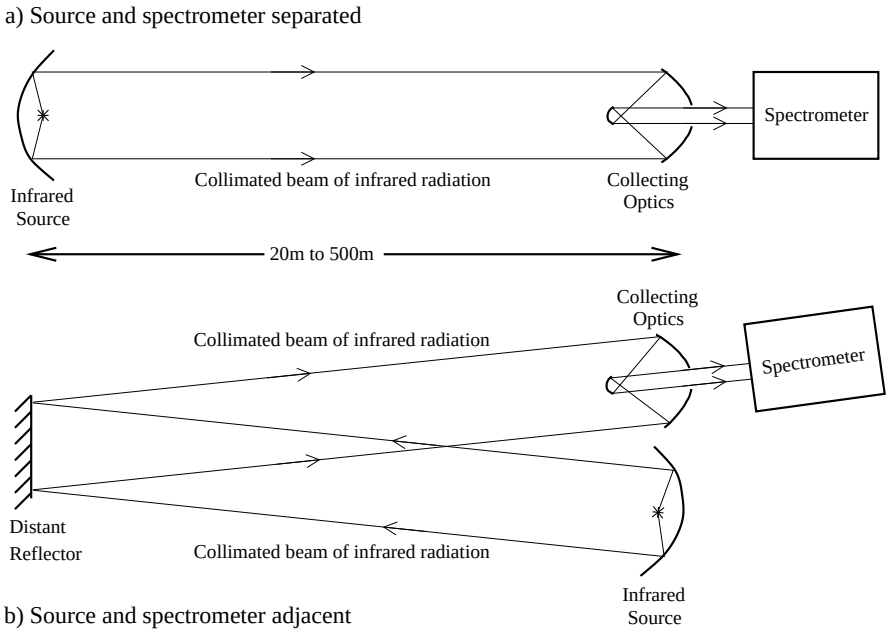

Figure 2.8: Possible spatial arrangements of optical components for long path FTIR spectroscopy

were only used for test purposes and the results from the measurements thus recorded have not been included in this document. All measurements of air pollution were recorded using monostatic configurations in which the spectrometer and source are in close proximity and

light from the source is reflected off a distant mirror. Spatial arrangements belonging to this category have the advantage that a source of power is only required at one end.

The experimental setups used to take measurements of air pollution during the course of this study will be discussed in the following two sections. The first section will cover those measurements recorded in Oxford University's science area, where the spectrometer was situated in a laboratory in the atmospheric physics building. The second section will cover those measurements recorded during field measurements on the streets of Oxford.

2.5.1 Science Area Experimental Setup

The laboratory used in this study is situated on the top (third) floor of the atmospheric physics building. The laboratory has two skylights, one of which has been replaced by a periscope (see section 2.5.1). The spectrometer is positioned with the collimator directly below the periscope, with the axis of the collimator in a vertical position. The external source is mounted on the flat roof, which is 15 m above ground level, above the laboratory and a 500 mm by 800 mm (long axis is vertical) rectangular plane mirror mounted on

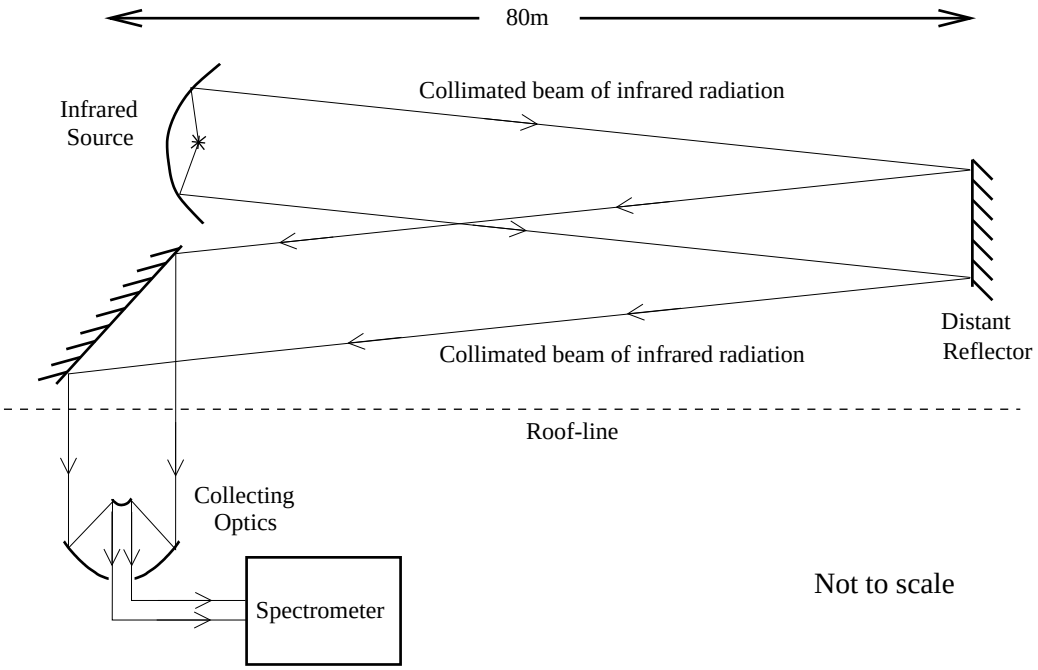

Figure 2.9: Configuration of optical path as utilised in Oxford University's science area.

the roof of a nearby building enables an optical pathlength of 160 m to be achieved. A schematic of the optical configuration is given in figure 2.9. A plan of part of Oxford University's science area, which shows the positions of the periscope, source and mirror, is given in figure 2.10.

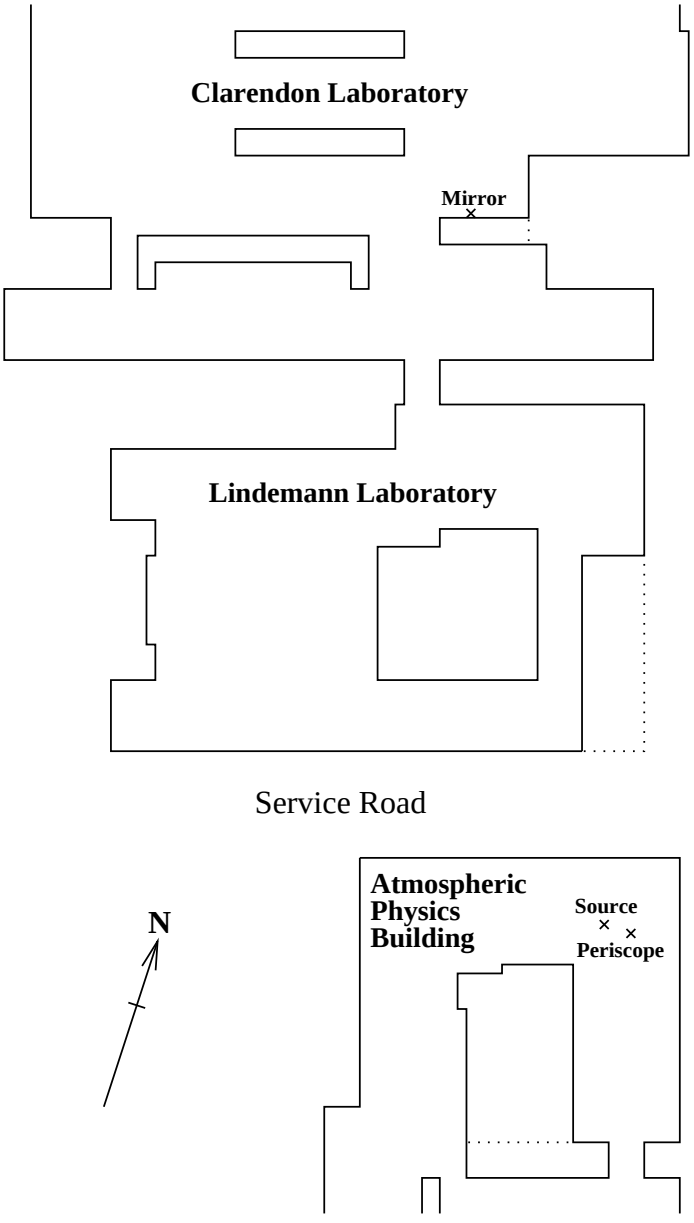

Figure 2.10: Plan of part of the science area[11]

[11] Based on the 1970 Ordnance Survey 1:1250 maps SP5107SW and SP5106NW

The atmospheric physics building is situated close to Oxford city centre, next to a busy main road. The optical path used in this study passes over a service road which is used by low levels of traffic.

Periscope

The periscope (see figure 2.11) installed above the laboratory was custom built for this study. The 410 mm by 670 mm plane periscope mirror is mounted at 45° to the vertical.

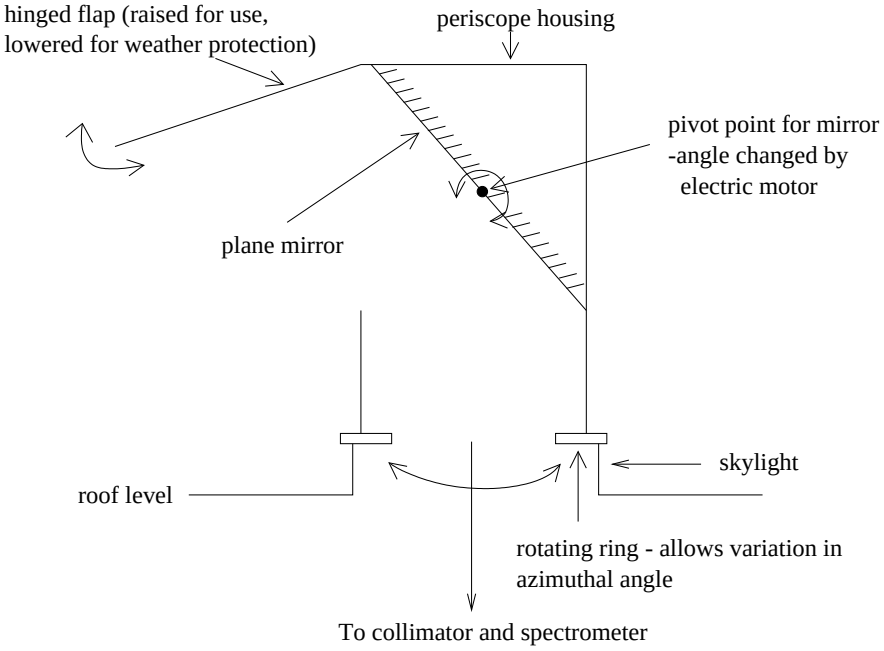

Figure 2.11: Roof Periscope for use with spectrometer in the lab

This angle can be adjusted by a couple of degrees by a small, electric motor which provides both fine control and the ability to adjust the angle from the floor of the lab. The mirror is housed in a weatherproof casing made of aluminium which is mounted on a rotating ring co-centred with the skylight aperture. An actuator attached to the ring gives the operator control over the azimuthal angle of the periscope from the floor of the lab.

Alignment Procedure

The 500 mm by 800 mm plane mirror affixed to the Clarendon laboratory was adjusted to bring the line of sight from the periscope to a suitable position for mounting the external source, and then fixed in position.

The part of the roof of the atmospheric physics building which is used in this study is enclosed by scaffolding railings, which are positioned so as not to obscure any part of the optical path used in the study. The external source is attached to the railings by seven plastic ball joints, four of which are mounted directly on the source. The source is anchored by its top mount, about which it can pivot, to a spur of the railings. The bottom mount

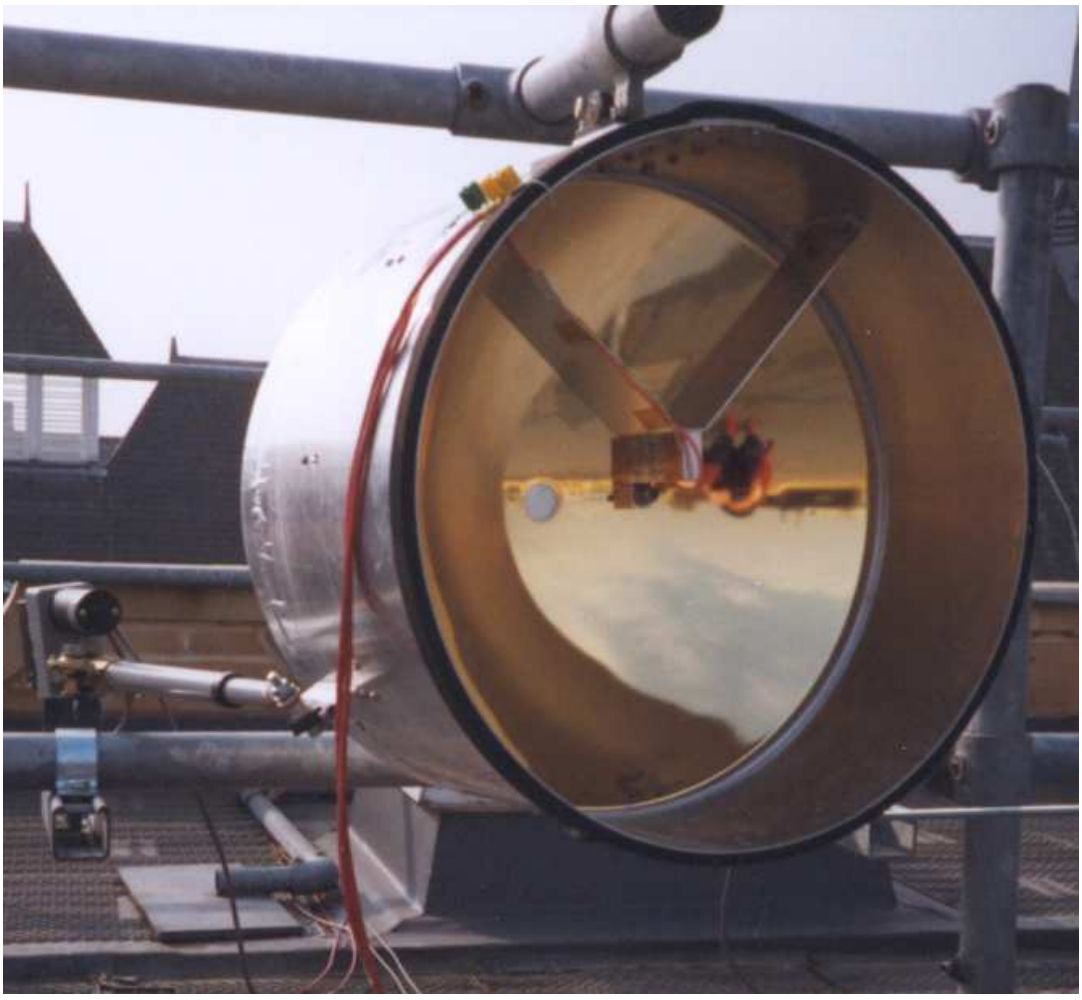

Figure 2.12: External source as installed on the roof of the atmospheric physics department.

is attached to a rod, which is itself attached to the railing by a plastic ball joint, and thus provides a pivot point for the source with a limited amount of motion in the horizontal and vertical planes. The two remaining mounts, at 4 o'clock and 8 o'clock, are attached via further ball joints to actuators (mass produced items for steering satellite TV antennae) which are fixed to the railings. When moved in phase they tilt the vertical plane of the source, changing its polar angle. When moved in anti-phase, the actuators rotate the source about the vertical, changing its azimuthal angle.

Figure 2.13: Back of external source as installed on the roof of the atmospheric physics department, showing the actuators used to control its aspect.

To aid the initial alignment of the source a board to which reflectors and LEDs were

attached was made. The six triangular vehicle trailer reflectors are arranged hexagonally, with the circumference of the hexagon approximating that of the collimator. Four red or orange LEDs were arranged at the corners of a square, such that the inner edge of each LED coincides with the perimeter of the hexagon. The LEDs emit bright light with a very small divergence that can be seen over 200 m away. To initially align the source, the board is positioned on top of the collimator such that the LEDs define its circumference. The LEDs were viewed from directly behind the source, and the position of the source was adjusted until the LEDs were centred on the source. The LED board is removed from the optical path after the initial alignment. It was determined that the source, as viewed by the collimator, is slightly occulted by the plane mirror on the Clarendon laboratory. The outermost 62 mm on each side, as measured on the horizontal diameter, of the source are occulted.

Fine alignment is carried out whilst monitoring the energy reaching the MCT detector of the spectrometer (the Spectrum for Windows software has a mode which enables this to be carried out). The alignment of the periscope and external source are then adjusted, by means of the actuators and electric motor, until the peak of the energy curve is found. The optical system is then fully aligned.

2.5.2 Experimental Setups Used for the Field Measurements

Field measurements were carried out at two sites in Oxford. The first was on the northwest pavement of Hythe Bridge Street outside Blackwell's offices. The second was across the Botley Road from the station bicycle park on the north side of the road to the car park on the south side, adjacent to the pedestrian bridge. The experimental setups used at each site are described in the following two sections.

Hythe Bridge Street

Field measurements on Hythe Bridge Street were carried out on two successive days in October (19 October and 20 October). The experimental setup was the same on each day.

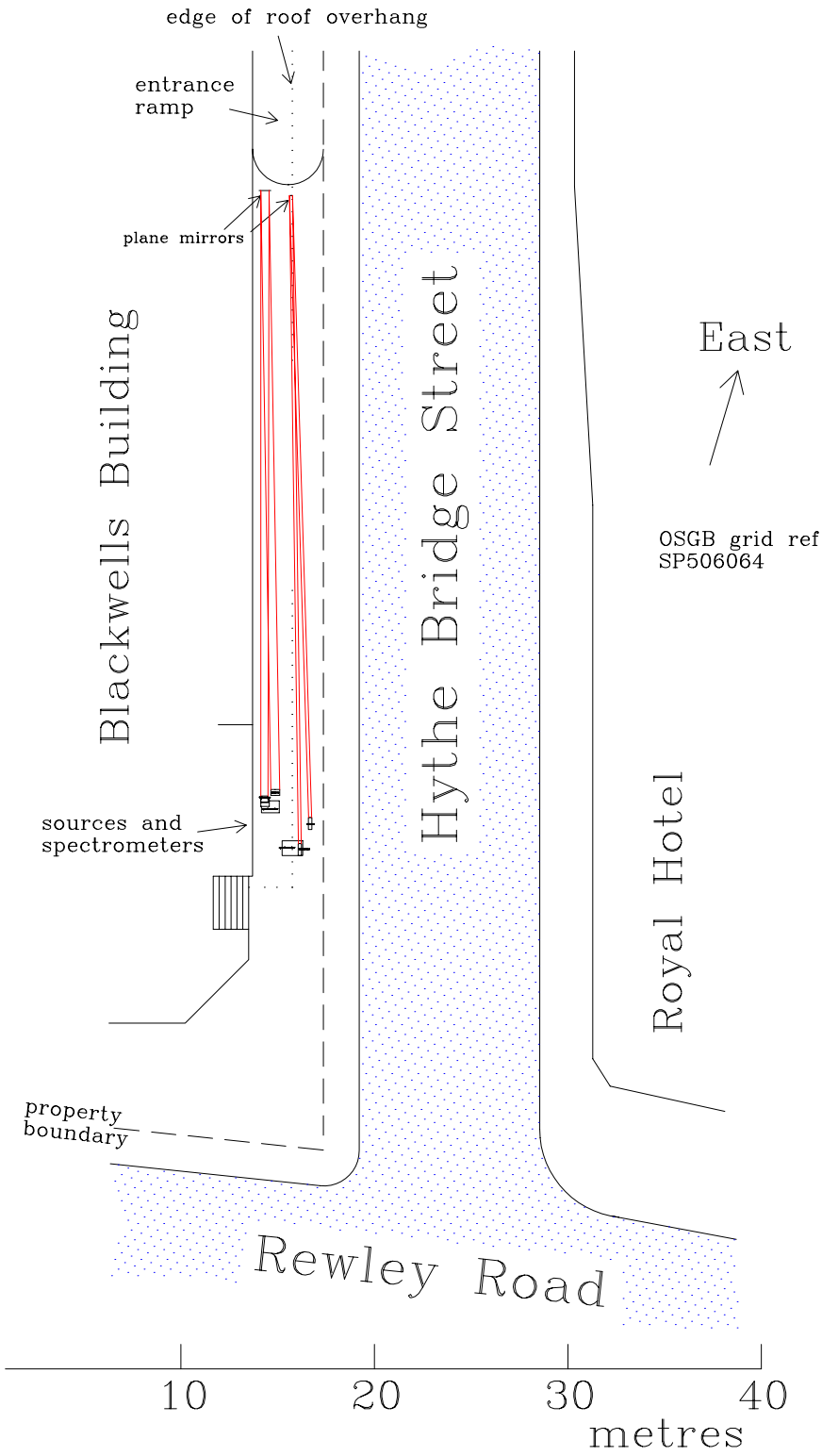

Figure 2.14: Plan of Hythe Bridge Street

Figure 2.14 shows a scale plan of the site. The spectrometer, mirror and source closest to the Blackwell's building are those used in this study. The spectrometer, mirror and source closest to the road belong to NPL with whom an intercomparison was carried out.

The external source was hung from its top joint off a short horizontal spur of 45 mm diameter steel pole which was attached to a vertical 45 mm diameter steel pole which in turn was attached to a heavy (15 kg) circular steel base. Once the source had been aligned it was clamped firmly in place. The source was located next to the spectrometer (see figure 2.15) and a plane front-silvered glass mirror aproximately 0.6 m by 0.7 m by 0.006 m was

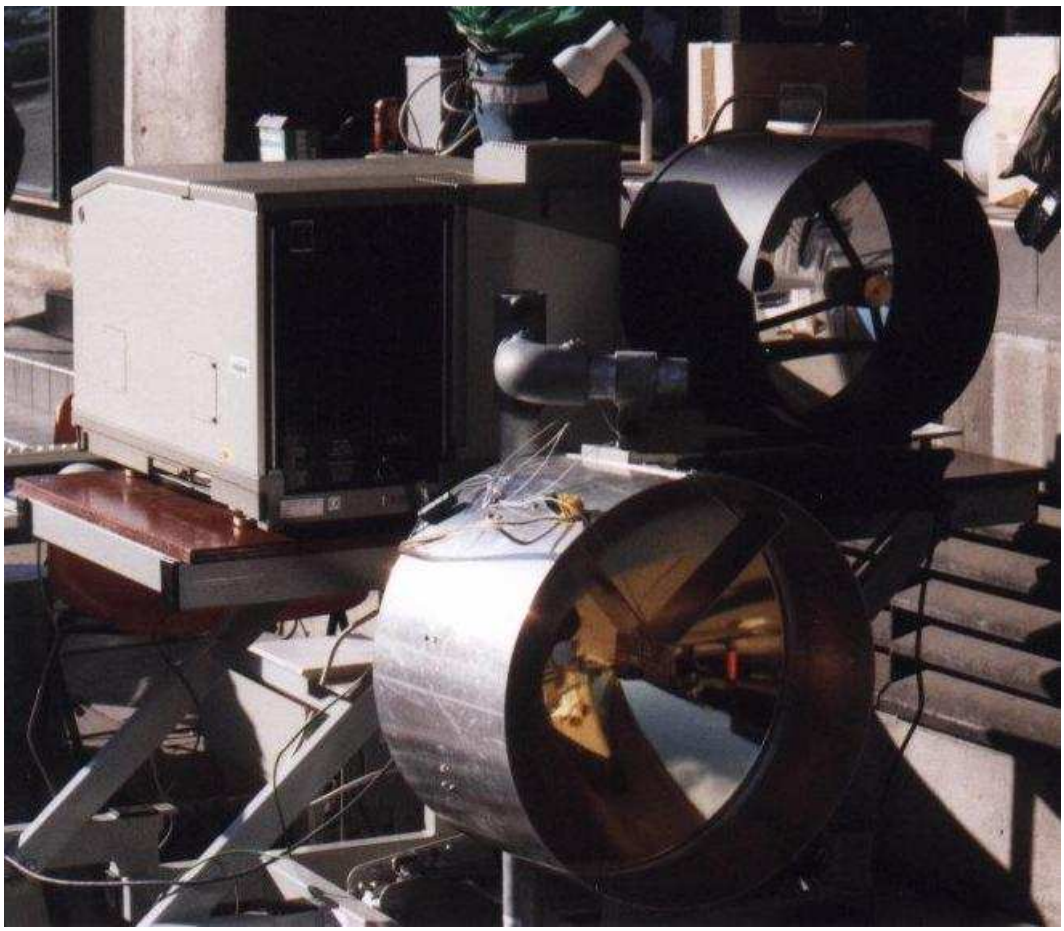

Figure 2.15: Spectrometer, collimator and source in place on Hythe Bridge Street.

located approximately 33 m away, thus providing an overall optical path in air of 68 m. The mirror was mounted, with its reflective surface vertical, in a wooden frame which was

bolted to a stand made from angle steel, with a mass (approximately 60 kg) placed on the base in order to minimise vibration (see figure 2.16). The mirror was adjustable in azimuth and elevation using screw rods in combination with plastic ball joints. Power for

Figure 2.16: Plane mirror (on left) in position on Hythe Bridge Street. The mirror on the right is that belonging to NPL.

the spectrometer, source and PC came from a petrol generator supplied by NPL and was fed through an uninterruptible power supply (APC Smart-UPS 1400). A plastic 'Chapter 8' barrier was placed around the equipment, which together with tall cones and polyethylene red stripped barrier tape excluded the public from the optical paths of the two infrared

beams.

The source, collimator and mirror were initially aligned by eye. Fine alignment was carried out whilst monitoring the energy reaching the MCT detector of the spectrometer. This required two people (one to monitor and one to adjust the alignment) who were in contact by radio link.

Oxford Railway Station

Field measurements across the Botley Road by Oxford railway station were carried out on two successive days in October (25 October and 26 October) in the week following those made on Hythe Bridge Street. The experimental setup was similar on each day; the source was moved approximately 3 m further west on the second day[12]. Figure 2.18 shows a scale plan of the site.

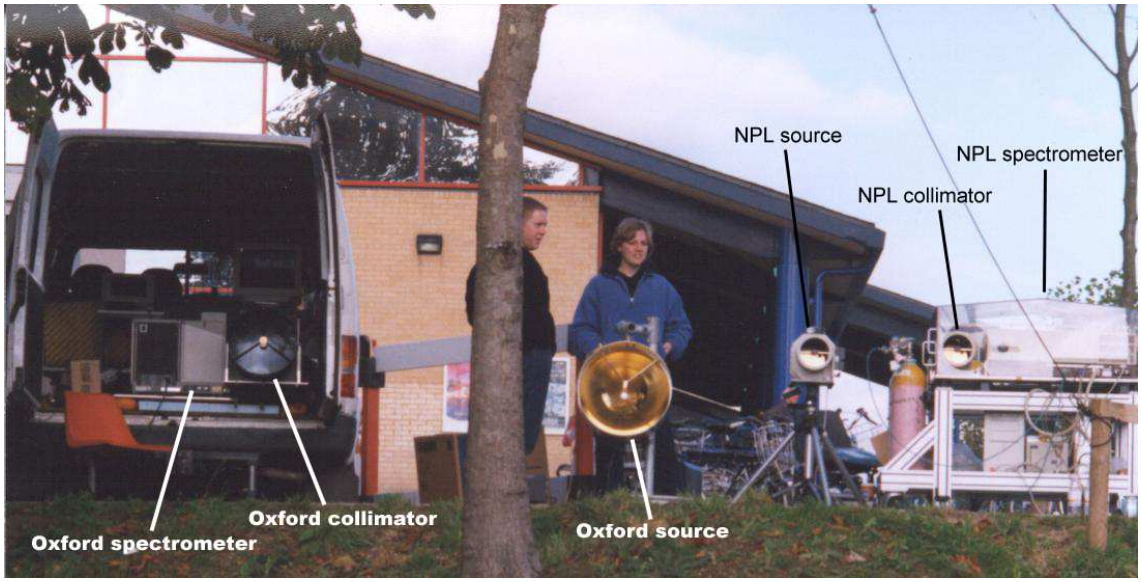

Figure 2.17: Spectrometers, sources and collimators in place at Oxford railway station (view from the plane mirror location).

[12]NPL moved their plane mirror between the two days. It was initially attached to the railings of the pedestrian footbridge, as shown in figure 2.18, but high levels of vibration due to pedestrians walking on the bridge increased the noise on the spectrum. On the second day the mirror was moved to the fence below the pedestrian footbridge, where it was still just above the top of any double decker bus but did not suffer from high levels of vibration.

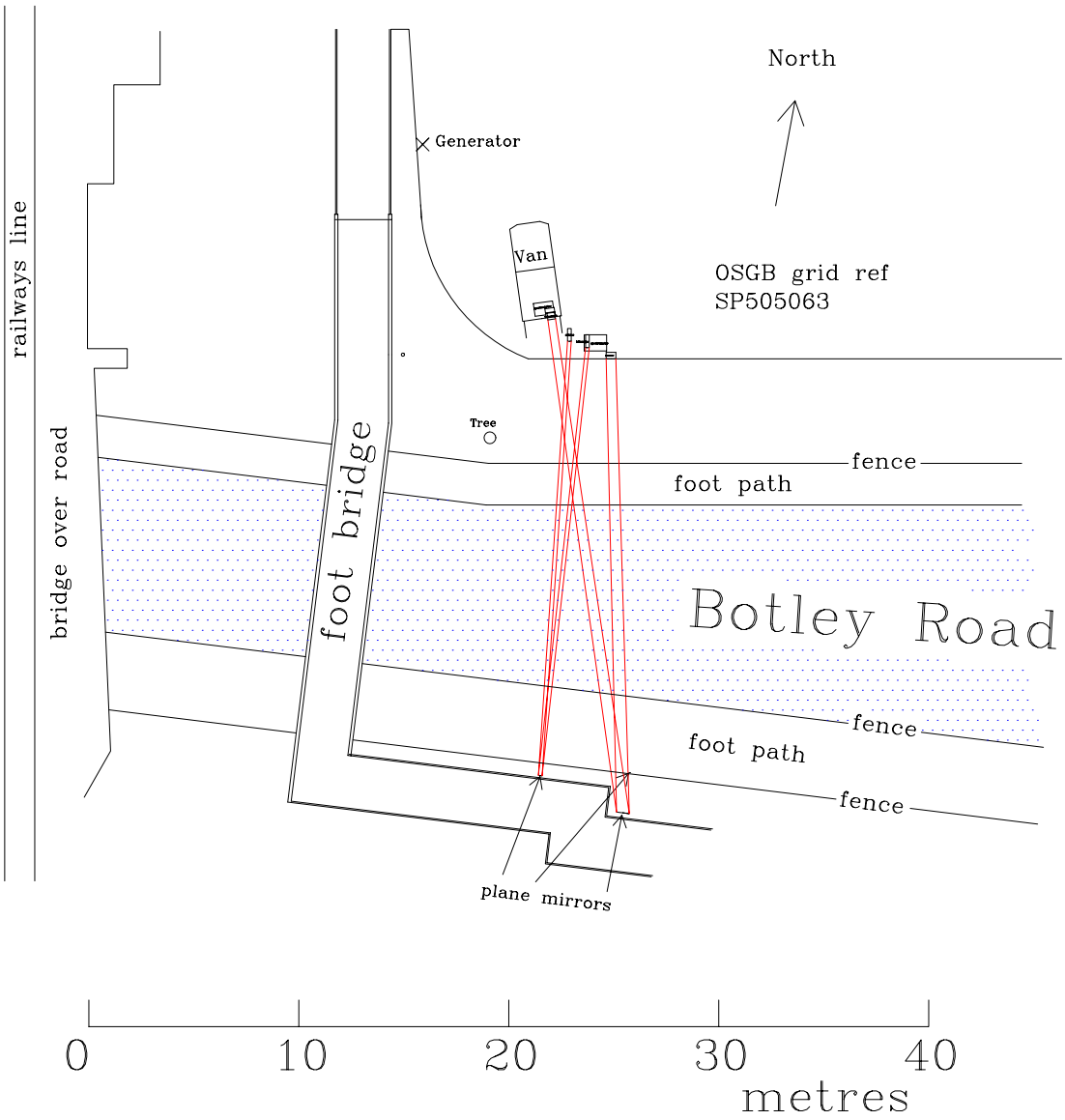

Figure 2.18: Plan of Oxford railway station.

The spectrometer and collimator were mounted on a titanium plate supported at the corners by four pallet spacers, which provided a degree of shock insulation, inside a Ford Transit van. The rear of the van was supported by two axle stands placed at either end of the steel bar to which the tow ball was attached, and the front of the van was supported by a jack under one corner of the van body. This provided a firm, horizontal base for the spectrometer which was not affected by people moving inside the van. The PC controlling

the spectrometer was also located in the van, and the operators were careful not to move for the duration of the recording of each spectrum.

The external source was mounted as for the Hythe Bridge Street measurements and positioned near the van. The mirror, which was still bolted to its steel frame, but without its base, was clamped to the railings of the pedestrian footbridge. Power was again provided by the same petrol generator and a plastic 'Chapter 8' barrier was placed around the equipment. Alignment of the source, collimator and mirror was carried out as at Hythe Bridge Street.

Chapter 3

Issues Relating to Spectrometer Performance

Initial performance testing of the spectrometer in long-path mode revealed three issues detrimental to the performance of the spectrometer. The issues involved are detector non-linearity, spectrometer self-emission and channelling. These issues will be discussed in greater depth in subsequent sections. A brief summary is included below.

The MCT (mercury cadmium telluride) detector has a linear response only at low photon fluxes. This manifests itself as a non-zero signal at wavenumbers lower than the low-wavenumber cut-off (700 cm^{-1}) of the detector (see figure 3.1).

Spectrometer self-emission results from the field of view of the MCT detector, which is cooled to liquid nitrogen temperatures (77 K), including the field stop iris. The latter is stopped right down to enable a resolution of 0.2 cm^{-1} to be used. As such the iris radiates energy as a room-temperature black body, thus increasing the photon flux recorded by the detector. The self-emission effect is most visible as an anomalously high signal recorded by the detector when the infrared source is switched off (see figure 3.2).

Channelling, is caused by interference between waves reflected off the parallel sides of a thin, transmitting optical component in the beam path of the spectrometer. It results in a sinusoidal wave that is superimposed on the required spectrum (see figure 3.3).

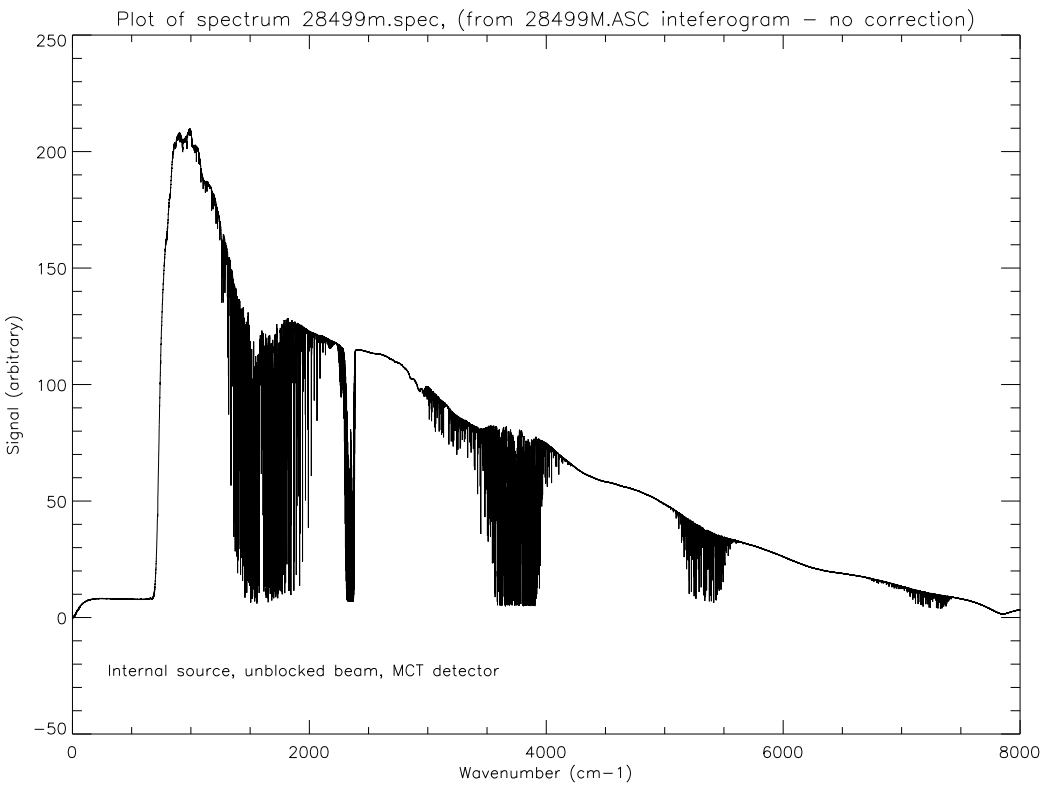

Figure 3.1: Spectrum recorded with a non-linear detector. Note the non-zero signal below 700cm^{-1}.

3.1 Detector Non-Linearity

The Perkin-Elmer Spectrum 2000 FTIR spectrometer, which is used in this study, is equipped with two infra-red detectors. One is a DTGS (Deuterated TriGlycine Sulphate) detector, which operates in the mid infra-red (15,600 cm^{-1} to 370 cm^{-1}) region. This is a pyroelectric bolometer, which detects infrared radiation via the change in polarisation with temperature of a ferroelectric material. The response is linear. The other detector is a liquid nitrogen cooled, narrow band (10,000 cm^{-1} to 700 cm^{-1}) MCT (Mercury Cadmium Telluride) detector. This is a photoconductive detector, in which infrared radiation is detected via photons exciting the electrons in a semiconductor[1] from one state to another in which their electrical properties are different. As will be shown, MCT detectors are

[1]MCT detectors are a mixture of two semiconductors; mercury-telluride and cadmium-telluride, but the same principle applies.

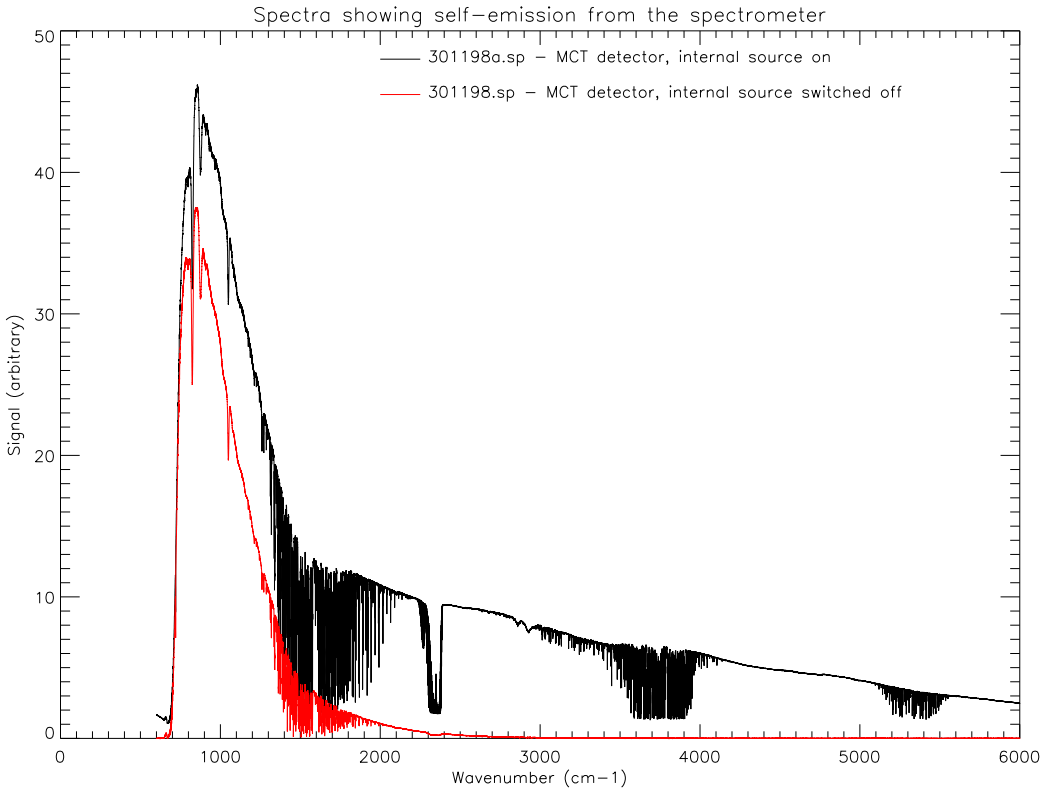

Figure 3.2: Spectra showing self-emission. Note the anomalously high signal recorded when the internal infrared source is switched off.

inherently non-linear. However, they are more sensitive than DTGS detectors. The narrow band MCT detector used in this study is five times more sensitive than the DTGS detector.

MCT detectors also have a faster response than DTGS detectors. The voltage responsivity of a pyroelectric detector, such as the DTGS detector, is inversely proportional to the modulation frequency. Hence the mirror scan speed should be kept at low as possible. Unlike pyroelectric detectors, the response of quantum detectors, such as the MCT detector, is independent of the modulation frequency. However, there is a component of detector noise, for these detectors, which varies inversely with modulation frequency. For MCT detectors therefore, the signal-to-noise ratio (SNR) increases with frequency up to about 1 kHz. It is then approximately constant with modulation frequency to about 1 MHz, before decreasing with frequency at higher values of the modulation frequency. Hence the scan speed should be set so as to be in the plateau region of the SNR. The difference in scan

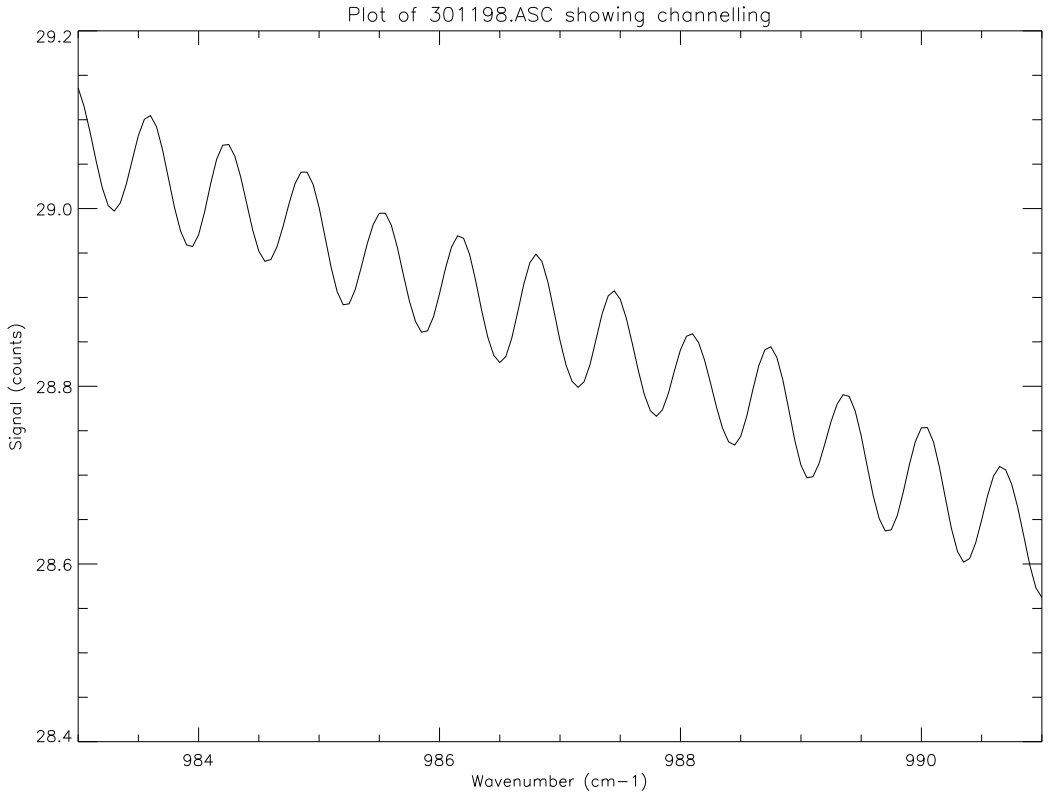

Figure 3.3: Section of a spectrum taken with the Perkin-Elmer Spectrum 2000 showing channelling

speeds is reflected in the time to acquire a spectrum with the two different detectors. With the spectrometer used in this study, the MCT detector takes about 6 seconds to record a single scan, whereas the DTGS detector takes about 1 minute to record a single scan (all other factors are kept the same). Since noise scales as the reciprocal of the square root of the number of scans, an increase in the signal-to-noise ratio of $\sqrt{10}$ can be achieved simply by the increased number of scans possible with the MCT detector in the same time span.

Typical signal-to-noise ratios for the two detectors used in this study are 667 for 100 co-added scans recorded by the MCT detector and 143 for 10 co-added scans recorded by the DTGS detector. The measurement time for each set of scans is 10 minutes and all other factors were kept the same, apart from switching between the 2 detectors (which changes the scan speed), so the SNRs are comparable. They show that the MCT has a

SNR approximately five times greater than the DTGS detector.

The increased sensitivity and faster response of the MCT detector has to be balanced against the fact that it is inherently non-linear. A study was undertaken to determine whether it is possible to correct spectra, or interferograms, taken with the MCT detector for the non-linearities introduced by the detector.

3.1.1 Background

It has been shown by Bartoli *et al.* (Bartoli et al. 1974) that for photon fluxes in excess of 10^{20} photons cm^{-2} s^{-1} the photoconductivity of an MCT detector is proportional not to the photon flux, Φ, but to $\Phi^{1/3}$. This is due to the minority charge carrier lifetime at these high flux levels being proportional to $\Phi^{-2/3}$, which has been demonstrated (Kinch & Borrello 1975) (Borrello, Kinch & Lamont 1977) to be consistent with Auger recombination of carriers within the detector.

Since the non-linearities are introduced at high photon flux levels, the obvious solution is to reduce the photon flux. This can be achieved by using a neutral density filter to reduce the photon flux uniformly across the spectral range, or by restricting the spectral range, the field of view, the aperture or a combination of these techniques. However, these methods negate the main reason for using an MCT detector; its higher signal-to-noise ratio. It has been found that the self-emission from the spectrometer used in this study, which is an ambient temperature instrument, is large enough to cause the MCT detector used in this study to behave non-linearly. It has been determined, by using neutral density filters, that the infrared radiation from the internal source needs to be attenuated to approximately 4% of its flux in order for the MCT detector to operate in within its linear response range. An attenuation to approximately 5% of its initial flux is required for the external source.

It has been shown that the detector's electronics can effect whether it is non-linear or not. Schindler (Schindler 1986) demonstrated that a resistor placed in series with the detector can cause the measurement to be non-linear, even at low photon fluxes. Chase (Chase 1984) showed experimentally that MCT detectors can be forced into a region of

non-linear response by application of too high a bias current. Carter *et al.* (Carter III, Lindsay & Beduhn 1990) demonstrated that replacing the MCT's constant-current preamplifier with a constant-voltage preamplifier allows the MCT to operate linearly at flux levels that previously caused non-linearities. Indeed a patent has been issued for an MCT detector/preamplifier/amplifier combination based on a similar technique (Curbelo 1993). However, the surrounding electronics can still introduce non-linearities necessitating a software correction (Ramelow 1997).

Various software methods have been suggested and implemented which correct for the non-linear effects. These methods (Abrams, Toon & Schindler 1994) (Keens & Simon 1990), although differing in detail, follow the same general scheme. The effect of the non-linearity on the interferogram is modelled, a correction factor calculated and then the correction is applied before the interferogram is phase corrected and the spectrum calculated. The exception to this is the correction scheme proposed by Richardson *et al.* (Richardson Jr, Yang & Griffiths 1998) which is applied directly to transmission spectra. This correction scheme was first employed with spectra recorded using an identical spectrometer and detector to that used in this study. However, the correction can only be applied to transmission spectra, not single beam spectra, and so is inapplicable for this study.

3.1.2 Modelling Detector Non-Linearity

The two main effects of detector non-linearities are a non-zero signal in the spectral region below the detector cut-off, and non-zero offsets beneath blacked out spectral lines. The non-zero signal below the detector cut-off is the main indication that an MCT detector is operating non-linearly.

As previously stated, if the non-linearity has been caused by too high a photon flux, then the measured signal is proportional to $\Phi^{1/3}$, where Φ is the flux. So, following Abrams *et al.* (Abrams, Toon & Schindler 1994):

$$I_S(x) = a\Phi^{1/3}(x) \tag{3.1}$$

The measured signal consists of an AC component, which is recorded as the interferogram,

and a discarded DC component, $I_0 = a\Phi_0^{1/3}(x)$, where Φ_0 is the dc part of the flux, and a is a constant of proportionality. The measured interferogram, which is non-linear, is thus, $I_1(x) = I_S(x) - I_0$. Since the true, linear, interferogram, $I(x)$, is proportional to the ac part of the flux, it can be estimated as follows:

$$I(x) = \frac{\Phi(x) - \Phi_0}{\left[\frac{\partial\Phi(x)}{\partial I_S(x)}\right]_{I_0}} \tag{3.2}$$

Now, $\Phi(x) - \Phi_0 = (I_S(x)/a)^3 - (I_0/a)^3$ and $(\partial\Phi(x)/\partial I_S(x))_{I_0} = 3I_0^2/a^3$, so substituting for these, and using $I_1(x) = I_S(x) - I_0$:

$$I(x) = I_1(x)\left\{1 + \frac{I_1(x)}{I_0} + \frac{1}{3}\left[\frac{I_1(x)}{I_0}\right]^2\right\} \tag{3.3}$$

It is worth noting that away from the centreburst of the interferogram $I_1(x) \ll I_0$ and the equation reduces to $I(x) = I_1(x)$. Therefore, the main effect of any non-linearity is to clip the centreburst.

The effects of non-linearities on spectra were first modelled by Chase (Chase 1984) in 1984. He showed that detector non-linearities cause a negative signal below the detector cut-off. However, when coupled with phase errors[2] and phase correction, this signal can be negative or positive and will have some structure to it. The reason for this can be demonstrated theoretically, as was shown by Chase:

Let

$$I(x) = \int_0^\infty B(\tilde{\nu})\cos(2\pi\tilde{\nu}x)\,d\tilde{\nu} \tag{3.4}$$

where $B(\tilde{\nu})$ = the spectrum incident upon the spectrometer

$I(x)$ = the interferogram that results if the spectrometer is ideal

(i.e. no phase errors and no non-linearity).

Since $B(\tilde{\nu})$ is real and even, and $I(x)$ is the cosine transform of $B(\tilde{\nu})$ over the positive frequencies, $I(x)$ is real and even.

[2]These arise due to optical, electronic or sampling effects and result in an asymmetric interferogram. Examples of effects causing phase errors are the beamsplitter introducing a wavelength-dependent phase change, electronic filters, employed in the amplification of the detected signal, introducing a wavelength-dependent phase lag, and the zero optical path difference not coinciding with a sampling point.

More conventionally, equation (3.4) is written as

$$I(x) = \int_{-\infty}^{\infty} B(\tilde{\nu}) e^{2\pi i \tilde{\nu} x} \, d\tilde{\nu} \tag{3.5}$$

where it is implied that the real part of the Fourier transform is taken.

A non-linear interferogram, $I_1(x)$, can be modelled as follows

$$\begin{aligned} I_1(x) &= I(x)\{1 - cI(x)\} \\ &= I(x) - cI^2(x) \end{aligned} \tag{3.6}$$

where c is a constant. If equation (3.6) is solved for $I(x)$, then using binomial expansion, we find:

$$I(x) = I_1(x)\left\{1 + cI_1(x) + 2c^2 I_1^2(x) + \cdots\right\} \tag{3.7}$$

which is of a similar form to equation (3.3), thus justifying the model. The spectrum resulting from such a non-linear interferogram, with no phase errors, is

$$\begin{aligned} S_1(\tilde{\nu}) &= \int_{-\infty}^{\infty} I_1(x) e^{-2\pi i \tilde{\nu} x} \, dx \\ &= \int_{-\infty}^{\infty} I(x) e^{-2\pi i \tilde{\nu} x} \, dx - c \int_{-\infty}^{\infty} I^2(x) e^{-2\pi i \tilde{\nu} x} \, dx \end{aligned}$$

where $S_1(\tilde{\nu})$ is the calculated spectrum (the real part of the Fourier transform is taken). This can be rewritten as

$$\begin{aligned} S_1(\tilde{\nu}) &= B(\tilde{\nu}) - c \int_{-\infty}^{\infty} I^2(x) e^{-2\pi i \tilde{\nu} x} \, dx \\ &= B(\tilde{\nu}) - cS_2(\tilde{\nu}) \end{aligned} \tag{3.8}$$

where

$$S_2(\tilde{\nu}) = \int_{-\infty}^{\infty} I^2(x) e^{-2\pi i \tilde{\nu} x} \, dx$$

then by the convolution theorem

$$S_2(\tilde{\nu}) = \int_{-\infty}^{\infty} B(\tilde{\nu}') B(\tilde{\nu} - \tilde{\nu}') \, d\tilde{\nu}'$$

which is the autoconvolution function of the spectrum.

In the case where there are no phase errors and the interferogram is symmetric, the Fourier transform of $I(x)$ is real and even, and $S_2(\tilde{\nu})$ is a smooth function. The non-linearity effectively subtracts a Dirac delta function ($I^2(x)$ is slightly broader than a Dirac delta function) from the interferogram, i.e. it clips the centreburst, which causes a smooth negative offset in the spectrum, as equation (3.8) demonstrates. This is most visible as a negative signal below the detector cut-off.

If, however, as in all actual FTIR spectrometers, there are phase errors, then the interferogram is asymmetric and the Fourier transform of $I(x)$ is real and complex. This causes a frequency shift in addition to phase correction errors and results in the kind of signal below the detector cut-off shown in figure 3.1.

When phase errors are introduced, the measured interferogram, in the case where there is no non-linearity, is no longer $I(x)$, but

$$I_2(x) = \int_{-\infty}^{\infty} B(\tilde{\nu}) e^{i(2\pi\tilde{\nu}x - \theta_{\tilde{\nu}})}\, d\tilde{\nu} \tag{3.9}$$

where $\theta_{\tilde{\nu}}$ is a wavenumber dependent phase lag. This is usually slowly varying and so can be written as

$$\theta_{\tilde{\nu}} = 2\pi\kappa\tilde{\nu} \tag{3.10}$$

where κ is a constant. Therefore

$$I_2(x) = \int_{-\infty}^{\infty} B(\tilde{\nu}) e^{2\pi i\tilde{\nu}(x-\kappa)}\, d\tilde{\nu} \tag{3.11}$$

which is the convolution of $B(\tilde{\nu})$ with $e^{2\pi i\tilde{\nu}\kappa}$. Now

$$\int_{-\infty}^{\infty} e^{2\pi i\tilde{\nu}(x-\kappa)}\, d\tilde{\nu} = \delta(x+\kappa) \tag{3.12}$$

Therefore

$$\begin{aligned} I_2(x) &= \int_{-\infty}^{\infty} \delta(x'+\kappa) I(x-x')\, dx \\ &= I(x) \otimes \delta(x+\kappa) \end{aligned} \tag{3.13}$$

which shows that the interferogram, $I(x)$ is frequency shifted by an amount κ. The spectrum, $S_3(\tilde{\nu})$, created from such an interferogram is complex

$$S_3(\tilde{\nu}) = B(\tilde{\nu})e^{-2\pi i\tilde{\nu}\kappa} \tag{3.14}$$

and must be phase corrected in order to extract the incident spectrum, $B(\tilde{\nu})$.

The most commonly used method is that of Mertz phase correction (Mertz 1965) (Mertz 1967). This uses the short double-sided section of the interferogram to create a low resolution phase spectum, by apodizing, zero-filling and Fourier transforming it. The full interferogram is then apodized, zero-filled and Fourier transformed. The resulting complex spectrum, $S_3(\tilde{\nu})$, is then multiplied by the complex exponential, $e^{i\phi(\tilde{\nu})}$, which is computed by interpolation from the low resolution phase spectrum (to bring it to the same resolution as that of the entire spectrum, $S_3(\tilde{\nu})$). The real part of the resulting array represents the measured spectrum. The imaginary part is non-zero because a full double-sided interferogram was not used. This method of phase correction is not perfect (i.e. $\phi(\tilde{\nu}) \approx 2\pi\tilde{\nu}\kappa$) and results in small errors.

In the case where there are both phase errors and detector non-linearities, then the recorded interferogram is

$$\begin{aligned} I_3(x) &= I_2(x)\left\{1 - cI_2(x)\right\} \\ &= I_2(x) - cI_2^2(x) \\ &= I(x) \otimes \delta(x+\kappa) - c\left\{I(x) \otimes \delta(x+\kappa)\right\}^2 \end{aligned} \tag{3.15}$$

and the calculated spectrum is

$$\begin{aligned} S_4(\tilde{\nu}) &= \int_{-\infty}^{\infty} I_3(x)e^{-2\pi i\tilde{\nu}x}\,dx \\ &= \int_{-\infty}^{\infty} I(x) \otimes \delta(x+\kappa)e^{-2\pi i\tilde{\nu}x}\,dx - c\int_{-\infty}^{\infty}\left\{I(x) \otimes \delta(x+\kappa)\right\}^2 e^{-2\pi i\tilde{\nu}x}\,dx \\ &= B(\tilde{\nu})e^{-2\pi i\tilde{\nu}\kappa} - c\int_{-\infty}^{\infty} B(\tilde{\nu}')e^{-2\pi i\tilde{\nu}'\kappa}B(\tilde{\nu}-\tilde{\nu}')e^{-2\pi i(\tilde{\nu}-\tilde{\nu}')\kappa}\,d\tilde{\nu}' \end{aligned}$$

$$= \quad B(\tilde{\nu})e^{-2\pi i\tilde{\nu}\kappa} - ce^{-2\pi i\tilde{\nu}\kappa} \int_{-\infty}^{\infty} B(\tilde{\nu}')B(\tilde{\nu}-\tilde{\nu}')\,d\tilde{\nu}'$$

If the phase correction were perfect, and $\phi(\tilde{\nu}) = 2\pi\tilde{\nu}\kappa$, then this case would be the same as the case with just non-linearities. However, the errors in the phase correction lead, as Chase showed, to a positive (not negative) offset, such as that shown in figure 3.1.

For this study, the following model was used:

$$I_{meas} = I_{lin} + aI_{lin}^2 \tag{3.16}$$

or

$$I_{lin} = I_{meas} - aI_{meas}^2 + 2a^2I_{meas}^3 + \cdots \tag{3.17}$$

where I_{meas} is the measured interferogram, I_{lin} is the linear interferogram that we want to find and a is a unknown, positive constant. Equation (3.16) is of the opposite sign to equation (3.6) in order to take account of the errors in phase correction, which change the offset in the spectrum from being negative, as modelled in equation (3.6), to positive.

3.1.3 Correcting for Detector Non-Linearity

Development of a correction method was initiated using simulated data. A non-linear interferogram, I_{meas}, was created from a linear interferogram by applying equation (3.16) with the value of a set to $1\text{x}10^{-7}$. The spectrum resulting from the Fourier transform of I_{meas}, showed the expected signs of non-linearity; a non-zero signal below the detector cut-off wavenumber and a non-zero offset below blacked out lines (see figure 3.4).

Two possible methods for correcting non-linear spectra were developed. The first uses the first two terms of equation (3.17) to create a corrected interferogram. The Fourier transform of this is the corrected spectrum. The value of a is determined iteratively, with the first guess being 1/(magnitude of the spectrum of I_{meas}^2).

Since the main effect of this correction is to subtract a sloping line from the non-linear spectrum, a second correction scheme was devised, whereby a sloping line was subtracted

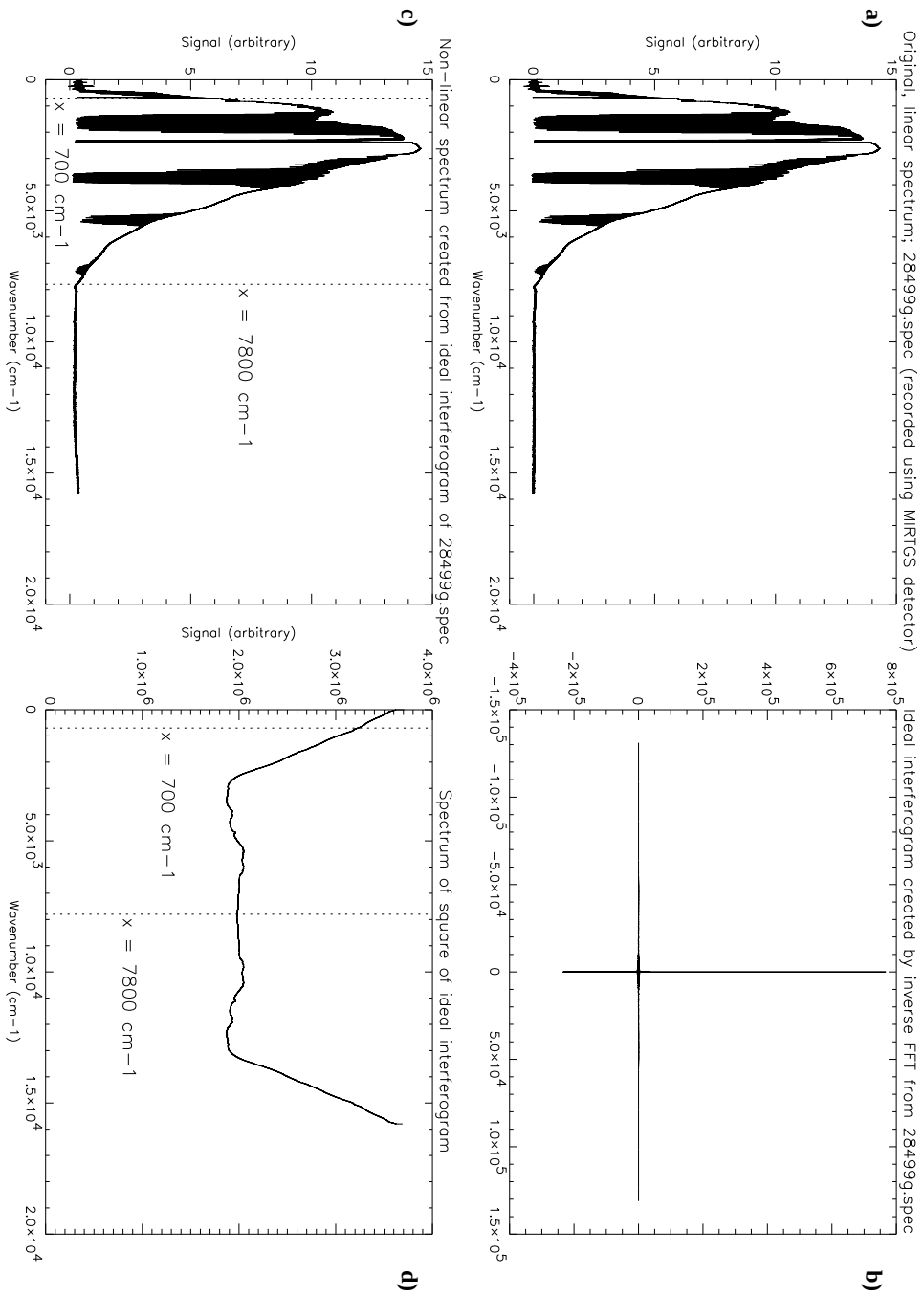

Figure 3.4: Simulated non-linear spectrum. (a) shows the original linear spectrum (28499g.spec), which was recorded with the DTGS detector. (b) shows the interferogram created from 28499g.spec (by an inverse Fourier transform). (c) shows the non-linear spectrum created from the interferogram of 28499g.spec, using equation (3.16). Note the non-zero signal below the detector cut-off at 370 cm^{-1}, indicating that the spectrum is non-linear. (d) shows the spectrum of the non-linearity; i.e. the spectrum of the square of the interferogram of 28499g.spec

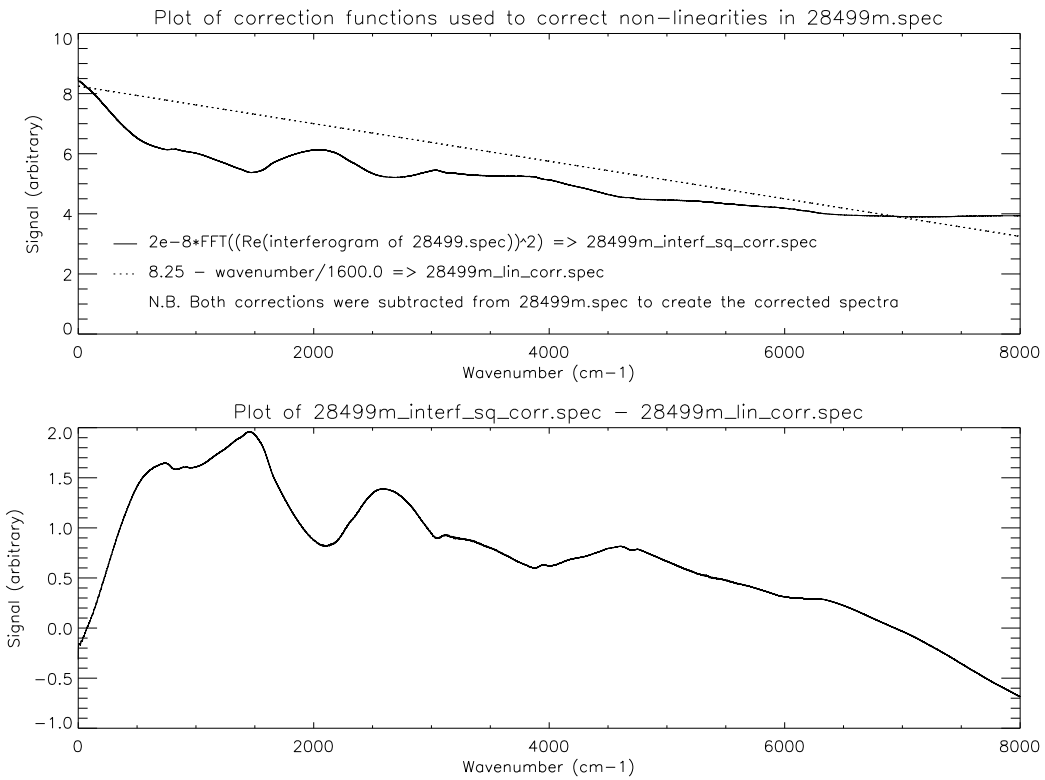

Figure 3.5: Plot showing the two corrections used on the non-linear spectra and the difference between them. In the upper plot the solid line is the spectrum of the correction using the first two terms of equation (3.17) applied to the spectrum 28499m.spec. Here $a = 2\text{x}10^{-8}$ and the corrected spectrum is 28499m_interf_sq_corr.spec. The dotted line is the spectrum of the correction using equation (3.18). Here $r = 8.25$, $s = 1600.0^{-1}$ and the corrected spectrum is 28499m_lin_corr.spec.

from the non-linear spectrum (see figure 3.5):

$$S_{corrected}(\tilde{\nu}) = S_{meas} - r - s\tilde{\nu} \tag{3.18}$$

where $S_{corrected}(\tilde{\nu})$ is the corrected spectrum, S_{meas} is the Fourier transform of I_{meas}, and r and s are constants.

The corrections produced plausible spectra (see figure 3.6). A more rigorous comparison of the correction schemes, using information from retrievals on simulated spectra, was implemented. Transmission spectra in the regions 1330 cm^{-1} to 1390 cm^{-1} and 2120 cm^{-1} to 2220 cm^{-1} were simulated, using known gas concentrations, with the RFM (Dudhia 1997). The first region contains the main (Q-branch) SO_2 band, and the second region

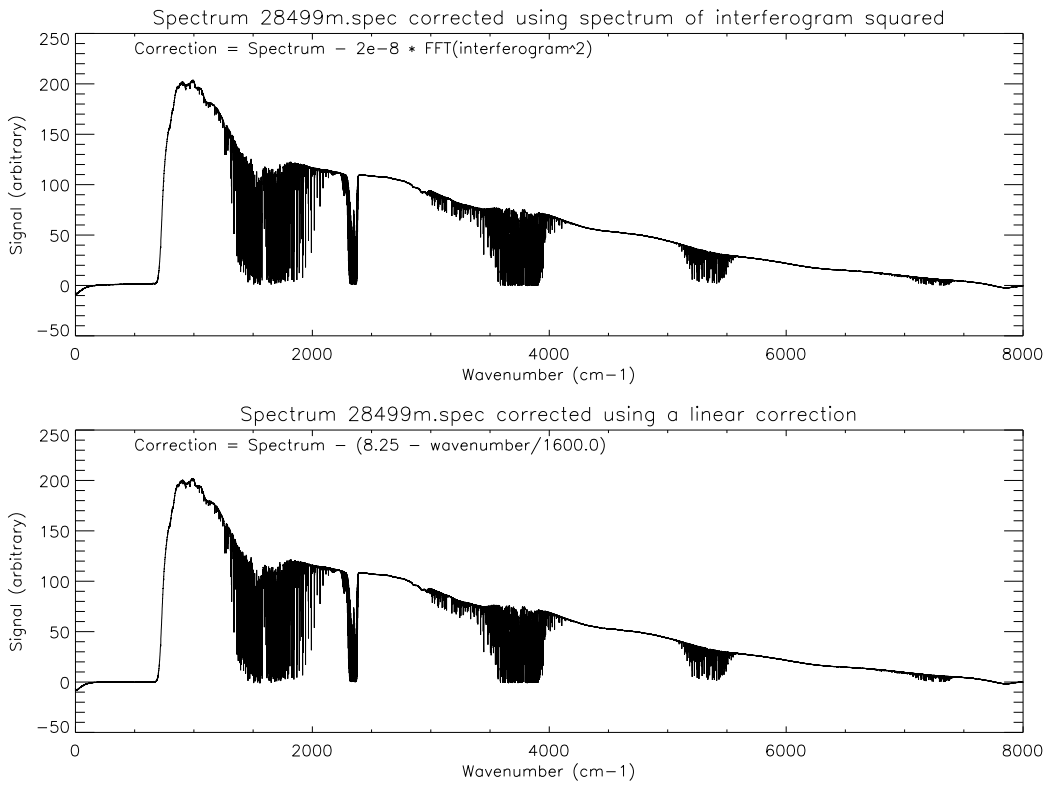

Figure 3.6: Plot showing the same spectrum corrected by each of the 2 different methods. The upper spectrum was corrected using the first two terms of equation (3.17) (using the square of the interferogram). The lower spectrum was corrected using equation (3.18) (using the linear correction).

contains the fundamental absorption band of CO. Gaussian distributed random noise of amplitude 0.1% was added to the spectra, and the whole convolved with an instrument line shape of 0.2 cm^{-1} resolution and strong Norton-Beer apodization. The spectra were multiplied by a quadratic gain term and a linear offset was added in order to transform the transmission spectra to single beam spectra (such as those in figure 3.4), which are used in this study. Non-linearities were added, following equation (3.16), to the spectra in the interferogram domain, and the two correction schemes applied. Retrievals (for more details of the retrieval method see Chapter 4) were then carried out on the (noisy) transmission spectra, single beam spectra, non-linear spectra and the two sets of corrected spectra.

The results are summarised in tables 3.1, 3.2, 3.3 and 3.4.

Table 3.1: SO_2 Retrievals

Spectrum	SO_2(ppmv)	H_2O(ppmv)	CH_4 (ppmv)
Actual values	*0.315*	*11700*	*2.43*
Transmission	0.340	11694	2.29
Single beam	0.250	11692	2.27
Non-linear	0.240	11702	2.31
Interferogram correction	0.252	11697	2.27
Sloping line correction	0.250	11700	2.31

Table 3.2: SO_2 Estimated Standard Deviation†

Spectrum	SO_2 % error	H_2O % error	CH_4 % error
Transmission	7.97	0.054	5.80
Single beam	20.7	0.068	6.58
Non-linear	23.9	0.019	5.14
Interferogram correction	20.1	0.027	8.24
Sloping line correction	20.7	0.003	8.35

† The % error given is the appropriate element of $\sqrt{\mathbf{S_x}}$, where $\mathbf{S_x}$ is the covariance error matrix of the retrieved profile.

Table 3.3: CO Retrievals

Spectrum	CO (ppmv)	H_2O(ppmv)	N_2O(ppmv)
Actual values	*5.35*	*10569*	*1.70*
Transmission	5.17	10083	1.64
Single beam	5.87	11515	1.87
Non-linear	5.64	11060	1.80
Interferogram correction	5.89	11556	1.88
Sloping line correction	5.93	11638	1.89

Table 3.4: CO Estimated Standard Deviation†

Spectrum	CO % error	H_2O % error	N_2O % error
Transmission	3.44	4.60	3.70
Single beam	9.67	8.95	10.0
Non-linear	5.48	4.64	5.76
Interferogram correction	10.0	9.34	10.4
Sloping line correction	10.8	10.1	11.1

† The % error given is the appropriate element of $\sqrt{\mathbf{S_x}}$, where $\mathbf{S_x}$ is the covariance error matrix of the retrieved profile.

These results indicate that the performance of the retrieval is not affected by the non-linearities. The results are similar for all non-transmission spectra. This is due to two effects. The superiority of retrievals on the transmission spectra is due to correlation

between the gain terms, of the non-transmission spectra, and the volume mixing ratio terms. This is easily determined from the off-diagonal terms of the covariance error matrix of the retrieved profile.

The lack of effect on retrieval performance of the non-linearities is due to the form of the non-linearity in spectral space. Figure 3.5 shows that both correction functions are smoothly varying curves. Over regions of 100 cm^{-1}, the typical width of a retrieval window, they can be completely described by a quadratic curve and a linear, vertical offset. Therefore their only effect is to modify the gain, which is a quadratic curve, and offset terms (see section 4.6 for details of the gain and offset terms). Figure 3.4 shows that the form of the non-linearity is similar to that of the correction functions, and hence its only effect is to modify the gain and offset terms. The gain and offset terms are due to several different instrumental effects. It is necessary to retrieve 'gain' and 'offset' in order to accurately retrieve the gas volume mixing ratios. It is not necessary to separate out the different instrumental effects forming these composite terms.

Final testing of the correction methods was performed on a real spectrum that was known to be non-linear (28499m.spec - see figure 3.1). The retrievals were carried out both on the original spectrum and on two corrected versions (see figure 3.6). The retrievals were carried out in two regions: 2120 cm^{-1} to 2220 cm^{-1}, and 2320 cm^{-1} to 2350 cm^{-1}. The first region contains the main CO band and the second is a region containing just CO_2. Details are given in tables 3.5, 3.6 and 3.7 and figures 3.7 and 3.8.

Table 3.5: Retrievals of CO from a Real Spectrum

Spectrum	CO (ppmv)	H_2O (ppmv)	N_2O (ppmv)
Non-linear	6.58	13667	0.339
Interferogram correction	7.08	14744	0.352
Sloping line correction	7.15	14918	0.368

The 9% difference between volume mixing ratio values for the CO retrieval from the different spectra is within the retrieval error. The CO_2 values are identical. It is therefore

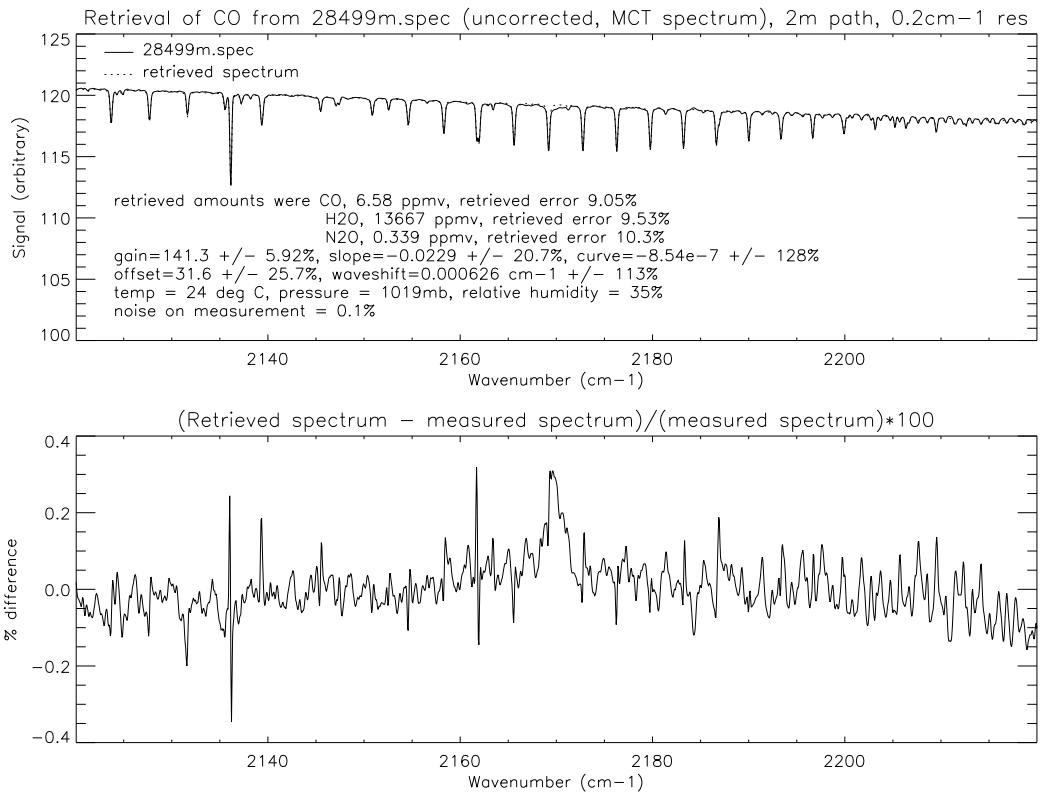

Figure 3.7: Retrieval of CO from 28499m.spec (non-linear spectrum). The solid line in the upper plot is the measured spectrum, 28499m.spec. The dotted line in the upper spectrum (visible in places) is the retrieved spectrum created by the RFM using the values given in the plot. The stated retrieved errors are the appropriate elements of $\sqrt{\mathbf{S_x}}$. The lower curve is the residuals of the retrieval (retrieved spectrum - measured spectrum) expressed as a percentage of the measured spectrum.

Table 3.6: Errors on Retrievals of CO from a Real Spectrum

Spectrum	CO retrieval % error†	H_2O retrieval % error†	N_2O retrieval % error†
Non-linear	9.05	9.53	10.3
Interferogram correction	9.01	9.46	10.3
Sloping line correction	8.99	9.45	10.1

† The retrieval % error given is the appropriate element of $\sqrt{\mathbf{S_x}}$, where $\mathbf{S_x}$ is the covariance error matrix of the retrieved profile.

concluded that no correction scheme need be applied to the non-linear spectra recorded with the MCT detector due to the ability of the retrieval scheme to correct for the non-linearities.

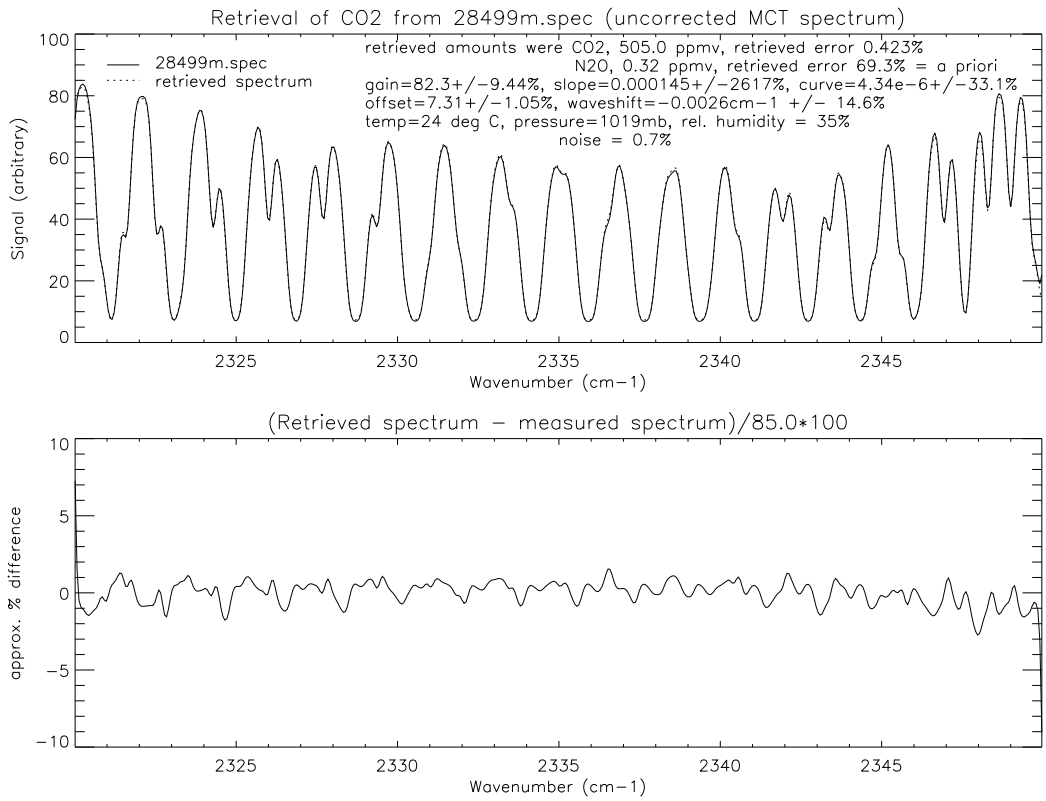

Figure 3.8: Retrieval of CO_2 from 28499m.spec (non-linear spectrum). The solid line in the upper plot is the measured spectrum, 28499m.spec. The dotted line in the upper spectrum (visible in places) is the retrieved spectrum created by the RFM using the values given in the plot. The stated retrieved errors are the appropriate elements of $\sqrt{\mathbf{S_x}}$, where $\mathbf{S_x}$ is the covariance error matrix of the retrieved profile. The lower curve is the residuals of the retrieval (retrieved spectrum - measured spectrum) expressed as a percentage of the measured spectrum.

Table 3.7: CO_2 Retrievals

Spectrum	CO_2 (ppmv)	CO_2 retrieval % error†
Non-linear	505.0	0.423
Interferogram correction	505.0	0.388
Sloping line correction	505.0	0.394

† The retrieval % error given is the appropriate element of $\sqrt{\mathbf{S_x}}$, where $\mathbf{S_x}$ is the covariance error matrix of the retrieved profile.

3.2 Self-Emission

Self-emission is thermal emission emanating from the spectrometer components, rather than the hot source. In this study, self-emission is detected when the MCT detector, a cooled

detector, is used. The ambient temperature DTGS detector is not sensitive to thermal emission from ambient temperature sources.

Self-emission alters the emission levels detected. It either adds to or subtracts from the emission from the source depending on the phase of the emission. The phase of the self-emission depends on whether the emission is modulated by the interferometer in transmission or reflection. Emission arising from optical elements between the source and the interferometer[3] (the source port) has the same phase as emission from the source. Emission arising from optical elements between the detector and the interferometer (the detector port) is modulated in reflection by the interferometer and is thus π radians out of phase with the radiation coming from the source.

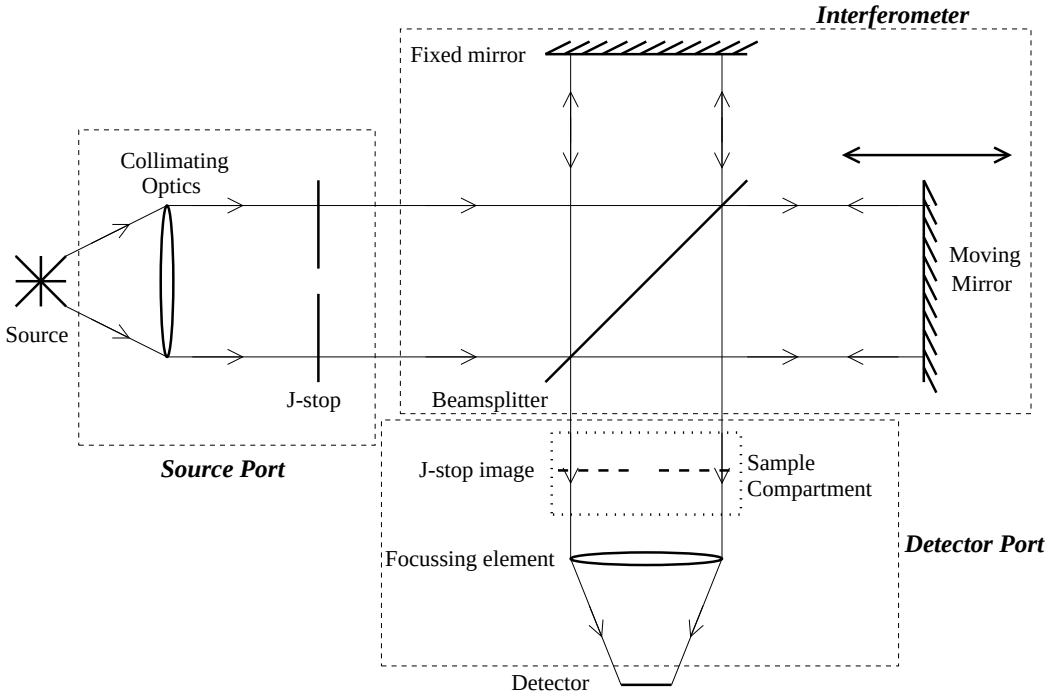

Figure 3.9: Schematic of the spectrometer showing the source port, detector port and interferometer.

Emission arising from sources in the detector port will also reach the detector without passing through the interferometer, in either transmission or reflection. Since it has not

[3]The interferometer consists of the beamsplitter, fixed and moving mirrors.

been modulated by the interferometer, it will be DC radiation, and thus will be filtered out electronically.

3.2.1 Self-Emission in the Spectrum 2000

In the spectrometer used in this study, the main source of self-emission is from the field stop, or J-stop. This is located in the source port, and therefore its emission is of the same phase as that from the source, and adds to the total emission. Emission from the J-stop iris is recorded by the detector because the image of the J-stop aperture, at the resolution, 0.2cm^{-1}, used in this study, is smaller than the size of the detector. Therefore, radiation emitted by the J-stop iris falls on the detector and, since it has been modulated by the interferometer, is recorded in the interferogram (see figure 3.2).

Following Ballard, Remedios and Roscoe (Ballard, Remedios & Roscoe 1992), the measured spectral signal can be modelled as follows:

$$\begin{aligned} S &= R(\tilde{\nu})\{B(T_s,\tilde{\nu})\tau_1\tau_2\tau_3 A_s\Omega_s + B(T_1,\tilde{\nu})(1-\tau_1)\tau_2\tau_3 A_s\Omega_s + B(T_J,\tilde{\nu})\tau_2\tau_3(A_d\Omega_d - A_s\Omega_s) \\ &\quad + B(T_2,\tilde{\nu})(1-\tau_2)\tau_3 A_d\Omega_d - B(T_3,\tilde{\nu})(1-\tau_3)A_d\Omega_d\} \end{aligned} \tag{3.19}$$

where $R(\tilde{\nu})$ = the spectrometer response function

$B(T,\tilde{\nu})$ = the Planck function at temperature, T, and wavenumber, $\tilde{\nu}$

T_s, T_J = temperature of the source, temperature of the J-stop

T_1 = temperature of the atmosphere between the source and J-stop

T_2 = temperature of the atmosphere between the J-stop and interferometer

T_3 = temperature of the atmosphere between the interferometer and MCT detector

$\tau_1(\tilde{\nu})$ = the transmission of the atmosphere between the source and the J-stop

$\tau_2(\tilde{\nu})$ = the transmission of the atmosphere between the J-stop and the interferometer

$\tau_3(\tilde{\nu})$ = the transmission of the atmosphere between the interferometer and the MCT detector

A_s = the area of the aperture in the J-stop

Ω_s = the solid angle of radiation collected by the collimator from the J-stop aperture

A_d = the area of the detector element

Ω_d = the solid angle of radiation collected by the detector element.

The model includes terms for the emission from the source, the J-stop iris, and from the atmosphere. The emission from the atmosphere is split into three parts. The first split is into emission from the source port, $(1-\tau_1)$ and $(1-\tau_2)$, and emission from the detector port, $(1-\tau_3)$, because of the change of phase involved. The source port emission is further split between emission originating before the J-stop, $(1-\tau_1)$, and emission originating after the J-stop, $(1-\tau_2)$. This split is necessary because the J-stop is the system field stop, and the etendue of the emission is different depending on whether or not it passes through the stop.

For the spectrometer used in this study, when operating with the MCT detector and at a resolution of 0.2 cm^{-1}, $A_s\Omega_s = 7.57\times10^{-5}$ mm^2 and $A_d\Omega_d = 8.37\times10^{-4}$ mm^2.

An estimate of the size of the self-emission, relative to the signal from the 1000 K, infrared source, was calculated using these values and is shown in figure 3.10. For clarity the transmission terms were set to 1.

It can be calculated from figure 3.10 that the self-emission varies between 35% of that of the source at 850 cm^{-1} (at lower wavenumbers the sensitivity of the MCT detector to infrared radiation is significantly reduced) and 0% at 3000 cm^{-1}. In practice, self-emission is more significant than this simple model indicates, as can be seen from figures 3.2 and 3.12. From these figures it was calculated that the self-emission contributes up to 70% of the total signal.

Figure 3.11 shows that the J-stop and the internal source, when at room temperature, emit radiation according to the Planck curve of blackbody radiation. The discrepancies between the recorded spectrum and the Planck curve are due to the reduced detector response below 850 cm^{-1} and to atmospheric absorption over the 1.7 m atmospheric path

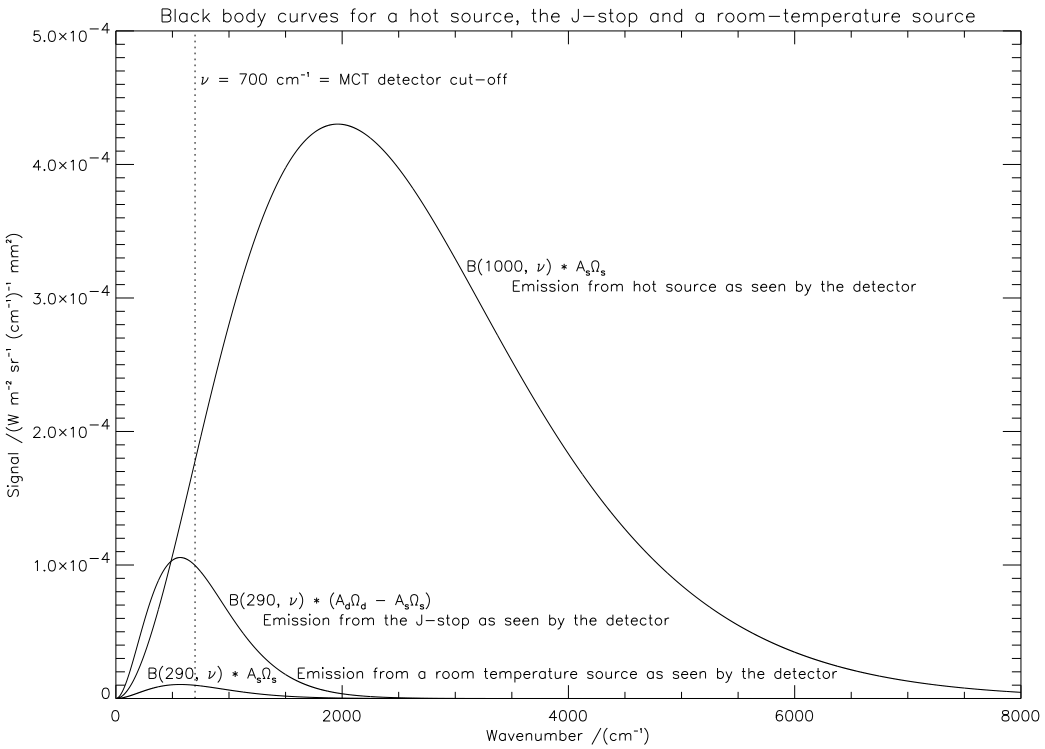

Figure 3.10: Estimate of size of self-emission. The plot shows the emission from a hot (1000 K) source as seen by the MCT detector ($B(1000, \tilde{\nu})A_s\Omega_s$), the emission from the same source when at room-temperature (290 K) ($B(290, \tilde{\nu})A_s\Omega_s$), and the emission from the J-stop iris as seen by the MCT detector ($B(290, \tilde{\nu})(A_d\Omega_d - A_s\Omega_s)$).

between the J-stop and MCT detector.

The spectrum taken with the internal source switched off, shown in figure 3.11, is the sum of the self-emission and the emission from the internal source at room temperature and the atmosphere within the spectrometer. From figure 3.10 it can be seen that the self-emission is 90% of the total. These figures show that self-emission is a significant effect which needs to be accounted for. Although the quoted figures are for the internal source, they apply equally, with minor adjustments, to the external source since the J-stop is still in the optical path.

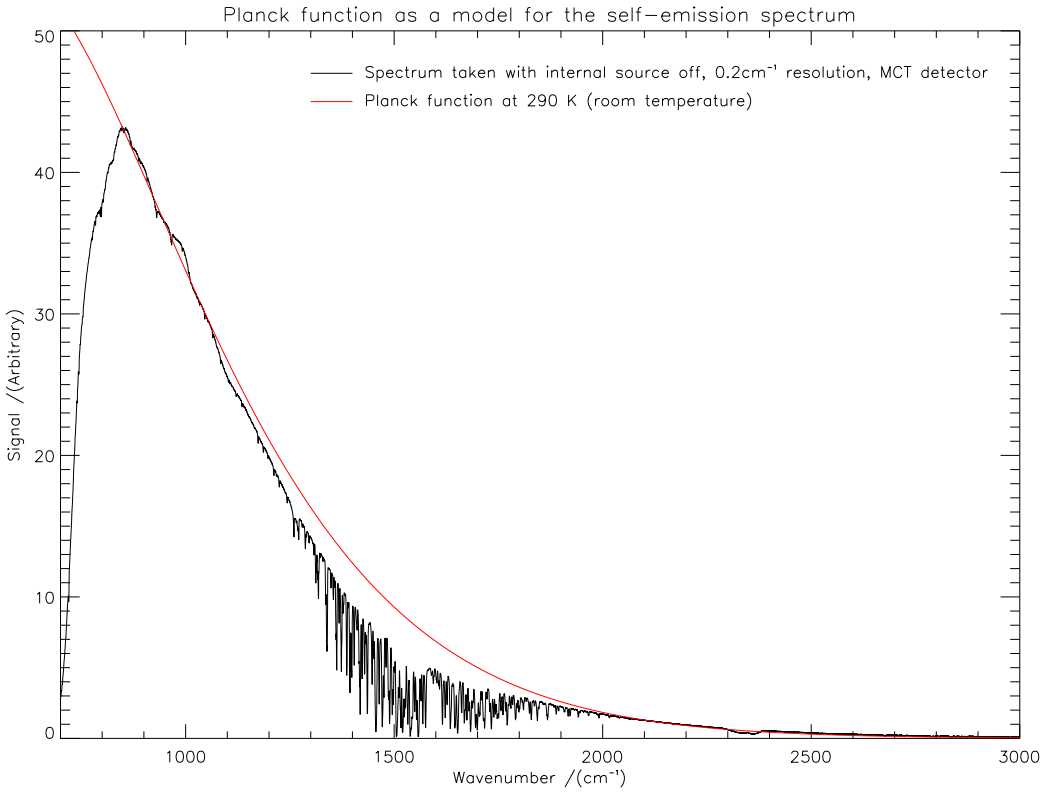

Figure 3.11: Comparing the room-temperature Planck function ($B(290, \tilde{\nu})$ with a spectrum recorded with the source switched off (i.e. at room temperature).

3.2.2 Solutions to Account for the Effects of Self-Emission

There are two possible solutions to account for the effects of self-emission. The first is to move the J-stop from the source port to the detector port.

Moving the J-stop

Moving the J-stop to the detector port should eliminate nearly all self-emission, since most of the radiation which reaches the detector from the J-stop iris will be DC and thus will be filtered out. There may still be a small amount of self-emission due to radiation from the J-stop being modulated by the interferometer in reflection, and due to self-emission from the rest of the spectrometer optics, which will be small due to their high reflection or transmission coefficients. However, the main source of self-emission will be removed. The results from implementing this adjustment to the J-stop are shown in figure 3.12. Note that

although the tests were carried out using the internal source, the conclusions apply equally well to the external source, since the J-stop is still the field stop for the external source.

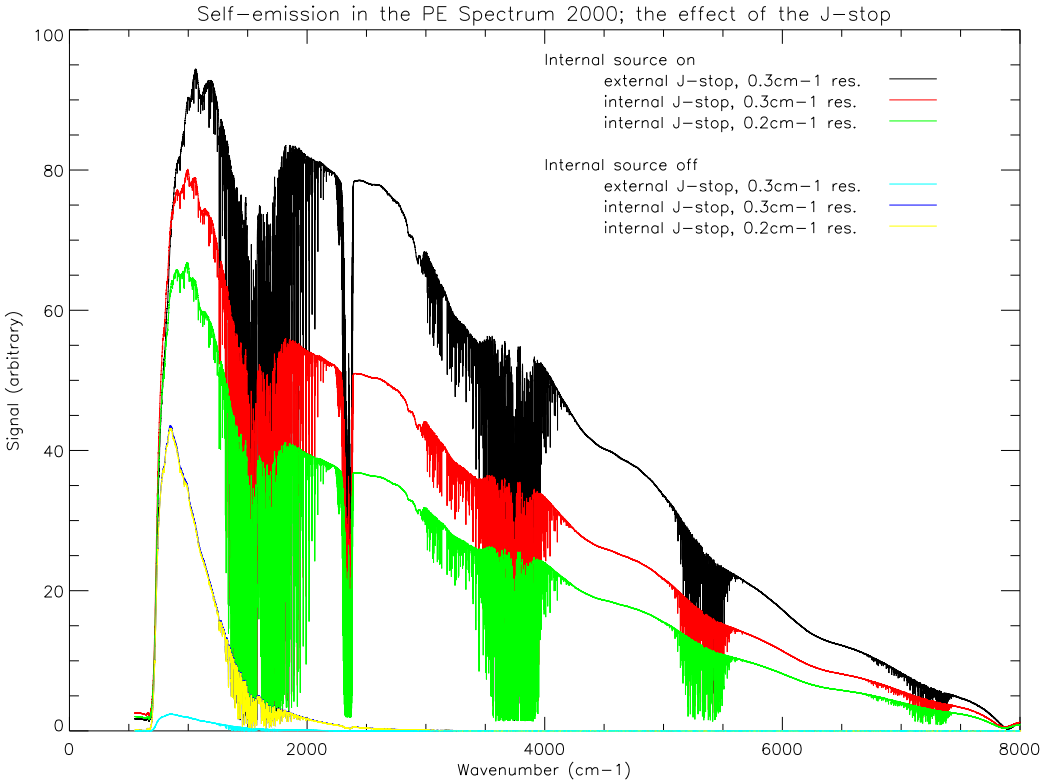

Figure 3.12: The effect of the position, and size, of the J-stop on self-emission. The green and yellow spectra were recorded at 0.2 cm^{-1} resolution, which is the standard resolution that the spectrometer is operated at. The highest available detector port (external) J-stop resolution is 0.3 cm^{-1}, and so spectra were recorded at this resolution with the source port (internal) J-stop for comparison (the red and dark blue (almost hidden by the yellow spectrum) spectra). The black and pale blue spectra were recorded using the detector port (external) J-stop at 0.3 cm^{-1} resolution. The magnitude of the spectra recorded with the source switched off is approximately 110% of the magnitude of the self-emission spectra. Note that the signal recorded with the detector port (external) J-stop and source switched off is 6% of the signal recorded with the source port (internal) J-stop and source switched off.

The spectrometer is normally operated at 0.2 cm^{-1} resolution. However, the highest resolution for which Perkin-Elmer supply a J-stop for use in the detector port is 0.3 cm^{-1}. Therefore spectra were recorded at each resolution. It can be seen, from figure 3.12, that the signal recorded with the detector port (external) J-stop and the source switched off is only

6% of that with the source port (internal) J-stop and the source switched off. Since emission from the switched off source accounts for 10% of the spectrum recorded with the J-stop in the source port, moving the J-stop to the detector port has eliminated self-emission.

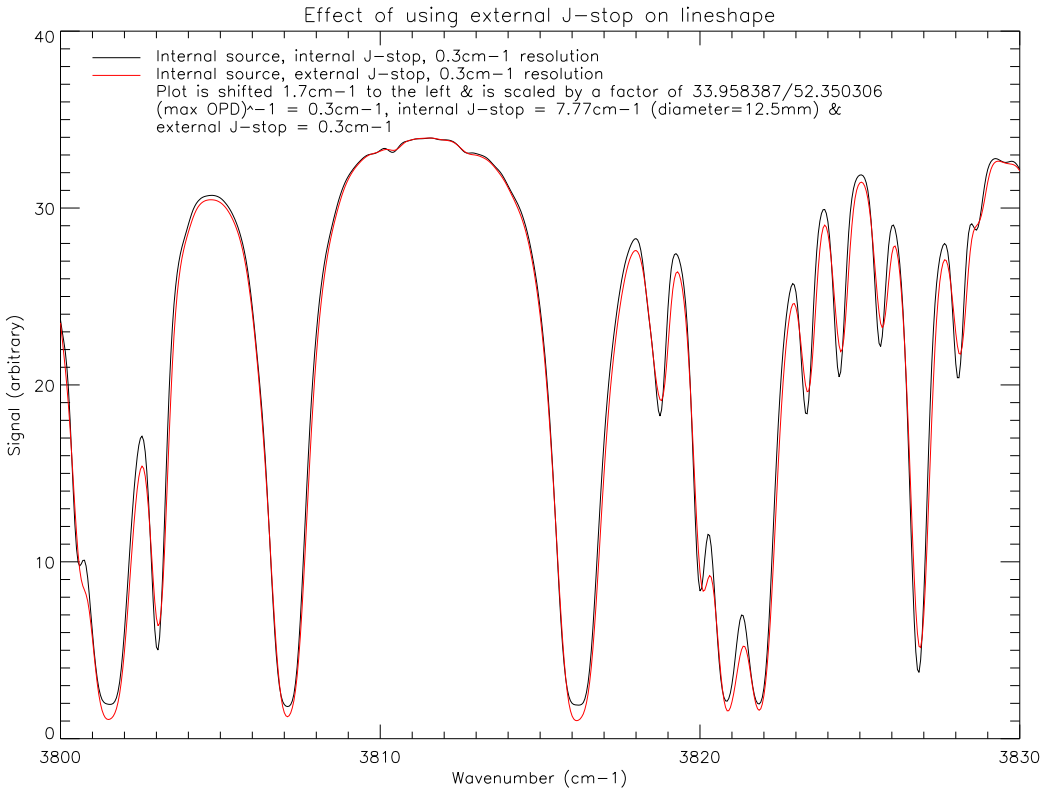

Figure 3.13: The effect of the position of the J-stop on lineshape. Both spectra were recorded at 0.3 cm^{-1} resolution with the MCT detector; one (black line) with the source port (internal) J-stop and one (red line) with the detector port (external) J-stop. The latter has been shifted 1.7 cm^{-1} to the left and scaled, so that it matches the former plot at 3811.5 cm^{-1}. Note that the two spectra are not identical.

As well as eliminating self-emission, moving the J-stop from the source port to the detector port also changes the instrument lineshape and shifts the positions of the line centres. The two spectra in figure 3.13 were recorded consecutively; the first using the source port (internal) J-stop and the second the detector port (external) J-stop. As can be seen from figure 3.13, the lineshape for the two spectra is different, and the shift of the positions of the line centres varies across the 30 cm^{-1} region.

The shift in positions of the line centres occurs because Perkin-Elmer use the size

of the source port J-stop aperture to correct the abscissa scale. When the detector port J-stop was in use, the source port J-stop aperture was set to its largest value in order to eliminate any self-emission. Thus the value used to correct the abscissa scale was larger than the true scale, resulting in a shift in positions of the line centres. The correction is proportional to the wavenumber, so the error in the line centre position increases linearly with wavenumber.

There are two potential causes for the change in lineshape. The first is that the positioning of the external J-stop in the infra-red beam is critical. Accurately positioning this J-stop is problematic due to the supplied J-stop holder only having coarse adjustment, and the need to work in the infra-red. The other cause of the change in lineshape is that the supplied external J-stop is oversized since it has not been machined accurately enough.

These problems led to the solution of moving the J-stop being abandoned in favour of an alternative solution; that of modelling the self-emission and including it in the retrieval.

Modelling self-emission

The self-emission is adequately modelled by $R(\tilde{\nu})B(T_J, \tilde{\nu})\tau_2(A_d\Omega_d - A_s\Omega_s)$, as has been shown in section 3.2.1. Where $\tau_2 = 1$, which is mainly outside the region 1200 cm^{-1} to 2000 cm^{-1} as can be seen from figure 3.11, self-emission can be accounted for in the retrieval by modifying the gain and offset terms, in a similar manner to the correction for detector non-linearity which is discussed in section 3.1. However, where $\tau_2 \neq 1$, a correction must be applied which accounts for the change in absorption and lineshape due to the self-emission, and also emission from the atmosphere.

Two factors determine the resolution of a spectrometer. One is the travel of the moving mirror. Various measures, such as the full-width at half-maximum (FWHM), the full-width at half-height (FWHH), the Raleigh criterion and simply the inverse of the maximum optical path difference, have been used to define the resolution. In this work, the value of the inverse of the maximum optical path difference is adopted for the resolution limitation due to the finite mirror travel. The other factor that determines the resolution

is concerned with the limiting solid angle in the system (Ω_l). The resolution limitation due to the limiting solid angle is then $\tilde{\nu}\Omega_l/(2\pi)$. The limiting solid angle, Ω_l, is either the solid angle of the detector, Ω_d, or the solid angle of the field stop (the J-stop in this system), Ω_s, depending on their relative sizes. For 0.2 cm^{-1} resolution, $\Omega_d > \Omega_s$, therefore the limiting solid angle for any emission originating before the J-stop is Ω_s. However, for emission from the J-stop itself and for emission from any atmosphere between the J-stop and the detector, the limiting solid angle is Ω_d. Now, the resolution limitation due to the finite mirror travel and that due to the limiting solid angle, when the solid angle is Ω_s, are the same in this case. However, if the limiting solid angle is Ω_d, then the resolution is determined by the limiting solid angle, and is lower than the nominal resolution (that of the inverse of the maximum optical path difference). Hence, self-emission and emission from the atmosphere between the J-stop and the detector is recorded at a lower resolution than that from the source and atmosphere between the source and J-stop. Therefore, self-emission distorts the line-shapes of the measured atmospheric lines.

Ballard, Remedios and Roscoe (Ballard, Remedios & Roscoe 1992) demonstrated that self-emission can be corrected for by recording spectra at two different temperatures of the source. The simplest way to implement this procedure is to record spectra with the source switched off, so that it is at room temperature, and with the source switched on. The latter is the required spectrum which needs correcting. Use equation (3.19) to model the 2 cases of the source on spectrum and the source off spectrum

$$\begin{aligned} S_{on} &= R(\tilde{\nu})\{B(T_{s_{on}},\tilde{\nu})\tau_1\tau_2\tau_3 A_s\Omega_s + B(T_1,\tilde{\nu})(1-\tau_1)\tau_2\tau_3 A_s\Omega_s + B(T_J,\tilde{\nu})\tau_2\tau_3(A_d\Omega_d - A_s\Omega_s) \\ &\quad + B(T_2,\tilde{\nu})(1-\tau_2)\tau_3 A_d\Omega_d - B(T_3,\tilde{\nu})(1-\tau_3)A_d\Omega_d\} \qquad (3.20) \\ S_{off} &= R(\tilde{\nu})\Big\{B(T_{s_{off}},\tilde{\nu})\tau_1'\tau_2'\tau_3' A_s\Omega_s + B(T_1,\tilde{\nu})(1-\tau_1')\tau_2'\tau_3' A_s\Omega_s + B(T_J,\tilde{\nu})\tau_2'\tau_3'(A_d\Omega_d - A_s\Omega_s) \\ &\quad + B(T_2,\tilde{\nu})(1-\tau_2')\tau_3' A_d\Omega_d - B(T_3,\tilde{\nu})(1-\tau_3')A_d\Omega_d\} \end{aligned}$$

where the τ' indicate that the atmosphere has potentially changed its state between the two measurements. However, if the two spectra are recorded close enough together in time for the atmosphere to remain essentially unchanged, then the transmission terms in the two

equations are the same, and it can be seen that subtracting the source off spectrum, S_{off}, from the source on spectrum, S_{on}, removes the terms for self-emission and atmospheric emission from the source on spectrum.

$$S_{on} - S_{off} = R(\tilde{\nu}) \left\{ B(T_{s_{on}}, \tilde{\nu}) - B(T_{s_{off}}, \tilde{\nu}) \right\} \tau_1 \tau_2 \tau_3 A_s \Omega_s \tag{3.21}$$

This is just the required transmission spectrum, τ_1, with a modified gain term, $R(\tilde{\nu})\{B(T_{s_{on}}, \tilde{\nu}) - B(T_{s_{off}}, \tilde{\nu})\}\tau_2\tau_3 A_s\Omega_s$ as opposed to $R(\tilde{\nu})B(T_{s_{on}}, \tilde{\nu})\tau_2\tau_3 A_s\Omega_s$. The retrieval method used in this study requires the retrieval of gain in order to accurately retrieve the gas volume mixing ratios. However, it is not necessary to separate this composite term out into its component parts. Hence, modifying the gain term does not affect the accuracy of the retrieval. Therefore subtracting a spectrum recorded with the source switched off, as long as it was taken sufficiently close in time to the measured spectrum being corrected, from the source on spectrum requiring correction, will adequately correct for the effects of self-emission and atmospheric emission.

If the atmosphere changes significantly between the time the source-off spectrum is measured and the source-on spectrum is measured, then subtracting the former from the latter, will not properly correct for the effects of self-emission and the lineshapes of measured lines will be slightly distorted. It is mainly the lines of CO_2 and H_2O which will be affected.

3.3 Channelling

Channelling, also known as interference fringes, is caused by interference between waves reflected off the parallel sides of a thin, transmitting optical component in the beam path of the spectrometer. This produces a sinusoidal wave that is superimposed on the required spectrum. The fringes add to the noise in the spectrum, distort large absorption features and can obscure small ones.

Such fringes were found in spectra taken with the Perkin-Elmer Spectrum 2000 spectrometer, see figure 3.3. There is a formula (Griffiths & de Haseth 1986) which relates the thickness, b, and refractive index, n, of the optical component causing the fringes to the

number of fringes, N, in a wavenumber range, $\tilde{\nu}_1 - \tilde{\nu}_2$:

$$b = \frac{1}{2n} \frac{N}{(\tilde{\nu}_1 - \tilde{\nu}_2)} \tag{3.22}$$

It was therefore possible to identify which optical component was causing the fringes. From figure 3.3, it was found that the peak of the first fringe is at 983.57 cm^{-1}, and the peak of the eleventh fringe is at 990.02 cm^{-1}. Therefore, $N = 10$, $\tilde{\nu}_1 - \tilde{\nu}_2 = 6.45$ cm^{-1} and $bn = 0.775$ cm. It was thought that the fringes were caused by the 5 mm thick KBr, potassium bromide, window between the interferometer and the sample compartment (there is a corresponding

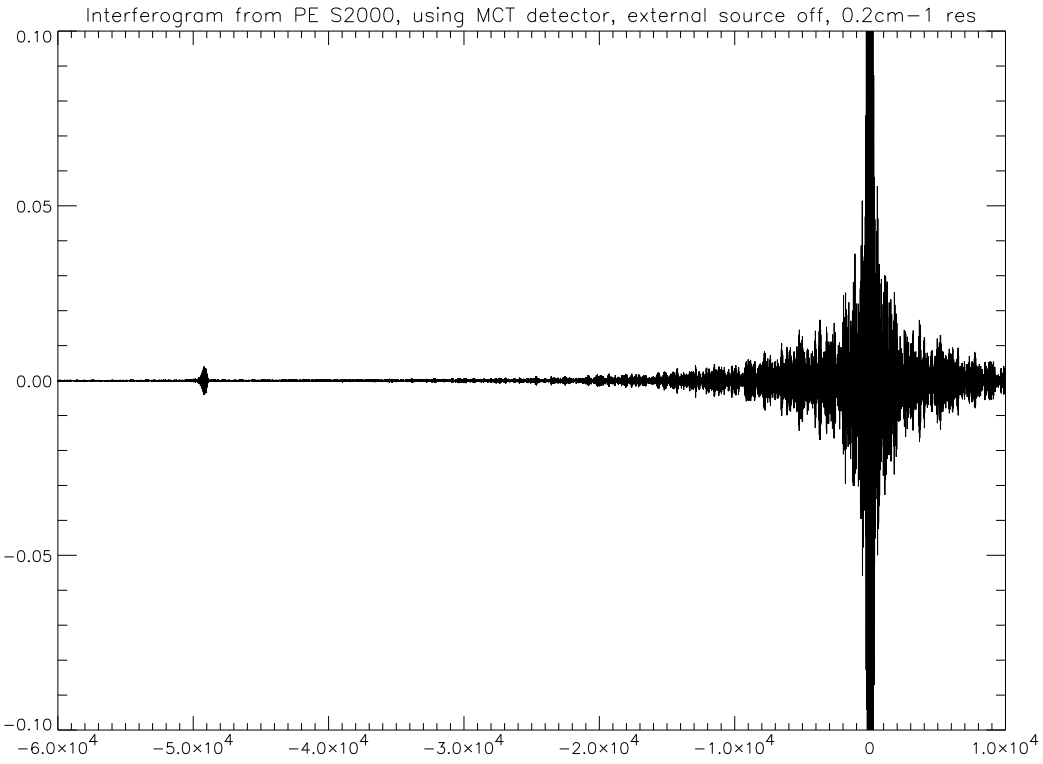

Figure 3.14: Interferogram recorded at 0.2 cm^{-1} resolution with the MCT detector and external source switched off. Channelling is caused by the wavepacket at -5x10^4. Note that this is well separated from the main part of the interferogram.

window where the beam from the external source enters the spectrometer). This window has parallel sides and is at an angle of 3° to the infrared beam. The refractive index of KBr is 1.5599 (Kaye & Laby 1973). Substituting for n in $bn = 0.775$ cm, we find that $n =$ 4.97 mm. This confirms that the KBr window is the cause of the interference fringes.

The KBr windows are required because the beamsplitter is hygroscopic and therefore needs to be kept in a desiccated environment. KBr is used because it has a transmission greater than 90% in the infrared region. Removal of the KBr windows was avoided because of the desiccation requirement. Instead, removal of the channelling from the interferogram was investigated.

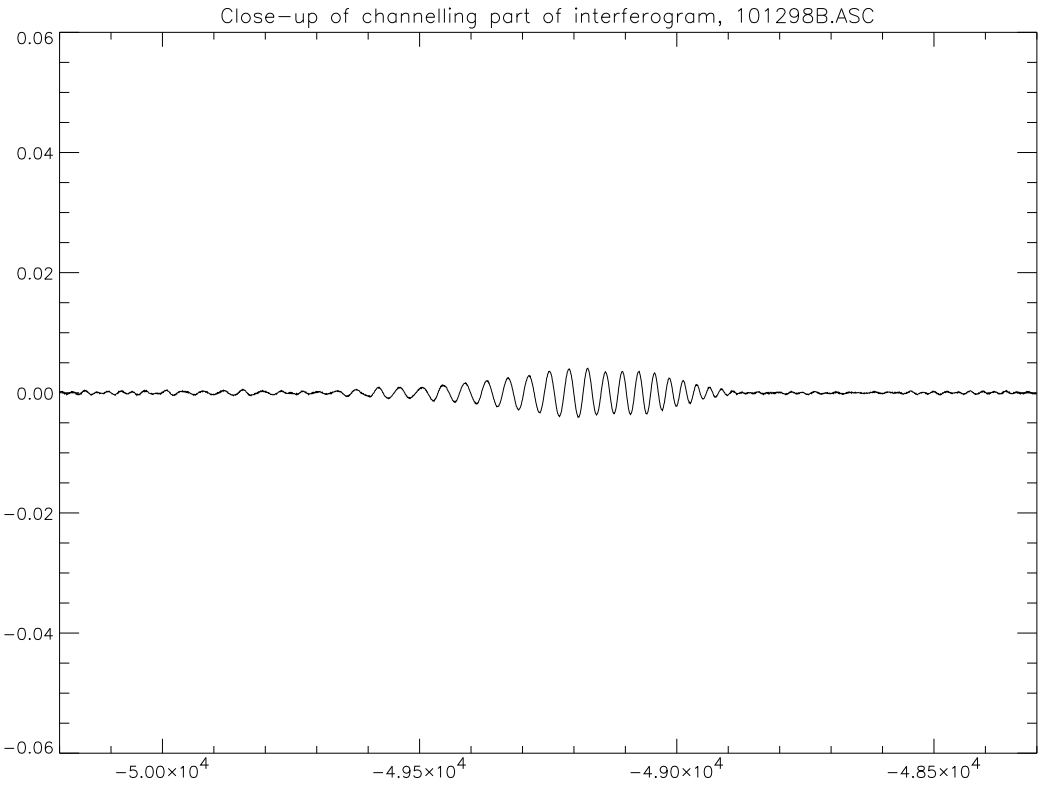

Figure 3.15: Close-up of the wavepacket in the interferogram, shown in figure 3.14, which causes channelling.

A pure sinusoidal wave in spectrum is Fourier transformed to a Dirac delta function in an ideal interferogram. Real interferograms are not ideal due to phase errors. Therefore the Dirac delta function becomes a short envelope of sine waves. If this is isolated from the rest of the interferogram, it can be replaced by a straight line interpolated from the points either side. The procedure was tested on an interferogram taken with the source switched off. As can be seen from figures 3.14 and 3.15, the wavepacket causing the channelling is isolated from the rest of the interferogram and is easily replaced by a straight line. The

effect of this is shown in figure 3.16.

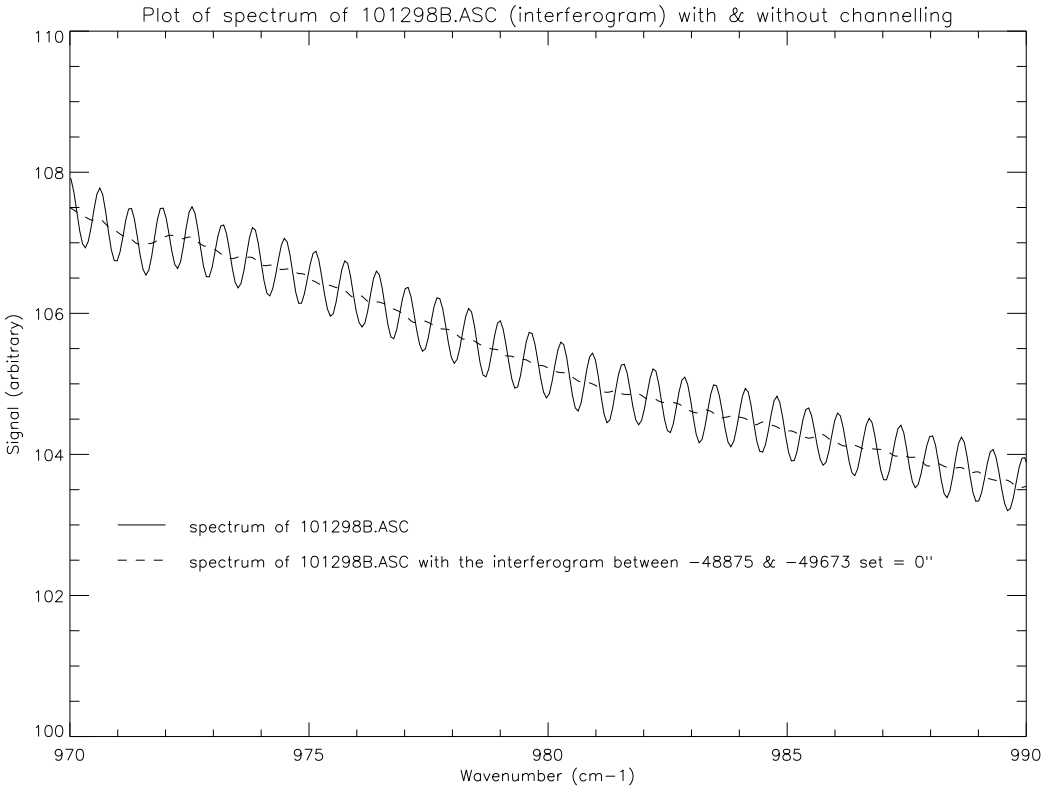

Figure 3.16: Spectrum of the interferogram shown in figure 3.14. The solid line is the spectrum of the unchanged interferogram and shows channelling. The dotted line is the spectrum of the interferogram when the wavepacket shown in figure 3.15 is replaced by a straight line at zero. Note that channelling has been removed from this spectrum, and the overall shape of the spectrum maintained.

Interferograms recorded with the source switched on, however, contain signal across the region where the channelling is located. Therefore the region containing the interference wavepacket cannot be replaced by a straight line. It was therefore necessary to physically remove the KBr windows for the duration of each measurement. This is easily accomplished in the case of the KBr window into the sample compartment. The KBr window for the external source, however, is more problematic to remove since it abuts the collimator, and so it has been left in place. However, its effects are noticeable, and therefore it will have to be removed and a method found for keeping the interferometer airtight when measurements are not being taken.

3.4 Summary

It has been shown that the non-linearity of the MCT detector results in a smoothly varying function being added to the spectrum. The effects of this are most visible as a non-zero signal in the region below the detector cut-off, and non-zero offsets beneath blacked out spectral lines. In addition, it has been demonstrated that this non-linearity is corrected for by the gain and offset terms used in the retrieval. Therefore, the non-linearity of the MCT detector does not affect the retrieved values of the gas volume mixing ratios.

It has been demonstrated that self-emission in the Spectrum 2000 spectrometer, which occurs with both the internal and external sources, predominately emanates from the J-stop. It has been shown that self-emission and atmospheric emission contribute up to 70% of the signal at the detector and that the spectrum deriving from this emission, all except the small part emanating from the atmosphere between the source and the J-stop, is at a lower resolution than the spectrum deriving from the source emission. Further, it has been shown that self-emission, and atmospheric emission, can be corrected for by subtracting a spectrum recorded with the source switched off from the measured spectrum, as long as the atmosphere has remained essentially unchanged in the period between the two measurements.

It has been shown that the main source of channelling in the spectrometer is the two KBr windows in the spectrometer. Removing these windows eliminates the channelling, but exposes the hygroscopic beamsplitter to the external, non-desiccated, environment. Therefore the time during which they are removed should be minimised.

Chapter 4

Retrievals

4.1 Introduction

Once measurements have been made, it is necessary to extract the required information from the spectra. In the case of this study, the information required is the volume mixing ratios (VMRs) of the gases of interest present in the atmospheric volume sampled by the spectrum.

The transmission of radiation along a homogeneous path of length l, where scattering and emission is negligible, is, from radiative transfer theory,

$$\tau(\tilde{\nu}) = \exp^{-k(\tilde{\nu})\rho l} \tag{4.1}$$

where ρ is the absorber number density and $k(\tilde{\nu})$ is the absorption coefficient. The absorption coefficient for a spectral line of a molecule at a wavenumber $\tilde{\nu}$ is

$$k(\tilde{\nu}, T, p) = S(T) f(\tilde{\nu}, \tilde{\nu}_0, T, p) \tag{4.2}$$

where S is the line strength (which is the integral of the absorption cross-section over the entire line), $f(\tilde{\nu} - \tilde{\nu}_0)$ is the line shape, T is the temperature and p is the pressure. Since ρ is related to the VMR of a gas (see equation 1.4) it is possible, provided that the spectroscopy of the gas is known, to determine the VMRs of the constituent gases present along an atmospheric optical path from a spectrum recorded along the path.

The problem of using indirect measurements, such as spectra, and any relevant prior information, to obtain the best estimate of the state of a system, such as the concentrations

of gases in a given volume of atmosphere, is known as the *retrieval problem* or the *inverse problem*. The theory of how to solve such problems is outlined in the next section. For a more extensive discussion of the retrieval problem see (Rodgers 2000).

4.2 Retrieval Theory

Consider a set of measurements (such as an infrared spectrum over a range of wavenumbers), $\mathbf{y}$, a set of errors (or noise) associated with the measurements, ϵ, and a set of parameters whose values are to be determined, the '*state vector*', (such as the concentrations of the gases of interest), $\mathbf{x}$. The retrieval problem is then to find $\mathbf{x}$ given $\mathbf{y}$. The measurements, $\mathbf{y}$, are related to the state vector, $\mathbf{x}$, by the *forward model*, F, where

$$\mathbf{y} = F(\mathbf{x}) + \epsilon \tag{4.3}$$

The forward model is the best approximation of the physics of the measurement and combines knowledge of how the measuring instrument (in this case an FTIR spectrometer) works together with the relationship of the measured quantity to the required quantity (in this case the relation between atmospheric transmission and gas concentration).

In order to determine the value of $\mathbf{x}$, it is useful to linearise equation 4.3 about a linearisation point, $\mathbf{x}_0$:

$$\mathbf{y} - F(\mathbf{x}_0) = \frac{\partial F(\mathbf{x})}{\partial \mathbf{x}}(\mathbf{x} - \mathbf{x}_0) + \epsilon = \mathbf{K}(\mathbf{x} - \mathbf{x}_0) + \epsilon \tag{4.4}$$

where $\frac{\partial F(\mathbf{x})}{\partial \mathbf{x}}$ is the sensitivity of the measurement to a change in the state vector. It is known as the Jacobian or the *weighting function* matrix, $\mathbf{K}$.

Redefining $\mathbf{y}$ as the measurement minus the forward model at the linearisation point, and $\mathbf{x}$ as the state vector minus the linearisation point, equation 4.4 can be written as

$$\mathbf{y} = \mathbf{K}\mathbf{x} + \epsilon \tag{4.5}$$

The problem is then to find $\mathbf{D}$, the contribution function, where

$$\mathbf{x} = \mathbf{D} \cdot \mathbf{y} \tag{4.6}$$

or

$$\mathbf{D} = \frac{d\mathbf{x}}{d\mathbf{y}}$$

Note that $\mathbf{D} \neq \mathbf{K}^{-1}$, indeed $\mathbf{K}^{-1}$ may not exist, since $\mathbf{K}$ is not constrained to be a square matrix.

There are several solutions to equation 4.5, two of which will be discussed here.

4.2.1 Least Squares Solution

The simplest solution, and one which is often used, is the least squares solution. This solution finds the value of $\mathbf{x}$ which minimises the difference between the measurement, $\mathbf{y}$, and the forward model, $F(\mathbf{x})$, subject to the errors on the measurement, as given by the error covariance matrix, $\mathbf{S_y}$. The cost function, J, is

$$\mathbf{J} = (\mathbf{y} - \mathbf{Kx})^T \mathbf{S_y}^{-1} (\mathbf{y} - \mathbf{Kx})$$

Minimising the cost function gives

$$\frac{d\mathbf{J}}{d\mathbf{x}} = 0 = \mathbf{K}^T \mathbf{S_y}^{-1} (\mathbf{y} - \mathbf{Kx})$$

which can be rewritten as

$$\mathbf{x} = (\mathbf{K}^T \mathbf{S_y}^{-1} \mathbf{K})^{-1} \mathbf{K}^T \mathbf{S_y}^{-1} \mathbf{y} \tag{4.7}$$

When this is compared to equation 4.6 it can be seen that $\mathbf{D} = (\mathbf{K}^T \mathbf{S_y}^{-1} \mathbf{K})^{-1} \mathbf{K}^T \mathbf{S_y}^{-1}$.

4.2.2 A Priori Solution

The retrieval problem, even in the absence of noise, is often formally ill-posed. This is the case when a continuous function, such as a temperature profile through the atmosphere or a spectrum, is approximated by a discrete function with too many degrees of freedom. It is necessary to add *a priori* constraints to the problem in order to solve it. Information gained from climatology or previous measurements is often used for these constraints, or 'virtual measurements'. The technique of optimal estimation (Rodgers 1976) finds the statistically most likely solution given the measurements and the constraints.

If Gaussian statistics are assumed, then the cost function, given a set of *a priori* constraints, $\mathbf{x}_a$, with error covariance matrix, $\mathbf{S}_a$, becomes

$$J = (\mathbf{y} - \mathbf{K}\mathbf{x})^T \mathbf{S_y}^{-1} (\mathbf{y} - \mathbf{K}\mathbf{x}) + (\mathbf{x}_a - \mathbf{x})^T \mathbf{S}_a^{-1} (\mathbf{x}_a - \mathbf{x}) \tag{4.8}$$

The solution for $\mathbf{x}$, when the cost function is minimised, is then

$$\begin{aligned} \mathbf{x} &= \mathbf{x}_a + \mathbf{S_a}\mathbf{K}^T(\mathbf{K}\mathbf{S_a}\mathbf{K}^T + \mathbf{S_y})^{-1}(\mathbf{y} - \mathbf{K}\mathbf{x}_a) & (4.9) \\ &= \mathbf{x}_a + (\mathbf{K}^T \mathbf{S_y}^{-1}\mathbf{K} + \mathbf{S_a}^{-1})^{-1}\mathbf{K}^T \mathbf{S_y}^{-1}(\mathbf{y} - \mathbf{K}\mathbf{x}_a) & (4.10) \end{aligned}$$

Comparing equation 4.10 with equation 4.7, and removing the a priori constraint, then

$$\mathbf{x} = (\mathbf{K}^T \mathbf{S_y}^{-1}\mathbf{K})^{-1}\mathbf{K}^T \mathbf{S_y}^{-1}\mathbf{y}$$

as before.

4.3 Retrieval Diagnostics

The technique of optimal estimation enables the calculation of the error covariance matrix of the retrieved state vector and a set of diagnostics about the quality of the retrieval. The error covariance matrix of the retrieved state vector is

$$\begin{aligned} \hat{\mathbf{S}}_\mathbf{x} &= \mathbf{D_y}\mathbf{S_y}\mathbf{D_y^T} + \mathbf{D_a}\mathbf{S_a}\mathbf{D_a^T} & (4.11) \\ &= \left(\mathbf{K^T}\mathbf{S_y^{-1}}\mathbf{K} + \mathbf{S_a^{-1}}\right)^{-1} & (4.12) \end{aligned}$$

where $\mathbf{S_y}$ = the error on the measurement

$\mathbf{S_a}$ = the error on the *a priori*

$\mathbf{K}$ = the weighting function matrix

$\mathbf{D_y}$ = the matrix of contribution functions from the measurement, $\partial\hat{\mathbf{x}}/\partial\mathbf{y}$

$\mathbf{D_a}$ = the *a priori* contribution function, $\partial\hat{\mathbf{x}}/\partial\mathbf{x_a}$.

and the systematic error due to forward model approximations and to parameter errors is assumed to be small and so has been omitted.

$\hat{\mathbf{S}}_\mathbf{x}$ is the sum of the random measurement error, $\mathbf{D_y}\mathbf{S_y}\mathbf{D_y^T}$, and the a priori error, $\mathbf{D_a}\mathbf{S_a}\mathbf{D_a^T}$, and quantifies the accuracy to which the retrieved values are known.

The diagnostics which have been included in the retrieval program (see section 4.4) are the measurement contribution function, $\mathbf{D_y}$, the *a priori* contribution function, $\mathbf{D_a}$, the averaging kernel, $\mathbf{A}$, and χ^2, which indicates how good the retrieval is.

$$\mathbf{D_y} \equiv \frac{\partial \hat{\mathbf{x}}}{\partial \mathbf{y}} = \left(\mathbf{S_a^{-1}} + \mathbf{K^T S_y^{-1} K}\right)^{-1} \mathbf{K^T S_y^{-1}} \tag{4.13}$$

$$\mathbf{D_a} \equiv \frac{\partial \hat{\mathbf{x}}}{\partial \mathbf{x_a}} = \left(\mathbf{S_a^{-1}} + \mathbf{K^T S_y^{-1} K}\right)^{-1} \mathbf{S_a^{-1}} = \mathbf{I} - \mathbf{A} \tag{4.14}$$

$$\mathbf{A} \equiv \frac{\partial \hat{\mathbf{x}}}{\partial \mathbf{x}} = \left(\mathbf{S_a^{-1}} + \mathbf{K^T S_y^{-1} K}\right)^{-1} \mathbf{K^T S_y^{-1} K} \tag{4.15}$$

$$\chi^2 = (\mathbf{y} - \mathbf{f})^{\mathbf{T}} \mathbf{S_y^{-1}} (\mathbf{y} - \mathbf{f}) + (\mathbf{x_a} - \hat{\mathbf{x}})^{\mathbf{T}} \mathbf{S_a^{-1}} (\mathbf{x_a} - \hat{\mathbf{x}}) \tag{4.16}$$

where $\mathbf{y}$ = the measurement

$\mathbf{f}$ = the forward model

$\mathbf{x_a}$ = the *a priori*

$\hat{\mathbf{x}}$ = the retrieved state vector

$\mathbf{x}$ = the true state vector.

The measurement contribution function, $\mathbf{D_y}$, indicates the sensitivity of the retrieval to errors in the measurement.

The *a priori* contribution function, $\mathbf{D_a}$, quantifies the contribution the *a priori* makes to the retrieved profile. The value of each element of $\mathbf{D_a}$ lies between zero and one and indicates the fraction of information that came from the *a priori*. For each element on the leading diagonal of $\mathbf{D_a}$ a value of zero indicates that all the information about the value of that particular element of the retrieved state vector came from the measurement, whereas a value of one indicates that all the information came from the *a priori*.

The averaging kernel, $\mathbf{A}$, indicates how well changes in the real profile, $\mathbf{x}$, can be detected in the retrieved profile, $\hat{\mathbf{x}}$.

χ^2 provides information about how good the retrieval is (Marks & Rodgers 1993). For a good retrieval, χ^2 should be approximately equal to the number of measurements (one measurement is the value at any particular wavenumber in the spectral region being

retrieved). If χ^2 is too large, then the retrieval does not fit the measurements. This could be for various reasons; the measurement errors have been underestimated, the *a priori* is too far from the true state, the *a priori* error has been underestimated, or the forward model is inadequate (for example, it does not model the instrument line shape well enough). If χ^2 is too small, then the retrieval fits the measurement too well. This could be due to one of two possibilities; the measurement errors have been overestimated, or the *a priori* error has been overestimated.

4.4 Implementation of Retrieval Theory

The retrieval scheme implemented in this study is that of optimal estimation. Although the retrieval problem of determining gas concentrations from a measured spectrum is not formally ill-posed, it can be ill-conditioned. In this case small errors in the measurement become magnified, leading to large uncertainties in the gas concentrations. This is particularly likely when the concentrations of several gases are retrieved simultaneously. An a priori constraint is then required to convert the retrieval problem to a well-conditioned problem. The a priori constraint used in this study is derived from previous measurements of atmospheric concentrations at ground level of the gases of interest. Such information has been taken from the measurements of urban air pollution in the UK made by the National Environmental Technology Centre (NETCEN) (Bower, Broughton & Willis 1995) and the 'US Standard Atmosphere'.

4.4.1 Joint Retrievals

The simultaneous retrieval of the concentrations of several gases is called a 'joint retrieval'. Joint retrievals are particularly useful when contaminant gases, such as H_2O and CO_2 which have spectral lines at intervals throughout the infrared spectral region, have spectral lines in the region of the spectrum that is used to retrieve a particular gas of interest. In these cases both the gas of interest and any contaminant gases are jointly retrieved in order to determine the concentration of the gas of interest. For the gases retrieved in this study:

CO is jointly retrieved with H_2O and N_2O, SO_2 is jointly retrieved with H_2O and CH_4, and NO_2 and NO are both jointly retrieved with H_2O.

4.4.2 Iterative Procedure

The retrieval scheme is implemented as an iterative procedure. The iterative forms of equation 4.10 are

$$\mathbf{x}_{n+1} = \mathbf{x}_a + \mathbf{S}_a\mathbf{K}_n^T(\mathbf{K}_n\mathbf{S}_a\mathbf{K}_n^T + \mathbf{S}_\mathbf{y})^{-1}\left(\mathbf{y} - \mathbf{F}(\mathbf{x}_n) - \mathbf{K}_n(\mathbf{x}_a - \mathbf{x}_n)\right) \quad (4.17)$$

$$\mathbf{x}_{n+1} = \mathbf{x}_n + (\mathbf{S}_a^{-1} + \mathbf{K}_n^T{\mathbf{S}_\mathbf{y}}^{-1}\mathbf{K}_n)^{-1}\left(\mathbf{K}_n^T{\mathbf{S}_\mathbf{y}}^{-1}(\mathbf{y} - \mathbf{F}(\mathbf{x}_n)) + \mathbf{S}_a^{-1}(\mathbf{x}_a - \mathbf{x}_n)\right) \quad (4.18)$$

where the subscripts n and $n+1$ denote the number of the iteration. Equations 4.17 and 4.18 are, respectively, equations 101 and 99 of (Rodgers 1976). The former is called the n-form and the latter the m-form, which refers to the size of the matrix which is inverted; m is the number of elements of the measurement, $\mathbf{y}$, and n the number of elements of the state vector, $\mathbf{x}$. Although algebraically equivalent, equation 4.18 is computationally faster where $\mathbf{y}$ has more elements than $\mathbf{x}$, which is the case for the retrievals carried out in this study, and hence the m-form of the iterative equation is used.

The iterative procedure which is used to determine the 'most likely' value of the state vector, $\mathbf{x}$, given the measured spectrum, $\mathbf{y}$, with associated error covariance matrix, $\mathbf{S}_\mathbf{y}$, and a priori, $\mathbf{x}_a$, with associated error covariance matrix, $\mathbf{S}_a$, is as follows

1. Make a first guess at the state vector, $\mathbf{x}$. The first guess can be (and for the retrievals carried out in this study is) the same as the a priori.

2. Use the forward model to calculate the spectrum, $\mathbf{F}(\mathbf{x})$ that would result from the values given in the state vector.

3. Calculate the weighting function, $\mathbf{K}$

4. Improve the guess using equation 4.18

5. Compare the new guess with the previous guess. If the difference is less than the error

on the state vector, then the current value of $\mathbf{x}$ is the required answer. Otherwise repeat steps 2 to 4.

4.4.3 Convergence Criterion

The actual criterion used to test for convergence of the retrieval is that each element of the state vector (except that for wavenumber offset, see section 4.8, for which the test is whether the offset is less than the spacing of the wavenumber grid used by the forward model) should have changed by less than 10% of the square root of the relevant element on the leading diagonal of the state vector error covariance matrix, $\hat{\mathbf{S}}_{\mathbf{x}}$, between iterations. That is

$$(\mathbf{x}_{n+1})_i - (\mathbf{x}_n)_i \leq 0.1\sqrt{(\hat{\mathbf{S}}_{\mathbf{x}})_{ii}} \qquad \forall i$$

If the retrieval has not converged after 15 iterations, then it is assumed that it will not converge and the retrieval is terminated. In practice this happens only occasionally. It can be the case that one of the elements of the state vector converges to a limit cycle, rather than a point, and cycles through 2 or 3 values which are sufficiently different that the retrieval does not meet the criterion for convergence stated above.

4.4.4 State Vector

The state vector, $\mathbf{x}$, used in this study consists of the following elements:

- the natural logarithm of the volume mixing ratio (VMR) of the gas of interest
- the natural logarithm of each VMR for all contaminant gases which have significant (i.e. above the noise level) absorption in the spectral region which is used to retrieve the VMR of the gas of interest
- the wavenumber offset of the spectrum (see section 4.8)
- the three quadratic coefficients of gain (see section 4.6)
- the offset in the y-axis of the spectrum (see section 4.6).

The natural logarithm of the VMR is retrieved instead of the VMR because the relationship between ln(VMR) and transmission is linear (see equation 4.1 and note that ρ is proportional to VMR). The VMR of the gas of interest is the required value. The other retrieved parameters are necessary in order to correctly characterise the synthetic spectrum created by the forward model, and thus enable the retrieval of the VMR of the gas of interest.

4.4.5 Measurement Vector

The measurement, $\mathbf{y}$, is a segment of an infrared spectrum. The segment used depends on the gas of interest being retrieved. The spectral regions used in this study are given in table 4.1.

Table 4.1: Spectral regions used for retrievals

Gas	Spectral region in cm^{-1}
CO	2120.0 - 2220.0
SO_2	1350.0 - 1390.0
NO_2	1560.0 - 1660.0
NO	1825.0 - 1925.0
benzene	670.0 - 680.0

4.4.6 Measurement Error

A single value for the measurement noise of the whole spectrum is calculated at the start of the retrieval. The measurement noise actually varies slightly with wavenumber. However, the value used is the best estimate of the noise. The noise is calculated in three regions across the spectrum, where there is no absorbance, and the mean is calculated in order to provide an estimate of the noise throughout the spectrum. The noise in each region is calculated as the standard deviation of the spectral points in the region when, the measured spectrum is divided by the spline approximating 100% transmittance in the spectrum (see section 4.6).

It is assumed that the noise on the spectrum is not correlated, and thus that the measurement error covariance matrix, $\mathbf{S_y}$, is a diagonal matrix with each element being equal to the square of the measurement noise. This assumption is not strictly valid since the interferogram, from which the spectrum is calculated, is zero filled and apodized, both of which introduce correlations. However, it is thought that these correlations are negligible.

4.4.7 A Priori

The a priori for the gas VMRs is derived from previous measurements of atmospheric concentrations at ground level of the gases of interest. For H_2O, N_2O, and CO_2 this information is taken from the 'US Standard Atmosphere'. For CO, SO_2, NO_2, and NO this information is taken from measurements of urban air pollution in the UK made by NETCEN. These a priori data could be, but have not been, updated in light of the measurements made in the course of this study. The a priori for the wavenumber offset is taken to be zero, since the offsets are generally of the order of $\pm$ 0.005 cm^{-1}. An estimate of the a prioris for the three quadratic coefficients of gain and the offset in the y-axis of the spectrum is calculated from the spectrum being retrieved from (see section 4.6). These are not strictly a prioris, since the information is not independent. However, only one or two spectral points, out of a total of 240 to 400 covering the entire spectrum, from the spectral region of the retrieval are used to calculate the a prioris; thus the a prioris are approximately independent of the measurements.

4.4.8 A Priori Error

The error on the a priori for the gas VMRs is taken to be 100%. The error on the a priori for the wavenumber offset is taken to be the spacing of the wavenumber grid used by the forward model, which is 0.005 cm^{-1}. Estimates of the errors on the a prioris for the three quadratic coefficients of gain and the offset in the y-axis of the spectrum are calculated at the same time that the a prioris themselves are calculated (see section 4.6). It is assumed that the a priori errors are not correlated, and thus that the a priori error covariance matrix,

$\mathbf{S}_a$, is diagonal.

4.4.9 Weighting Functions

The weighting functions for the gas VMRs are calculated as

$$\mathbf{K} = \frac{\mathbf{F}(\mathrm{e}^{1.1\mathbf{x}}) - \mathbf{F}(\mathrm{e}^{\mathbf{x}})}{\ln(1.1)} \tag{4.19}$$

which is an approximation to $\frac{\partial \mathbf{F}(\mathbf{x})}{\partial \mathbf{x}}$, given that the state vector element is the natural logarithm of the VMR.

The weighting function for the wavenumber offset is calculated as follows. $\mathbf{F}(\mathbf{x} + \delta\mathbf{x})$ is calculated by shifting the RFM spectrum (see section 4.5) along one interval of the spacing of the wavenumber grid used by the RFM, removing the last spectral point and duplicating the first, and then multiplying by the gain calculated for this shifted spectral interval. $\mathbf{F}(\mathbf{x})$ is the original RFM spectrum multiplied by the gain calculated over the original spectral interval. The weighting function is then approximated by

$$\mathbf{K} \approx \frac{\mathbf{F}(\mathbf{x} + \delta\mathbf{x}) - \mathbf{F}(\mathbf{x})}{\delta\mathbf{x}} \tag{4.20}$$

where $\delta\mathbf{x}$ in this case is the spacing of the wavenumber grid used by the RFM. Note that this grid spacing is ten times finer than that used in the measured spectrum (see section 4.5). Note also that the RFM spectrum encompasses a wider spectral region than that of the measured spectrum. It is wider at each end of the spectral region by half the extent of the instrument lineshape function in spectral space (see section 4.5).

The weighting functions for the gain and offset (see section 4.6) can be calculated exactly. They are

$$\begin{aligned}
\frac{\partial \mathbf{F}(\mathbf{x})}{\partial \mathbf{x}_{g_0}} &= \tau \\
\frac{\partial \mathbf{F}(\mathbf{x})}{\partial \mathbf{x}_{g_1}} &= \tau\tilde{\nu} \\
\frac{\partial \mathbf{F}(\mathbf{x})}{\partial \mathbf{x}_{g_2}} &= \tau\tilde{\nu}^2 \\
\frac{\partial \mathbf{F}(\mathbf{x})}{\partial \mathbf{x}_{o}} &= 1
\end{aligned} \tag{4.21}$$

where τ is the RFM spectrum (a transmission spectrum) after convolution with the instrument line shape and 'interpolation' (every 10th spectral point is selected) onto the same spectral grid as the measured spectrum, g_0 is the constant coefficient of the gain, g_1 is the linear coefficient of the gain, g_2 is the quadratic coefficient of the gain and o is the offset in the y-axis. See also equation 4.23 and section 4.6.

4.5 The Forward Model

The forward model as implemented in this study consists of three parts. The first is a detailed representation of the radiative transfer processes in the atmosphere, which is described in this section. The second is a model of how the FTIR spectrometer used in this study works, as encapsulated in the instrument line shape. This is described in section 4.7. The final part is a model of the effect on the spectrum of the source emission characteristics and the response of the FTIR spectrometer to infrared radiation. This is described in section 4.6.

The model of the radiative transfer processes in the atmosphere used in this study is the MIPAS[1] Reference Forward Model (RFM) (Dudhia 1997). The RFM is based on the General Line-by-Line Atmospheric Transmittance and Radiance Model, 'GENLN2' (Edwards 1992). GENLN2 was originally developed in 1977 at Atmospheric, Oceanic and Planetary Physics, Department of Physics, University of Oxford, but is now managed by D Edwards at the National Center for Atmospheric Research (NCAR) in Boulder, Colorado.

The RFM was designed to calculate atmospheric limb spectra, where several layers of the atmosphere may be viewed at once. A spectrum along a single homogeneous path at ground level, as required for this study, is a special case of an atmospheric limb spectrum.

The inputs to the RFM are

- the current guess at the VMRs of all the gases in the state vector
- the spectral range and spacing of the wavenumber grid to be used

[1] Michelson Interferometer for Passive Atmospheric Sounding - an instrument on the European Space Agency's environmental satellite Envisat-1, which is due to be launched in late 2001

- HITRAN (Rothman et al. 1992) spectroscopic data (for benzene and 1,3-butadiene retrievals the absorption cross-sections measured as part of this study (see chapter 5) converted to the appropriate format were used)
- CTM option - includes pretabulated continuum absorption for H_2O and CO_2 if they are selected as one of the absorbing species (see (Dudhia 1997))
- MIX option - includes line-mixing for any CO_2 lines for which pretabulated data exists (see (Dudhia 1997)) if CO_2 is included as an absorbing species
- SHP option - enables used of a lineshape with sub-Lorentzian wings for CO_2, when line-mixing is invoked (all other gases are modelled with a Voigt lineshape).

The spectral range used is determined by the main gas to be retrieved (see table 4.1). The spectral range used in the RFM is wider than that used in the measurement vector, $\mathbf{y}$, by the extent of the instrument lineshape function in spectral space (10.0 cm^{-1}). The spectral range is extended equally (5.0 cm^{-1}) at each end. This is carried out so as to remove the edge effects of convolving the transmission spectrum created by the RFM with the instrument line shape from the spectral region over which the retrieval will be carried out. The spacing of the wavenumber grid (0.005 cm^{-1}) is ten times finer than that of the measured spectrum. A finer wavenumber grid is used in order to reduce errors in the convolution of the transmission spectrum created by the RFM with the instrument line shape (which has the same grid spacing) and in order to improve the retrieval of the wavenumber offset of the spectrum.

The continuum absorption, for H_2O or CO_2, accounts for the extra absorption seen in the atmosphere, which cannot be accounted for by any of the standard line shapes (which are based on theory). An empirical formula, based on observation, is used to model this 'anomalous' absorption.

Line-mixing occurs due to collisions between molecules, one of which is undergoing a transition, and thus radiating energy, at the time of the collision. This changes the

population distribution between rotational-vibrational states, and thus redistributes the spectral intensity within a band. In the atmosphere this is visible in the Q-branch (the main spectral branch) and also in the P- and R-branches. It is only important for CO_2. Line-mixing also results in a changed line shape for individual lines. Therefore a lineshape which has sub-Lorentzian wings is used for the spectral lines affected by line-mixing. The RFM uses the Voigt lineshape for all other spectral lines. This is the convolution of the Doppler lineshape (which is important at high altitudes, i.e. low pressures) and the Lorentz lineshape (which is important at low altitudes, i.e. high pressures).

The RFM outputs a transmission spectrum for the gases and spectral region selected. This transmission spectrum is then convolved with the instrument line shape (see section 4.7), 'interpolated'[2] onto the same spectral grid as used by the measured spectrum, multiplied by the gain (see section 4.6) and has the y-axis offset added to it in order to form the forward model spectrum used in the retrieval ($\mathbf{F}(\mathbf{x})$).

4.6 Modelling Gain and Offset

The spectra measured in this study are single beam spectra. They can be converted to transmission spectra by dividing by an appropriate background spectrum. The background spectrum should be recorded under identical conditions to the single beam spectrum, the only difference should be the absence of the sample of which the spectrum is required. In the case of this study, the sample is the volume of air in the optical path between the source and detector. It is obviously impracticable to evacuate the air from the optical path, and therefore a true background spectrum cannot be recorded. An alternative solution must be found.

The usual solution, as described in section 1.8, is to either measure an approximate background spectrum (such as recording one upwind of the measurements, or if levels of a

[2]Since the spacing of the wavenumber grid used by the RFM is exactly ten times finer than that used in the measured spectrum, the RFM spectrum is not interpolated onto the wavenumber grid used by the measured spectrum, rather every 10^{th} spectral point in the RFM spectrum (after it has been convolved with the instrument line shape) is extracted to form the forward model spectrum that is used in the retrieval.

transient gas are measured continuously, then using a spectrum with no absorption by the gas in it) or in some cases to use a synthetic background. The solution used in this study is not to use a background spectrum, but to retrieve for the effects that would be removed by using one to convert the single beam spectrum to a transmission spectrum.

The effects retrieved for include the variation with wavenumber of the radiance emitted by the source (which can be approximated by a Planck function), the variation with wavenumber of the detector response, the variation with wavenumber of the transmittance of the beamsplitter and compensator, and the variation with wavenumber of the reflectance of all the mirrors in the optical path. It also, incidentally, accounts for the effect of a non-linear detector (see section 3.1) and any continuum transmission, such as from aerosol particles (H_2O droplets, soot particles etc.), not accounted for in the RFM. All these effects can, in general, be modelled in the 100 cm^{-1} -wide spectral regions over which retrievals are carried out, by multiplying the RFM calculated transmission spectrum by a quadratic curve (the 'gain') and adding a constant offset (the 'offset'). The equation for gain is therefore

$$\text{Gain} = (g_0 + g_1\tilde{\nu} + g_2\tilde{\nu}^2) \tag{4.22}$$

where g_0 is the constant coefficient of the gain, g_1 is the linear coefficient of the gain, g_2 is the quadratic coefficient of the gain and $\tilde{\nu}$ is the wavenumber scale of the forward model spectrum. The relationship between gain and offset and the forward model is given by

$$\mathbf{F}(\mathbf{x}) = (g_0 + g_1\tilde{\nu} + g_2\tilde{\nu}^2)\tau + o \tag{4.23}$$

where τ is the RFM transmission spectrum after convolution with the instrument line shape and interpolation onto the same spectral grid as the measured spectrum and o is a constant offset in the y-axis.

The effect of the gain is to convert the units of the y-axis of the spectrum from transmittance, which has a maximum value of 1, to signal in counts, which has an arbitrary maximum value dependent upon the detector, the source, the J-stop diameter, the distance of the source from the detector and other instrument dependent factors. Thus the signal levels in two measured spectra are not directly comparable, unless they were recorded under

identical instrument conditions. The effect of the offset is to correct for any errors (e.g. those produced by a non-linear detector) in the zero signal level.

All three coefficients of the gain, together with the offset coefficient, are included in the state vector and therefore retrieved along with the other elements of the state vector. The weighting functions for both gain and offset are given in section 4.4.9.

The a prioris, and the errors on the a prioris, for the gain coefficients are estimated as follows. A spline is fitted to a set of points on the measured spectrum, $\mathbf{y}$, which were chosen to be representative of the 100% transmittance curve of the spectrum. The entire set of 57 points lies between 500 cm^{-1} and 8000 cm^{-1}. A subset of these points is used when the measured spectrum does not extend over the full spectral window from 500 cm^{-1} to 8000 cm^{-1}. Each spline point is calculated as the mid-point of each of 57 ranges (of 1 cm^{-1} to 2 cm^{-1}) for the x-value and the mean y-value of the points in each range for the y-value. A second order polynomial is fitted to the spectral region over which the retrieval will be carried out. This determines the a prioris of the three gain coefficients. The error on the a priori for each of the three gain coefficients is the square root of the appropriate element on the leading diagonal of the covariance matrix of the gain coefficients. In order to calculate the gain covariance matrix, the weighting functions, $\mathbf{k}$, of each of the three gain coefficients with respect to the points used to compute the spline is calculated. The gain covariance matrix is then $\mathbf{k}\mathbf{S}_{point}\mathbf{k}^T$ where $\mathbf{S}_{point}$ is the covariance matrix of the points used to compute the spline. It is a diagonal matrix and the elements on its leading diagonal are the variances of the y-values of the points used to compute the spline.

The offset a priori and its associated error is calculated in a similar manner to that for the gain coefficients. A spline is fitted to a set of points on the measured spectrum, $\mathbf{y}$, which were chosen to be representative of the zero transmittance curve of the spectrum. The set of 13 points lies between 600 cm^{-1} and 7900 cm^{-1}, and a subset of these points is used when the measured spectrum falls within this range. The y-value of each spline point is calculated as the minimum y-value of the points in each of 13 ranges (of 100 cm^{-1}), and the x-value of the spline point is the corresponding value for the chosen point. The value

of the offset a priori is then the mean value of the spline in the spectral region over which the retrieval will be carried out, and the a priori error is the standard deviation.

4.7 Instrument Lineshape

In section 2.1.3 the instrument lineshape (ILS) was discussed mathematically, and the equation that defines it, equation 2.19, was derived. How the instrument effects encapsulated in the ILS are included in the forward model of the retrieval is discussed in this section.

4.7.1 Modelling the ILS

The RFM has an option to convolve the spectrum it calculates with a user-defined ILS in spectral space. However, the maximum allowed extent of such an ILS function is 2.0 cm^{-1} ($\pm$ 1.0 cm^{-1}). This limitation arises from the fact that the RFM was designed for a high resolution (0.025 cm^{-1}) spectrometer. It was found that only using the central 2.0 cm^{-1} portion of the ILS for an instrument operated at 0.2 cm^{-1} resolution produced unacceptable errors in the forward model. Therefore the extent of the ILS function in spectral space was increased to 10.0 cm^{-1} ($\pm$ 5.0 cm^{-1}) and the convolution in spectral space of the ILS with the RFM transmission spectrum is carried out in the retrieval program and not in the RFM.

The ILS function is modelled by a dedicated computer program[3] and saved to file, from where it can be read in for each retrieval for which it is required. The program implements equation 2.19. The inputs required by the computer program are the maximum retardation, the limiting solid angle and the apodising function required by the user. It calculates the ILS in interferogram space and then Fourier transforms it to spectral space for output to file.

A 10.0 cm^{-1} wide centralized segment of the ILS function includes enough of the sidelobes of an ILS at 0.2 cm^{-1} resolution with a Norton-Beer strong apodising function that errors due to truncating the extent of the ILS function in spectral space are negligible. However, the modelled ILS does not adequately represent the actual ILS function of the

[3] Written by Frank Murcray (University of Denver) and extracted from the GENLN2 line-by-line software.

spectrometer. The effect of this can be seen in the residuals in figure 4.1. Note that the spikes, which are asymmetric, all correspond to the positions of gas lines.

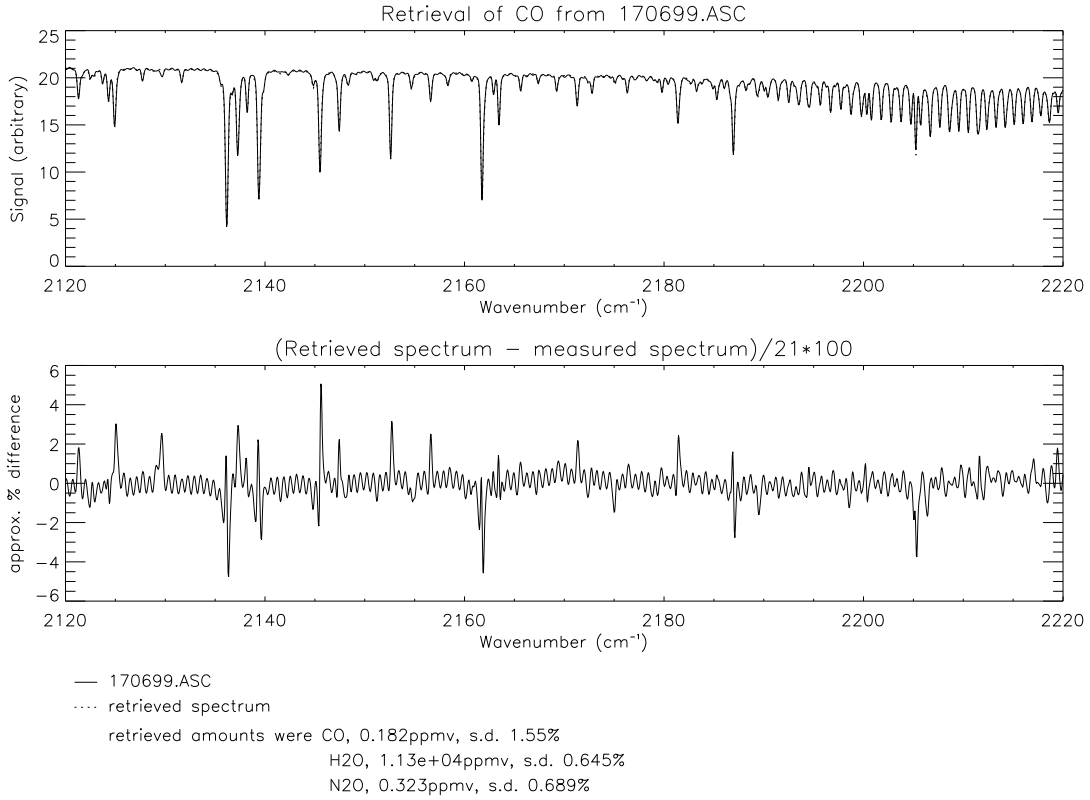

Figure 4.1: A retrieval of CO which shows large residuals due to the ILS used not adequately representing the real ILS. The solid line in the upper plot is the measured spectrum, 170699.ASC. The dotted line in the upper spectrum (visible in places) is the retrieved spectrum created by the RFM using the values given in the plot. The stated retrieved errors are the appropriate elements of $\sqrt{\mathbf{S_x}}$, where $\mathbf{S_x}$ is the covariance error matrix of the retrieved profile. The lower curve is the residuals of the retrieval (retrieved spectrum - measured spectrum) expressed as a percentage of the measured spectrum.

The discrepancies between the modelled and actual ILS functions are thought to be due to two causes. The first is the effect of beam divergence[4] through the spectrometer which is discussed in 2.1.3. The expression given for the effect of beam divergence in equation 2.17 is only correct for monochromatic light. The full expression for polychromatic

[4]The effect of beam divergence is that the position and shape of absorption lines are modified by the off-axis rays which are able to pass through the spectrometer. The ideal monochromatic case is accounted for by the use of the limiting solid angle in the computer program used to model the ILS.

light (Bell 1972) (Chamberlain 1979) is more complicated and must be applied to the RFM spectra in interferogram space. The second possible cause is instrumental effects, such as optical mis-alignments and aberrations, which are not included in the model of the ILS. These will also produce differences between the actual and modelled ILS functions.

In light of these discrepancies, it was decided to measure the instrument lineshape.

4.7.2 Measuring the ILS

The instrument lineshape of an FTIR spectrometer can be determined from a measurement of a narrow spectral line with a full width at half maximum significantly less than the resolution of the spectrometer. The standard method of doing so is to measure the spectrum of a low pressure gas in a gas cell placed in the optical path of the spectrometer. This was the method used in this study. Researchers at NPL have developed a technique, and the equipment required, to use an expanded infrared laser beam to determine the ILS of an FTIR spectrometer (Davies et al. 1998). However, such equipment was not available for this study.

The choice of gas to use in the low pressure cell was determined by three criteria. The gas should have a simple spectrum consisting of narrow, isolated lines. It should absorb in an atmospheric window, away from the majority of CO_2 and H_2O lines, and its abundance in the atmosphere should be low. These criteria resulted in the choice of three gases: CO, N_2O, and HCl. In order to ensure that the gas' spectral linewidths were determined by Doppler broadening and not a combination of Doppler and Lorentz broadening, the pressure of the gas in the gas cell was chosen to be a hundredth of the pressure at which the Doppler and Lorentz linewidths for that gas are equal. This led to a pressure of 0.3 mb of CO, 0.15 mb of N_2O, and 0.35 mb of HCl being used. The Doppler line widths at 293 K of the three gases are 0.0060 cm^{-1} for CO, 0.0028 cm^{-1} for N_2O in the 1200 cm^{-1} to 1350 cm^{-1} region and 0.0049 cm^{-1} for N_2O in the 2150 cm^{-1} to 2265 cm^{-1} region, and 0.0071 cm^{-1} for HCl. CO has lines in the region 2100 cm^{-1} to 2220 cm^{-1} and HCl has lines in the region 2700 cm^{-1} to 3050 cm^{-1}.

The gas cell used for the low pressure measurements is shown in figure 4.2 and came from the Rutherford Appleton Laboratory (RAL). It is a 50.6 mm long pyrex glass cylinder with two wedged[5] silicon windows. The windows are wedged in order to eliminate channelling. The gas cell is sealed with two valves (see figure 4.2) in order to minimise any leakage of air into the cell.

Figure 4.2: The 50.6 mm pathlength low pressure gas cell used to measure the ILS of the Perkin-Elmer Spectrum 2000 FTIR spectrometer.

The gas cell was evacuated and filled at the Molecular Spectroscopy Facility (MSF) at RAL on a clean glass and PTFE vacuum line using a 10 torr full scale Baratron capacitance gauge. The gauge was zeroed under hard vacuum before any measurements were made and the zero reading checked at the end of the series of measurements. The procedure used for validating the pressure readings of the gauge was as described in section 5.2. The pressure readings were again found to be accurate to $\pm$ 2.5 Pa.

The cell was evacuated before being filled with each gas in turn. After each evacuation the evacuated cell was mounted inside the sample compartment of the Bruker IFS120 HR

[5]The windows are wedged in such a way as to ensure that the interior length of the cell, between the inner surfaces of the two windows, is constant for all points round the circumference of either window.

FTIR spectrometer at RAL and a spectrum at 0.05 cm^{-1} resolution was recorded in order to check for outgassing or leaks. In each case the vacuum was satisfactory.

A sample (102.4 kPa) of N_2O was transferred from a lecture bottle to a clean, evacuated glass sample tube attached to the vacuum line (the line was flushed with pure nitrogen gas and then evacuated before the transfer). Three freeze-pump-thaw sequences were employed to remove any residual atmosphere present. 0.149 mb of N_2O was then transferred to the sample cell, which was attached to the vacuum line, using a mixing bulb (capacity 1.0 l) as a buffer. The same procedure was used to fill the sample cell with 0.353 mb of HCl. A sample of 0.307 mb of CO was transferred directly from a lecture bottle to the sample cell, via the vacuum line (which was flushed with pure nitrogen gas and then evacuated before the transfer) using the evacuated mixing bulb as a buffer. The sample of N_2O (C.K. Gas Products Ltd.) had a stated purity of 99.3%, that of CO (Cambrian Gases) had a stated purity of 99.5%, and that of HCl (ARGO International Ltd.) had a stated purity of 99.0%.

After filling, the cell was mounted inside the sample compartment of the Bruker IFS120 HR FTIR spectrometer at RAL and a spectrum at 0.05 cm^{-1} resolution was recorded in order to provide a reference spectrum. Another spectrum, under identical conditions, was recorded after the cell was used to measure the ILS of the Perkin-Elmer Spectrum 2000 FTIR spectrometer. This was compared to the reference spectrum in order to determine whether any leakage of air into the cell, or low pressure gas out of the cell had taken place. Leakage did not occur for any of the three gases.

In order to measure the ILS of the Perkin-Elmer Spectrum 2000 FTIR spectrometer the sample cell was placed in the sample compartment of the spectrometer (see figure 2.1). It was positioned so that the J-stop image lay in the middle of the sample cell. The external source was used and was positioned directly in front of the collimator, which was horizontal (see figure 4.3). The alignment of the source and collimator was adjusted so as to maximise the signal reaching the MCT detector. During the measurements of the ILS, the two KBr windows in the spectrometer were removed. For each gas used in the low pressure gas cell

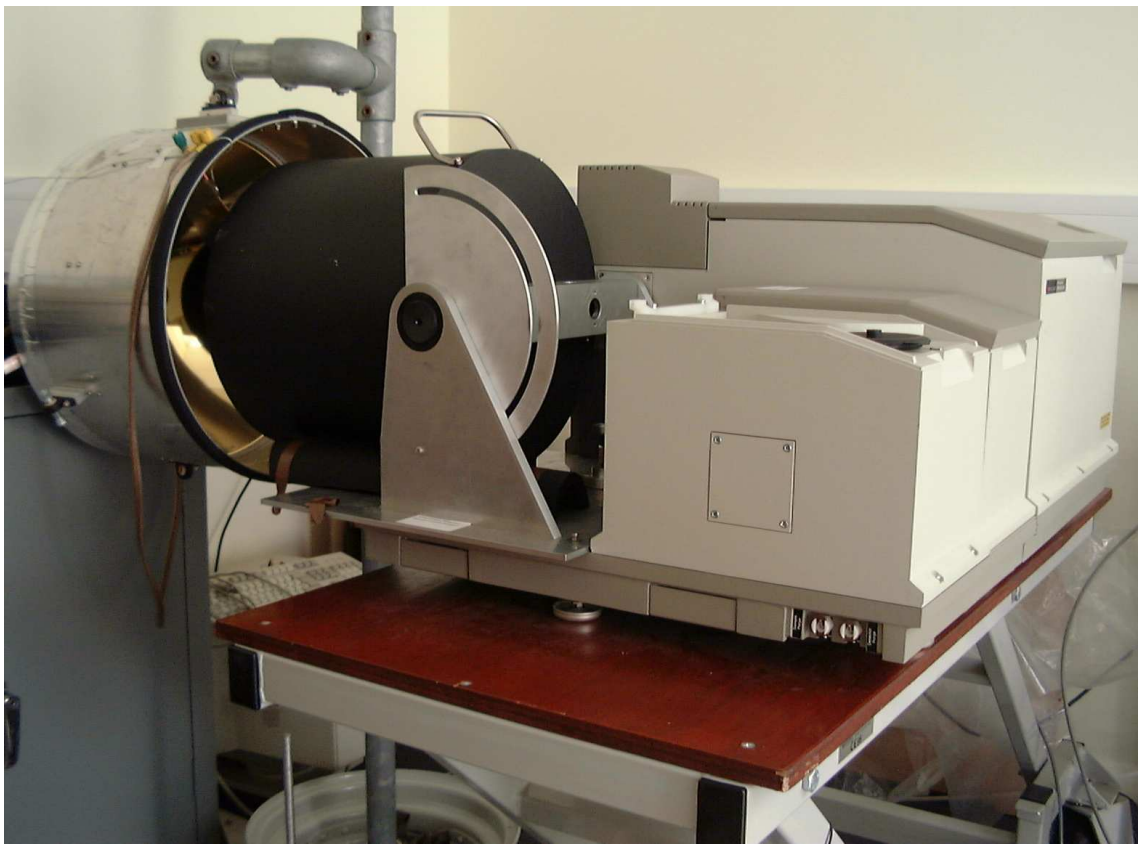

Figure 4.3: The external source, collimator and Perkin-Elmer Spectrum 2000 FTIR spectrometer aligned for the ILS measurements.

the following measurements were made

- Self-emission spectra recorded with the source switched off.
  - Spectra with the MCT detector.
    - Spectrum with strong Norton-Beer apodisation.
    - Spectrum with no (Boxcar) apodisation.
  - Single-sided interferogram with the MCT detector.
- Background spectra with no gas cell in the sample compartment.
  - Spectra with the MCT detector.
    - Spectrum with strong Norton-Beer apodisation.

        * Spectrum with no (Boxcar) apodisation.
    - Single-sided interferogram with the MCT detector.
    - Spectra with the DTGS detector.
        * Spectrum with strong Norton-Beer apodisation.
        * Spectrum with no (Boxcar) apodisation.
    - Single-sided interferogram with the DTGS detector.

- Sample spectra with the gas cell aligned in the sample compartment.
    - Spectra with the MCT detector.
        * Spectrum with strong Norton-Beer apodisation.
        * Spectrum with no (Boxcar) apodisation.
    - Single-sided interferogram with the MCT detector.
    - Spectra with the DTGS detector.
        * Spectrum with strong Norton-Beer apodisation.
        * Spectrum with no (Boxcar) apodisation.
    - Single-sided interferogram with the DTGS detector.

all at 0.2 cm^{-1} resolution. For the duration of the measurements the spectrometer and detector compartment were purged with 2 litres per minute of dry nitrogen gas in order to minimise the concentrations of water vapour and CO_2 in the spectrometer.

The spectrum of low pressure CO recorded with no (boxcar) apodisation and the MCT detector was used to extract the best estimate of the ILS. For the procedure, it was assumed that the CO spectral lines were Dirac delta functions. This is a reasonable assumption since the CO lines are approximately 40 times narrower than the ILS. The following procedure was followed in order to extract the best estimate of the ILS of the Perkin-Elmer Spectrum 2000 FTIR spectrometer.

The background spectra that were recorded were recorded without the gas cell in the optical path, rather than with the evacuated gas cell in the optical path because time constraints did not allow the evacuated gas cell to be transported to Oxford from RAL. Since the silicon windows absorb in the infrared, it was not possible to use the appropriate background spectrum to create a transmission spectrum from the sample spectrum. Instead CO, H_2O, and N_2O were retrieved[6] from the spectrum over the interval 2060 cm^{-1} to 2220 cm^{-1}, which include all potentially useful low pressure CO lines, using the modelled ILS. This determined the gain and offset for the spectral region which could then be used to create a pseudo transmission spectrum from the sample spectrum.

Seven CO lines in the region 2095 cm^{-1} to 2175 cm^{-1} were chosen. Each line was picked because it was at least 3 cm^{-1} from any other spectral lines (CO or H_2O) on each side. Each line was extracted as a section up to 4 cm^{-1} ($\pm$ 2 cm^{-1}) wide. The boundaries of the line being the point at which it was thought that the sidelobes from the neighbouring line had a significant influence. The lines that were chosen had their centres at 2103.3 cm^{-1}, 2111.55 cm^{-1}, 2119.7 cm^{-1}, 2127.7 cm^{-1}, 2131.65 cm^{-1}, 2158.3 cm^{-1}, and 2165.6 cm^{-1}.

Pseudo absorption spectra were created from each of the seven spectral sections by subtracting them from 1.0. Each section now formed an estimate of the ILS of the Perkin-Elmer Spectrum 2000 spectrometer. To smooth the spectra they were fast Fourier transformed to interferogram space, zero filled so that the spacing of points in spectral space was reduced from 0.05 cm^{-1} to 0.0005 cm^{-1}. The zero filled interferogram sections were then fast Fourier transformed back to spectra space. These smoothed spectral sections were then scaled to the same peak height and the peaks centred on 0.0 cm^{-1}(see figure 4.4).

To create a single ILS from the seven estimates, the mean of the seven estimates was calculated. Contributions from each of the seven estimates were excluded from the mean when either the amplitude of a sidelobe was significantly larger or smaller than the

[6]The retrieval of CO from the CO boxcar MCT spectrum failed to converge. Therefore the gain and offset from the retrieval of CO from the CO Norton-Beer strong MCT spectrum, which was taken immediately before the CO boxcar MCT spectrum and overlays it, were used instead. The residuals of the retrieval were spikes on either side of a horizontal line at zero.

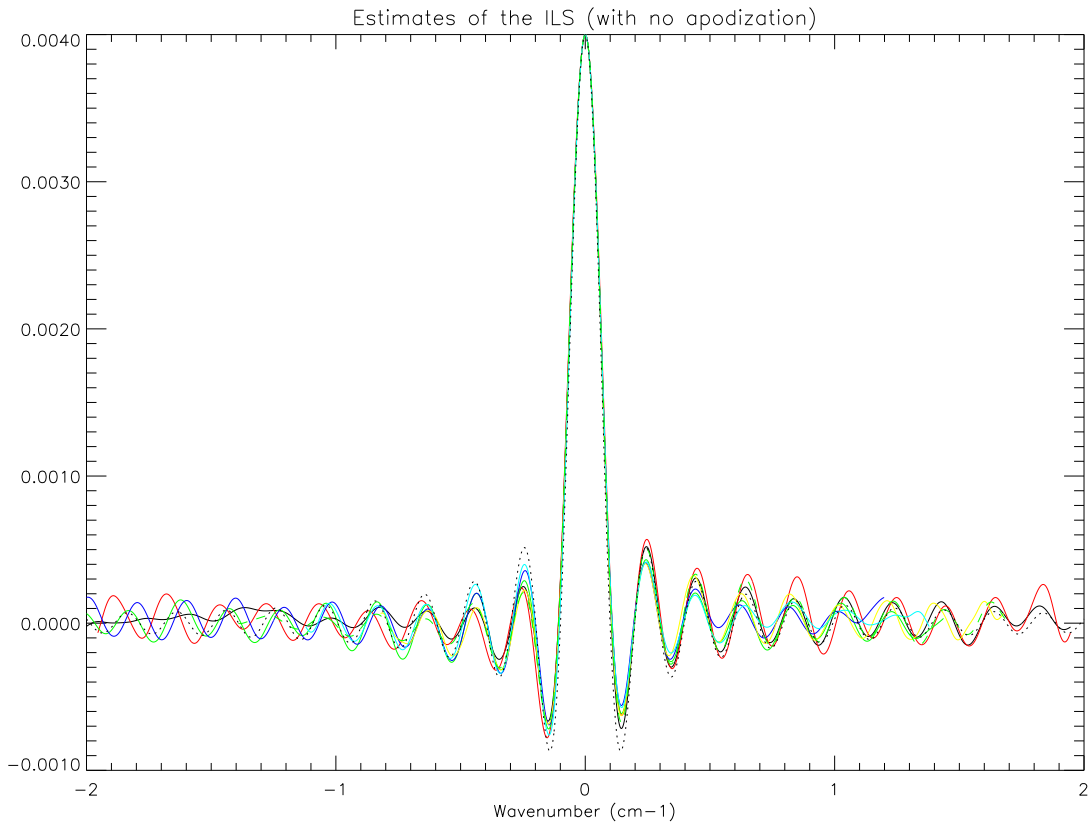

Figure 4.4: A plot of the 7 estimates that were extracted from the CO MCT boxcar spectrum of the 0.2 cm^{-1} resolution boxcar ILS. The dotted black line is the theoretical 0.2 cm^{-1} resolution boxcar ILS, and is included for comparison.

amplitude of the sidelobe in the other estimates, or when the sidelobes became noticeably out of phase with the other estimates. The further from the central peak of the spectrum, the smaller the amplitude of the sidelobes and thus the greater the influence of noise (the signal to noise ratio of the spectrum was 667, which leads to the amplitude of the noise being equivalent to the amplitude of the 16^{th} sidelobe, or 8^{th} maximum, of the theoretical boxcar ILS at $\pm$ 1.65 cm^{-1}). Also the further from the central peak of the spectrum, the closer to the central peak of adjacent lines and so the greater the relative (to the amplitudes of the sidelobes of the estimate) amplitude of the sidelobes of adjacent lines. Since the instrumental effects which were thought to be the cause of the discrepancies between the actual and modelled ILS functions have their greatest affect closest to the central peak,

the actual ILS will tend to the theoretical (modelled) ILS. This fact was used in order to create the measured ILS at increasing wavenumber when the amplitude of the noise and sidelobes from adjacent spectral lines became a significant proportion of the amplitude of the sidelobes of the measured ILS. From approximately $\pm$ 0.5 cm^{-1}, where the amplitude of the noise was approximately one third of the amplitude of the sidelobes, phase information for the measured ILS was taken from the theoretical ILS and amplitude information from the estimates of the measured ILS. Further away from the central maximum of the measured ILS the amplitude of the sidelobes was tapered to smoothly match that of the theoretical ILS at $\pm$ 2.0 cm^{-1}. A smooth transition is necessary in order to avoid spectral artifacts. From $\pm$ 2.0 cm^{-1} to $\pm$ 5.0 cm^{-1} the measured ILS is identical to the theoretical ILS. Figure 4.5 shows a plot of the measured ILS.

An ILS with Norton-Beer strong apodization could not be created from the CO Norton-Beer strong MCT spectrum because the amplitude of all the sidelobes in the theoretical ILS was below the noise level (the spectrum had a SNR of 667) in the spectrum. Therefore, in order to create an ILS with Norton-Beer strong apodization, the measured boxcar ILS was convolved in spectral space with the theoretical Norton-Beer strong ILS. The result is similar to, allowing for noise, the seven estimates of the ILS with Norton-Beer strong apodization extracted from the CO Norton-Beer strong MCT spectrum (see figure 4.6). The main difference is that the 'averaged' ILS does not have the offset at positive wavenumbers that the seven estimates have. The offset may be an artifact of the way the sample spectrum, from which the seven estimates were extracted, was converted to a pseudo transmission spectrum.

The actual ILS to be used in the retrieval is not that shown in figure 4.5 (for a boxcar ILS) or figure 4.6 (for a Norton-Beer strong ILS), but the mirror image, reflected about 0.0 cm^{-1}, of each ILS. The mirror image is required because of the process used to extract the 7 estimates from which the ILS was created and how convolution works. If the mirror image is used, then the asymmetry in the ILS appears on the correct side of the central maximum of a spectral line in a synthetic spectrum.

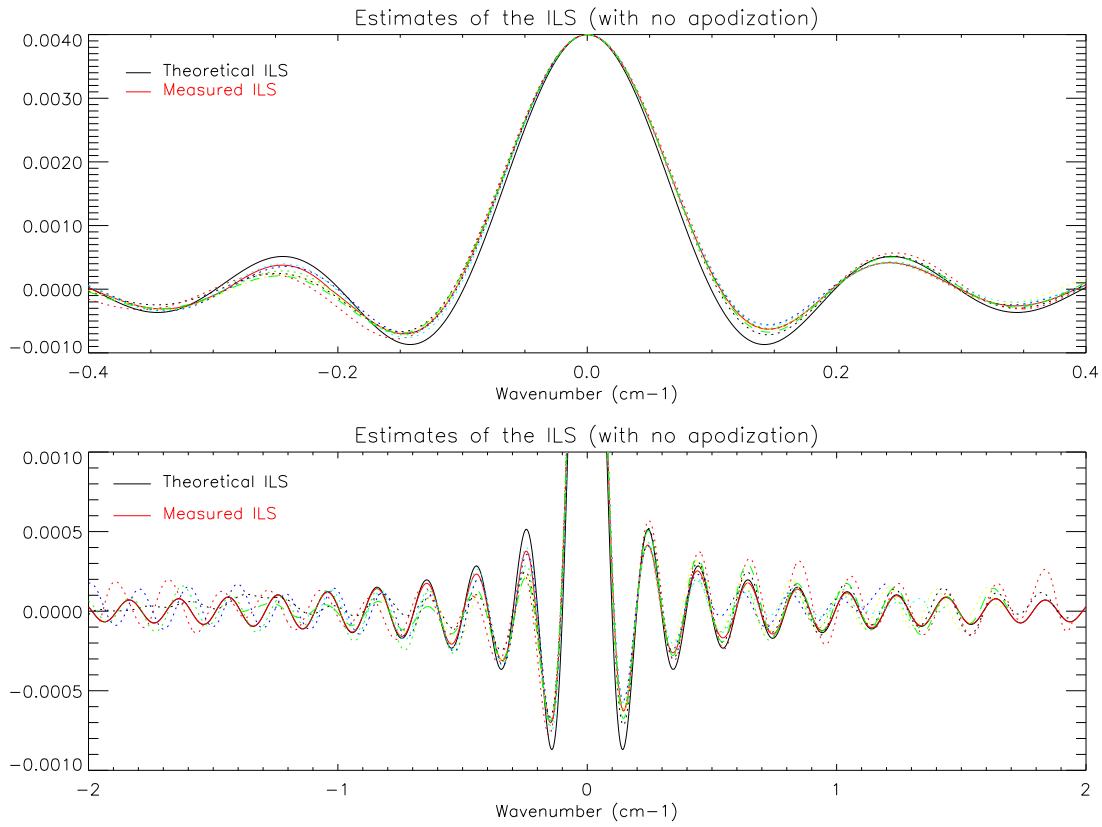

Figure 4.5: A plot of the measured 0.2 cm^{-1} resolution boxcar ILS (solid red line) together with the theoretical ILS (solid black line) and 7 ILS estimates for comparison (which are repeated from figure 4.4).

4.7.3 Comparison of the Measured and Modelled Instrument Lineshapes

A comparison of the measured and modelled instrument lineshapes was carried out to see if the measured ILS reduced the discrepancies in retrievals between the shapes of the spectral lines in the measured and synthetic spectra. Surprisingly, given the obvious asymmetries of the measured ILS, there was little difference in the size of the residuals for each ILS. In general, the measured ILS is the best fit for the lower wavenumber wing of each spectral line and the theoretical ILS the best fit for the centre of the line. However, the differences are small. Two examples are shown in figures 4.7 and 4.8.

When retrievals were carried out on two of the spectra recorded during the field measurements at Oxford railway station on 26/09/99 (26109ag.asc and 26_1099c.asc) of

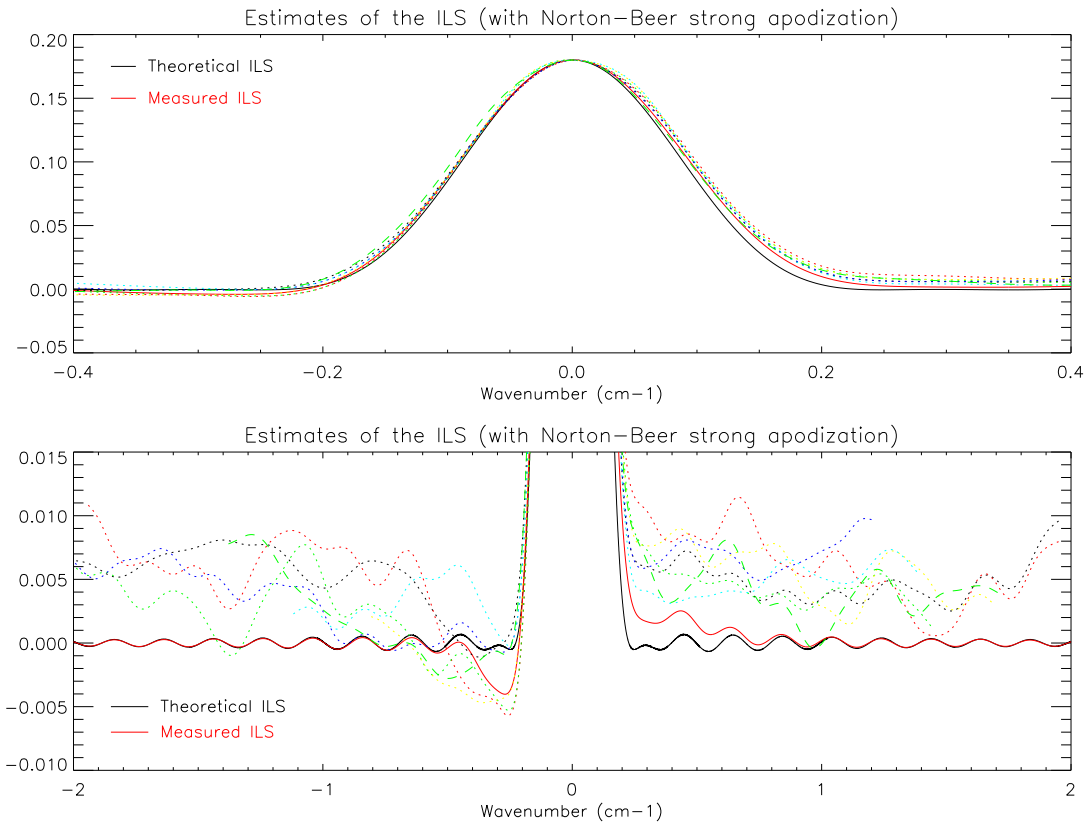

Figure 4.6: A plot of the measured 0.2 cm^{-1} resolution Norton-Beer strong ILS (solid red line) together with the theoretical ILS (solid black line) and 7 estimates of the 0.2 cm^{-1} resolution Norton-Beer strong ILS extracted from the CO Norton-Beer strong MCT spectrum for comparison.

CO and NO it was found that in general there were only small (less than 5%) differences between the retrieved values. In general the retrieval made with the measured ILS had slightly lower retrieval error and a priori contribution, but the retrieval made with the modelled (theoretical) ILS had slightly lower residuals and normalised Chi squared values closer to one. It was therefore decided to use the measured, rather than the theoretical, ILS in all retrievals.

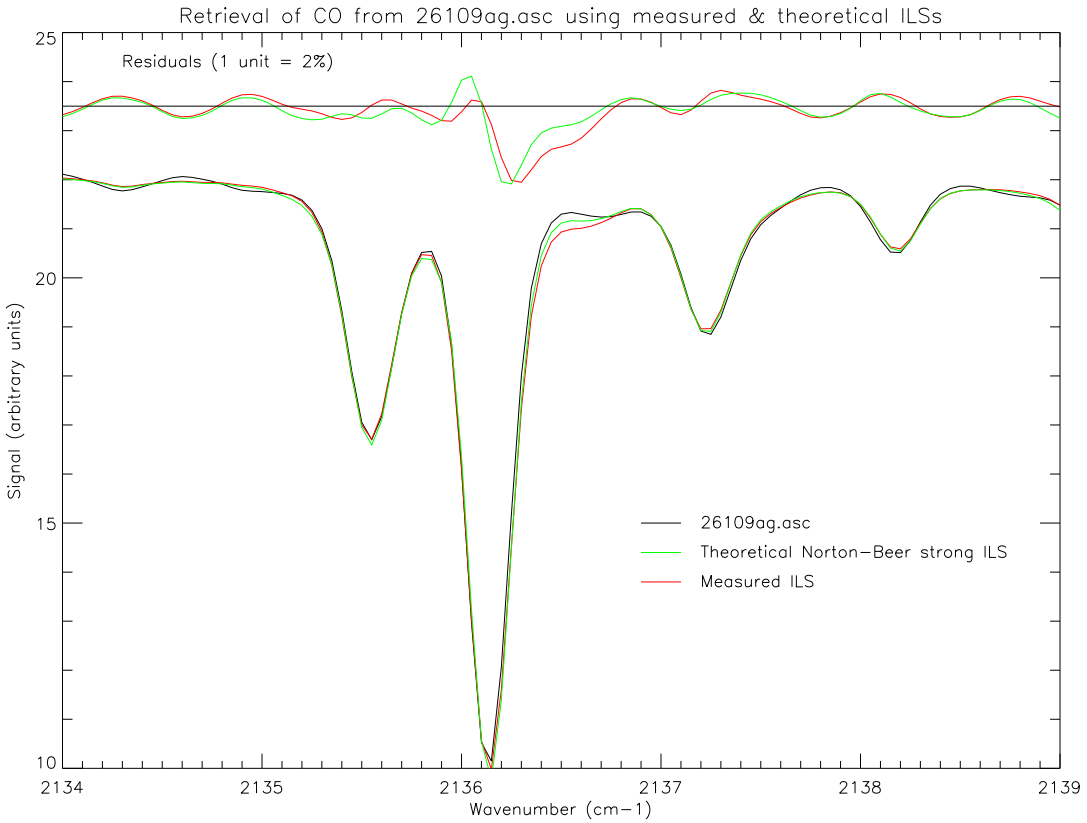

Figure 4.7: A plot of CO and water lines in the region 2134 cm^{-1} to 2139 cm^{-1}. The black line is from a spectrum recorded during the field measurements at Oxford railway station on 26/09/99. The green and red lines are from retrievals over the region 2120 cm^{-1} to 2220 cm^{-1} using the theoretical Norton-Beer strong ILS and the measured Norton-Beer strong ILS respectively.

4.8 Wavenumber Offset

Errors in the wavenumber scale can be caused by several effects in the spectrometer. The most usual cause is that the reference He-Ne laser, which is used to enable the interferogram to be sampled at intervals of equal optical path difference, is slightly misaligned, which introduces a small wavenumber shift. Another cause is the finite size of the infrared source and of any apertures at focal points of the beam, which allows off-axis rays to pass through the spectrometer. The effect of this beam divergence changes the instrument line shape and slightly shifts the position of spectral lines. Wavenumber shifts can also be introduced

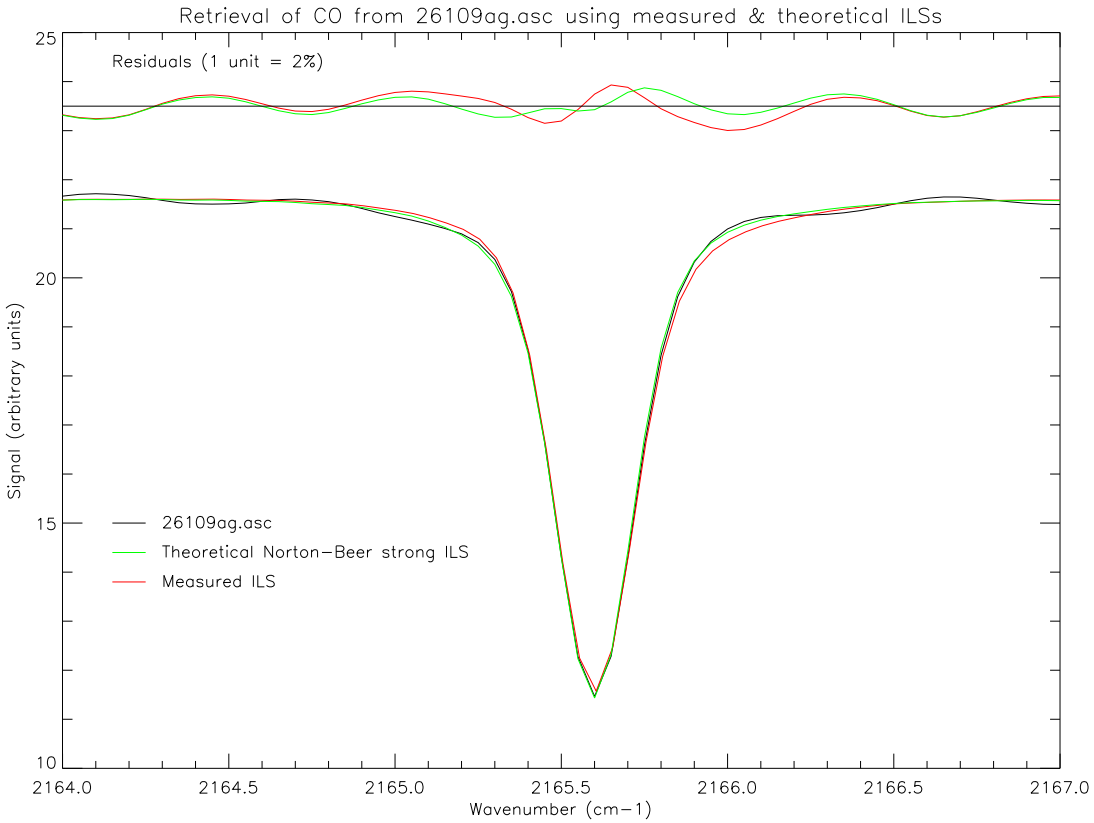

Figure 4.8: A plot of a CO spectral line over the region 2164 cm^{-1} to 2167 cm^{-1}. The black line is from a spectrum recorded during the field measurements at Oxford railway station on 26/09/99. The green and red lines are from retrievals over the region 2120 cm^{-1} to 2220 cm^{-1} using the theoretical Norton-Beer strong ILS and the measured Norton-Beer strong ILS respectively.

by other optical misalignments, particularly at focal points of the beam, and by deflection of the beam by transmitting optical components which are set at an angle to the beam, such as the KBr windows and the wedged gap between the beamsplitter and compensator.

The wavenumber offset which is retrieved is the most likely value of the difference in positions of spectral lines in the section of the measured spectrum over which the retrieval is being carried out and those given in the HITRAN database from which the RFM extracts the line data it needs to simulate the measured spectrum. The retrieved offsets are of the order of $\pm$ 0.005 cm^{-1}. The a priori which is used is 0.0 cm^{-1} with an error of 0.005 cm^{-1}. The weighting function for the wavenumber offset is given in equation 4.20,

and its calculation is discussed in section 4.4.9.

4.9 Scaling

It was discovered that, in practice, the elements of the weighting function matrix vary by ten orders of magnitude. This is due to the inclusion of gain in the state vector, $\mathbf{x}$. The expression for gain is given in equation 4.22 and the weighting functions for its three coefficients are given in equation 4.21. Now, $0 \leq \tau \leq 1$ and $\tilde{\nu}$ lies in the range 900 cm^{-1} to 4000 cm^{-1}, therefore these three weighting functions can vary between 0.001 and 1.6x10^7; a range of ten orders of magnitude.

The algorithm used to invert matrices incorrectly inverts any matrix whose singular values vary over more than three orders of magnitude. This includes the weighting function, $\mathbf{K}$ and, depending on the relative magnitudes of $\mathbf{S_a}^{-1}$ and $\mathbf{S_y}^{-1}$, the matrix $(\mathbf{S_a^{-1}} + \mathbf{K^T S_y^{-1} K})^{-1}$. For the range of values used in the retrievals in this study, the relative magnitudes of $\mathbf{S_a}^{-1}$ and $\mathbf{S_y}^{-1}$ are such that $(\mathbf{S_a^{-1}} + \mathbf{K^T S_y^{-1} K})^{-1}$ was being incorrectly inverted by the algorithm. Thus the error affected not only the calculation of the retrieved profile, $\hat{\mathbf{x}}$, but also the retrieval diagnostics described in section 4.3.

The solution was to scale the state vector, $\mathbf{x}$, (and thus also the *a priori*, $\mathbf{x_a}$) by a factor $\mathbf{\Gamma}$ so that all values would be within two orders of magnitude. This also necessitated scaling both the error on the a priori, $\mathbf{S_a}$, and the weighting function, $\mathbf{K}$:

$$\mathbf{x}' = \mathbf{\Gamma x} \tag{4.24}$$

$$\mathbf{K}' = \mathbf{K\Gamma}^{-1} \tag{4.25}$$

$$\mathbf{S'_a} = \mathbf{\Gamma S_a \Gamma} \tag{4.26}$$

where prime denotes the scaled values. $\mathbf{\Gamma}$ is defined as $\sqrt{\mathbf{K}^T \mathbf{S_y}^{-1} \mathbf{K}}$ and each element is rounded to the nearest power of 10. Note that $\mathbf{\Gamma}$ is diagonal, and therefore $\mathbf{\Gamma}^T = \mathbf{\Gamma}$ and $(\mathbf{\Gamma^{-1}})^T = \mathbf{\Gamma}^{-1}$.

Therefore

$$\begin{aligned}\mathbf{y} &= \mathbf{K}\mathbf{x} + \epsilon \\ &= \mathbf{K}'\mathbf{x}' + \epsilon\end{aligned}$$

and

$$\begin{aligned}\mathbf{x}_{n+1} &= \mathbf{\Gamma}^{-1}\mathbf{x}'_{n+1} \\ &= \mathbf{\Gamma}^{-1}\left[\mathbf{x}'_n + \left(\mathbf{S}'^{-1}_{\mathbf{a}} + \mathbf{K}'^{\mathbf{T}}\mathbf{S}^{-1}_{\mathbf{y}}\mathbf{K}'\right)^{-1}\left(\mathbf{K}'^{\mathbf{T}}\mathbf{S}^{-1}_{\mathbf{y}}(\mathbf{y}-\mathbf{f_n}) + \mathbf{S}'^{-1}_{\mathbf{a}}(\mathbf{x}'_{\mathbf{a}} - \mathbf{x}'_{\mathbf{n}})\right)\right]\end{aligned}$$

and the diagnostics become

$$\begin{aligned}\hat{\mathbf{S}}_{\mathbf{x}} &= \mathbf{\Gamma}^{-1}\hat{\mathbf{S}}'_{\mathbf{x}}\mathbf{\Gamma}^{-1} \\ \mathbf{D_y} &= \mathbf{\Gamma}^{-1}\mathbf{D}'_{\mathbf{y}} \\ \mathbf{D_a} &= \mathbf{\Gamma}^{-1}\mathbf{D}'_{\mathbf{a}}\mathbf{\Gamma} \\ \mathbf{A} &= \mathbf{\Gamma}^{-1}\mathbf{A}'\mathbf{\Gamma} \\ \chi^2 &= \chi'^2\end{aligned}$$

where the primed values are calculated using the same expressions as for the non-primed values, but with $\mathbf{x}$, $\mathbf{x_a}$, $\mathbf{K}$ and $\mathbf{S}_a$ replaced by their primed values.

Chapter 5

Benzene and 1,3-Butadiene

5.1 Introduction

Benzene (C_6H_6) and 1,3-butadiene (C_4H_6) are two of the eight pollutants included in the UK government's National Air Quality Strategy (Department of the Environment, Welsh Office & Scottish Office 1997), which was published in March 1997 and updated in January 2000 (Department of the Environment, Transport and the Regions et al. 2000). The original document sets out objectives, to be achieved by 2005, for the allowable atmospheric concentrations of the eight pollutants believed to pose most danger to health (see figure **??**). The updated strategy is in most cases more stringent (see figure **??**). The other six pollutants included in the NAQS are: carbon monoxide (CO), lead (Pb), nitrogen dioxide (NO_2), ozone (O_3), PM_{10} (Particulate Matter less than 10 micrometres in diameter) and sulphur dioxide (SO_2).

Benzene is a known human genotoxic[1] carcinogen and 1,3-butadiene is a suspected human genotoxic carcinogen (it is known to cause a variety of cancers in rodents), hence their inclusion in the NAQS.

The main source of atmospheric benzene in the UK is motor vehicles, which in 1997 accounted for approximately 60% of total emissions(Department of the Environment, Transport and the Regions et al. 2000). Benzene is a minor constituent of petrol (both leaded and unleaded), approximately 2% by volume, and approximately 4% of total emissions in

[1] i.e. it damages the genetic structures of the cell

1997 resulted from evaporation of benzene from petrol vehicles. The main source of benzene in vehicle exhausts is not unburnt benzene, but benzene formed by the combustion of other aromatic compounds in petrol. Benzene is also formed in the combustion of diesel, but in 1997 this contributed approximately 4% of total emissions, less than a tenth of the contribution from petrol vehicles. Industry, where benzene is an important chemical feedstock, or intermediate, in the synthesis of many chemicals, such as dyes, is the second largest source of atmospheric benzene and in 1997 it accounted for approximately 19% of total emissions.

The main source of 1,3-butadiene in the atmosphere in the UK is also from road transport, which in 1996 accounted for approximately 68% of total emissions (Department of the Environment, Transport and the Regions et al. 2000). The majority of emissions from road transport is from combustion in petrol vehicles, where 1,3-butadiene is formed from the cracking of higher olefines. The second largest source of 1,3-butadiene in the atmosphere, and the only other major source, is industry, in particular the chemical industry and production of synthetic rubber for tyres. In 1996 emissions from industry accounted for approximately 18% of total emissions.

National monitoring of air pollution in the UK is undertaken by the National Environmental Technology Centre (NETCEN), which is part of AEA Technology, on behalf of the Department of the Environment, Transport and the Regions. The hourly concentrations of benzene and 1,3-butadiene are monitored at 13 sites across the UK through the national Automatic Hydrocarbon Network. The measurements are made by continuous gas chromatography on approximately 300 cm^3 volume of air sampled each hour on either a Chrompack VOCAIR or a Perkin Elmer ATD400 system(Bower, Broughton & Willis 1995). The accuracy of these measurements is $\pm$ 10% and the precision is $\pm$ 0.1 ppbv.

In principle it is possible to measure both benzene and 1,3-butadiene by FTIR spectroscopy, since both gases absorb in the mid-infrared part of the spectrum. In order to do so it is necessary to have spectroscopic data for each gas. This can either be line-by-line data or absorbance cross-sections. At the start of this study high quality spectroscopic data for gaseous benzene and 1,3-butadiene in the mid-infrared was not readily available.

Absorbance cross-section spectra were available from two sources; the U. S. Environmental Protection Agency (EPA) and Infrared Analysis, Inc.[2]. In 1992 the US EPA published the infrared spectra of over 100 hazardous air pollutants, benzene and 1,3-butadiene amongst them. Most of the spectra are contaminated by water vapour. Corrected spectra are also published; however the water vapour spectrum used to correct them contained CO_2 and so the corrected spectra have negative peaks near 2350 cm^{-1} and 667 cm^{-1}. Details of the method used to obtain these spectra are given in (Geyer, Plummer & Dunder 1992). Infrared Analysis's QASoft database contains spectra of 269 gaseous compounds, including those of benzene and 1,3-butadiene. This data appears to be of higher quality than the EPA's, however details of how it was obtained are sparse.

The highest resolution of the absorbance spectra from both the US EPA and Infrared Analysis is 0.25 cm^{-1}. This is lower than the operating resolution (0.2 cm^{-1}) of the Perkin-Elmer FTIR spectrometer used in this study. The need for higher resolution absorbance cross-section spectra, and lack of confidence in the published data, led to the measurement of the absorption cross-sections of benzene and 1,3-butadiene as part of this study.

5.2 Experimental Details

Absorption spectra of benzene and 1,3-butadiene were recorded using a Bruker IFS120 HR Fourier transform infrared spectrometer (maximum optical path difference 600 cm) at the Molecular Spectroscopy Facility (MSF) at the Rutherford Appleton Laboratory (RAL). The experimental setup used was similar to that described by Newnham and Ballard (Newnham & Ballard 1995), so only a general description and details of modifications made will be given here. The spectrometer was operated with a globar source and KBr beamsplitter. For the 600 cm^{-1} to 1800 cm^{-1} spectral region a broadband liquid nitrogen-cooled mercury-cadmium-telluride (MCT) detector was utilised. For the 2600 cm^{-1} to 3300 cm^{-1} spectral region a liquid nitrogen-cooled Indium Antimonide (InSb) detector was used.

[2]President and Founder of the company is Dr Philip L. Hanst, who has worked in this field for many years. The company's website is at http://www.infrared-analysis.com/.

A stainless steel gas cell of optical pathlength 26 cm with KBr windows was used for the main absorption cross-section measurements. It is similar to the 5 cm stainless steel absorption cell described by Ballard *et al.*(Ballard et al. 1985). A shorter optical pathlength was required in order to measure the main Q branch of benzene. For these measurements, the 5 cm stainless steel cell was used. The cell temperature was monitored using 8 thermistors in thermal contact with the exterior surface of the gas cell. The temperature readings, which were accurate to ± 0.3 K, were logged directly into a personal computer using a SignaloggerPC interface (Laplace Instruments).

The cell was mounted inside the sample compartment of the spectrometer, which is evacuated to below 0.2 Pa by a 340 ls^{-1} turbomolecular pump backed by a rotary pump in order to minimise the amount of water vapour and carbon dioxide in the optical path of the spectrometer. The presence of infrared absorbance features due to these species in the transmittance spectra, would lead to errors in the measured absorbance cross-sections.

Gas handling and pressure measurement was carried out on a clean glass and PTFE vacuum line using 10 torr and 1000 torr full scale Baratron capacitance gauges (Chell Instruments, Type MKS-390, accuracy 0.08% of reading). These were zeroed under hard vacuum before any measurements were made and the zero reading checked at the end of the series of measurements. The pressure readings of the 10 torr gauge were validated by measuring identical air pressures with both the 10 torr and the 1000 torr gauge, which was itself checked for consistency with an Aneroid barometer (Negretti, type M2236A, accuracy ± 40 Pa) at atmospheric pressure. The pressure readings of the 10 torr gauge were found to be accurate to ± 2.5 Pa (± 0.019 torr).

Two millilitres of liquid benzene (Fluka Chemicals), which had a stated purity of 99.98%, were transferred to a clean, evacuated glass sample tube in a pure nitrogen atmosphere. The sample tube was attached to the vacuum line and three freeze-pump-thaw sequences[3] were carried out in order to remove any residual atmosphere above, or dis-

[3]The sample was frozen by immersing the sample tube in liquid nitrogen (the freezing point of benzene being above the temperature of liquid nitrogen). The sample tube was then opened to the vacuum line and any atmosphere above the frozen sample pumped off. The sample was then allowed to thaw before the

solved in, the benzene before the benzene was transferred into the absorption cell for the measurements.

The sample of 1,3-butadiene (ARGO International Ltd.) had a stated purity of 99.5%. 1,3-butadiene is a gas at room temperature and pressure, and so the vacuum line was used to directly transfer a sample (80.7 kPa) of 1,3-butadiene from its gas cylinder to a clean, evacuated glass sample tube attached to the vacuum line (the line was flushed with pure nitrogen gas before the transfer). The repeated sequence of freeze-pump-thaw (the freezing point of 1,3-butadiene is also above the temperature of liquid nitrogen) was again employed to remove any residual atmosphere present, before the 1,3-butadiene was analysed.

A survey infrared spectrum of a sample of 205.85 Pa benzene vapour at 295 K was measured at a resolution of 0.1 cm^{-1} by co-adding 200 scans and ratioing against a background empty cell spectrum, also of 200 scans. No optical filter was used for this measurement (see figure 5.1). This shows the main Q branch of benzene at 674 cm^{-1} and the secondary band at around 3100 cm^{-1}, as well as several other minor bands. The spectrum was recorded before the spectrometer was fully evacuated, and so it also includes some residual CO_2 and H_2O lines. A similar survey spectrum was taken of 207.58 Pa 1,3-butadiene vapour, using the same set up (see figure 5.2). This shows the main Q branch at 908 cm^{-1} and several other bands, including the C-H stretch band at around 3000 cm^{-1}.

For the absorbance cross-section measurements in the 600 cm^{-1} to 1800 cm^{-1} spectral range, the absorption spectra were recorded at a resolution of 0.03 cm^{-1} using Norton-Beer strong apodization. The spectrometer aperture was restricted to 1.0 mm to ensure that the intensity of infrared radiation falling on the MCT detector was such that the detector showed only a minimal nonlinear response, whilst keeping signal-to-noise levels reasonably high. An optical filter further restricted the radiation falling on the sample and detector to the spectral region between 550 cm^{-1} and 1900 cm^{-1}, thus reducing photon shot noise and detector non-linearity.

For the benzene Q branch measurements, the absorption spectra were recorded at a

sequence was repeated, so that any gases trapped in the frozen sample could be pumped off.

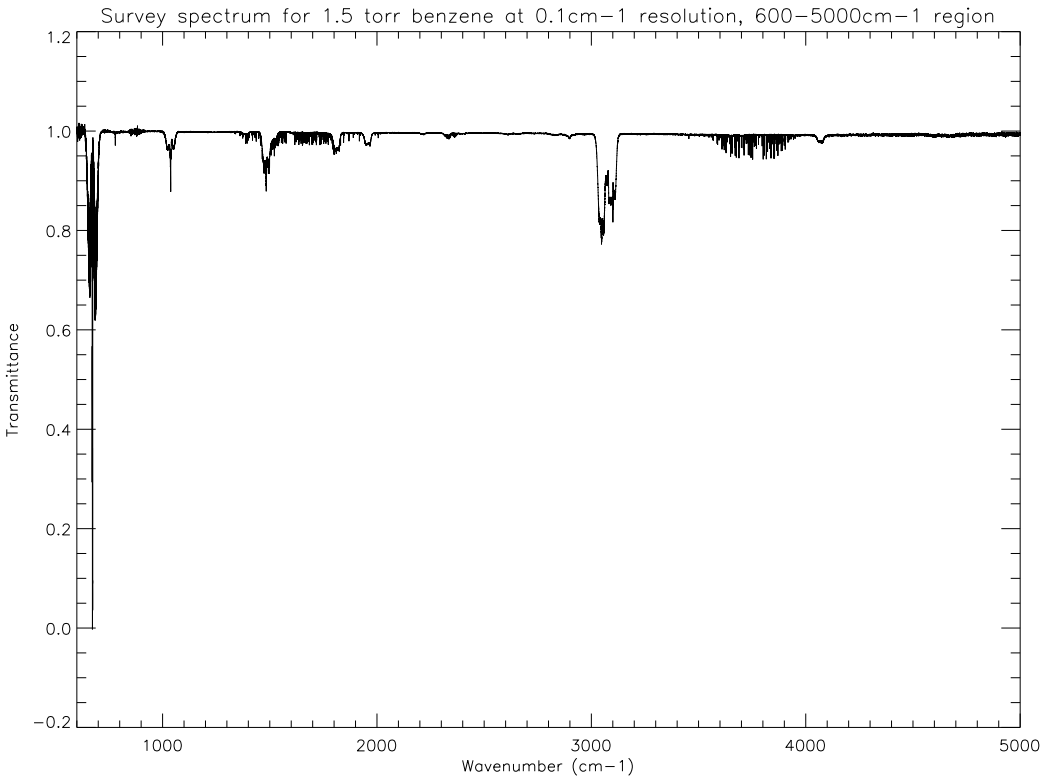

Figure 5.1: Survey spectrum of benzene

resolution of 0.03 cm^{-1} using Norton-Beer strong apodization. The spectrometer aperture was restricted to 1.7 mm, which gave a good signal-to-noise ratio, whilst ensuring that the MCT detector response was linear. An optical filter further restricted the radiation falling on the sample and detector to the spectral region between 600 cm^{-1} and 1300 cm^{-1}, thus reducing photon shot noise.

For the absorbance cross-section measurements in the 2600 cm^{-1} to 3300 cm^{-1} spectral range, the absorption spectra were recorded at a resolution of 0.01 cm^{-1} using Norton-Beer medium apodization. The spectrometer aperture was set to 1.7 mm. An optical filter restricted the radiation falling on the sample and detector to the spectral region between 2400 cm^{-1} and 3570 cm^{-1}, thus reducing photon shot noise.

For the main benzene and 1,3-butadiene measurements spectra were recorded at each

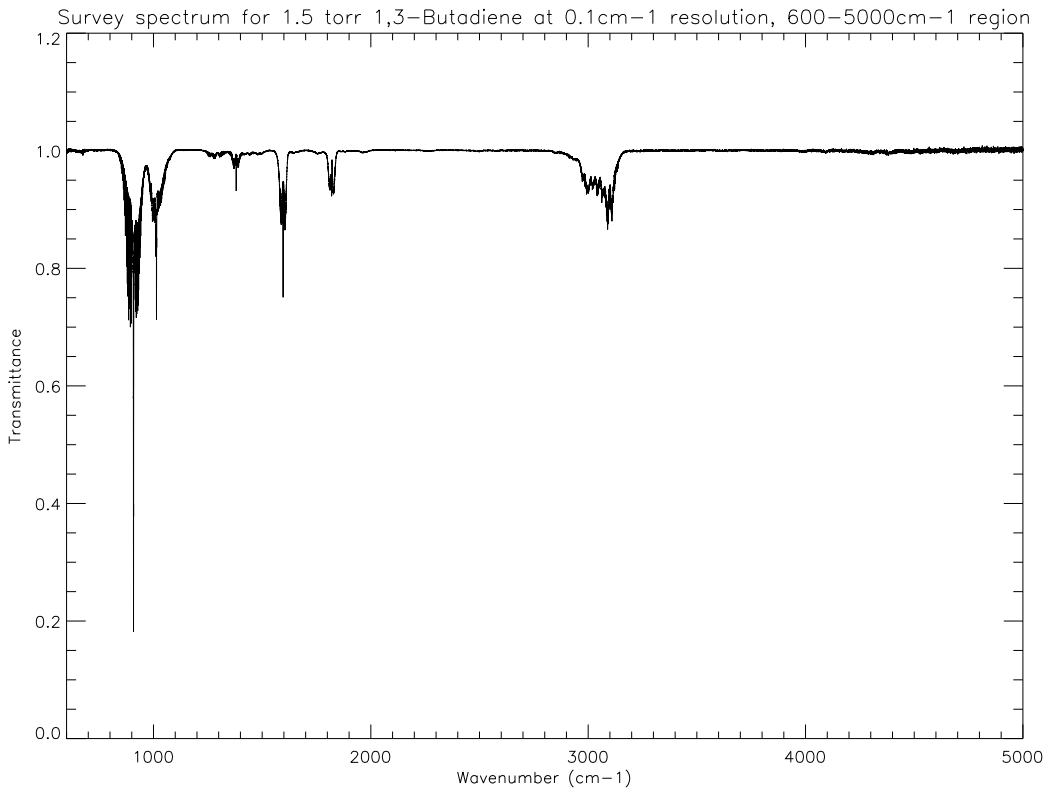

Figure 5.2: Survey spectrum of 1,3-butadiene

of three different pressures; 200 Pa, 133 Pa and 67 Pa. The temperature in each case being approximately 295 K. At each pressure spectra were recorded in both spectral regions, 600 cm^{-1} to 1800 cm^{-1} and 2600 cm^{-1} to 3300 cm^{-1}. In the former case 100 scans were co-added to form the spectrum, in the latter 25 scans were used.

The sample pressures were chosen to produce reasonably intense absorption bands without causing saturation of the strong features. The intensity of the benzene Q branch was such that even at the shorter optical pathlength, a lower set of pressures was required. The pressures used for this set of measurements were: 133 Pa, 67 Pa and 33 Pa. The temperature in each case was approximately 295 K. The spectra were recorded in the region 600 cm^{-1} to 1300 cm^{-1}, and 100 scans were co-added to form each spectrum.

For both gases, but benzene in particular, it was noticeable that the gas adsorbed onto the interior cell walls after the initial filling of the cell. Therefore pressure readings were noted every minute during the recording of the absorption spectra, and the mean values, which were corrected for the slight leakage of air into the cell (recorded during the measurements of the corresponding background spectra, i.e. when the gas cell was evacuated), were used in the determination of absorbance cross-sections.

Transmittance spectra were calculated by ratioing each sample spectrum with background (evacuated cell) spectra averaged from 100 (or 25 for the 2600 cm^{-1} to 3300 cm^{-1} region) co-added scans recorded before and after each sample measurement. The calculated noise (standard deviation) on the transmittance spectra varied between 0.0004 and 0.001 in the 2600 cm^{-1} to 3300 cm^{-1} region, between 0.001 to 0.01 in the 600 cm^{-1} to 1800 cm^{-1} region, and between 0.0006 and 0.0007 in the 600 cm^{-1} to 1300 cm^{-1} region.

As well as the pure gas spectra, measurements were also taken of benzene, and of 1,3-butadiene, in dry synthetic zero grade air (Air Products, 79% N_2 + 21% O_2). The mixtures used were 255 Pa and 500 Pa benzene in 100 kPa dry synthetic zero grade air for the main benzene measurements, 133 Pa and 273 Pa benzene in 100 kPa dry synthetic zero grade air for the benzene Q branch measurements and 250 Pa, 300 Pa and 510 Pa 1,3-butadiene in 100 kPa dry synthetic zero grade air (or approximately 0.25% and 0.5% mixtures for the main benzene measurements, 0.1% and 0.2% mixtures for the benzene Q branch measurements and 0.25%, 0.3% and 0.5% mixtures for 1,3-butadiene). Samples were carefully prepared in a round 1 dm^3 glass bulb and left overnight, to ensure adequate mixing of the gases prior to introduction into the sample cell.

For the 2600 cm^{-1} to 3300 cm^{-1} spectral region, the absorption spectra of the benzene (or 1,3-butadiene) / air mixture were recorded at a resolution of 0.03 cm^{-1} using strong Norton-Beer apodization. The aperture, optical filter, detector and number of scans used were the same as for the pure gas measurements in this region. A lower resolution could be used because pressure broadening of the spectral lines at 100 kPa pressure blurs out the finer details of the spectrum, and thus the spectrum can be completely resolved at a

lower resolution. For the benzene Q branch measurements the number of co-added scans per spectrum was reduced to 60, due to time constraints and the need to determine the rate of adsorption. All other settings were kept the same as for the pure gas measurements. For the 600 cm^{-1} to 1800 cm^{-1} spectral region, the set up used was the same as for the pure gas measurements in this region.

5.3 Results

The absorbance cross-section per molecule ($cm^2 \cdot molecule^{-1}$) at the experimental spectral resolution and temperature T is determined by the following expression:

$$\sigma(\tilde{\nu}, T) = \frac{-\ln[\tau_c(\tilde{\nu}, T)]}{N_A c l} \tag{5.1}$$

where $\tau_c(\tilde{\nu}, T)$ is the transmittance at wavenumber $\tilde{\nu}$ (in cm^{-1}) of an optical pathlength l (in cm) of spectroscopic gas at concentration c (in $mole \cdot cm^{-3}$) and temperature T (in K). N_A is Avogadro's constant.

The concentration c in units of $mole \cdot cm^{-3}$ of a pressure (or partial pressure) p of benzene (or 1,3-butadiene) vapour at temperature T is given by:

$$c = \frac{10^{-6} p}{RT} \tag{5.2}$$

where R is the molar gas constant, p is in units of Pa and T in K.

The integrated band strength ($cm \cdot molecule^{-1}$) at temperature T (in K) is given by:

$$S_{int}(T) = \int_{band} \sigma(\tilde{\nu}, T)\, d\tilde{\nu} \tag{5.3}$$

Plots of the absorption cross-sections for benzene (figures 5.3, 5.4, 5.5, 5.6, 5.7 and 5.8) and 1,3-butadiene (figures 5.9, 5.10, 5.11 and 5.12), both as the pure gas and in air, can be found on the following pages.

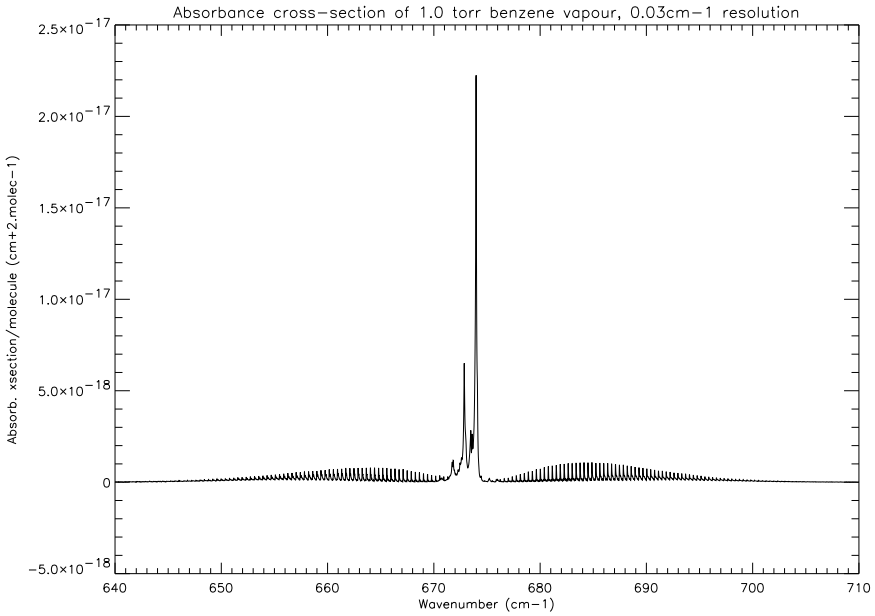

Figure 5.3: Absorption Cross-section of benzene in the 640 cm^{-1} to 710 cm^{-1} region, showing the main Q branch

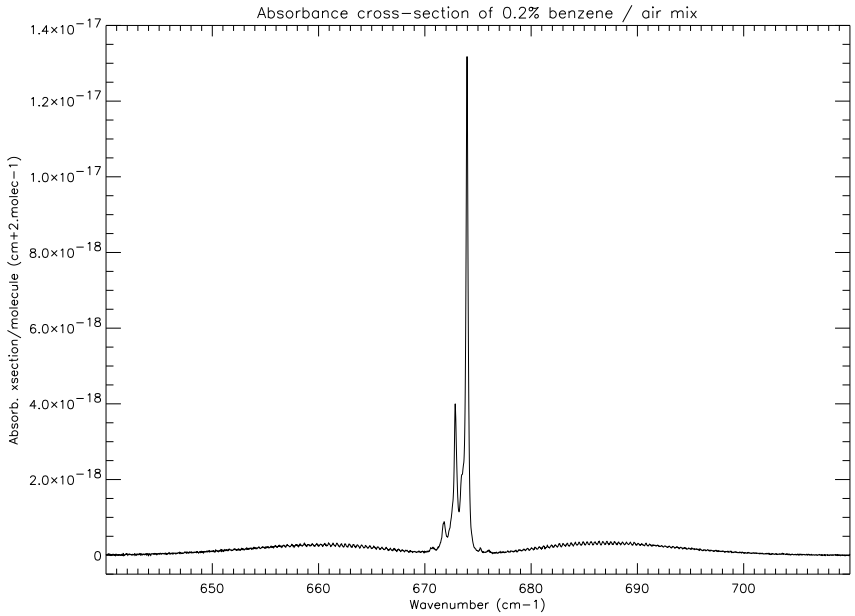

Figure 5.4: Absorption Cross-section of benzene in air in the 640 cm^{-1} to 710 cm^{-1} region, showing the main Q branch

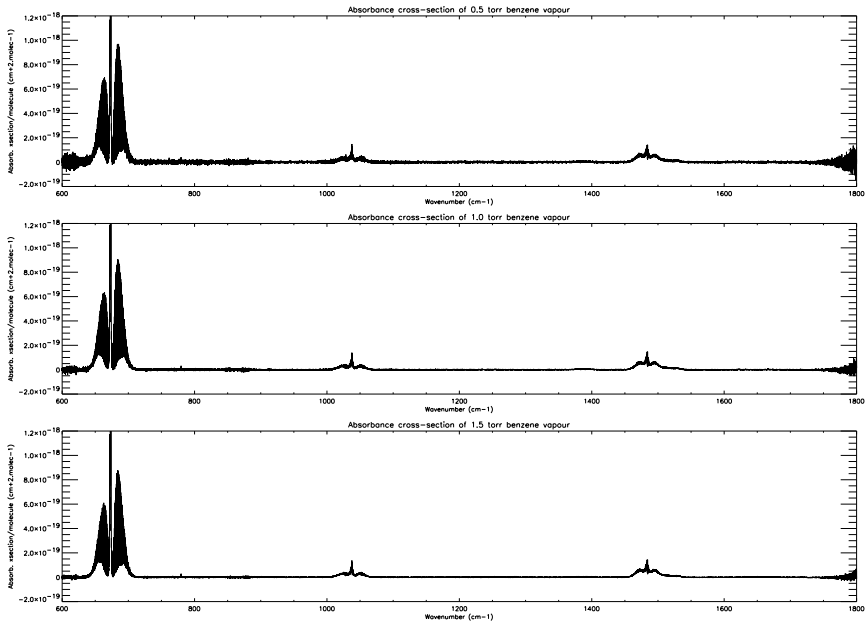

Figure 5.5: Absorption Cross-section of benzene in the 600 cm^{-1} to 1800 cm^{-1} region showing the minor absorption bands

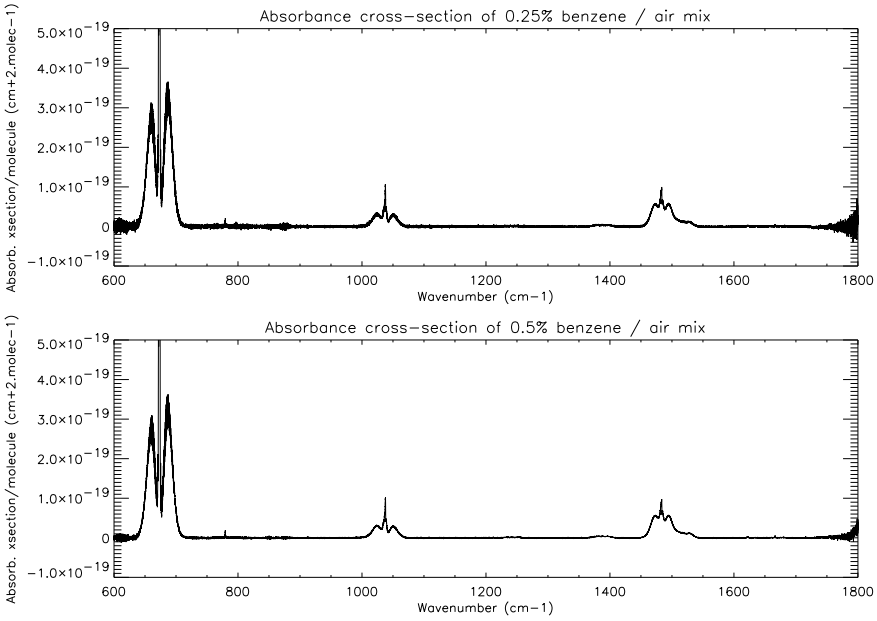

Figure 5.6: Absorption Cross-section of benzene in air in the 600 cm^{-1} to 1800 cm^{-1} region

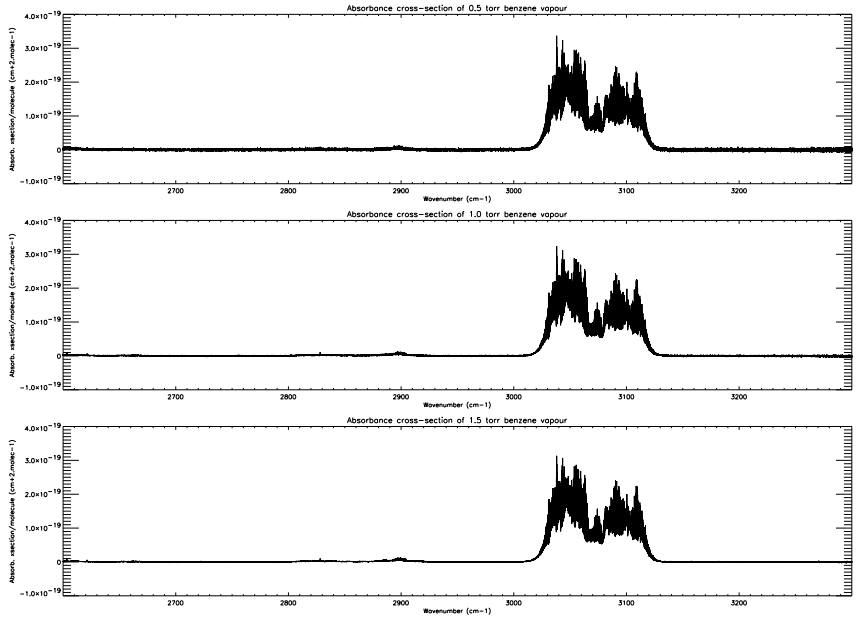

Figure 5.7: Absorption Cross-section of benzene in the 2600 cm^{-1} to 3300 cm^{-1} region

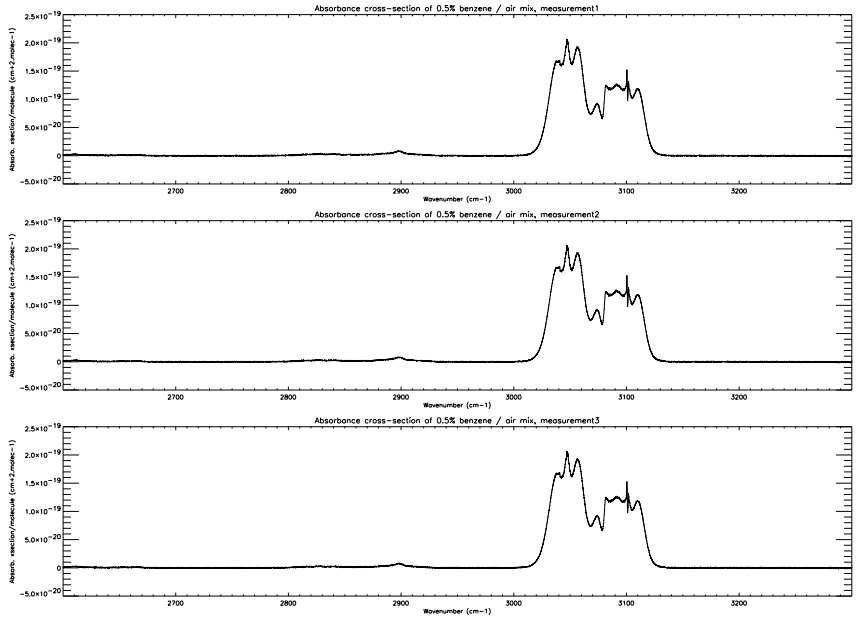

Figure 5.8: Absorption Cross-section of benzene in air in the 2600 cm^{-1} to 3300 cm^{-1} region

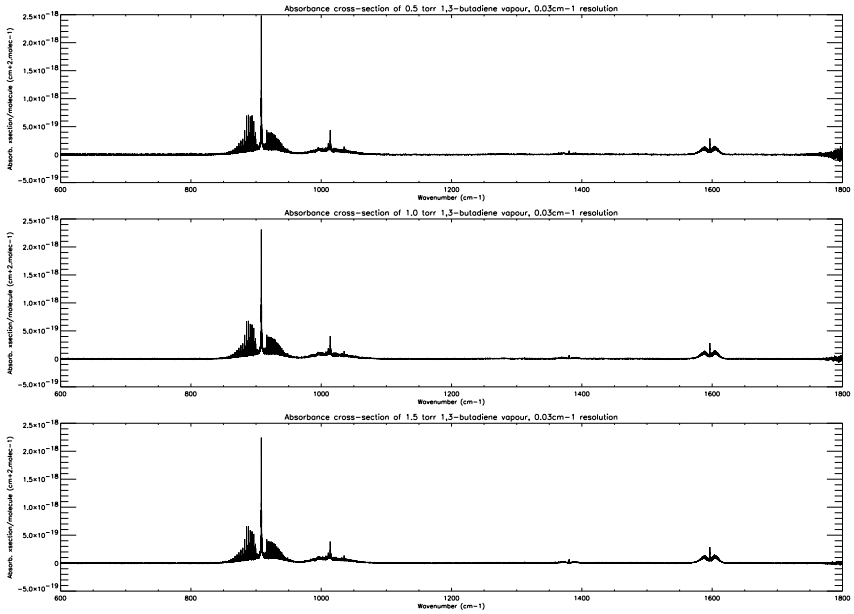

Figure 5.9: Absorption Cross-section of 1,3-butadiene in the 600 cm^{-1} to 1800 cm^{-1} region

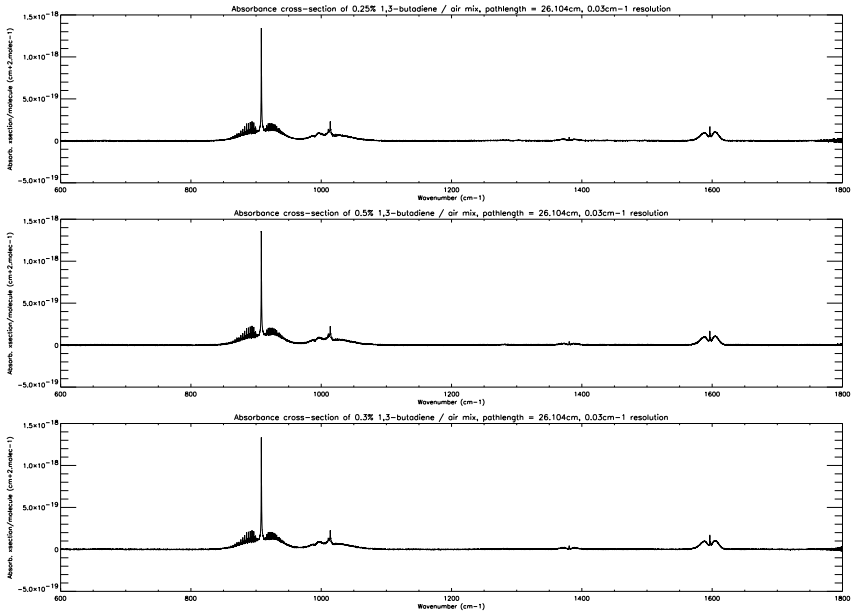

Figure 5.10: Absorption Cross-section of 1,3-butadiene in air in the 600 cm^{-1} to 1800 cm^{-1} region

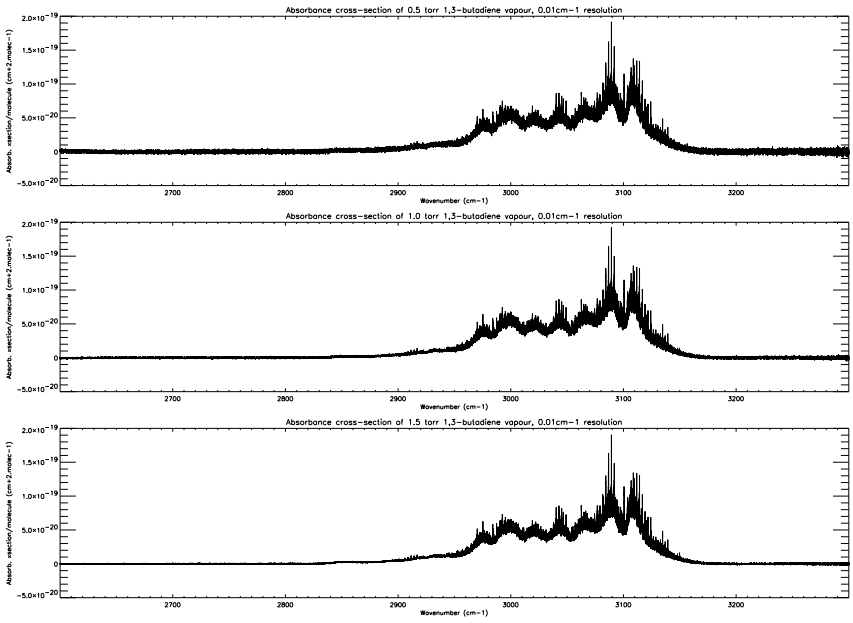

Figure 5.11: Absorption Cross-section of 1,3-butadiene in the 2600 cm^{-1} to 3300 cm^{-1} region

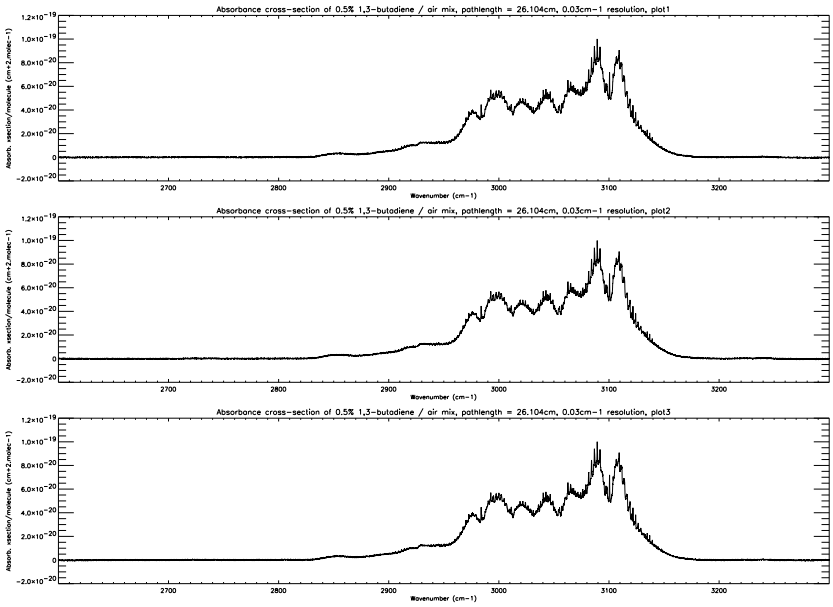

Figure 5.12: Absorption Cross-section of 1,3-butadiene in air in the 2600 cm^{-1} to 3300 cm^{-1} region

5.4 Error Analysis

The accuracy of the calculated absorption cross-sections is determined by the purity of the measured gases and by the errors in the pressure and temperature measurements, the optical pathlength and the photometric accuracy of the spectrometer. This last source of errors is the hardest to quantify. Assuming that the errors which make up the photometric accuracy are small, the overall uncertainty in the absorbance cross-sections is less than 1%.

Equation 5.2 can be re-written as follows:

$$c = \frac{10^{-6} p f}{RT} \tag{5.4}$$

where p is the total gas pressure in the absorption cell in Pa, f is the absorber (benzene, or 1,3-butadiene) gas fraction (this is 1.0 for the pure gas spectra, and equal to the partial pressure divided by the total pressure for the spectra in synthetic air), R is the molar gas constant, and T is the temperature in K.

Therefore the error in the sample concentration, σ_c can be calculated as follows:

$$\sigma_c = c\sqrt{\left(\frac{\sigma_p}{p}\right)^2 + \left(\frac{\sigma_f}{f}\right)^2 + \left(\frac{\sigma_T}{T}\right)^2} \tag{5.5}$$

where σ_p is the error in the pressure, σ_f is the error in the gas fraction or mixing ratio and σ_T is the error in the temperature.

Before the start of the measurements of benzene, the benzene Q branch and 1,3-butadiene the 10 torr and 1000 torr pressure gauges were zeroed under hard vacuum. The zero readings were then checked at the end of each set of measurements. In all 3 cases, the zero had not drifted. At the end of each of the 3 sets of measurements the pressure gauges were calibrated. This was performed by using each gauge to measure the same pressure in the vacuum line (measurements were recorded every torr over the range 0 to 10 torr; each measurement was repeated).

For the main benzene measurements, the difference between the pressure readings of the 2 gauges amounted to 1%, for 1,3-butadiene it was 0.5%. In both cases this was thought to be an overestimation of the error on the gauges, because the 1000 torr gauge is

likely to have higher percentage errors at such low pressures (since it is designed to measure pressures up to 1000 torr). However, the manufacturers stated accuracy of 0.08% of the reading was thought to be too optimistic. In both cases the 1000 torr gauge was used to measure atmospheric pressure and this reading was compared with that of an Aneroid barometer. The difference in the 2 readings was 0.12% in the benzene case and 0.21% in the 1,3-butadiene case. This was thought to be a more realistic estimate of the error in the pressure measurement. Since both the 10 torr and 1000 torr pressure gauges are of the same type and made by the same manufacturer, it was decided that the error could be applied to measurements made by either gauge.

For the benzene Q branch measurements, which were made at a later date, the difference between the 2 gauges decreased from 4% at 1.0 torr to 0.6% at 10 torr, with an averaged difference of 1.3%. For these measurements, the difference between the aneroid barometer and the 1000 torr gauge was 0.90%. In this case, the best estimate of the error in the pressure measurement was thought to be 1.3%, and this was used in the error analysis.

The rate of leakage of air into the cell and vacuum line during the recording of the background spectra was measured. This was assumed to be the same as that during the recording of the pure gas spectra; a reasonable assumption since the pressures in each case were low and the same volume was being monitored, and so was used to correct the pure gas spectra pressure measurements.

To account for the adsorption of benzene and 1,3-butadiene onto the cell's walls, pressure measurements were recorded every minute during the recording of each spectrum. The mean pressure, corrected for air leakage, was taken to be the representative pressure, p, for the measurement.

This technique could not be directly applied to the air-broadened spectra, because the total pressure, and not the partial pressure of benzene or 1,3-butadiene, was measured. Therefore, to determine whether adsorption was occurring, 3 consecutive spectra of each air-broadened mixture were recorded in the 2600 cm^{-1} to 3300 cm^{-1} spectral region (for the benzene Q branch measurements the 600 cm^{-1} to 1800 cm^{-1} region was used).

The transmittances of each set of three spectra were then compared to determine whether they increased with time, which would indicate that benzene, or 1,3-butadiene, was being adsorbed onto the gas cell's walls (thus reducing the amount of gaseous benzene, or 1,3-butadiene, available to absorb the infrared radiation of the spectrometer).

In order to quantify the change in partial pressure due to adsorption, it was assumed that the integrated absorbance cross-section is the same in the air-broadened and pure gas cases, provided that the spectra are fully resolved in each case. The correct partial pressure can then be found by multiplying the initial partial pressure (when the gas cell was filled) by the ratio of the integrated cross-section of the pure gas to that of the mixture (obtained by using the initial partial pressure). The correct absorbance cross-section can then be calculated by using the corrected partial pressure.

The error on the pressure measurements, σ_p, was taken to be 0.0012 p for the main benzene measurements, 0.0021 p for the 1,3-butadiene measurements and 0.013 p for the benzene Q branch measurements, where p is the representative pressure for the measurement (either the corrected mean pressure for the pure gas measurements, or the corrected partial pressure for the air-broadened measurements).

The error in the mixing ratio, f, depends on the purity of benzene, or 1,3-butadiene, and, in the cases of the air-broadened spectra, on the purity of the synthetic air. The error in each case was calculated from the purity values stated on the supplier's data certificates. This gave values of $\sigma_f = 0.0002f$ for pure benzene, $\sigma_f = 0.00401f$ for the benzene and air mixtures, $\sigma_f = 0.005f$ for pure 1,3-butadiene and $\sigma_f = 0.00812f$ for the 1,3-butadiene and air mixtures.

The temperature of the gas was calculated from the readings, taken every 15 seconds during the recording of each spectrum, of 8 thermistors attached to the absorption cell. The mean and standard deviation of these temperature measurements were calculated for each thermistor. These readings were then combined to give a temperature, and an error on that temperature, for each spectrum. The best estimate of the temperature is given by

the mean of the thermistor measurements, $\bar{T}$, and the error on $\bar{T}$ is σ_T, where

$$\frac{1}{\sigma_T^2} = \sum_{i=1}^{n} \frac{1}{\sigma_i^2} \tag{5.6}$$

where σ_i is the standard deviation of the temperature measurements of thermistor i.

The absorbance cross-section is given in equation 5.1. The error on the absorbance cross-section is calculated as follows:

$$\sigma_{\sigma(\tilde{\nu},T)} = \sigma(\tilde{\nu},T)\sqrt{\left(\frac{\sigma_{A_e(\tilde{\nu},T)}}{A_e(\tilde{\nu},T)}\right)^2 + \left(\frac{\sigma_c}{c}\right)^2 + \left(\frac{\sigma_l}{l}\right)^2} \tag{5.7}$$

where $\sigma_{A_e(\tilde{\nu},T)}$ is the error on the napierian absorbance, $A_e(\tilde{\nu},T) = -\ln[\tau_c(\tilde{\nu},T)]$, σ_l is the error on the optical pathlength l (in cm) and σ_c is the error in the sample concentration as defined by equation 5.5.

The error on napierian absorbance depends on the photometric accuracy of the spectrometer, the signal-to-noise ratio (SNR) of the transmittance spectra and errors in the 100% transmittance level (due to imperfect ratioing of the sample and background spectra). The latter were corrected for in the transmittance spectra themselves, before the absorbance cross-sections were calculated from them. The SNR of the transmittance spectra was calculated after the spectra were corrected for any errors in the 100% transmittance level. The SNR of each transmittance spectrum was defined as the mean value of the standard deviation of spectral points in fully-transmitting spectral regions.

The photometric accuracy of the spectrometer refers to the accuracy of the x-scale (wavenumber / wavelength) and the y-scale (signal / transmittance / absorbance) measured by the spectrometer, as compared to the 'true' values that would be measured by an ideal instrument. It is affected by many instrument factors, such as the non-linearity of detectors, sample emission, self-emission, channelling, fluctuations in the intensity of the source, and calibration of the wavelength of the spectrometer's HeNe laser (used to determine the wavenumber scale). Where possible these effects have been eliminated or minimised through optimising the setup of the spectrometer for each set of measurements and through regular calibration of the spectrometer, using measurements of both a wavelength standard and an infrared transmittance standard, by staff at the MSF.

Two major sources of error are the non-linearity of detectors and measuring at an inadequate spectral resolution. The former was eliminated[4] by reducing the light intensity reaching the detector through using an optical filter and a small aperture. The latter leads to under-resolving of spectral features and consequent errors in the absorbance cross-section. Errors in the pure-gas absorbance cross-section due to inadequate spectral resolution would be propagated to the air-broadened cross-sections, since the pure-gas integrated absorbance cross-sections were used to correct for the effects of adsorption of benzene, or 1,3-butadiene, on the air-broadened spectra. In order to eliminate these errors, survey spectra were recorded at a range of resolutions in order to determine the resolution which just fully resolved the spectral lines of each gas in each spectral region.

Assuming good photometric accuracy, the SNR of the transmittance spectra was used as the best estimate of the error on the napierian absorbance. The noise on the transmittance spectra varied between 0.0004 and 0.001 in the 2600 cm^{-1} to 3300 cm^{-1} region, between 0.001 to 0.01 in the 600 cm^{-1} to 1800 cm^{-1} region, and between 0.0006 and 0.0007 in the 600 cm^{-1} to 1300 cm^{-1} region.

The error on the optical pathlength, σ_l, was $\pm$ 0.0024 cm on the 26.1040 cm pathlength gas cell, and $\pm$ 0.01 cm on the 5.12 cm pathlength cell. This is purely the error on the length of the gas cell. There is also an error due to beam divergence, such that not all rays travel the same distance through the sample. However, this error has not been quantified.

The overall error on the absorbance cross-sections, assuming good photometric accuracy, is $\pm$ 2% for the benzene Q branch cross-sections, $\pm$ 1% for the main benzene cross-sections and $\pm$ 1% for the 1,3-butadiene cross-sections.

5.5 Detection

An annual report on the levels of air pollution monitored around the UK is published by NETCEN at the request of the Department of the Environment, Transport and the Regions

[4]This was indicated by the lack of signal outside the limits of the optical filter in any of the measured spectra.

(Bower, Broughton & Willis 1995). The 1997 edition is available on the world-wide-web at: <http://www.aeat.co.uk/netcen/report96/>.
This includes an archive of the annual statistics of benzene and 1,3-butadiene for the years 1993 (1994 for 1,3-butadiene) to 1997 inclusive, with the data reported by measuring site.

Of the sites that monitor benzene and 1,3-butadiene, the ones that are relevant to this study are those described as 'Urban Background' or 'Urban Centre' (8 sites) and 'Roadside' or 'Kerbside' (2 sites). The former pair have relevance for measurements made in the University Science Area, and the latter pair have relevance for the field measurements made by busy roads in Oxford.

5.5.1 Benzene

For benzene, the mean hourly concentration at the 'Urban Background' and 'Urban Centre' sites is 1.5 ppbv, with a standard deviation of 2.3, and a maximum hourly concentration of 53.1 ppbv (which occurred on 15/1/1997 at Southampton Centre). The mean and standard deviation are similar for the 'Roadside' site at London UCL. The 'Kerbside' site, at London Marylebone Road, only came into operation in August 1997 and so only limited data is available. For this site, the mean hourly concentration is 5.0 ppbv, with a maximum hourly concentration of 15.9 ppbv (which occurred on 8/10/1997).

Using the absorption cross-sections measured at RAL, benzene detection limits for the equipment used in this study have been calculated. The main band of benzene lies below the low wavenumber cut-off wavenumber of the MCT detector (which is 700 cm^{-1}). Therefore, in order to detect benzene in this region the TGS detector, which has a lower signal-to-noise ratio (SNR) than the MCT detector, must be used. The SNR of the TGS detector in the 670 cm^{-1} to 680 cm^{-1} region is 53 for 6 co-added scans. Another factor which must be considered if using this region to detect benzene, is that the main band of carbon dioxide is located at 671 cm^{-1}. Carbon dioxide is strongly absorbing in this region and transmission by 360 ppmv[5] CO_2 at 674 cm^{-1} decreases to 3% by 100 m. However,

[5]Current accepted value for the atmospheric concentration of CO_2 at ground level.

for optical pathlengths less than about 100 m, it is possible to use this region to detect benzene. The detection limits are given in table 5.1.

Table 5.1: Detection Limits for Benzene in the 670 cm^{-1} to 680 cm^{-1} region.

Pathlength (m)	Minimum detection limit (ppbv)
10	325
25	100
50	144
75	175
100	275

When these values are compared with the concentrations measured by NETCEN, it can be seen that the detection limits are above the maximum hourly concentration measured in the period 1993 to 1997 inclusive. A detector with a higher SNR in the 670 cm^{-1} to 680 cm^{-1} region would lower these detection limits. MCT detectors which are sensitive to this region do exist, but were not available for this study. Since the NETCEN hourly averages are based on analysis of air samples collected over 30 minutes in each hour (Bower, Broughton & Willis 1995), it is probable that peak levels of benzene are greater than reported. The SNR given for the TGS detector in this region is for 6 co-added scans, which take 6 minutes to record. Therefore it is likely that the maximum concentrations of benzene detectable, in principle, by FTIR spectroscopy will be greater than those measured by NETCEN. The combination of these two factors indicate that it might be possible to use the 670 cm^{-1} to 680 cm^{-1} region to detect benzene, but not in this study.

The secondary benzene band lies in the region 3020 cm^{-1} to 3120 cm^{-1}, which lies within the region that the MCT detector is sensitive to. The SNR of the MCT detector in this region is 175 for 16 co-added scans (which take a minute and a half to record) and that for the TGS detector is 53 for 6 co-added scans (which take six minutes to record). The other, contaminant, gases in the 3020 cm^{-1} to 3120 cm^{-1} region are water and methane. For the detection limit calculations 7745 ppmv of water and 1.7 ppmv of methane[6] were

[6]These are the accepted 'US Standard Atmosphere' concentrations at ground level.

included in the spectra, and were retrieved. The detection limits are given in table 5.2.

Table 5.2: Detection Limits for Benzene in the 3020 cm^{-1} to 3120 cm^{-1} region.

Pathlength (m)	Minimum detection limit (ppbv)
100	72
250	1.5
400	0.1

When these values are compared with the concentrations measured by NETCEN, it can be seen that a pathlength of 400 m is needed before useful measurements can be made. An interesting comparison can be made between the detection limits at 100 m for the two spectral regions. Although the secondary band of benzene, in the 3020 cm^{-1} to 3120 cm^{-1} region, is sixty times weaker than the main benzene band, in the 670 cm^{-1} to 680 cm^{-1} region, the detection limit for benzene is less than four times smaller in the 3020 cm^{-1} to 3120 cm^{-1} region than in the 670 cm^{-1} to 680 cm^{-1} region, because the 670 cm^{-1} to 680 cm^{-1} region is nearly obscured by CO_2 over a 100 m pathlength.

5.5.2 1,3-Butadiene

For 1,3-butadiene, the mean hourly concentration at the 'Urban Background' and 'Urban Centre' sites, as recorded by NETCEN, is 0.22 ppbv, with a standard deviation of 2.1, and a maximum hourly concentration of 29.0 ppbv (which occurred on 20/11/1996 at Liverpool Speke). The mean hourly concentration at the 'Roadside' site at London UCL is 0.4 ppbv, with a standard deviation of 2.1, and a maximum hourly concentration of 8.8 ppbv (on 13/2/1994). The 'Kerbside' site, at London Marylebone Road, only came into operation in August 1997 and so only limited data are available. For this site, the mean hourly concentration is 1.5 ppbv, with a maximum hourly concentration of 4.7 ppbv (which occurred on 8/10/1997).

The main 1,3-butadiene band lies in the region 870 cm^{-1} to 950 cm^{-1}, which lies within the region that the MCT detector is sensitive to. The SNR of the MCT detector in this region is 175 for 16 co-added scans. Water is the only other main contaminant gas in

this region. For the detection limit calculations 7745 ppmv of water was included in the spectra, and was retrieved. The detection limits are given in table 5.3.

Table 5.3: Detection Limits for 1,3-Butadiene in the 870 cm^{-1} to 950 cm^{-1} region.

Pathlength (m)	Minimum detection limit (ppbv)
50	116
100	35
250	3
400	0.1

When these values are compared with the concentrations measured by NETCEN, it can be seen that a pathlength of 400 m is needed before useful measurements of the concentration of 1,3-butadiene can be made. Since the NETCEN hourly averages are based on analysis of air samples collected over 30 minutes in each hour (Bower, Broughton & Willis 1995), it is probable that concentrations of 1,3-butadiene measured by FTIR spectroscopy will be greater than those measured by NETCEN due to the shorter measuring times[7].

Given the detection limits for benzene and 1,3-butadiene, and the optical pathlengths that it was possible to use in this study, it is unsurprising that no benzene or 1,3-butadiene was detected in any of the spectra recorded during the period of this study.

[7]It takes less than 2 minutes to record 16 co-added scans with the MCT detector.

Chapter 6

Results

6.1 Detection Limits

Detection limits have been calculated for the gases included in the National Air Quality Strategy (CO, SO_2, NO_2, O_3, benzene and 1,3-butadiene) and for three other gaseous pollutants which are regularly retrieved (NO, N_2O, and CH_4). The calculated detection limits are compared with the levels of air pollution monitored around the UK by the National Environmental Technology Centre (NETCEN)[1] and published in their annual report (Bower, Broughton & Willis 1995). The 1997 edition is available on the world-wide-web at:
<http://www.aeat.co.uk/netcen/report96/>.
and the pollutant concentrations used for comparison came from this edition.

NETCEN runs three automated monitoring networks - the Automatic Urban Network (AUN), the Automated Rural Network (ARN) and the Hydrocarbon Network. The AUN monitors SO_2, NO_x, CO, O_3 and particulate matter (PM_{10}) at a range of urban locations. These are classified as 'Urban Background', 'Urban Centre', 'Roadside', 'Urban Industrial', and 'Suburban'. Only data from sites classified as one of the first three types are relevant for comparison with measurements in this study. The Hydrocarbon Network monitors 25 volatile organic compounds (VOCs) including benzene and 1,3-butadiene at 'Urban Background', 'Roadside' and 'Rural' locations across the country. The detection limits for benzene and 1,3-butadiene were compared with data from this network in section 5.5.

[1] NETCEN is part of AEA Technology and undertakes national monitoring of air pollution in the UK on behalf of the Department of the Environment, Transport and the Regions.

The standard definition of the detection limit is 'a signal to noise of one'. That is that the random measurement error on the gas concentration is equal to the concentration of the gas. The random measurement error for an optimal estimation retrieval is $\mathbf{D_y S_y D_y^T}$ (see section 4.3). Since the random measurement error does not depend on the gas concentration (retrieved or true), the detection limit can be determined from any retrieval of the gas in question from any spectrum recorded under the required conditions (path length, detector, source, number of scans etc.).

If the natural logarithm of the gas concentration is retrieved (as it is in this study), rather than the concentration itself, then determining the detection limit is more complicated. The detection limit is still that the error on the gas concentration is equal to the concentration of the gas, which corresponds to a 100% random measurement error on the retrieved variable, $\hat{\mathbf{x}}$. However, the estimated random measurement error, $\mathbf{D_y S_y D_y^T}$, now depends on the retrieved gas concentration, and so the detection limit must be determined iteratively from a series of synthetic spectra with the appropriate level of random noise, gain and offset[2] applied to the spectrum, and then apodised with the instrument line shape. The detection limits given in this section were calculated in this manner.

Gaseous absorption varies with the concentration of the gas concerned and of any contaminant gases with absorptions in the relevant spectral region and with significant optical pathlength. Variations in atmospheric temperature and pressure affect the line shape of absorption lines, and thus, indirectly, the level of absorption.

If scattering and emission are neglected, then

$$A = 1 - \tau$$

where A is absorption and τ is transmission. Now,

$$\tau = \exp\left\{-\int \rho k_{\tilde{\nu}}\, dl\right\} \tag{6.1}$$

where ρ is absorber density, l is optical pathlength and $k_{\tilde{\nu}} = Sg(\tilde{\nu} - \tilde{\nu}_0)$ is the absorption coefficient. S is the line strength and $g(\tilde{\nu} - \tilde{\nu}_0)$ is the line shape. For a homogeneous path,

[2] (see section 4.6)

such as those included in this study, neither ρ nor $k_{\tilde{\nu}}$ is a function of optical pathlength. Therefore, the expression for τ can be re-written as follows.

$$\tau = \exp\left(-\rho k_{\tilde{\nu}} l\right)$$

From the above equation it can be seen that increasing the optical pathlength will increase the absorption and thus the detectability of a pollutant gas. However, in certain cases absorption by contaminant species can reach 100% within a short optical pathlength (less than 200 m), thus limiting detectability of the pollutant gas in that particular spectral region. When this occurs in the main absorption band of a pollutant gas, it may be more expedient to use a shorter optical pathlength and utilize the main absorption band, rather than a weaker absorption band at a much longer pathlength (typically 500 m to 1 km).

6.1.1 Carbon Monoxide (CO)

Carbon monoxide (CO) is a naturally occurring trace gas in the atmosphere with a background concentration of 0.15 ppmv in the northern mid-latitudes. In the urban atmosphere 90% of emissions emanate from motor vehicles. NETCEN measures CO concentrations by gas filter correlation (infra red absorption) with an accuracy of ± 8% and a precision of ± 0.6 ppmv. Concentrations of CO measured by NETCEN in 1997 are given in table 6.1.

Table 6.1: CO concentrations recorded by NETCEN in 1997

Site type	Number of sites	Mean Hourly concentration (ppmv)†	Standard Deviation	Maximum Hourly Concentration		
				Amount (ppmv)	Date	Location
Urban Background	9	0.6	2.2	12.2	11/11/1997	London Brent
Urban Centre	18	0.6	2.1	18.5	15/01/1997	Southampton Centre
Roadside	12	1.4	2.2	27.6	14/01/1997	Exeter Roadside

† This is the mean for all sites of the given type for the entire year.

The main band of CO is in the region 2120 cm^{-1} to 2220 cm^{-1} (see figure 6.1). The

two main contaminant species in the region are water vapour (see figure 6.2) and N_2O (see figure 6.3). However, the absorption of both these species is such that the region can still

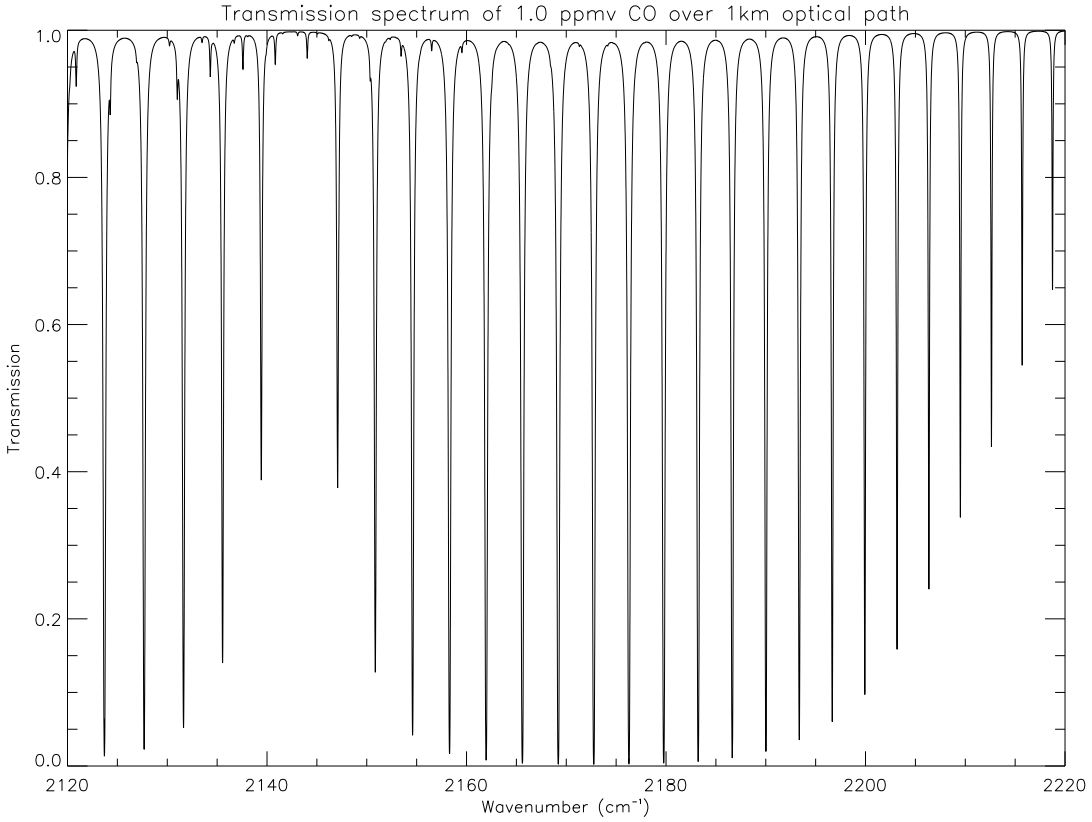

Figure 6.1: Transmission spectrum of CO (no contaminants included) in the spectral region 2120 cm^{-1} to 2220 cm^{-1}.

be used to detect CO at optical pathlengths greater than 1 km.

For the detection limit calculations 0.32 ppmv N_2O and 7745 ppmv of water vapour[3] were included in the spectra, and were jointly retrieved with CO. The level of random noise used in the spectra was 0.0055, since the signal-to-noise ratio (SNR) of the MCT detector in both spectral regions is 180 for 16 co-added scans (which take a minute and a half to record).

The calculations show that the detection limit for CO over an optical path of 50 m is 0.005 ppmv (5 ppbv). This value is 170 times less than the mean hourly concentrations

[3]These are the accepted 'US Standard Atmosphere' concentrations at ground level at mid-latitudes.

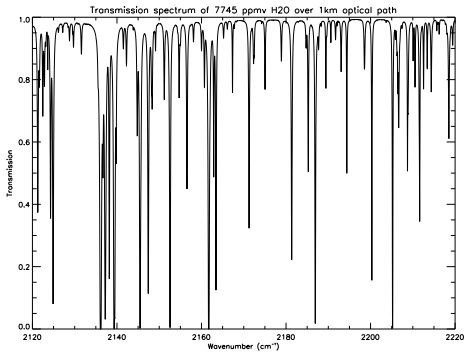

Figure 6.2: Transmission spectrum of H_2O in the spectral region of the main CO band, 2120 cm^{-1} to 2220 cm^{-1}.

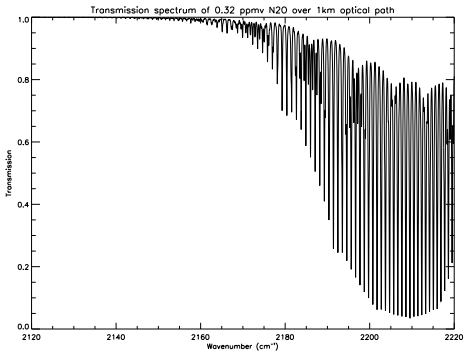

Figure 6.3: Transmission spectrum of N_2O in the spectral region of the main CO band, 2120 cm^{-1} to 2220 cm^{-1}.

recorded by NETCEN. It is also 30 times less than the concentration of CO in unpolluted air (0.15 ppmv).

6.1.2 Sulphur Dioxide (SO_2)

The main sources of sulphur dioxide (SO_2) are anthropogenic, in the UK this is mainly the burning of fossil fuels at power stations and in industry. SO_2 is also produced naturally through volcanic eruptions and oxidation of H_2S. NETCEN measures SO_2 concentrations using UV fluorescence with an accuracy of ± 10% and a precision of ± 1.2 ppbv. Concentrations of SO_2 measured by NETCEN in 1997 are given in table 6.2.

Table 6.2: SO_2 concentrations recorded by NETCEN in 1997

Site type	Number of sites	Mean Hourly concentration (ppbv)†	Maximum Hourly Concentration		
			Amount (ppbv)	Date	Location
Urban Background	13	5.0	159	31/01/1997	Barnsley 12
Urban Centre	20	5.4	242	11/07/1997	Leeds Centre
Roadside	5	8.2	108	31/01/1997	BuryRoadside

† This is the mean for all sites of the given type for the entire year.

The main band of SO_2 is located in the region 1240 cm^{-1} to 1340cm^{-1} (see figure

6.4). The two main contaminant species in the region are water vapour (see figure 6.5) and CH_4 (see figure 6.6); the water vapour absorption is fairly strong in this spectral interval.

Over a 1 km optical pathlength the transmittance of H_2O is less than 70% for a low

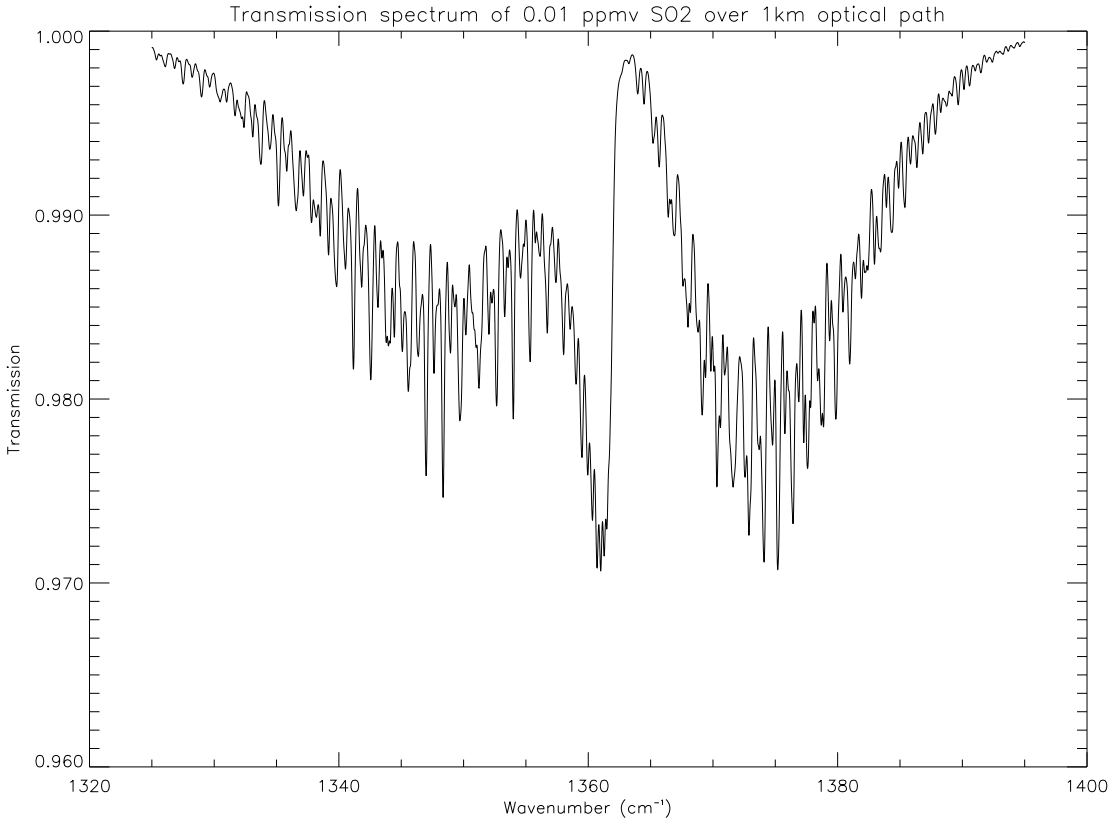

Figure 6.4: Transmission spectrum of SO_2 (no contaminants included) in the spectral region 1240 cm^{-1} to 1340cm^{-1}.

concentration of water vapour (4370 ppmv[4]), less than 50% for a 'standard' concentration of water vapour (7745 ppmv[5]) and less than 30% for a high concentration of water vapour (13200 ppmv[6]). Although some parts of the spectral region are obscured by water vapour at 1km, it is still possible to detect SO_2 at levels below 5 ppbv.

For the detection limit calculations 7745 ppmv of water vapour and 1.7 ppmv of

[4]Lowest concentration of H_2O measured by the equipment used in this study. Measured on 10/2/00 in Oxford University's science area.

[5]This is the accepted 'US Standard Atmosphere' concentrations at ground level at mid-latitudes.

[6]Highest concentration of H_2O measured by the equipment used in this study. Measured on 8/10/99.

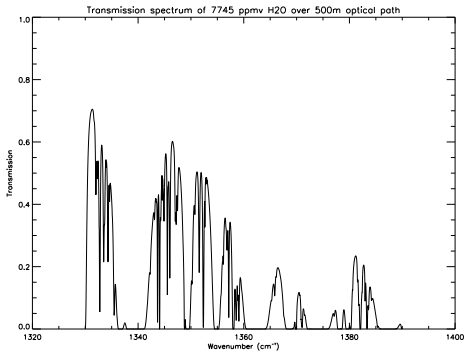

Figure 6.5: Transmission spectrum of H_2O in the spectral region of the main SO_2 band, 1240 cm^{-1} to 1340cm^{-1}.

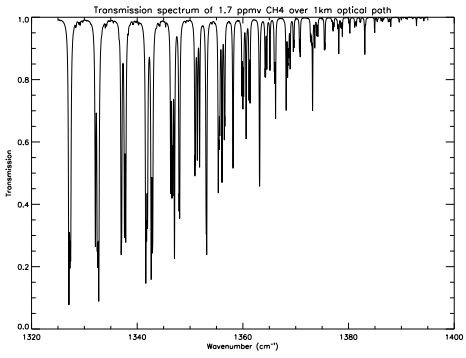

Figure 6.6: Transmission spectrum of CH_4 in the spectral region of the main SO_2 band, 1240 cm^{-1} to 1340cm^{-1}.

methane[7] were included in the spectra, and were retrieved. The level of random noise used in the spectra was 0.0055, since the signal-to-noise ratio (SNR) of the MCT detector in both spectral regions is 180 for 16 co-added scans. The detection limits are given in table 6.3. When these values are compared with the concentrations measured by NETCEN, it can be seen that the mean hourly concentrations of SO_2 can be measured with pathlengths under 100 m.

Table 6.3: Detection limits for SO_2

Pathlength in m	Detection limit in ppbv
50	5.0
100	2.0

6.1.3 Nitrogen Dioxide (NO_2)

Nitrogen dioxide is an important precursor of photochemical smog. There are several natural sources including lightning and forest fires. However, the main source of NO_2 in the UK is combustion of fossil fuels in motor vehicles and power stations. NO_2 is also formed by the oxidation of NO. NETCEN measures NO_2 concentrations nationally using ozone chemiluminescence, which is the reference method specified by the EC NO_2

[7]These are the accepted 'US Standard Atmosphere' concentrations at ground level at mid-latitudes.

Directive. The accuracy of these measurements is ± 10% - 11% and the precision is ± 3.5 ppbv. Concentrations of NO_2 measured by NETCEN in 1997 are given in table 6.4.

Table 6.4: NO_2 concentrations recorded by NETCEN in 1997

Site type	Number of sites	Mean Hourly concentration (ppbv)†	Standard Deviation	Maximum Hourly Concentration		
				Amount (ppbv)	Date	Location
Urban Background	15	22.7	2.0	215	31/10/1997	West London
Urban Centre	20	23.7	1.9	249	31/10/1997	London Southwark
Roadside	13	33.5	1.8	227	31/10/1997	Camden Roadside

† This is the mean for all sites of the given type for the entire year.

The main band of nitrogen dioxide is located between 1560 cm^{-1} and 1660 cm^{-1} (see figure 6.7), which coincides with a region of absorption by water vapour. Over a 200 m optical pathlength the transmittance of H_2O is less than 38% for 4370 ppmv H_2O, less than 17% for 7745 ppmv H_2O, and less than 5% for 13200 ppmv H_2O. Over a 500 m optical pathlength the transmittance of H_2O is less than 9% for 4370 ppmv H_2O, less than 2% for 7745 ppmv H_2O, and with 13200 ppmv H_2O the region is completely obscured.

The secondary band of NO_2 lies in the spectral region 2850 cm^{-1} to 2940 cm^{-1} (see figure 6.8) and is ten times weaker than the main band. However, the absorption by water vapour in this region is also weaker (see figure 6.9), and the maximum absorption of any methane line in the region is 94% (see figure 6.10), thus this region can be used for detection of NO_2.

The detection limits for both bands of NO_2 are given in table 6.5. For the detection limit calculations 7745 ppmv of water and, for the spectral region 2850 cm^{-1} to 2940 cm^{-1} only, 1.7 ppmv of methane[8] were included in the spectra, and were retrieved. The level of random noise used in the spectra was 0.0055, since the signal-to-noise ratio (SNR) of the

[8]These are the accepted 'US Standard Atmosphere' concentrations at ground level at mid-latitudes.

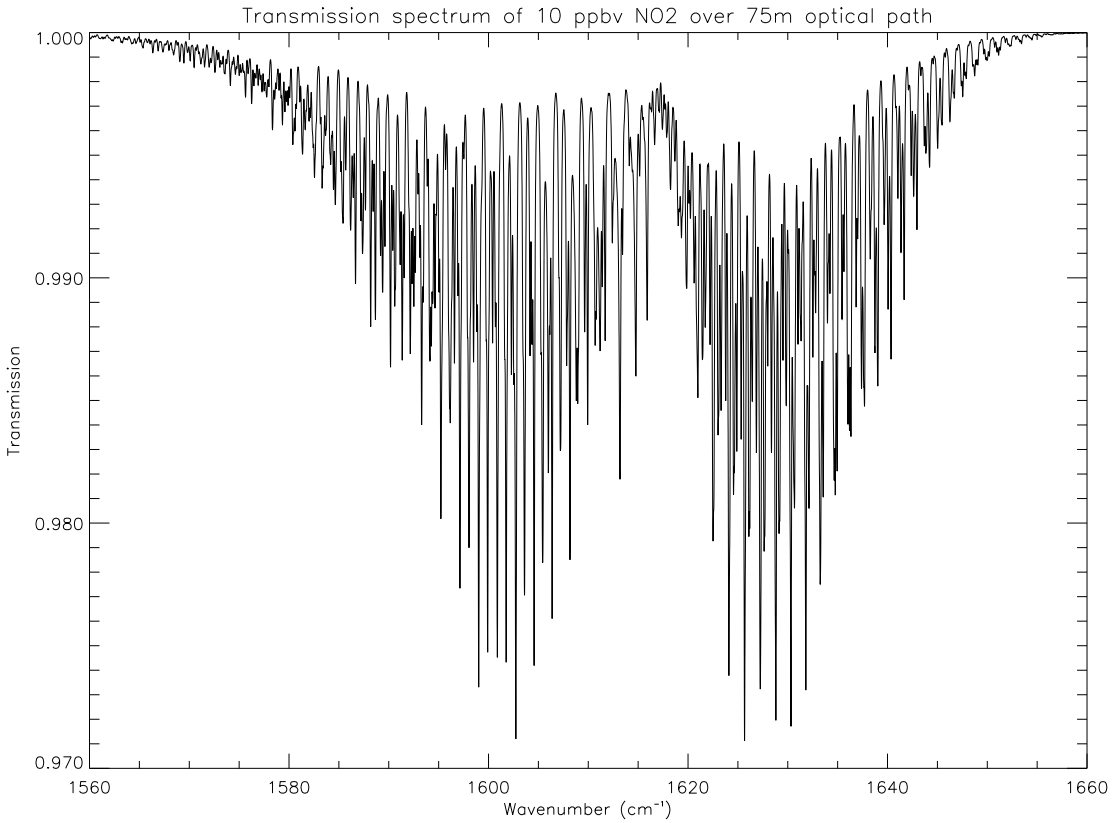

Figure 6.7: Transmission spectrum of NO_2 only (no contaminants included) in the spectral region 1560 cm^{-1} to 1660 cm^{-1}.

MCT detector in both spectral regions is 180 for 16 co-added scans. The table shows that the optimum optical pathlength for NO_2 detection in the 1560 cm^{-1} to 1660 cm^{-1} spectral region is approximately 75 m. A pathlength of over 200 m in the 2850 cm^{-1} to 2940 cm^{-1} spectral region is required to obtain a similar detection limit. Therefore, the 1560 cm^{-1} to 1660 cm^{-1} spectral region and a pathlength of less than 100 m have been used to detect NO_2 in the field measurements carried out in this study.

When these values are compared with the concentrations measured by NETCEN, it can be seen that the mean hourly concentrations of NO_2 could be detected using the 1560 cm^{-1} to 1660 cm^{-1} spectral region at pathlengths up to and including 200 m, and from 100 m using the 2850 cm^{-1} to 2940 cm^{-1} spectral region.

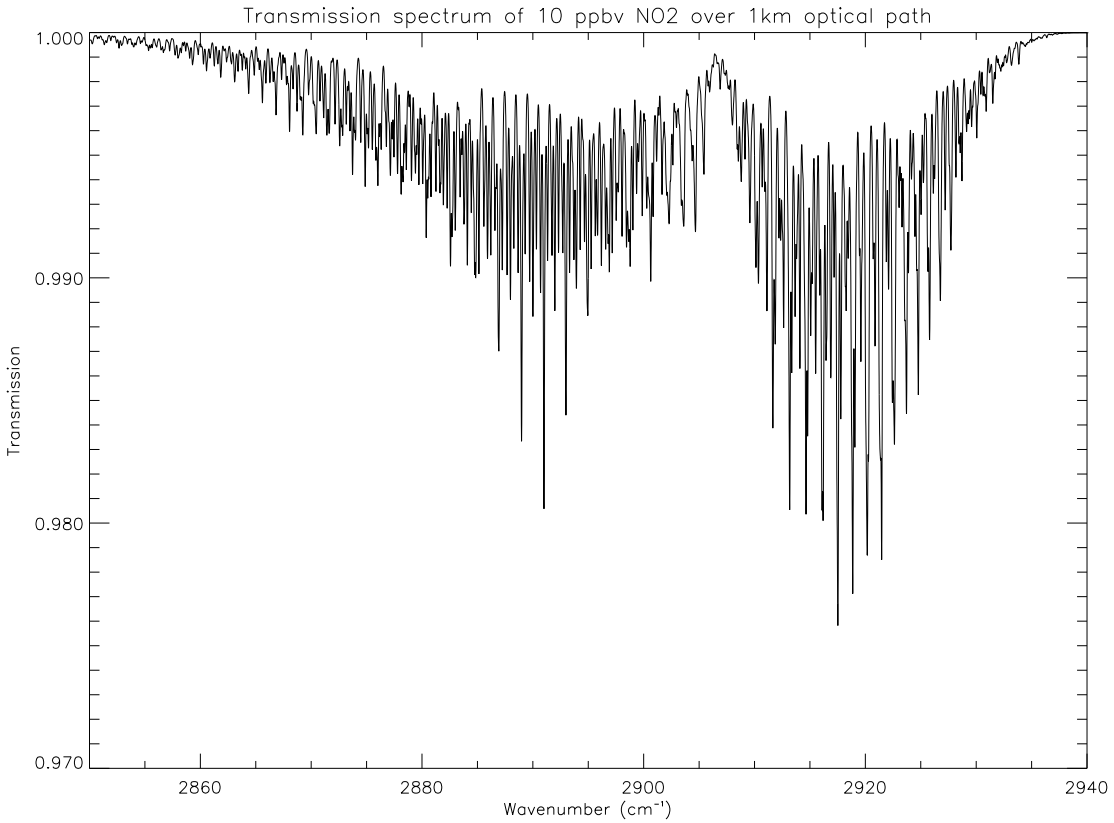

Figure 6.8: Transmission spectrum of NO_2 only (no contaminants included) in the spectral region 2850 cm^{-1} to 2940 cm^{-1}.

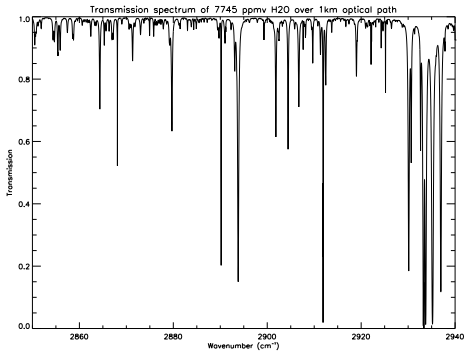

Figure 6.9: Transmission spectrum of H_2O in the spectral region of the secondary band of NO_2, 2850 cm^{-1} to 2940 cm^{-1}.

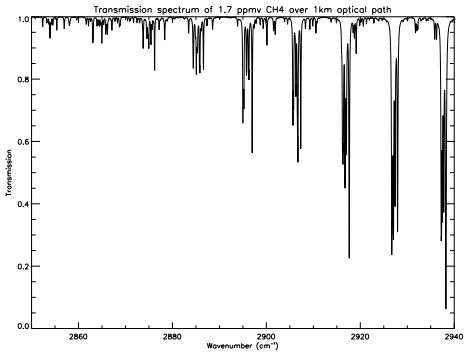

Figure 6.10: Transmission spectrum of CH_4 in the spectral region of the secondary band of NO_2, 2850 cm^{-1} to 2940 cm^{-1}.

Table 6.5: Detection limits for NO_2

	Detection limits in ppbv in region:	
Pathlength/m	1560 cm^{-1} to 1660 cm^{-1}	2850 cm^{-1} to 2940 cm^{-1}
50	4.4	-
75	4.1	9.8
100	6.0	6.8
200	6.5	4.9
500	-	2.7

6.1.4 Ozone (O_3)

Ozone in the urban boundary layer is a secondary pollutant formed by photochemical reactions between oxides of nitrogen and hydrocarbons. NETCEN measures O_3 concentrations by UV absorption, with an accuracy of ± 11% and a precision of ± 2 ppbv. Concentrations of O_3 measured by NETCEN in 1997 are given in table 6.6.

Table 6.6: O_3 concentrations recorded by NETCEN in 1997

Site type	Number of sites	Mean Hourly concentration (ppbv)†	Standard Deviation	Maximum Hourly Concentration		
				Amount (ppbv)	Date	Location
Urban Background	10	15.4	2.9	116	10/08/1997	Leamington Spa
Urban Centre	22	14.5	2.7	100	10/08/1997	London Haringey and London Southwark
Roadside	3	12	2.2	86	10/06/1997	Exeter Roadside

† This is the mean for all sites of the given type for the entire year.

The main band of O_3 is located in the region 980 cm^{-1} to 1070 cm^{-1} (see figure 6.11). The two main contaminant species in the region are water vapour (see figure 6.12) and CO_2 (see figure 6.13). Both species have only weak absorption in the region, although this is greater than that of O_3 for typical concentrations of all three species.

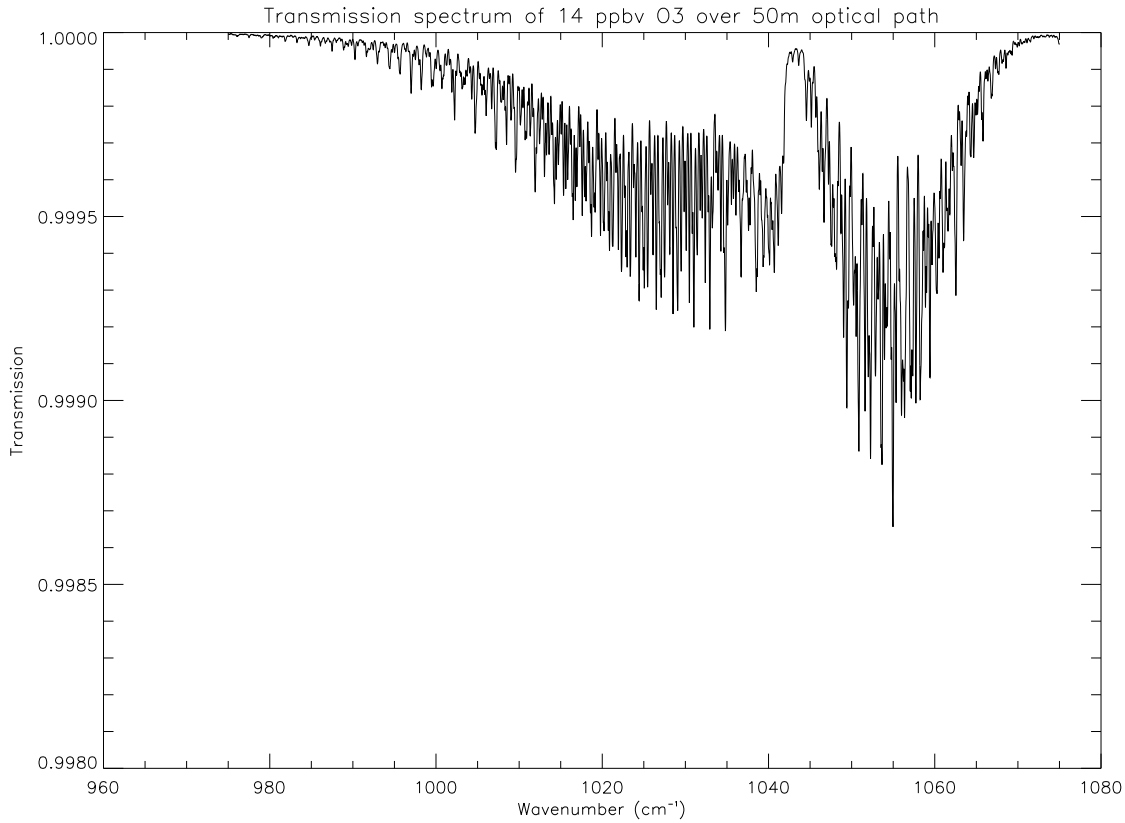

Figure 6.11: Transmission spectrum of O_3 (no contaminants included) in the spectral region 980 cm^{-1} to 1070 cm^{-1}.

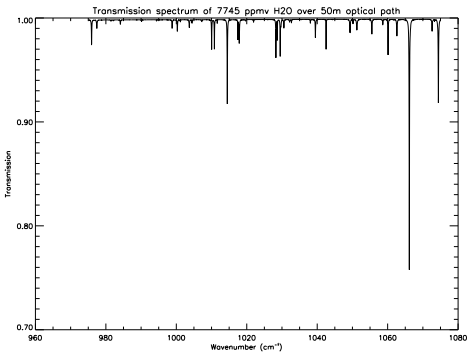

Figure 6.12: Transmission spectrum of H_2O in the spectral region of the main O_3 band, 980 cm^{-1} to 1070 cm^{-1}.

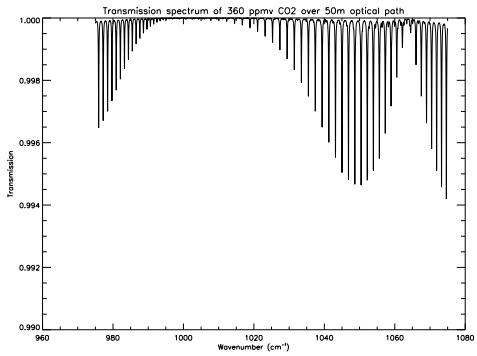

Figure 6.13: Transmission spectrum of CO_2 in the spectral region of the main O_3 band, 980 cm^{-1} to 1070 cm^{-1}.

For the detection limit calculations 360 ppmv CO_2 and 7745 ppmv of water vapour[9]

[9]These are the accepted 'US Standard Atmosphere' concentrations at ground level at mid-latitudes. The

were included in the spectra, and were jointly retrieved with O_3. The level of random noise used in the spectra was 0.025, since channelling in the region increases the noise level from 0.0055, which it is elsewhere in the spectrum when the MCT detector and 16 co-added scans are used. The detection limits are given in table 6.7. When these values are compared with the concentrations measured by NETCEN, it can be seen that the mean hourly concentrations of O_3 can be measured with pathlengths around 100 m.

Table 6.7: Detection limits for O_3

Pathlength in m	Detection limit in ppbv
50	20
100	5
200	1.8

6.1.5 Benzene

The detection limits for benzene were discussed extensively in section 5.5.1. It was shown that it is necessary to use the secondary band of benzene, in the 3020 cm^{-1} to 3120 cm^{-1} region, and pathlengths of 400 m before useful measurements of benzene concentrations can be made.

6.1.6 1,3-Butadiene

The detection limits for benzene were discussed extensively in section 5.5.2. It was shown that it is necessary to use a pathlength of 400 m before useful measurements of 1,3-butadiene concentrations can be made.

6.1.7 Nitric Oxide (NO)

Natural sources of nitric oxide include lightning, forest fires and bacterial activity in soils. However, the main source of NO in the UK is the combustion of fossil fuels in motor vehicles and power stations. NETCEN does not currently measure concentrations of nitric oxide (NO). Instead it measures nitrogen dioxide (NO_2) and nitrogen oxides (NO_x), which is

CO_2 concentration is for 1995.

the sum of the concentrations of nitric oxide (NO) and nitrogen dioxide (NO_2). NETCEN measures NO_x using ozone chemiluminescence, which is the reference method specified by the EC NO_2 Directive. The accuracy of these measurements is ± 10% and the precision is ± 2.5 ppbv. Concentrations of NO_x measured by NETCEN in 1997 are given in table 6.8.

Table 6.8: NO_x concentrations recorded by NETCEN in 1997

Site type	Number of sites	Mean Hourly concentration (ppbv)†	Standard Deviation	Maximum Hourly Concentration		
				Amount (ppbv)	Date	Location
Urban Background	15	51.7	2.5	1098	31/10/1997	West London
Urban Centre	20	57.9	2.3	1191	15/01/1997	Southampton Centre
Roadside	13	137.9	2.5	1470	31/10/1997	Camden Roadside

† This is the mean for all sites of the given type for the entire year.

The main band of nitric oxide is located between 1825 cm^{-1} and 1925 cm^{-1} (see figure 6.14). The main contaminant species in the region is water vapour (see figure 6.14). The water vapour absorption is fairly strong. Over a 1 km optical pathlength the transmittance of H_2O is less than 65% for 4370 ppmv H_2O, less than 45% for 7745 ppmv H_2O, and less than 25% for 13200 ppmv H_2O. Although some parts of the spectral region are obscured by water vapour at 1km, it is still possible to detect NO at levels below 5 ppbv.

For the detection limit calculations 7745 ppmv of water vapour[10] was included in the spectra, and was jointly retrieved with NO. The level of random noise used in the spectra was 0.0055, since the signal-to-noise ratio (SNR) of the MCT detector in both spectral regions is 180 for 16 co-added scans. The detection limits are given in table 6.9. When these values are compared with the concentrations of NO_2 and NO_x measured by NETCEN, it can be seen that the mean hourly concentrations of NO, which are approximately 30 ppbv for the 'Urban' sites and approximately 100 ppbv for the 'Roadside' sites, can be measured

[10]This is the accepted 'US Standard Atmosphere' concentration at ground level at mid-latitudes.

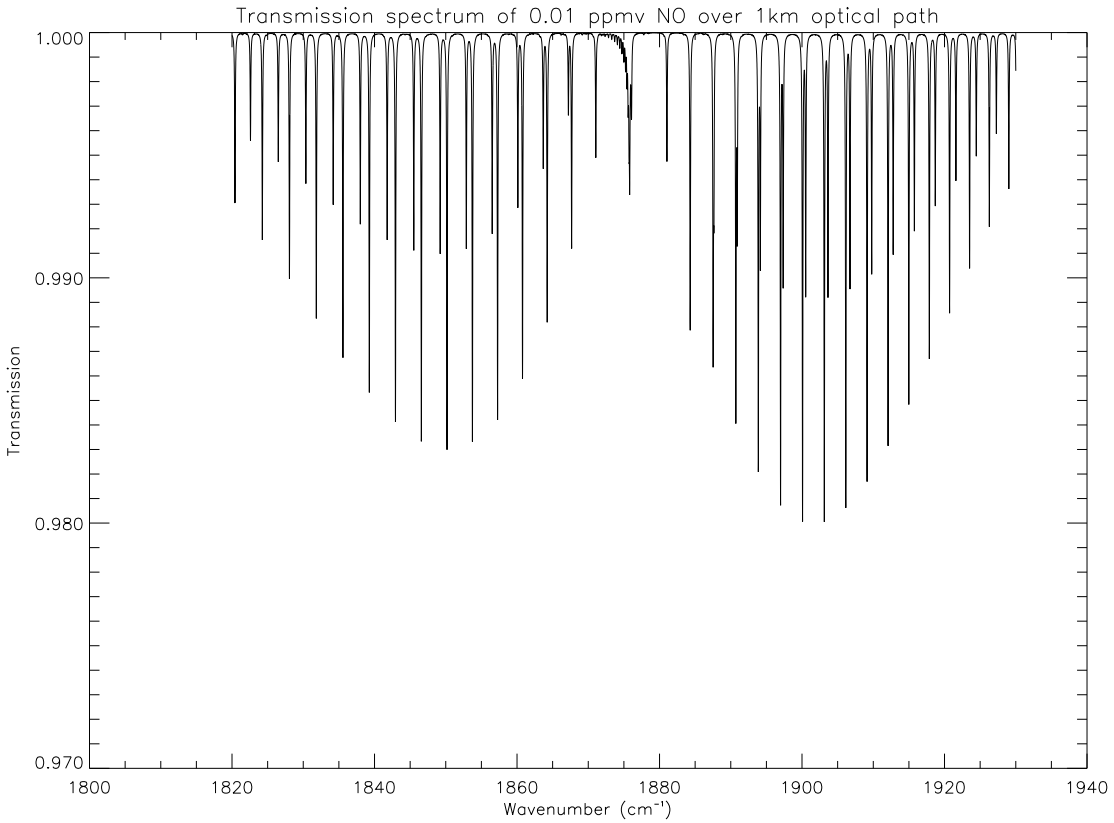

Figure 6.14: Transmission spectrum of NO only (no contaminants included) in the spectral region 1825 cm^{-1} and 1925 cm^{-1}.

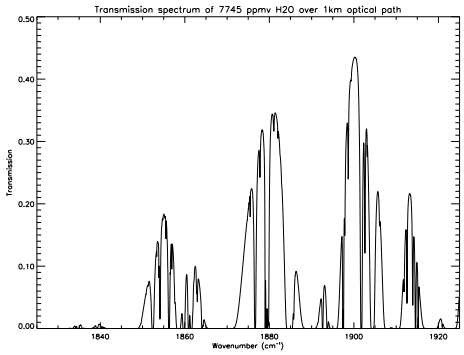

Figure 6.15: Transmission spectrum of H_2O in the spectral region of the main NO band, 1825 cm^{-1} and 1925 cm^{-1}.

with pathlengths under 50 m.

Table 6.9: Detection limits for NO

Pathlength in m	Detection limit in ppbv
50	6.8
1000	2.8

6.1.8 Nitrous Oxide (N_2O)

NETCEN does not currently measure concentrations of nitrous oxide (N_2O), which is a trace gas in the atmosphere. N_2O is released from soils as a result of incomplete microbiological nitrification or denitrification. Its ambient concentration is 0.32 ppmv. N_2O (see figure 6.3) is a contaminant species in the spectral region, 2120 cm^{-1} to 2220 cm^{-1}, from which CO is retrieved, and as such is jointly retrieved with CO, along with H_2O.

For the detection limit calculations 7745 ppmv of water vapour and 1.0 ppmv CO were included in the spectra, and were jointly retrieved with N_2O. The level of random noise used in the spectra was 0.0055. The calculations show that the detection limit for N_2O over an optical pathlength of 50 m is 2.0 ppbv. This value is 160 times less than the ambient concentration of N_2O, and as such N_2O can easily be detected.

6.1.9 Methane (CH_4)

NETCEN does not currently measure concentrations of methane (CH_4), which is a trace gas in the atmosphere. Methane is mainly produced by enteric fermentation in animals, mainly ruminants, and anaerobic decomposition of organic matter in swamps, wetlands and paddy fields. The ambient concentration of methane in the atmosphere at ground level is 1.7 ppmv. CH_4 (see figure 6.6) is a contaminant species in the spectral region, 1240 cm^{-1} to 1340cm^{-1}, from which SO_2 is retrieved, and as such is jointly retrieved with SO_2, along with H_2O.

For the detection limit calculations 7745 ppmv of water vapour and 30 ppbv SO_2 were included in the spectra, and were jointly retrieved with CH_4. The level of random noise used in the spectra was 0.0055. The calculations show that the detection limit for

CH_4 over an optical pathlength of 50 m is 27.1 ppbv. This value is 60 times less than the ambient concentration of CH_4, and as such CH_4 can easily be detected.

6.2 Typical Retrievals

In this section retrievals of CO, SO_2, NO_2, and NO from the spectrum 26_1099a.asc (which is a typical spectrum) are discussed. The spectrum 26_1099a.asc is one of the field measurement spectra recorded at 0.2 cm^{-1} resolution with the MCT detector, using 16 co-added scans, over a 46 m optical pathlength at Oxford railway station. Norton-Beer strong apodisation was applied to the spectrum, and for the retrievals of SO_2, NO_2, and NO it was corrected for self-emission by subtracting from it a spectrum recorded shortly afterwards (with the same instrumental settings) with the external infrared source blocked (see section 3.2).

6.2.1 Carbon Monoxide (CO)

Figure 6.16 shows the results of the retrieval of CO, together with H_2O and N_2O, from 26_1099a.asc. As can be seen from the residuals of the retrieval (shown in the lower plot in figure 6.16), the retrieved spectrum matches the measured spectrum well. Most of the residuals are due to channelling in the measured spectrum. The spikes in the residuals coincide with water lines in the spectrum. Detailed inspection of the retrieved spectrum and measured spectrum in these areas reveals that the spikes in the residuals are due to the retrieved spectral lines being offset slightly from the measured spectral lines. It is thought that these offsets are due to errors in the positions of water vapour lines in the HITRAN database. A wavenumber offset for the whole region is retrieved. However, this single value is the most likely value of the difference in position between the measured spectrum and the HITRAN database for all the spectral lines in the region. Therefore if the offset in line position is different for different species, due to errors in the HITRAN database, this single value will not correctly account for the wavenumber offsets of all spectral lines. The small errors in fitting the measured water vapour lines lead to small errors in the retrieved

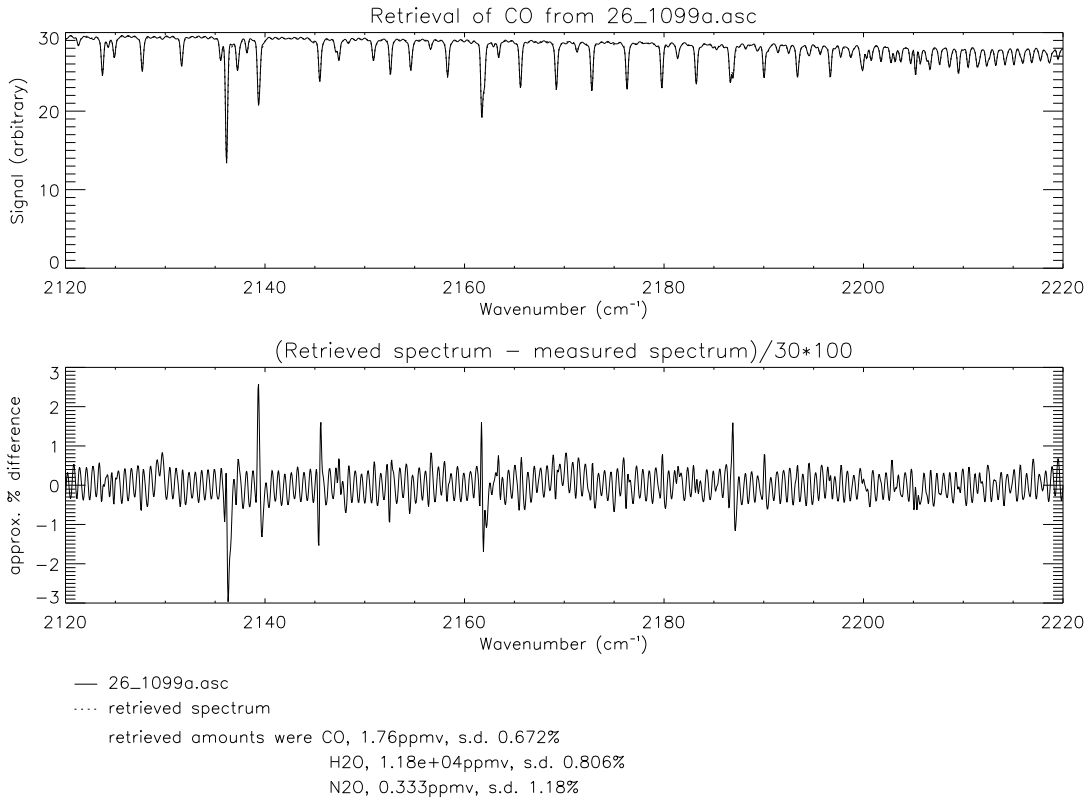

Figure 6.16: Retrieval of CO from 26_1099a.asc. The solid line in the upper plot is the measured spectrum, 26_1099a.asc. The dotted line in the upper spectrum (visible in places) is the retrieved spectrum created by the RFM using the values given in the plot. The stated retrieved errors are the appropriate elements of $\sqrt{\mathbf{S_x}}$. The lower curve is the residuals of the retrieval (retrieved spectrum - measured spectrum) expressed as a percentage of the maximum value of the measured spectrum.

concentration of water vapour.

6.2.2 Sulphur Dioxide (SO_2)

Figure 6.17 shows the results of the retrieval of SO_2, together with H_2O and CH_4, from 26_1099a_cor.spec (26_1099a.asc corrected for self-emission). The 1350 cm^{-1} to 1390 cm^{-1} region, rather than the whole SO_2 main band from 1330 cm^{-1} to 1390 cm^{-1}, was used because errors in the position and/or line strength of water vapour lines in the HITRAN database in the 1330 cm^{-1} to 1350 cm^{-1} region affect the SO_2 retrieval via the SO_2 con-

tribution function[11] and lead to falsely high concentrations of SO_2.

As can be seen from the residuals of the retrieval (shown in the lower plot in figure 6.17), the retrieved spectrum matches the measured spectrum less well than it does for CO. Most of the residuals match water vapour lines and are thought to be due to errors in either the line position or the line strength of the water vapour lines in the HITRAN database.

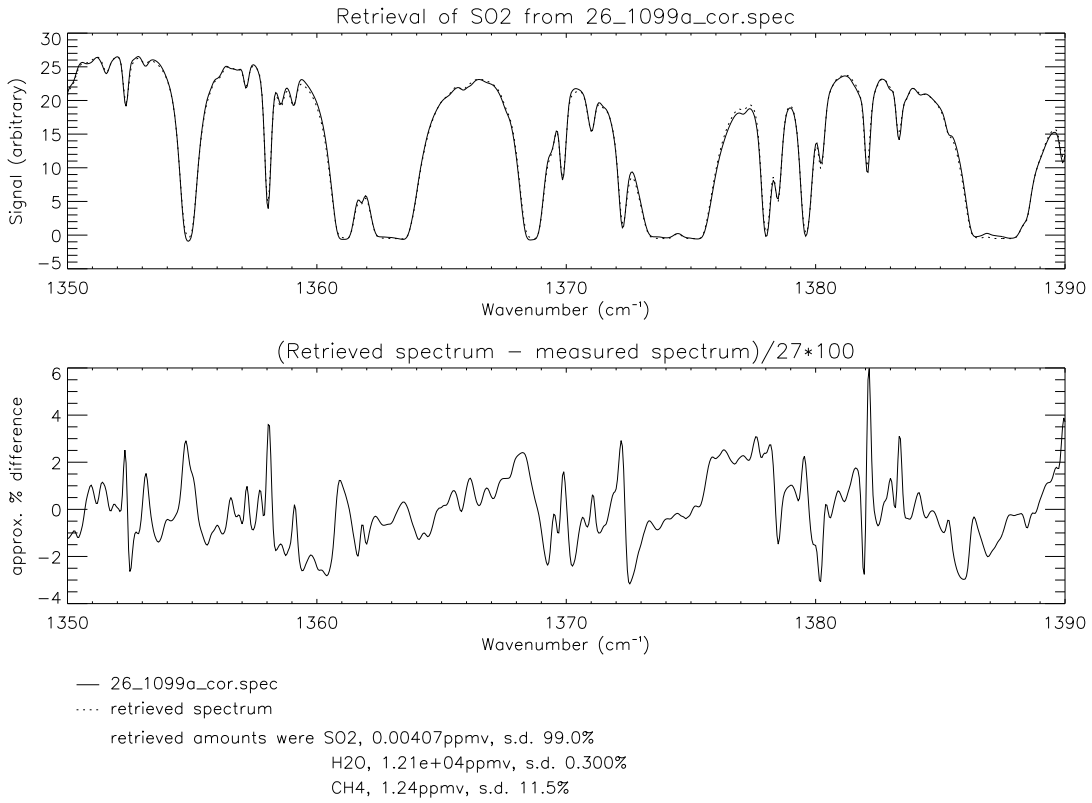

Figure 6.17: Retrieval of SO_2 from 26_1099a_cor.spec. The solid line in the upper plot is the measured spectrum, 26_1099a_cor.spec. The dotted line in the upper spectrum (visible in places) is the retrieved spectrum created by the RFM using the values given in the plot. The stated retrieved errors are the appropriate elements of $\sqrt{\mathbf{S_x}}$. The lower curve is the residuals of the retrieval (retrieved spectrum - measured spectrum) expressed as a percentage of the maxium value of the measured spectrum.

[11]The SO_2 contribution function is the appropriate element of $\mathbf{D_y} = \partial\hat{\mathbf{x}}/\partial\mathbf{y} = \left(\mathbf{S_a^{-1}} + \mathbf{K^T S_y^{-1} K}\right)^{-1} \mathbf{K^T S_y^{-1}}$.

6.2.3 Nitric Oxide (NO)

Figure 6.18 shows the results of the retrieval of NO, together with H_2O, from 26_1099a_cor.spec (26_1099a.asc corrected for self-emission). As can be seen from the residuals of the retrieval (shown in the lower plot in figure 6.18), the retrieved spectrum matches the measured spectrum fairly well. Most of the residuals consist of either channelling, or the spikes which indicate that the spectral lines in the retrieved and measured spectra are slightly offset with respect to each other, and so their lineshapes do not quite match.

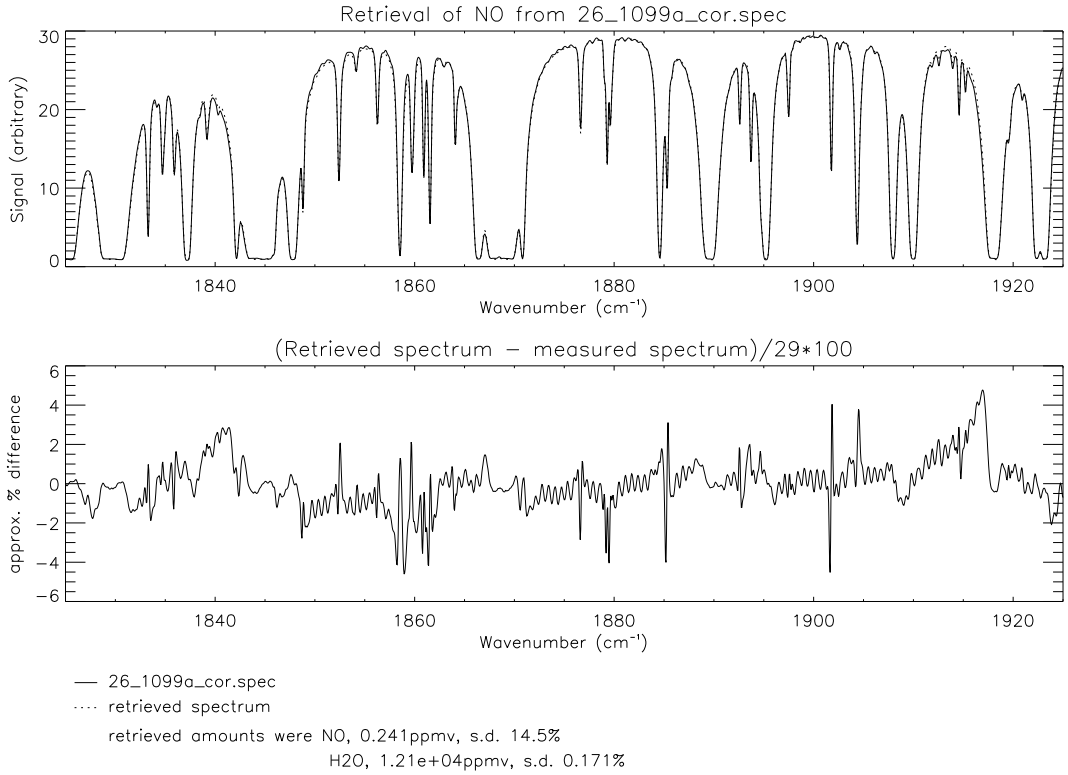

Figure 6.18: Retrieval of NO from 26_1099a_cor.spec. The solid line in the upper plot is the measured spectrum, 26_1099a_cor.spec. The dotted line in the upper spectrum (visible in places) is the retrieved spectrum created by the RFM using the values given in the plot. The stated retrieved errors are the appropriate elements of $\sqrt{\mathbf{S_x}}$. The lower curve is the residuals of the retrieval (retrieved spectrum - measured spectrum) expressed as a percentage of the maxium value of the measured spectrum.

6.2.4 Nitrogen Dioxide (NO_2)

Figure 6.19 shows the results of the retrieval of NO_2, together with H_2O, from 26_1099a_cor.spec (26_1099a.asc corrected for self-emission). The narrow peaks in the retrieval residuals (shown in the lower plot in figure 6.19) between 1580 cm^{-1} and 1615 cm^{-1}, correspond with lines in the NO_2 transmission spectrum as generated from the HITRAN database. In fact all main NO2 absorption lines included in the retrieved spectrum have corresponding spikes in the residuals. If the retrieval is repeated with H_2O *only*, i.e. no NO_2, then the residuals in this region are much reduced - leaving channelling and five spikes that match

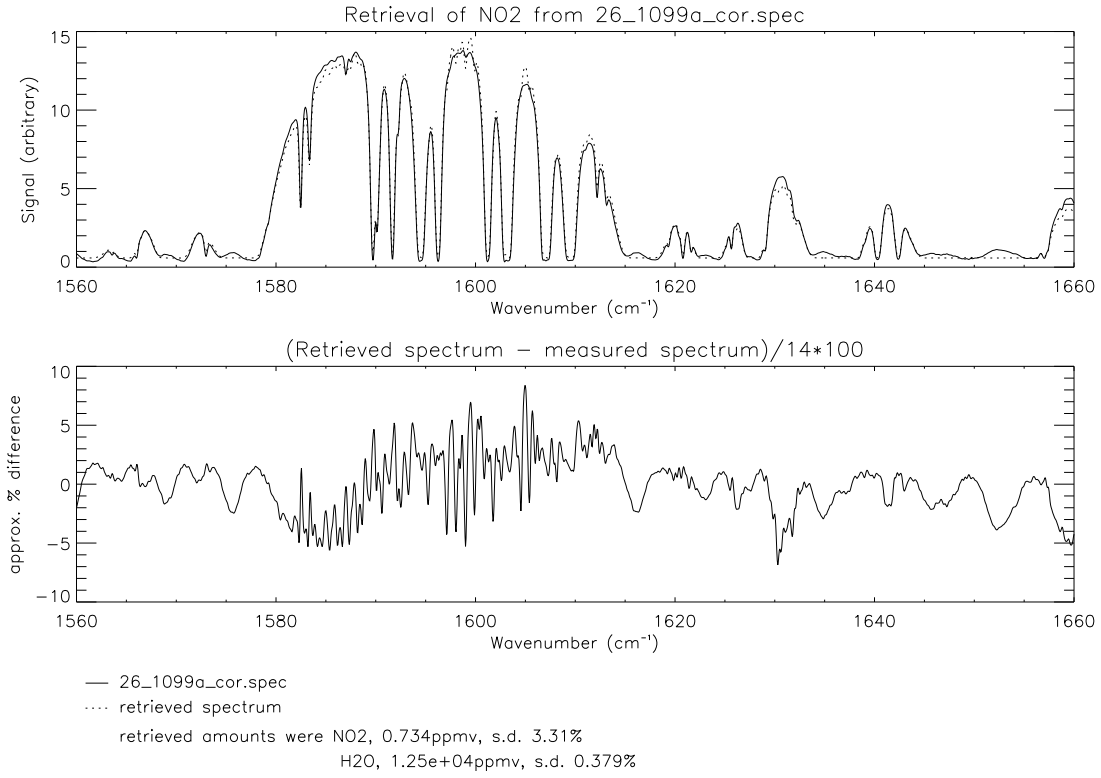

Figure 6.19: Retrieval of NO_2 from 26_1099a_cor.spec. The solid line in the upper plot is the measured spectrum, 26_1099a_cor.spec. The dotted line in the upper spectrum (visible in places) is the retrieved spectrum created by the RFM using the values given in the plot. The stated retrieved errors are the appropriate elements of $\sqrt{\mathbf{S_x}}$. The lower curve is the residuals of the retrieval (retrieved spectrum - measured spectrum) expressed as a percentage of the maxium value of the measured spectrum.

water vapour lines. The latter indicate that the spectral lines in the retrieved and measured spectra are slightly offset with respect to each other, and so their lineshapes do not quite match. This is probably due to errors in the line positions of water vapour lines in the HITRAN database.

From these results I infer that if there is any NO_2 absorption in the measured spectrum, 26_1099a_cor.spec, it is below the noise level. The retrieval is therefore retrieving a concentration of NO_2 far in excess of that supported by the data. If the retrieved concentration of NO_2 is compared with the maximum hourly concentrations measured by NETCEN, and given in table 6.4, it is found to be approximately three times these values. It is thought that the reason for these errors is that the retrieval is probably misinterpreting channelling and possibly also errors in the water vapour line position and/or strength in the HITRAN database.

Given that retrievals of NO_2 from the 1560 cm^{-1} to 1660 cm^{-1} region are not to be believed, it was decided to try the 2850 cm^{-1} to 2940 cm^{-1} region, where the secondary band of NO_2 resides. The results of one such retrieval are shown in figure 6.20. When the residuals of this retrieval (shown in the lower plot in figure 6.20) are examined a set of spectral lines are visible, particularly in the 2915 cm^{-1} to 2930 cm^{-1} region. These were found to correspond with the NO_2 lines included in the retrieved spectrum. The retrieval is again retrieving an unfeasibly high concentration of NO_2, which is not supported by the NO_2 absorption lines in the measured spectrum. The reason for this is probably that the retrieval is misinterpreting channelling in the measured spectrum as NO_2 absorption lines. The overall shape of the residuals in figure 6.20 is that of a cubic expression. Therefore the quadratic expression for gain does not model the 100% transmission curve well; a cubic would probably reduce the residuals and the errors in the retrieved concentrations.

In light of these results it was decided that it was not possible to reliably retrieve NO_2 from the spectra recorded in this study.

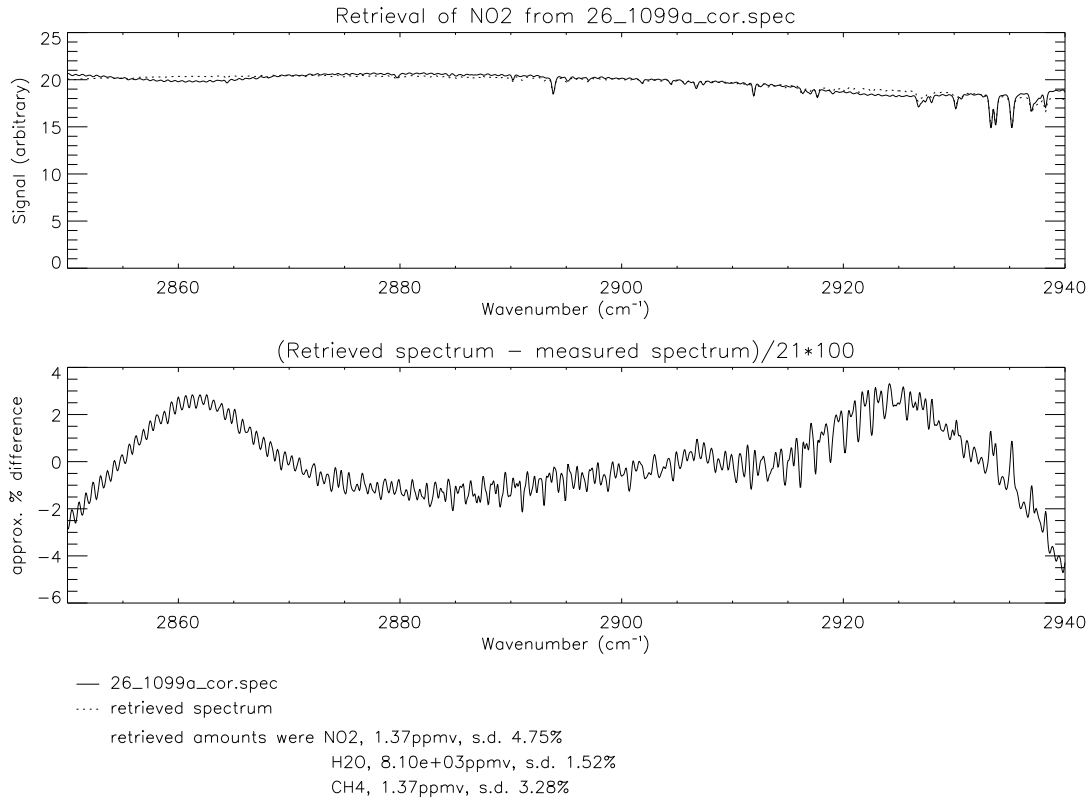

Figure 6.20: Retrieval of NO_2 from 26_1099a_cor.spec. The solid line in the upper plot is the measured spectrum, 26_1099a_cor.spec. The dotted line in the upper spectrum (visible in places) is the retrieved spectrum created by the RFM using the values given in the plot. The stated retrieved errors are the appropriate elements of $\sqrt{\mathbf{S_x}}$. The lower curve is the residuals of the retrieval (retrieved spectrum - measured spectrum) expressed as a percentage of the maxium value of the measured spectrum.

6.2.5 Ozone (O_3)

Figure 6.21 shows the retrieval of O_3 from 19_1099a_cor.spec (19_1099a.asc corrected for self-emission). It illustrates the difficulties experienced trying to detect O_3 with the equipment used in this study. The main problem is the relatively large amplitude of channelling in this spectral region, as can be seen in figure 6.21. A secondary problem is the anomalous dip in the 100% transmission curve between 1045 cm^{-1} and 1055 cm^{-1}. This is thought to be absorption by a liquid or solid, possibly a hydrocarbon based oil, on one of the optical surfaces in the spectrometer. It might be possible to model the anomalous dip as

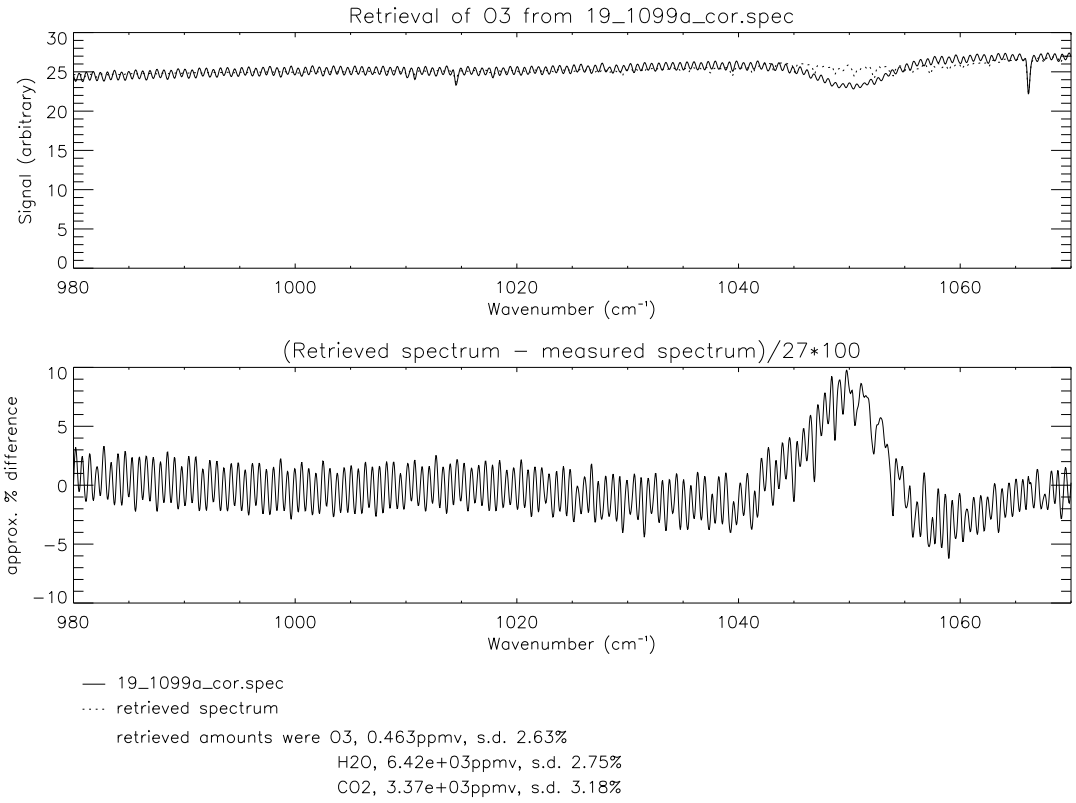

Figure 6.21: Retrieval of O_3 from 19_1099a_cor.spec. The solid line in the upper plot is the measured spectrum, 19_1099a_cor.spec. The dotted line in the upper spectrum (visible in places) is the retrieved spectrum created by the RFM using the values given in the plot. The stated retrieved errors are the appropriate elements of $\sqrt{\mathbf{S_x}}$. The lower curve is the residuals of the retrieval (retrieved spectrum - measured spectrum) expressed as a percentage of the maxium value of the measured spectrum.

an absorption cross-section in the RFM, since it has not been possible to locate and remove the substance causing the absorption.

As can be seen from the upper plot in figure 6.21, there are no visible O_3 spectral lines, only channelling and water vapour lines. However, the retrieved spectrum contains several visible O_3 spectral lines. In part this is due to the retrieval misinterpreting the regular channelling signal, which has a similar shape to atmospheric spectral lines convolved with the instrument lineshape, as O_3 spectral lines where the two coincide. Random noise with the same root-mean-square amplitude as the channelling would not cause these errors,

since the shape of the noise is too dissimilar to that of the spectral lines. The retrieved concentration of O_3 is therefore not valid. This is the case with all O_3 retrievals.

In light of these results it was decided that it was not possible to reliably retrieve O_3 from the spectra recorded in this study.

6.3 Results from the Science Area Measurements

The experimental set up for the spectra recorded in Oxford University's science area was described in section 2.5.1. Spectra were recorded over a 160 m optical pathlength at 0.2 cm^{-1} resolution with the MCT detector, using 100 co-added scans (which took 10 minutes to record). Norton-Beer strong apodisation was applied to each spectrum, and for the retrievals of SO_2, and NO they were corrected for self-emission by subtracting from each spectrum a spectrum recorded either immediately before or immediately afterwards with the external source switched off and the same instrumental settings. Temperature and pressure measurements were made using an Oregon Scientific electronic barometer BA-116. This has a precision of $\pm$ 1°C and $\pm$ 1 mb.

Spectra were recorded on 6 weekdays in October 1999 and on 20 weekdays between 2 February 2000 and 19 April 2000 inclusive. Nearly three weeks were lost between 14 February 2000 and 2 March 2000 due to the He:Ne laser in the spectrometer failing. Other days were lost due to poor weather (spectra are not recorded in the rain, because the spectrometer must be protected from getting wet).

Plots against time of the retrieved concentrations are shown in figures 6.22, 6.23, 6.24, 6.25, and 6.26. Data points which are connected by a dotted line are on consecutive days. The error bars shown (as solid lines) are the appropriate elements of the error covariance matrix of the retrieved state vector, $\hat{\mathbf{S}}_{\mathbf{x}}$.

The concentration of CO in unpolluted air is 0.15 ppmv, and the mean hourly concentration of CO measured by NETCEN at their 'Urban Centre' sites in 1997 was 0.6 ppmv. It can be seen from figure 6.22 that the concentrations of CO measured in Oxford University's science area lie between these two values, with two exceptions, on 12 and 14 October 1999.

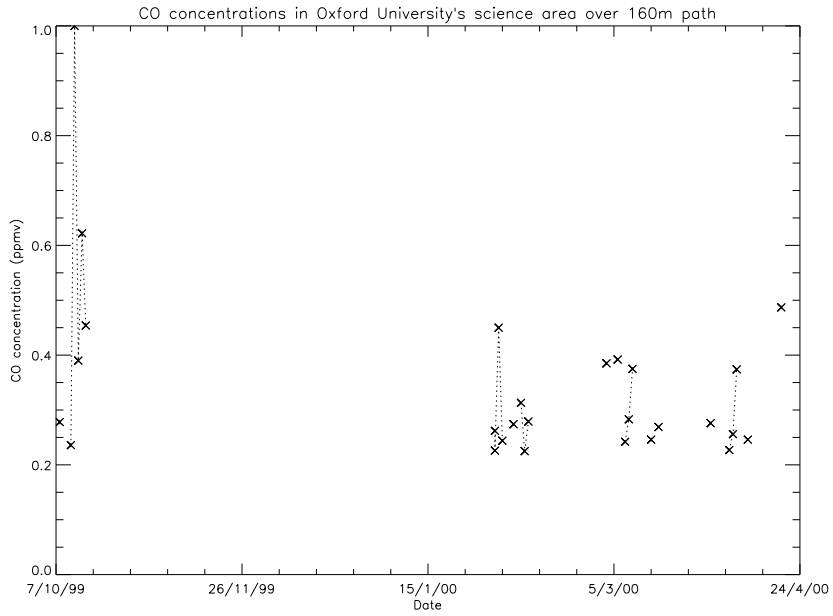

Figure 6.22: CO concentrations measured over a 160 m path in Oxford University's science area between 8/10/99 and 19/4/00 inclusive.

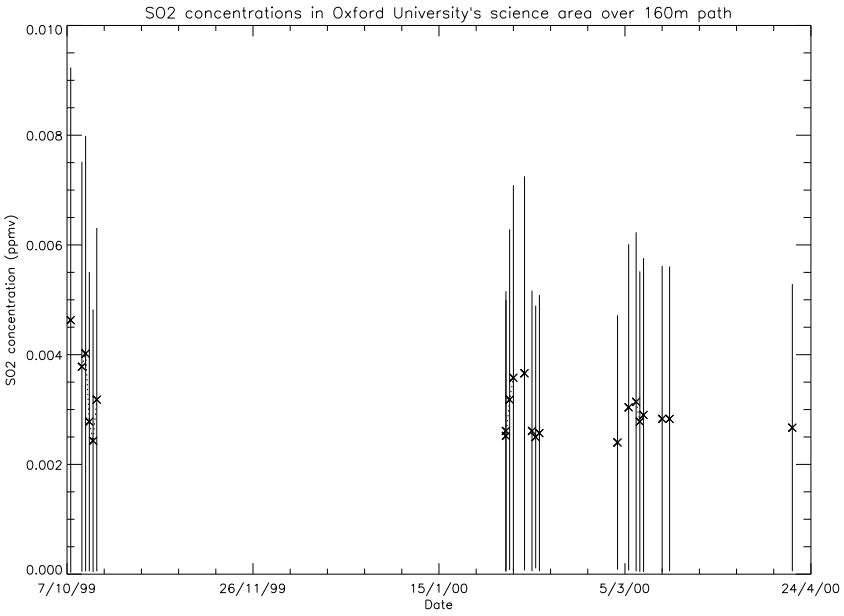

Figure 6.23: SO_2 concentrations measured over a 160 m path in Oxford University's science area between 8/10/99 and 19/4/00 inclusive.

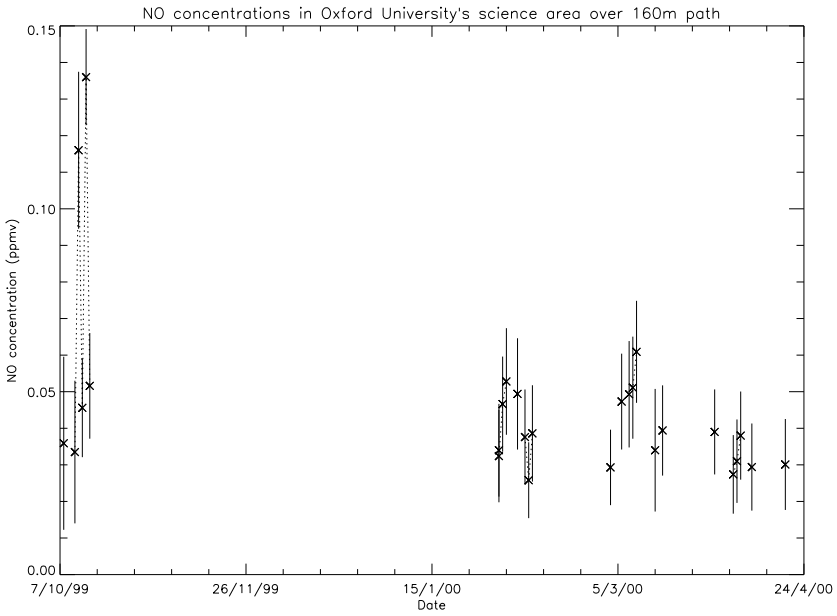

Figure 6.24: NO concentrations measured over a 160 m path in Oxford University's science area between 8/10/99 and 19/4/00 inclusive.

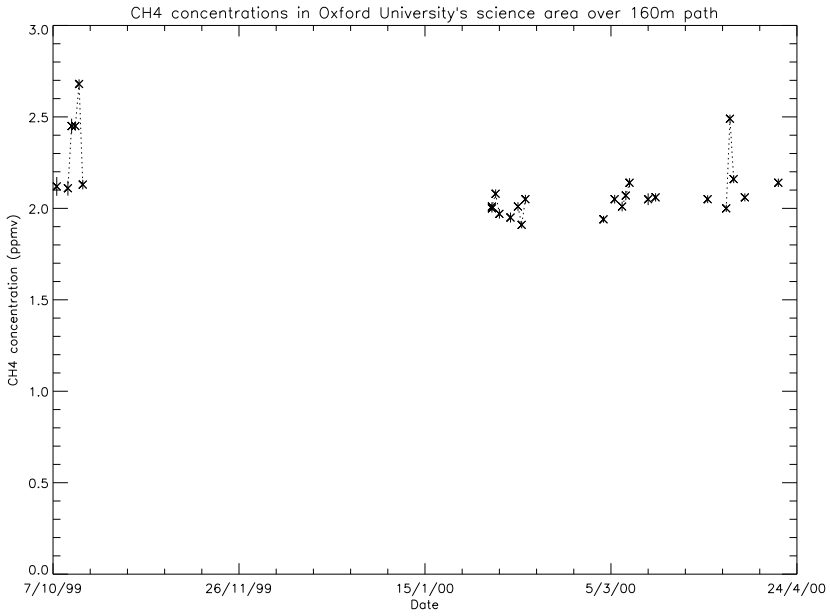

Figure 6.25: CH_4 concentrations measured over a 160 m path in Oxford University's science area between 8/10/99 and 19/4/00 inclusive.

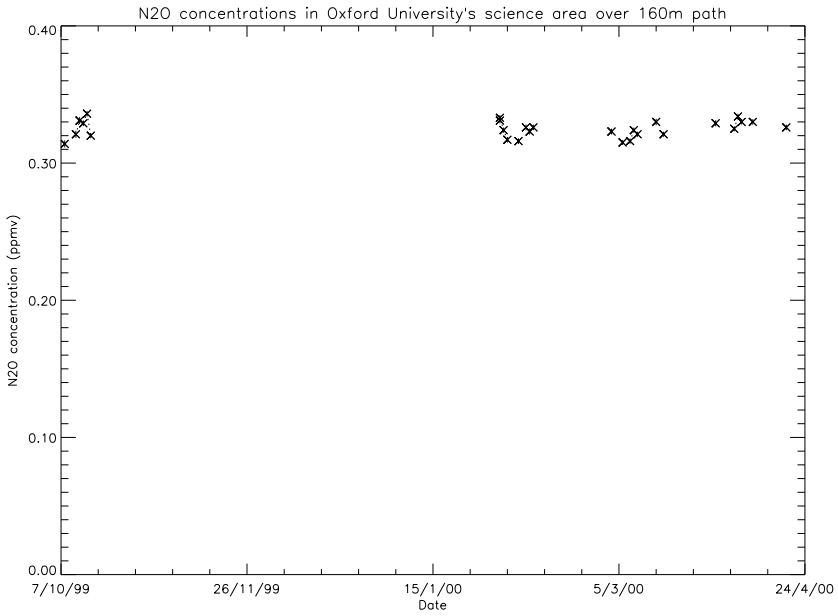

Figure 6.26: N_2O concentrations measured over a 160 m path in Oxford University's science area between 8/10/99 and 19/4/00 inclusive.

The mean hourly concentration of SO_2 measured by NETCEN at their 'Urban Centre' sites in 1997 was 5.4 ppbv. SO_2 concentrations plotted in figure 6.23 lie in the range 2.4 ppbv to 4.7 ppbv, which are slightly lower than the average measured by NETCEN, which shows that the site is relatively unpolluted for a city centre area. The standard deviations of the retrieved concentrations are high, in the range 96.4%-99.4%, which is due to the high a priori contributions to the retrieved concentrations, which are in the range 95.1% to 99.1%. Although the a priori contributions are very high, the retrieval is extracting information from the spectra. A plot (see figure 6.27) of percentage a priori contribution against retrieved SO_2 concentration does not show any correlation. Indeed, there are a range of values of the retrieved SO_2 concentration for each value of the percentage a priori contribution (for those a priori contribution values which are associated with more than one retrieval). There is a slight trend that the higher the percentage a priori contribution, the closer the retrieved SO_2 concentration is to the a priori. The a priori for all SO_2 retrievals is 6.2 ppbv $\pm$ 100%.

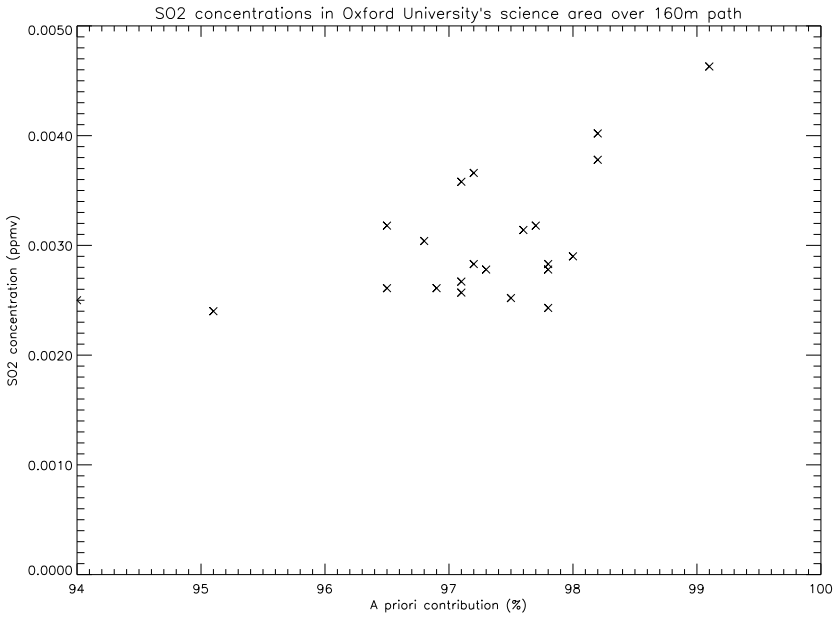

Figure 6.27: SO_2 concentrations measured over a 160 m path in Oxford University's science area between 8/10/99 and 19/4/00 inclusive plotted against their associated percentage a priori contributions.

Five of the retrievals of SO_2 needed extra iterations (the usual limit is 15 iterations), up to 30 in one case, in order to converge. Five more did not converge but instead oscillated between two concentrations. In these cases the retrievals converged on limit cycles rather than point values.

The mean hourly concentration of NO measured by NETCEN at their 'Urban' sites in 1997 was approximately 30 ppbv[12]. The concentrations of NO plotted in figure 6.24 are, with two exceptions (on 12 and 14 October 1999), in the range 25 ppbv to 65 ppbv, which is slightly higher than that measured by NETCEN, but can be explained by the shorter measurement time (10 minutes) for the FTIR measurements.

The measured concentrations of CH_4 are mainly scattered between 1.9 ppmv and 2.2 ppmv, which are slightly elevated above its ambient concentration at ground level of 1.7 ppmv. The measured concentrations of N_2O are fairly constant throughout the measuring period, ranging between 0.31 ppmv and 0.34 ppmv. The ambient concentration at

[12]NO concentrations are taken to be the difference between NO_x and NO_2.

ground level of N_2O is 0.32 ppmv. The uniformity of these measurements demonstrate the instrument stability over a long period of time and the reproducibility of the measuring and analysing process.

The figures show that the optical path used in Oxford University's science area passes through air with low levels of pollution, although 12 and 14 October 1999, and to a lesser extent 13 October, appear to be noticeably more polluted than any of the other measurement days. These three days are the only measurement days where there was no wind. On the 12 and 13 October the pressure was 1098 mb, although by the 14 October this had dropped to 1028 mb. All three days had over 8 hours of sunshine[13]. So these three days of elevated pollution levels correspond to a period of still, sunny days with a high pressure system over the country. These are ideal weather conditions for the build up of urban air pollution. As well as plotting the gas concentrations against time, they were also plotted against the temperature and pressure at the time of measurement, and the wind speed and wind direction at 9 am[14] at the Radcliffe Meteorological station. However, with the exception of 12, 13 and 14 October this did not reveal any correlations in the data.

6.4 Results from the Field Measurements

The experimental set up for the spectra recorded during field measurements in Oxford was described in section 2.5.2. Spectra were recorded at 0.2 cm^{-1} resolution, using 16 co-added scans (which took one and a half minutes to record), with the MCT detector and 6 co-added scans (which took 6 minutes to record) with the DTGS detector. Norton-Beer strong apodisation was applied to each spectrum, and for the retrievals of SO_2, and NO they were corrected for self-emission by subtracting from each spectrum a spectrum recorded either shortly before or shortly afterwards with the external source switched off and the same instrumental settings. Temperature and pressure measurements were made using the Oregon Scientific electronic barometer BA-116.

[13]Meteorological data from the Radcliffe Meterological Station, Oxford (Grid Reference SP509072) daily observations.

[14]Most spectra were recorded between 10 am and 11 am.

From the plots of the retrieved concentrations for CO, SO_2, NO, CH_4 and N_2O for each of the four field measurement days, it can be seen that the results retrieved from the DTGS spectra are noticeably different from those retrieved from the MCT spectra. When the results were examined more closely, it was noticed that the percentage a priori contribution for the retrievals from DTGS spectra were, with four exceptions (two of the CO retrievals and two of the NO retrievals on 26/10/99) noticeably higher, between 1.2 and 26 times higher (for the SO2 measurements, where the percentage a priori contribution is over 96% for all measurements, the difference between the percentage a priori contributions for retrievals from spectra measured by the two detectors is much smaller, but still noticeable), than for the retrievals from MCT spectra. It is thought that these differences in the percentage a priori contribution arise from the lower signal-to-noise ratio in the DTGS spectra (22 to 56 for the DTGS spectra compared with 77 to 120 for the MCT spectra). Other differences between the two sets of measurements include the longer measurement time for the DTGS detector (6 minutes versus 1.5 minutes) and the lack of self-emission in the room-temperature DTGS measurements. Self-emission is measured by the cooled MCT detector and has to be corrected for (see section 3.2). However, the effect is small and is unlikely to have any effect on the difference in percentage a priori contribution between the two detectors.

6.4.1 Hythe Bridge Street

The experimental set up for the spectra recorded in the field measurements on Hythe Bridge Street was described in section 2.5.2, with a plan of the layout given in figure 2.14. On both days the spectrometer, source and plane mirror were placed on the pavement, parallel to the road and adjacent to Blackwell's building. The optical pathlength was approximately 5 m from the kerb.

19 October 1999

The optical pathlength used on 19 October 1999 was measured and found to be 68 m. Plots against time of the retrieved concentrations are shown in figures 6.28 - 6.32.

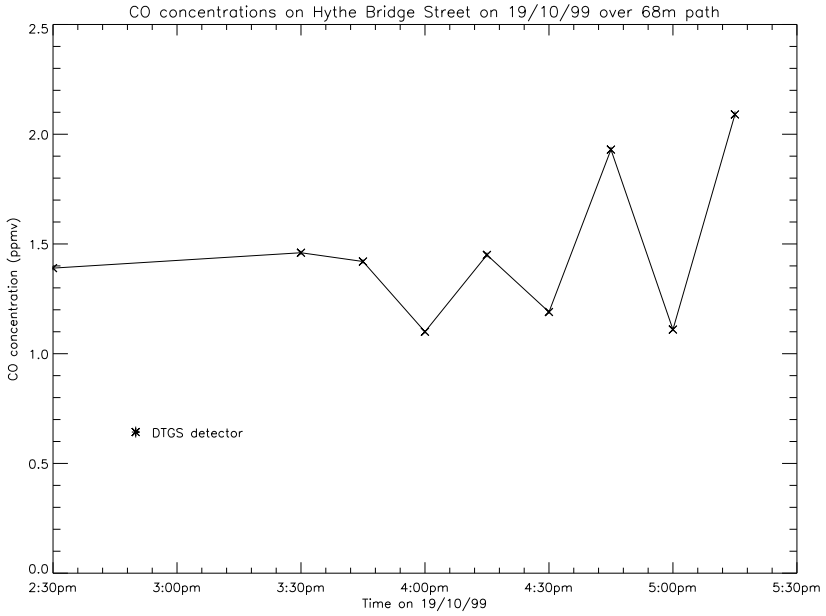

Figure 6.28: CO concentrations measured over a 68 m path on Hythe Bridge Street on 19 October 1999.

The concentration of CO in unpolluted air is 0.15 ppmv, and the mean hourly concentration of CO measured by NETCEN at their 'Roadside' sites in 1997 was 1.4 ppmv. The concentrations of CO plotted in figure 6.28 are well above those in unpolluted air, and are similar to those measured by NETCEN at their 'Roadside' sites in 1997. The National Atmospheric Emissions Inventory (NAEI)[15] states that 96% of all CO emissions around Hythe Bridge Street and Oxford railway station are from road transport, so this result is not surprising. Variations in the measured concentration of CO are due to the volume of traffic passing the equipment during the one and a half minute measuring period. During the measurements it was noted that the rush hour was from approximately 4:15 pm to 5:15 pm, as observed by the levels of passing traffic. The CO measurements show peaks at

[15]The National Atmospheric Emissions Inventory has a searchable (by postcode and map) database at http://www.aeat.co.uk/netcen/airqual/naei/postcode.html

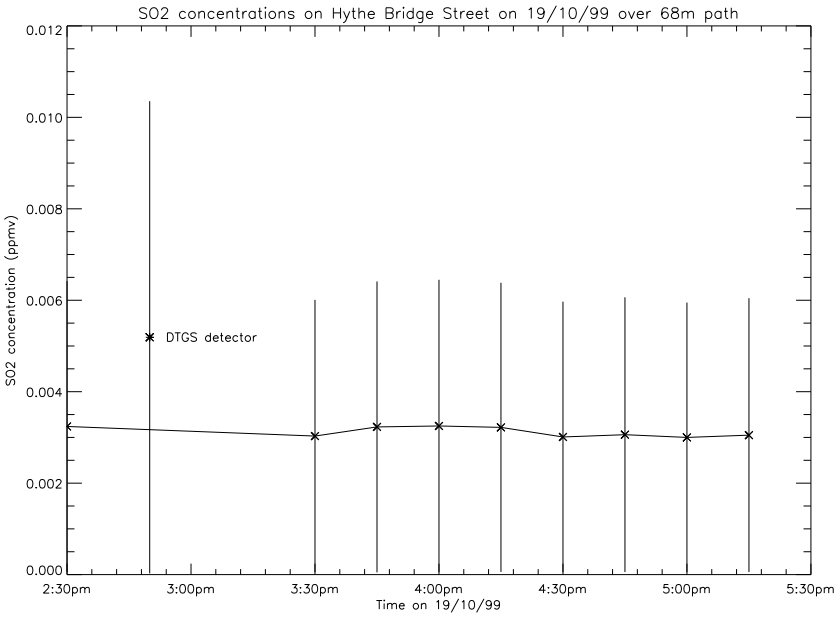

Figure 6.29: SO_2 concentrations measured over a 68 m path on Hythe Bridge Street on 19 October 1999.

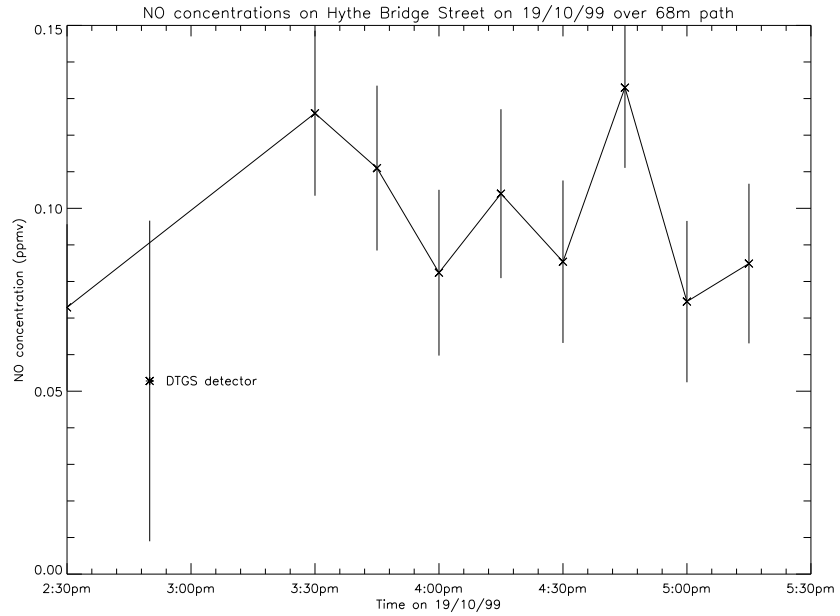

Figure 6.30: NO concentrations measured over a 68 m path on Hythe Bridge Street on 19 October 1999.

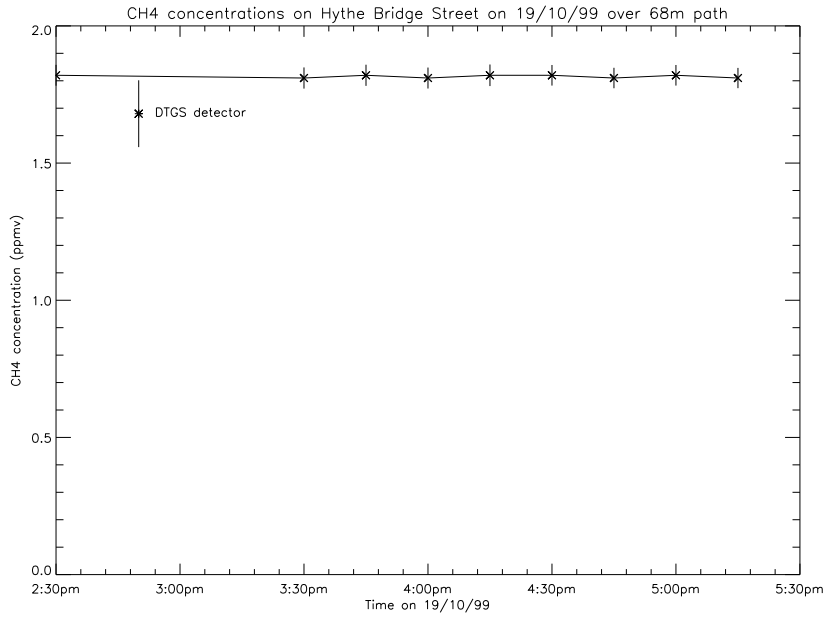

Figure 6.31: CH_4 concentrations measured over a 68 m path on Hythe Bridge Street on 19 October 1999.

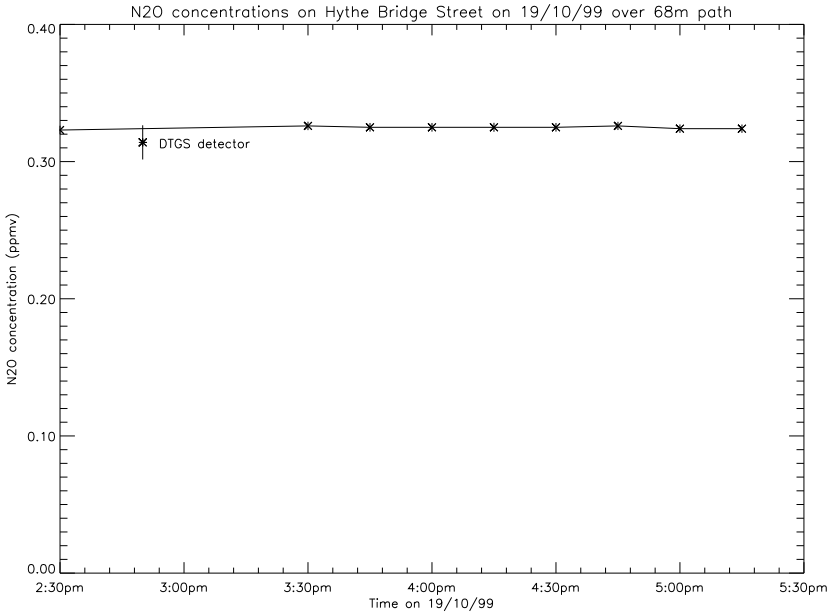

Figure 6.32: N_2O concentrations measured over a 68 m path on Hythe Bridge Street on 19 October 1999.

4:45 pm and 5:15 pm, which fall into this period. The lower levels of pollution measured during the rest of the rush hour period can be accounted for by temporary lulls in the traffic levels, possibly due to the phase of the traffic lights, during the actual one and a half minute measuring period.

The mean hourly concentration of SO_2 measured by NETCEN at their 'Roadside' sites in 1997 was 8.2 ppbv. The concentrations of SO_2 plotted in figure 6.29 lie between 3.0 ppbv and 3.5 ppbv, apart from the amount retrieved from the DTGS spectrum (5.2 ppbv), which are lower than the average measured by NETCEN. The NAEI gives the total emissions for the area around Hythe Bridge Street and Oxford railway station as 1 tonne/year/km^2. A typical level for cities is 5 to 50 tonnes/year/km^2, so the lower concentrations of SO_2 measured in this study are not surprising. The standard deviations of the retrieved concentrations are high, in the range 98.1% to 98.5% (and 99.5% for the concentration retrieved from the DTGS spectrum), which is due to the high a priori contributions to the retrieved concentrations, which are in the range 97.3% to 97.8% (and 99.3% for the concentration retrieved from the DTGS spectrum). Although the a priori contributions are very high, the retrieval is extracting information from the spectra; a plot of percentage a priori contribution against retrieved SO_2 concentration does not show any correlation.

The mean hourly concentration of NO measured by NETCEN at their 'Roadside' sites in 1997 was approximately 100 ppbv[16], which is similar to the concentrations plotted in figure 6.30. The main source (67% of NO_x emissions) of NO around Hythe Bridge Street is transport, and this is reflected in the variation in the measured concentrations of NO.

The measured concentrations of CH_4 and N_2O are fairly constant throughout the measuring period. The concentration of CH_4 is slightly elevated from its ambient concentration at ground level of 1.7 ppmv, whilst that of N_2O is at its ambient concentration at ground level of 0.32 ppmv. The uniformity of these measurements demonstrate the instrument stability and the reproducibility of the measuring and analysing process.

[16]NO concentrations are taken to be the difference between NO_x and NO_2.

20 October 1999

The optical pathlength used on 20 October 1999 was measured and found to be 69 m. Plots against time of the retrieved concentrations are shown in figures 6.33 - 6.37.

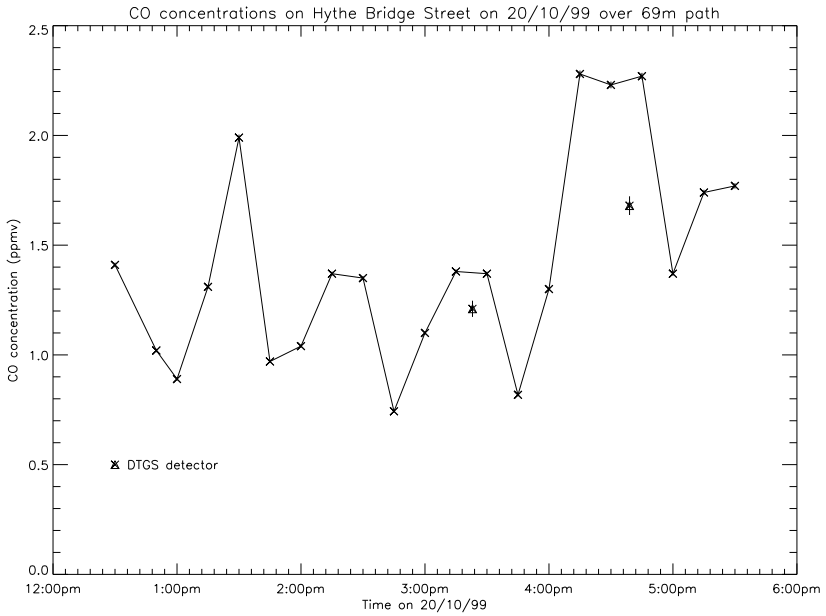

Figure 6.33: CO concentrations measured over a 69 m path on Hythe Bridge Street on 20 October 1999.

As with the concentrations of CO measured on 19 October 1999, the concentrations measured on 20 October 1999, and shown in figure 6.33 are similar to, or higher than, the 1.4 ppmv mean hourly concentration measured by NETCEN at their 'Roadside' sites in 1997. Two peaks in the data can be seen - one at 1:30 pm, corresponding to a late lunchtime rush, and one at 4:15 pm to 4:45 pm, corresponding to the evening rush hour.

SO_2 concentrations are similar to those measured on 19 October 1999, and once again less than half the 8.2 ppbv mean hourly concentration measured by NETCEN at their 'Roadside' sites in 1997. The standard deviations of the retrieved concentrations are again high due to the high a priori contributions (96.8%-97.1% and 99.6% for the DTGS retrieved values). The lack of correlation between percentage a priori contribution and retrieved concentration demonstrates that the retrieval is extracting information about the

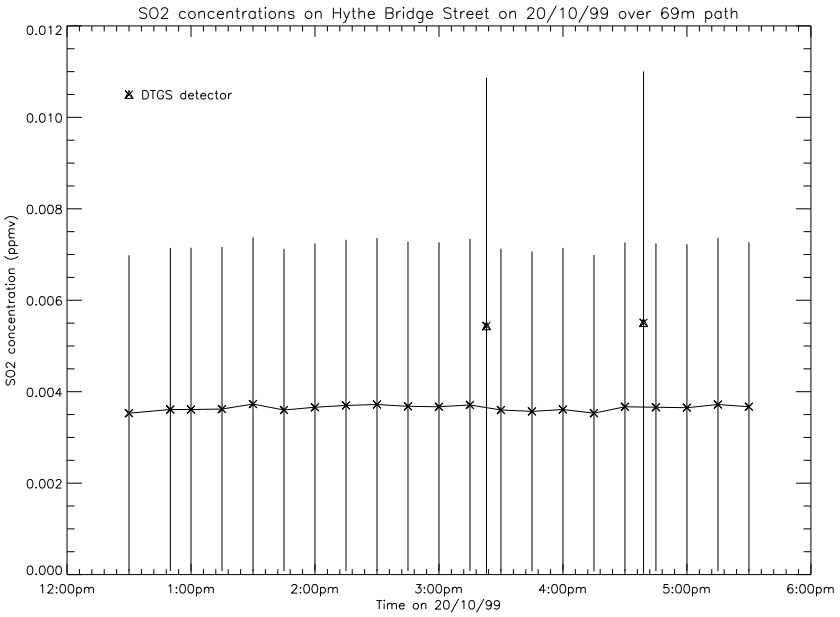

Figure 6.34: SO_2 concentrations measured over a 69 m path on Hythe Bridge Street on 20 October 1999.

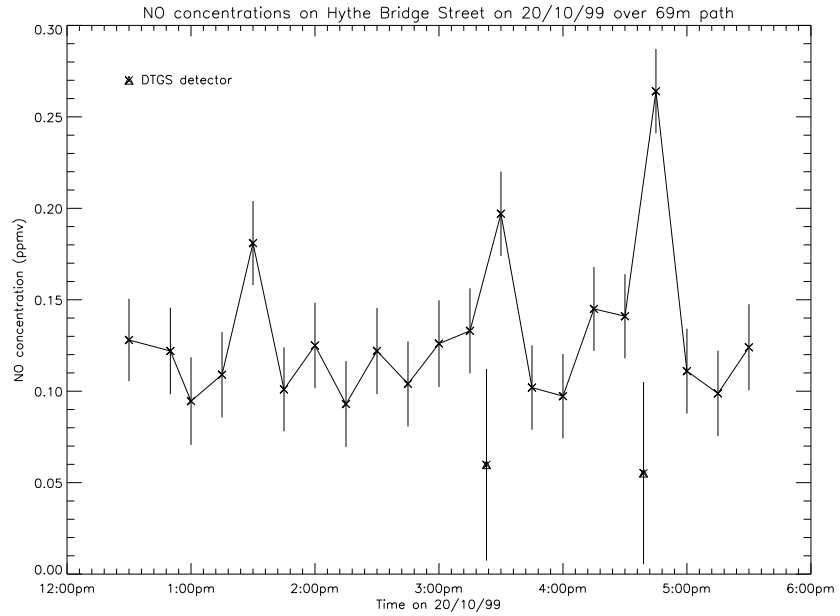

Figure 6.35: NO concentrations measured over a 69 m path on Hythe Bridge Street on 20 October 1999.

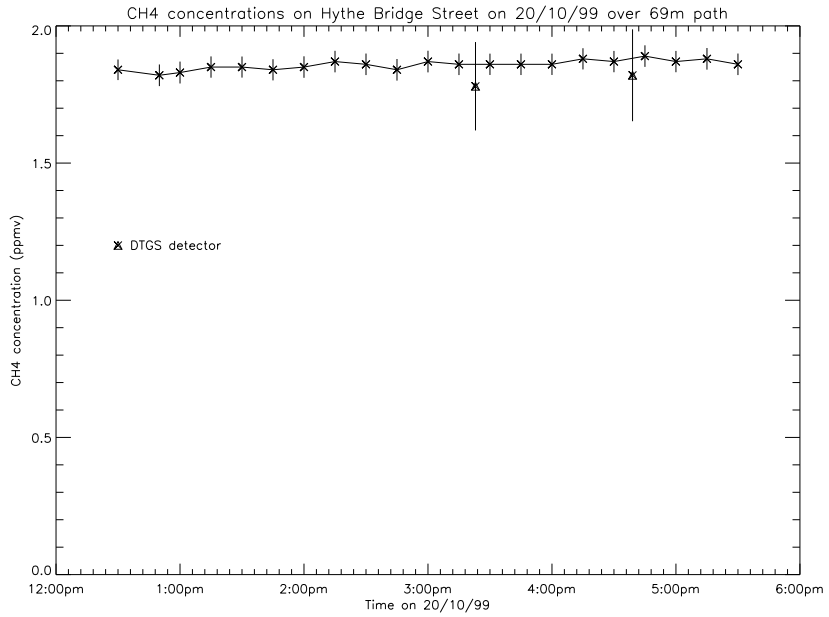

Figure 6.36: CH_4 concentrations measured over a 69 m path on Hythe Bridge Street on 20 October 1999.

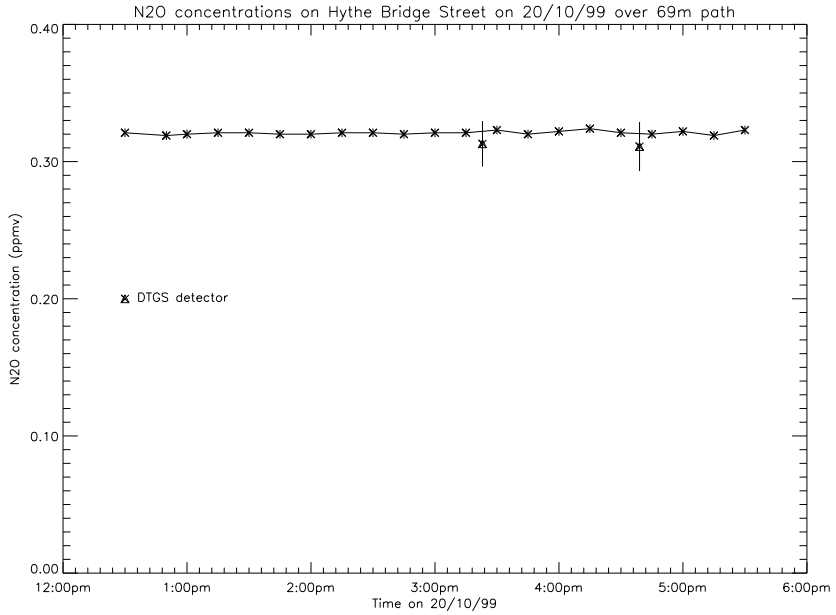

Figure 6.37: N_2O concentrations measured over a 69 m path on Hythe Bridge Street on 20 October 1999.

concentration of SO_2 from the spectra.

NO concentrations are higher than those measured on 19 October 1999. The baseline concentration is about 120 ppbv, which is slightly higher than the approximately 100 ppbv mean hourly concentration measured by NETCEN at their 'Roadside' sites in 1997. The three peaks, at 1:30 pm, 3:30 pm and 4:45 pm are much higher - up to 260 ppbv. The peaks at 1:30 pm and 4:45 pm correspond with similar peaks in the measured CO concentrations, but the 3:30 pm peak is not so apparent in the CO data.

Once again the measured concentrations of CH_4 and N_2O are fairly constant throughout the measuring period and close to their ambient concentrations at ground level, although the CH_4 concentrations are slightly elevated.

6.4.2 Oxford Railway Station

The experimental set up for the spectra recorded in the field measurements at Oxford railway station was described in section 2.5.2, with a plan of the layout given in figure 2.18. On both days the spectrometer was operated out of a Ford Transit van which was situated on an embankment above the Botley Road by Oxford railway station. The source was placed close to the Transit van, and the plane mirror was affixed to railings on the other side of the Botley Road at approximately the same height, which was just above the roof of any double decker bus, as the source and spectrometer.

25 October 1999

The optical pathlength used on 25 October 1999 was determined from the scale plan in figure 2.18, which was itself created from the appropriate OS 1:1250 map and triangulation measurements made on the day, and found to be 45 m. Plots against time of the retrieved concentrations are shown in figures 6.38 - 6.42.

CO concentrations, shown in figure 6.38, increased throughout the afternoon and early evening, reaching their maximum value, of 4.7 ppmv at 6:30 pm. The concentrations are initially, at 2:45 pm, below the 1.4 ppmv mean hourly concentration measured by NETCEN

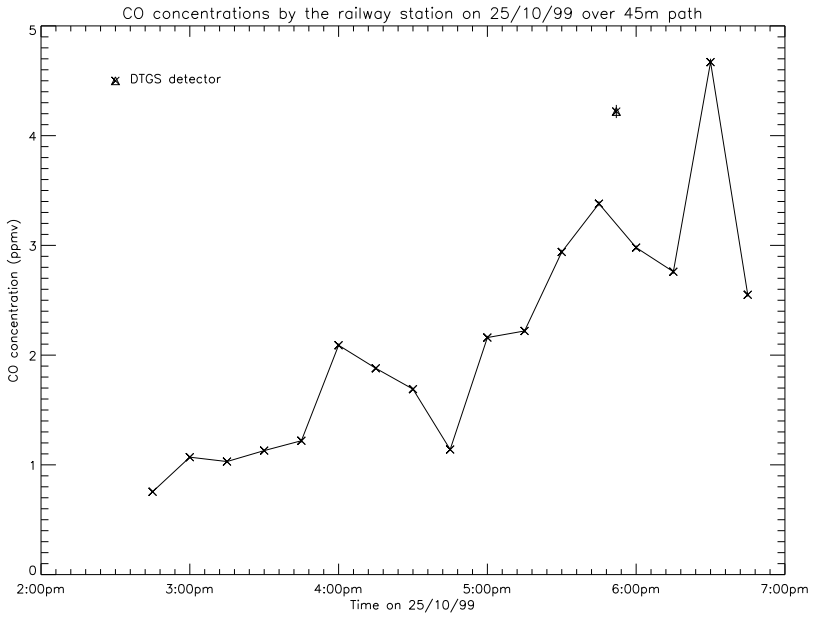

Figure 6.38: CO concentrations measured over a 45 m path by Oxford railway station on 25 October 1999.

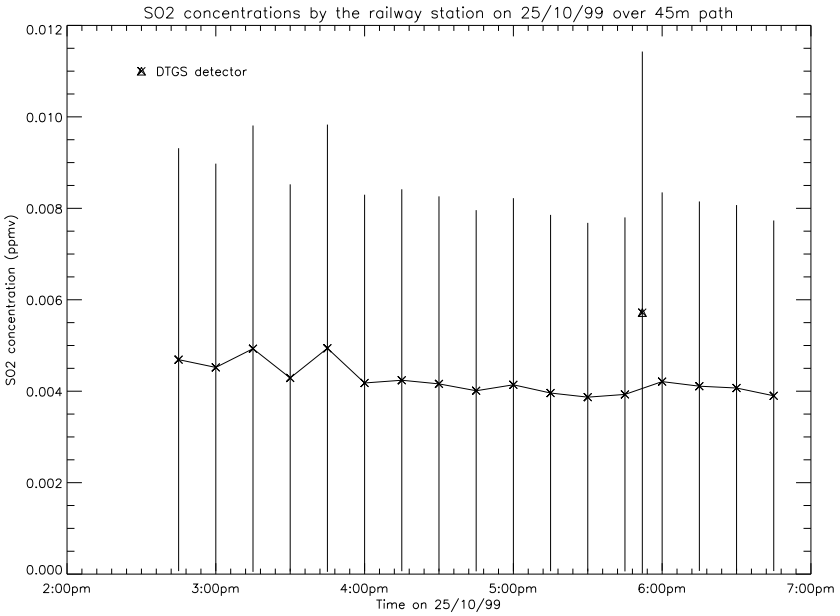

Figure 6.39: SO_2 concentrations measured over a 45 m path by Oxford railway station on 25 October 1999.

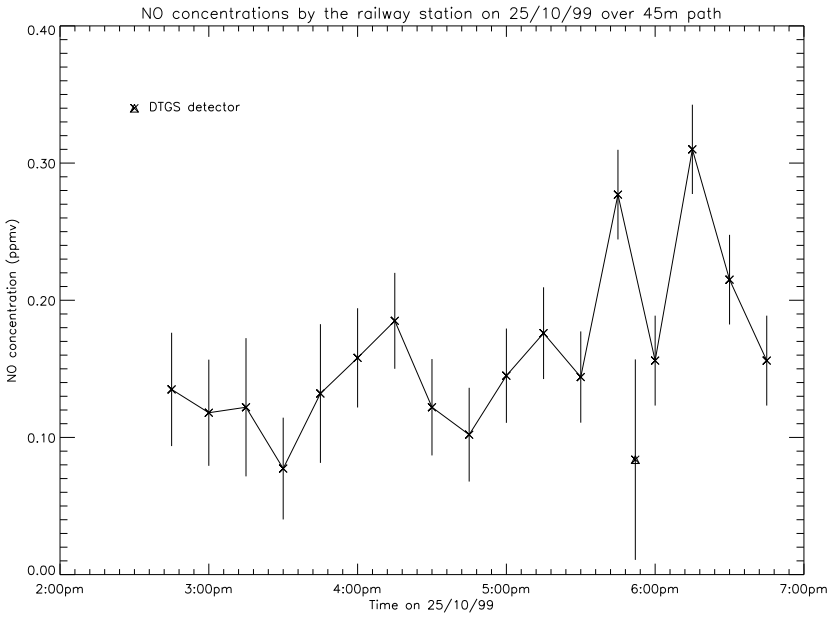

Figure 6.40: NO concentrations measured over a 45 m path by Oxford railway station on 25 October 1999.

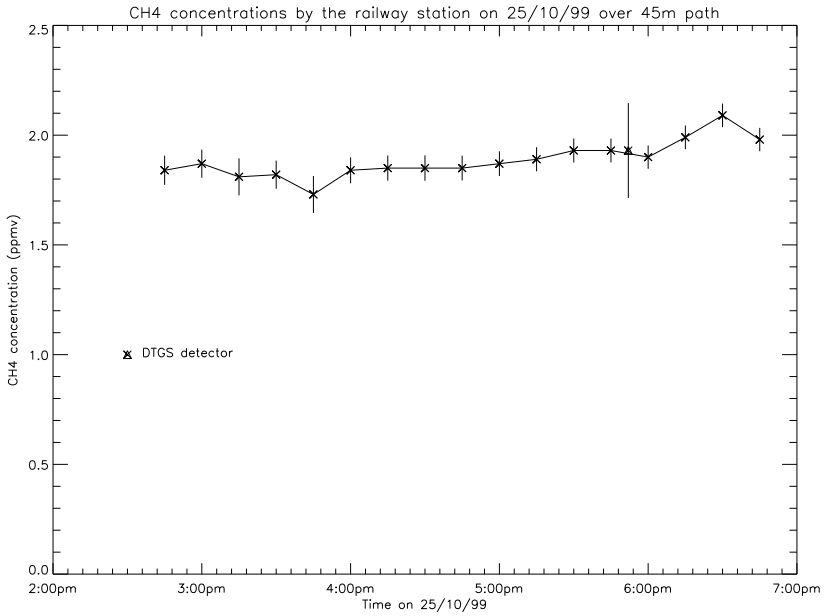

Figure 6.41: CH_4 concentrations measured over a 45 m path by Oxford railway station on 25 October 1999.

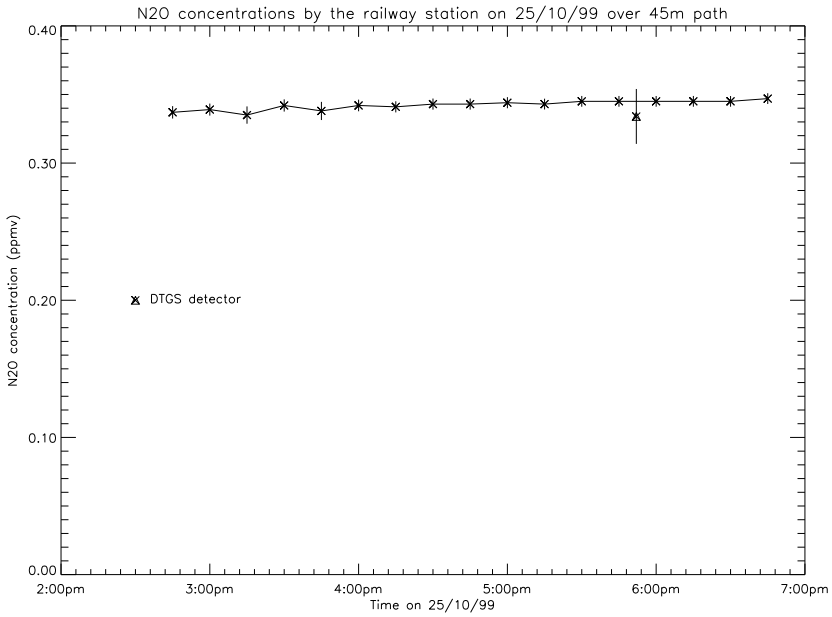

Figure 6.42: N_2O concentrations measured over a 45 m path by Oxford railway station on 25 October 1999.

at their 'Roadside' sites in 1997, but rise above this from 4:00pm onwards, apart from a dip at 4:45 pm. It was quite a still late afternoon and early evening, which may account for the build-up in pollution.

SO_2 concentrations are slightly higher than those measured on 19 and 20 October 1999, but still lower than the 8.2 ppbv mean hourly concentration measured by NETCEN at their 'Roadside' sites in 1997. The standard deviations of the retrieved concentrations are again high due to the high a priori contributions (98.3%-99.0% and 99.8% for the DTGS retrieved value). The lack of correlation between percentage a priori contribution and retrieved concentration demonstrates that the retrieval is extracting information about the concentration of SO_2 from the spectra.

NO concentrations are higher than those measured on 20 October 1999, and generally higher than the approximately 100 ppbv mean hourly concentration measured by NETCEN at their 'Roadside' sites in 1997. There is also a slight upward trend throughout the measuring period, culminating in two peaks at 5:45 pm and 6:15 pm, with a maximum

concentration of 310 ppbv.

Once again the measured concentrations of CH_4 and N_2O are fairly constant throughout the measuring period, although in both cases slightly elevated from their ambient concentrations at ground level.

26 October 1999

The optical pathlength used on 26 October 1999 was determined from the scale plan in figure 2.18, which was itself created from the appropriate OS 1:1250 map and triangulation measurements made on the day, and found to be 46 m. Plots against time of the retrieved concentrations are shown in figures 6.43 - 6.47.

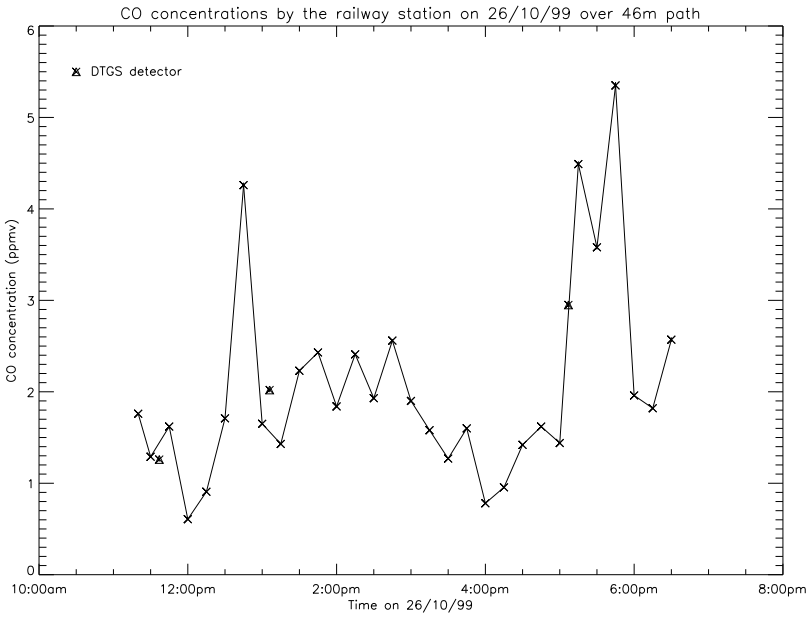

Figure 6.43: CO concentrations measured over a 46 m path by Oxford railway station on 26 October 1999.

CO concentrations, shown in figure 6.43, are mainly above the 1.4 ppmv mean hourly concentration measured by NETCEN at their 'Roadside' sites in 1997. The minimum at 12:00 pm was due to a man attempting to commit suicide[17] by jumping off the pedestrian footbridge and thus stopping the traffic. The traffic was still stationary at 12:15 pm, but

[17]He survived.

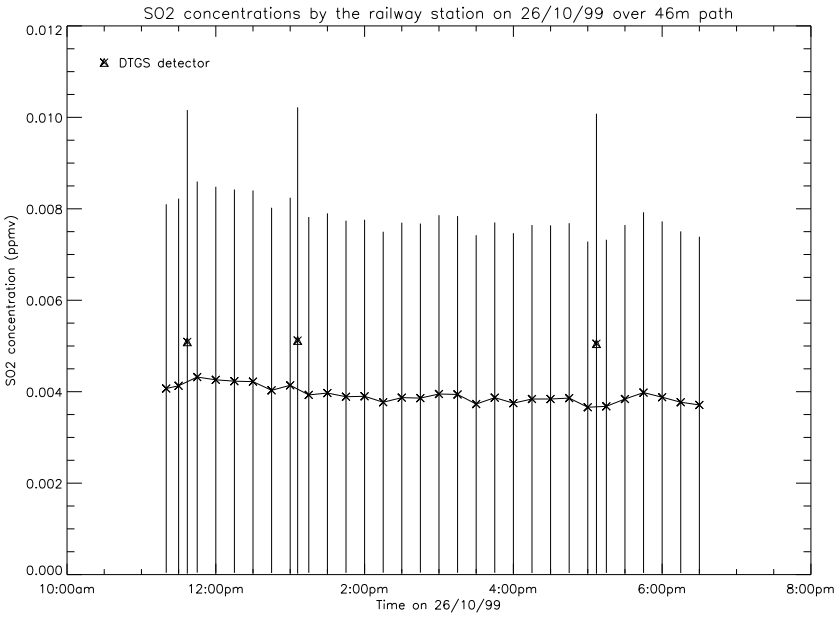

Figure 6.44: SO_2 concentrations measured over a 46 m path by Oxford railway station on 26 October 1999.

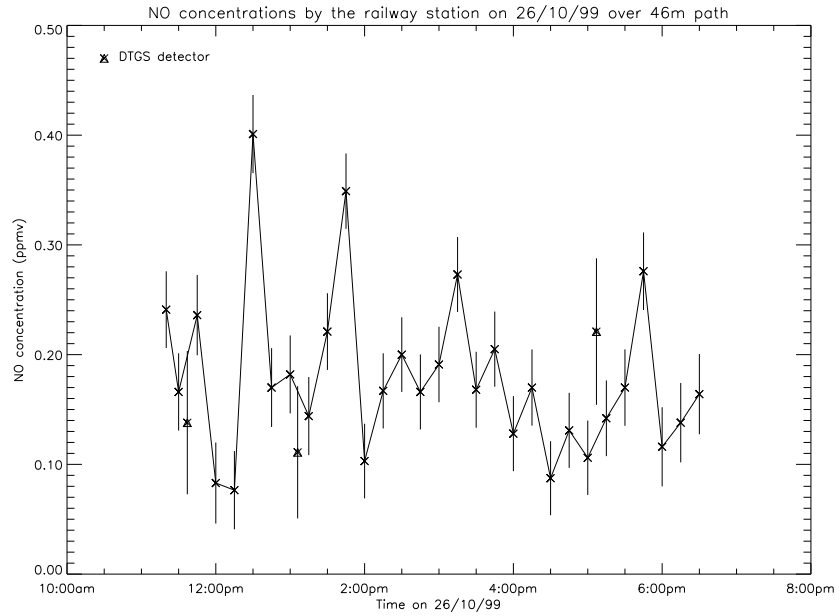

Figure 6.45: NO concentrations measured over a 46 m path by Oxford railway station on 26 October 1999.

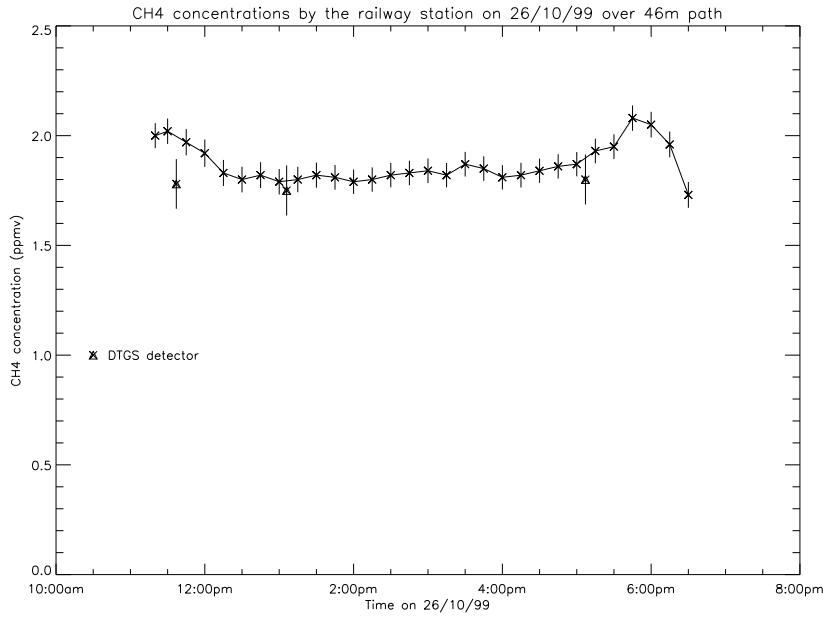

Figure 6.46: CH_4 concentrations measured over a 46 m path by Oxford railway station on 26 October 1999.

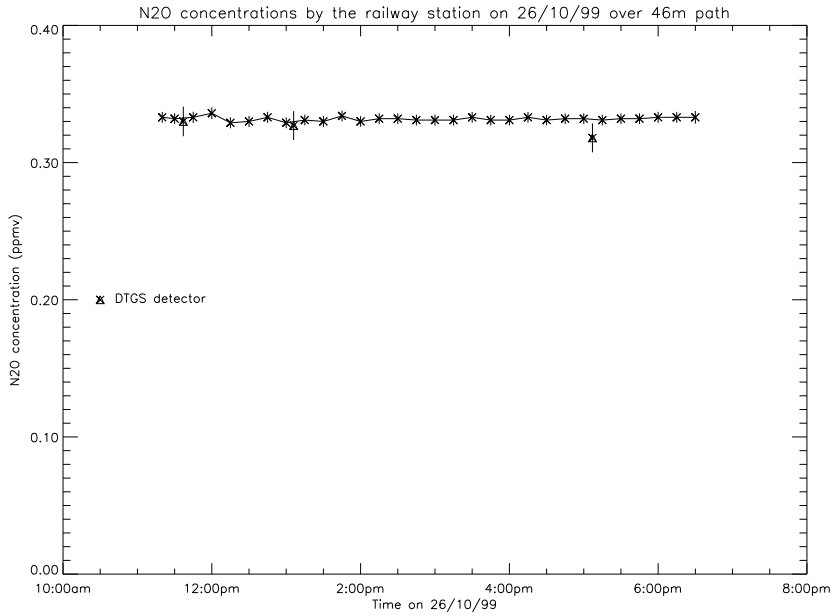

Figure 6.47: N_2O concentrations measured over a 46 m path by Oxford railway station on 26 October 1999.

police cars and an ambulance had arrived, thus elevating the CO levels. Traffic started moving, in one direction at a time, directly after the end of the 12:15 pm measurement, and was flowing in both directions by the time of the 12:30 pm measurement. The peak at 12:45 pm is due to the lunchtime rush hour and clearing of the queue that built up whilst traffic was stationary. A second peak between 5:15 pm and 5:45 pm, with a maximum concentration of 5.35 ppmv, is due to the evening rush hour.

SO_2 concentrations are similar to those measured on 25 October 1999, but still lower than the 8.2 ppbv mean hourly concentration measured by NETCEN at their 'Roadside' sites in 1997. The standard deviations of the retrieved concentrations are again high due to the high a priori contributions (98.5%-98.9% and 99.4% for the DTGS retrieved values). A lack of correlation between percentage a priori contribution and retrieved concentration demonstrates that the retrieval is extracting some information about the concentration of SO_2 from the spectra.

NO concentrations are slightly higher than those measured on 25 October 1999, and mainly higher than the approximately 100 ppbv mean hourly concentration measured by NETCEN at their 'Roadside' sites in 1997. The affect of stationary traffic (all with their engines switched off) can be seen in the minimum from 12:00 pm to 12:15 pm. The peak at 12:30 pm is due to the lunchtime rush hour and clearing of the queue that built up whilst traffic was stationary. The evening rush hour peak that was visible in the CO data is not so noticeable in the NO data, although there is a small peak at 5:45 pm. However, there is a peak at 1:45 pm which isn't present in the CO data. The maximum concentration of NO is 400 ppbv.

Once again the measured concentrations of CH_4 and N_2O are fairly constant throughout the measuring period, although in both cases slightly elevated from their ambient concentrations at ground level.

6.5 Intercomparison with the National Physical Laboratory

An intercomparison of the equipment and methods used in this study with those used by a group (Bill Bell, Clare Paton-Walsh, Nick Davies and Kate Lancaster were all present for at least one day of the field measurements) at the National Physical Laboratory (NPL) was carried out during the field measurements. The results of this intercomparison will be discussed in this section.

The spectrometer used by NPL was a Brucker IFS 66 model with a maximum optical path difference of 6.67 cm, giving a resolution[18] of 0.15 cm^{-1}. The spectrometer was used with an external infrared source and a collecting telescope, which are a matching pair of Newtonian telescopes also made by Brucker. The clear aperture diameter of the telescope is 15 cm. Spectra were recorded at 0.15 cm^{-1} resolution with boxcar apodisation, using 16 co-added scans (which took twenty seconds to record) with a liquid nitrogen cooled MCT detector.

For the intercomparison NPL utilized a basic retrieval routine, which uses the peak areas of the spectral lines to calculate the concentration of the gas in the optical path. A more complex routine using classical least squares fitting of spectra generated from HITRAN line data was used to fit a couple of spectra for comparison. Since the results agreed fairly well, NPL decided to use the basic routine for the intercomparison. The uncertainty in NPL's retrieved concentrations is ± 8% at 95% confidence limits.

The intercomparison was carried out by retrieving CO from spectra recorded simultaneously[19] in time with both the NPL equipment and the equipment used in this study on 20/10/99 (Hythe Bridge Street site) and 26/10/99 (Oxford railway station site). Retrievals of CO from each set of spectra were carried out by each group using their own retrieval techniques. The results are plotted in figures 6.48 and 6.49.

[18] following the definition used in this document of resolution = $1.0/L$, where L is the maximum optical path difference - see 2.1.3

[19] The start of the measuring period for each spectrum was simultaneous. However, owing to the difference in measurement times (the number of co-added scans was the same for comparison purposes) the end of the measurement periods was not simultaneous.

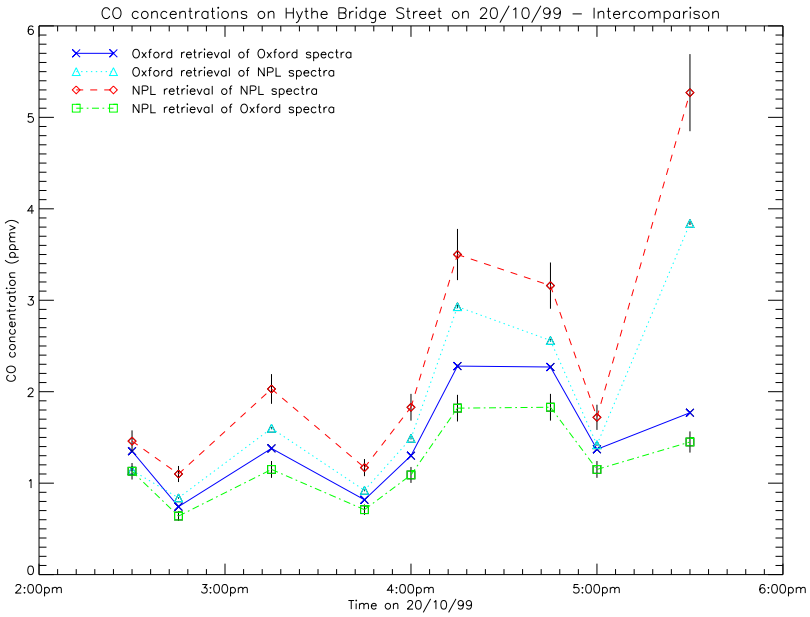

Figure 6.48: Comparison of concentrations of CO on Hythe Bridge Street on 20 October 1999, as retrieved by NPL and as detailed in chapter 4.

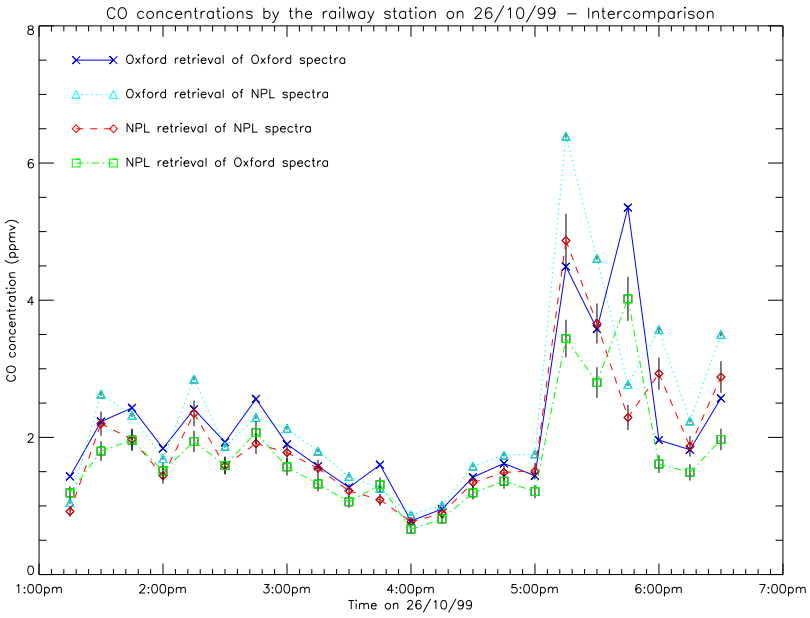

Figure 6.49: Comparison of concentrations of CO by Oxford railway station on 26 October 1999, as retrieved by NPL and as detailed in chapter 4.

For three of the sets of spectra the concentrations of CO retrieved by the retrieval method detailed in chapter 4 results in 10% - 35% higher concentrations of CO than those retrieved by NPL. The exception is the set of spectra recorded by NPL on 20/10/99, where the concentrations of CO retrieved by NPL's retrieval method results in 15% - 40% higher concentrations of CO than those retrieved using the method detailed in chapter 4. It is not known which set of results are more accurate, since the actual CO concentrations during the measurements are unknown.

From figures 6.48 and 6.49 it can be seen that the retrieved concentrations of CO follow similar trends with time. There are two notable exceptions to this; 5:30 pm on 20/10/99 and 5:45 pm on 26/10/99. In the first case the CO concentrations retrieved from the spectrum recorded by NPL are two to three times higher than those retrieved from the spectrum recorded using the equipment detailed in chapter 2. In the second case, the CO concentrations retrieved from the spectrum recorded using the equipment detailed in chapter 2 are approximately two times higher than those retrieved from the spectrum recorded by NPL. The reason for these discrepancies is not known. However, since both retrieval techniques record the difference in each case, the discrepancies are likely to be due to the slight difference in measurement times, or the difference in location of the optical paths.

Although all the retrieved concentrations on each day follow similar trends with time, there is closer agreement between the concentrations measured on 26/10/99 than those measured on 20/10/99. The reason for this is thought to be the differences in layout of the two sites. On the 26/10/99 there was some overlap in the optical paths used, and where the optical paths didn't overlap, they were close together (see figure 2.18). On 20/10/99 the two optical paths were parallel and about a metre apart, with the optical path used by NPL closer to the road, and hence the pollution source. Given that the CO concentrations retrieved from the spectra recorded using the equipment detailed in chapter 2 on 20/10/99 are lower than those retrieved from the spectra recorded by NPL, it is thought that the distance from the source of the pollution is the reason for the difference. It should also

be noted that the optical path used for the measurements given in section 6.4.1 was closer to Blackwell's building which had vents, at the same height as the optical path, through which warm air was expelled.

6.5.1 Comparison with CO Analyser Data

NPL set up a non-dispersive infrared (NDIR) CO analyser, which is standardly used to measure CO concentrations, alongside the two FTIR spectrometers for comparison purposes on 20/10/99 and 26/10/99. Unlike the spectrometers, which when used in long-path mode give an area averaged CO concentration, the CO analyser takes a point measurement. Therefore the measurements made by the spectrometers and by the CO analyser are not directly comparable. However, the CO analyser measurements can be used to confirm that the CO concentrations recorded by the spectrometers are realistic.

The NDIR instrument is a gas correlation instrument. Light from an infrared source located in the instrument passes alternately, at a rate of 30 Hz, through a gas cell containing a CO/N_2 mixture and a gas cell containing nitrogen only. The light then passes through a multi-pass sample cell, containing in this case the polluted air beside the spectrometers, which uses an arrangement of mirrors to give an optical pathlength through the sample of 16 m. The beam passes through an interference filter, with a bandpass of 1950 cm^{-1} to 2250 cm^{-1}, before impinging on the detector which is a thermoelectrically-cooled photoconductor. The change in intensity of the beam over each cycle is used to determine the concentration of CO in the air. The analyser was calibrated before use on both measurement days using NPL certified reference gas mixtures (it is normally calibrated every three months). It has a measurement time of 30 seconds and the uncertainty in measured CO concentrations is $\pm$ 5% at the 95% confidence level.

On 20/10/99 the analyser was placed on the pavement in front of NPL's spectrometer and next to the spectrometer used in this study. Figure 6.50 compares the CO concentrations measured by the analyser (averaged over 1 minute) with those retrieved from the spectra recorded by the two FTIR spectrometers. The analyser measurements show that

those concentrations retrieved from the recorded spectra are realistic. Although the concentrations measured by the analyser most closely match the concentrations retrieved by NPL from the spectra recorded using the equipment detailed in chapter 2, given the disparity in measurement techniques (in particular point versus area averaged measurements), this does not necessarily mean that these are more correct than the other sets of retrieved concentrations.

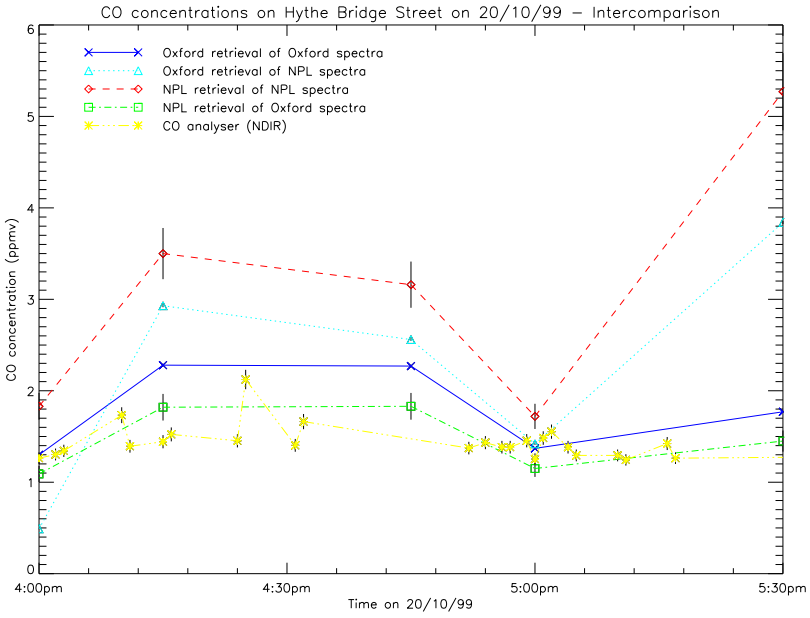

Figure 6.50: Comparison of concentrations of CO on Hythe Bridge Street on 20 October 1999, as measured by the CO analyser and retrieved by NPL and as detailed in chapter 4.

On 26/10/99 the analyser was placed on the ground next to NPL's spectrometer, on the far side from the spectrometer used in this study. Figure 6.51 compares the CO concentrations measured by the analyser (averaged over 15 minutes) with those retrieved from the spectra recorded by the two FTIR spectrometers. The analyser measurements show that those concentrations retrieved from the recorded spectra are realistic, although there is a discrepancy between the analyser and retrieved measurements in the 5:00 pm to 6:00 pm time period, where the retrieved measurements are much higher than the averaged analyser measurements. It was thought that this was due to low CO concentration for

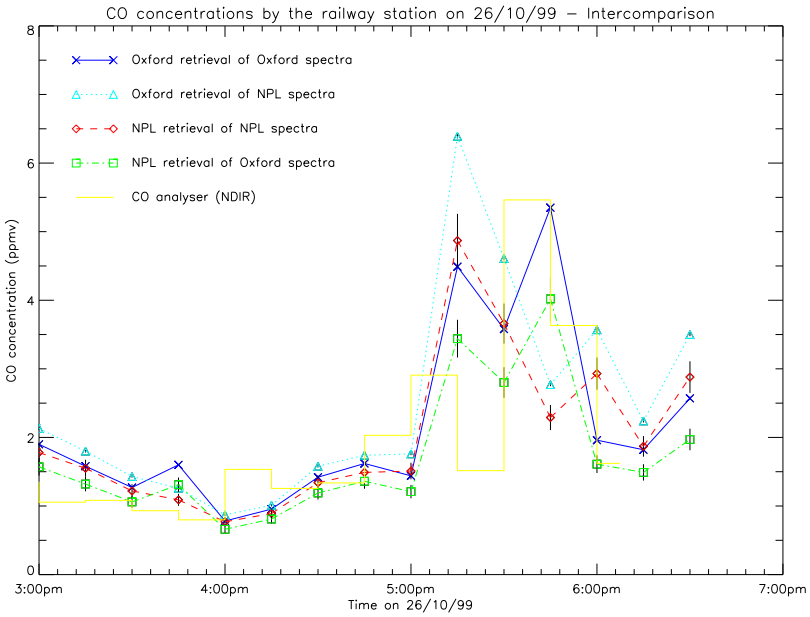

Figure 6.51: Comparison of concentrations of CO by Oxford railway station on 26 October 1999, as measured by the CO analyser and retrieved by NPL and as detailed in chapter 4.

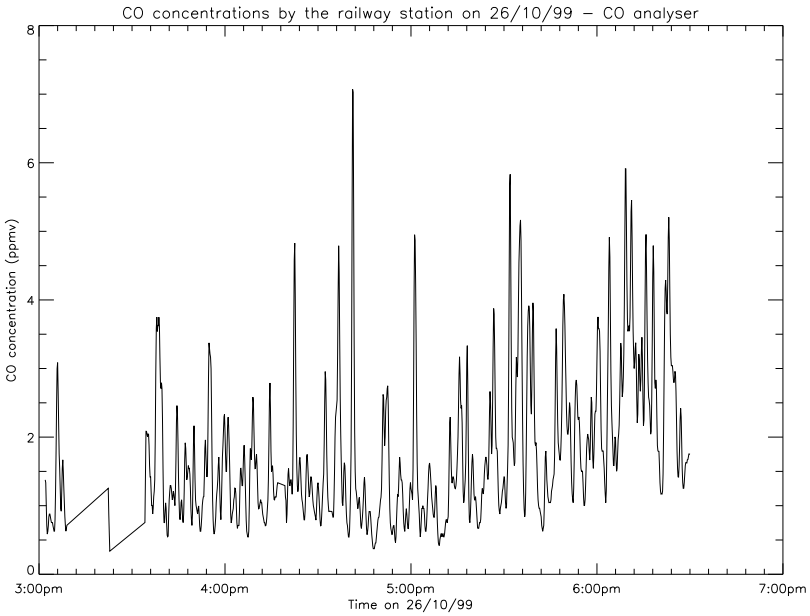

Figure 6.52: CO concentrations by Oxford railway station on 26 October 1999 as measured by the CO analyser.

most of each 15 minute averaging period, with peaks in the CO concentration coinciding with the FTIR spectrometer recording periods at 5:15 pm, 5:30 pm and 5:45 pm. However the raw data for the analyser (see figure 6.52) does not show this; although it does show considerable variation in the recorded CO concentration throughout the whole time period. The discrepancy is now thought to be due to the point measurements by the CO analyser not coinciding with the location of the area averaged measurements of the FTIR spectrometers.

Chapter 7

Conclusions and Further Work

The aim of this study was to determine the feasibility of using a FTIR spectrometer to make simultaneous measurements of a wide range of urban pollutants. The work described in this thesis shows that long path FTIR spectroscopy is a potentially viable technique for such measurements. It has been shown that it is possible to measure the concentrations of several pollutant gases (those of CO, SO_2, and NO) simultaneously and in short measurement times (less than 2 minutes). However, further work is necessary in order to improve the technique and extend it to include further important gaseous pollutants. The main obstacles to improved performance are channelling, which accounts for approximately 80% of the noise levels in the spectra, (see section 7.1) and the quality of the HITRAN96 spectral database (see section 7.3). This chapter discusses the conclusions of this study and suggestions for further work are presented.

7.1 Equipment

It was shown in section 3.1 that using the optimal estimation retrieval technique described in chapter 4 to jointly retrieve gain and offset together with the concentrations of the gaseous pollutants of interest corrects for the effects of using a non-linear MCT detector. It was also shown, in section 3.2.1, that it is possible to correct for the effects of self-emission and atmospheric emission by subtracting from the measured spectrum a spectrum recorded with the infrared source switched off, provided that the atmosphere remains essentially

unchanged during the period between the two measurements.

It has been demonstrated that the presence of channelling in a spectrum reduces the ability to retrieve the concentrations of gaseous pollutants from that spectrum. In section 3.3 it was shown that the cause of channelling in the Perkin-Elmer Spectrum 2000 spectrometer used in this study was the two KBr windows that seal the optical module of the spectrometer. Although channelling can be eliminated from the spectra by removing these two windows, this then exposes the spectrometer's optics, and in particular its hygroscopic KBr beamsplitter, to the harsh atmosphere (particulates, H_2O, acidic gases etc.) surrounding the spectrometer in its working environment. A large component of the noise (typical noise levels without channelling are 0.15% of the signal, with channelling this increases to 0.9%) in the spectra comes from channelling. In some spectral regions, for example the 980 cm^{-1} to 1070 cm^{-1} spectral region which contains the main ozone spectral band, channelling prevents gaseous pollutants from being detected at typical ambient concentrations over the pathlengths used in this study. A solution to the problem of channelling, such as using wedged as well as tilted KBr windows or modelling the channelling, needs to be found.

An improved signal-to-noise ratio (SNR) of the equipment used in this study would reduce the detection limits for the gaseous pollutants, and thus allow measurements of the concentrations of gases which are currently undetectable. This could be achieved by eliminating channelling, using a detector with a higher SNR, by using a longer measurement time (this would reduce the ability to detect rapid changes in the concentrations of pollutants), by using a lower resolution (this may increase the detection limits for some gases), using a more intense source, or by using a cold spectral filter (which should be placed between the beamsplitter and the detector, rather than between the beamsplitter and the source) to restrict the spectral region monitored to the minimum region that is necessary. In particular, a higher SNR in the 670 cm^{-1} to 680 cm^{-1} than that of the DTGS detector currently used, might enable detection of benzene by its main spectral band at typical concentrations in urban or roadside air.

7.2 Retrievals

The retrieval technique of optimal estimation used in this study enables joint retrievals, that is retrievals of more than one parameter simultaneously, to be carried out. One advantage of this is that equipment parameters, such as gain, offset and wavenumber offset, can be retrieved alongside the gas(es) of interest. The other advantage is that all gases in a spectral region which have significant absorption can be retrieved simultaneously. This allows the retrieval of gases, such as SO_2 and NO, which absorb in spectral regions where the main absorber is another gas, such as H_2O or CO_2. These gases have been thought to be undetectable by long path FTIR spectroscopy (de Castro et al. 1999) due to the absorption of H_2O or CO_2.

7.3 Detection of Gases

The two main limitations on the detection of gases in this study are the low signal-to-noise ratio caused by channelling (see section 7.1) and the quality of the HITRAN96 (Rothman et al. 1998) spectral database which is used by the forward model to generate the synthetic spectra used in the retrieval of the gas concentrations from the measured spectra. Since the spectral database is used by the forward model to create synthetic spectra which are compared to the measured spectrum in the retrieval process, any errors in the spectral database will propagate through into errors in the retrieved concentrations of gases. Thus the quality of the data is vital to the retrieval scheme used in this study.

All the retrievals of gases in this study have been affected, to a greater or lesser extent, by errors in the line position and/or line strength of spectral lines in the HITRAN96 database. Errors in water vapour data show up as peaks (positive and negative) in the residuals of the spectra (see section 6.2) and cause errors in the retrieved gas concentrations. Although a wavenumber offset for the spectral region is retrieved, it is one value for the whole region and so errors in individual lines can not be accounted for by the retrieval.

The HITRAN 2000 database (Goldman 2000), due to be published later this year,

includes updates (data is from R. A. Toth) for the line-by-line water vapour data in the 500 cm^{-1} to 2820 cm^{-1} spectral region. This may improve the accuracy of retrievals carried out on data recorded during this study. The National Institute of Standards and Technology (NIST) in the United States of America are in the process of creating a spectral database that is traceable back to primary measurement standards.

7.3.1 Carbon Monoxide, Sulphur Dioxide and Nitric Oxide

It has been shown that it is possible to routinely retrieve all three of these gases from measured spectra, although the typical concentrations of sulphur dioxide found in urban air are at the limit of detectability for the pathlengths used in this study. Carbon monoxide and sulphur dioxide are important pollutants included in the UK Government's National Air Quality Strategy (NAQS). Nitric oxide is a primary pollutant and precursor of nitrogen dioxide, which is one of the pollutants included in NAQS. Therefore, the ability to routinely measure the concentrations of these three pollutants by long path FTIR spectroscopy is important.

7.3.2 Nitrogen Dioxide and Ozone

The most important, because of their role in smog formation and their deleterious effect on health, NAQS gases that cannot currently be retrieved are NO_2 and O_3, although it is theoretically possible to do so (see sections 6.1.3 and 6.1.4). In the case of NO_2, it is not understood why the retrieval fails to correctly retrieve NO_2 and converges to a concentration which is unfeasibly high. This is a problem that should be investigated further, and as such has been included in the suggestions for further work. There are two problems with retrieving O_3 from the spectra recorded with the equipment used in this study. One is the anomalous dip in the 100% transmission curve between 1045 cm^{-1} and 1055 cm^{-1} which is thought to be absorption by a hydrocarbon based oil, which it is not possible to model with the quadratic expression used for gain. It might be possible to model the dip and include it in the RFM as an absorption cross-section. The other is the relatively large amplitude

of channelling in the region. This causes particular problems since the channelling has the same shape as a weak gas line, and so the retrieval program tries to fit to it. Random noise does not cause this problem, as it does not have the same regular form.

7.3.3 Benzene and 1,3-Butadiene

High resolution, infrared, absorption cross-section spectra of benzene and 1,3-butadiene have been measured as part of this study. These spectra have been used to calculate detection limits for these two gases when using the equipment used in this study. The detection limits calculations show that the concentrations of these two gases typically measured by NETCEN in the urban atmosphere are only detectable with the equipment used in this study with a pathlength greater than or equal to 400 m. Since it has not been possible to set up a path of this distance, neither benzene nor 1,3-butadiene have been detected in the course of this study.

7.3.4 Other Gases

Nitrous oxide (N_2O) and methane (CH_4) are currently routinely retrieved. N_2O is a contaminant species in the CO spectral region and is jointly retrieved with CO. CH_4 is a contaminant species in the SO_2 spectral region and is jointly retrieved with SO_2. The uniformity of the retrieved concentrations of CH_4, and in particular, N_2O around their concentrations in ambient air, are indicative of the stability of the instrument over short and long periods of time and the reproducibility of the measuring and analysing process.

Other gases that it would be useful to measure, but which have not been investigated are nitric acid and peroxyacetyl nitrate (PAN) along with a range of hydrocarbons such as ethane and acetone, all of which are components or precursors of photochemical smog.

7.4 Intercomparison with the National Physical Laboratory

An intercomparison of the equipment and retrieval techniques used in this study and similar equipment and different retrieval techniques used by the National Physical Laboratory was

undertaken. Concentrations of carbon monoxide retrieved from spectra recorded simultaneously on two separate days (20/10/99 and 26/10/99) were compared. On the 26/10/99, when the optical paths used overlapped and were positioned above the source of pollution (a busy road), the retrieved concentrations of CO were very similar. This indicates that the methods used are a valid technique for measuring the concentration of CO in the atmosphere.

On the 20/10/99, when the optical paths used were parallel to one another and to the source of the pollution (another busy road), with one path closer than the other, the results were noticeably different. The concentrations of CO retrieved from spectra recorded using the optical path closest to the source of pollution were higher than those retrieved from the spectra recorded using the optical path further away from the source of pollution, though both sets followed the same variations with time. The differences in this case can be attributed to distance from the source, and illustrate how pollution levels decrease with distance.

As well as comparing the results each group retrieved from their own spectra, the spectra were exchanged and each group used their own retrieval technique on the other's spectra. This intercomparison of retrieval techniques produced similar concentrations of CO, which followed the same variations with time. However, even with taking into consideration experimental error, the results of the two retrieval techniques were not the same. It is not possible to determine which retrieval technique produces the more accurate results, since the actual CO concentrations at the time of measurement are unknown. In order to determine the accuracy of the retrieval techniques, it would be necessary for each group to retrieve the concentration of one or more gases from a spectrum recorded under controlled conditions in which the concentrations of the target gases was known. This was not possible to carry out during this study.

7.5 Further Work

Some suggestions for further work that could be carried out on this project are made in this section.

7.5.1 Detection of Gases

Investigate the NO_2 retrieval to discover why it converges to an unfeasibly high concentration of NO_2.

Model the anomalous dip in the 100% transmission curve between 1045 cm^{-1} and 1055 cm^{-1} and include it in the RFM as an absorption cross-section. See whether jointly retrieving this with O_3 enables O_3 to be retrieved.

Investigate whether it is possible to detect other pollutant gases such as peroxyacetyl nitrate (PAN), nitric acid and a range of hydrocarbons.

Record some spectra with a longer pathlength to see what extra species can detect. If possible use $\geq$ 400 m in order to detect benzene and 1,3-butadiene.

It might be interesting to record the levels of pollutants over a 24 hour period in order to investigate any diurnal variation in concentrations.

There is now a Met-Log automatic weather station (made by R&D Instromet Ltd.) installed on the roof of the atmospheric physics building close to the periscope and mount for the external infrared source used in this study. Science area spectra could be recorded over a period of time and a study undertaken to see if there is any correlation between the concentrations of the measured pollutants and the weather parameters, such as wind speed and direction, recorded by the weather station during each measurement. The station will also provide more accurate temperature and pressure measurements than the Oregon Scientific electronic barometer BA-116 currently used.

7.5.2 Improvements to Retrieval Method

A useful improvement to the retrieval method would be to use specific criteria, such as information content (Bennett, Dudhia & Rodgers 1999), in order to select the spectral

regions, or microwindows, used to retrieve each gas. Currently an ad hoc method whereby a large section, or all, of the main spectral band of the gas in question is used.

The systematic errors in the method of measuring the spectra should be identified, quantified and included in the retrieval as part of the errors on the measurement.

It should be investigated whether changing the model of the offset (see section 4.6) in a spectral region from a constant to a constant plus a linear slope improves the retrieval accuracy.

There is also scope for changing the model for gain (see section 4.6) in the retrieval. Currently gain is modelled as $(g_0 + g_1\tilde{\nu} + g_2\tilde{\nu}^2)$, where g_0 is the constant coefficient of the gain, g_1 is the linear coefficient of the gain, g_2 is the quadratic coefficient of the gain and $\tilde{\nu}$ is the wavenumber scale of the forward model spectrum (see equation 4.22). Including an extra parameter to be retrieved, such as a cubic term, in the model of gain might improve the retrieval accuracy in those cases where a quadratic model of gain is not sufficient.

Investigate whether using the Marquardt-Levenburg method, rather than Gauss-Newton method of iteration currently used, would speed up the retrieval and enable it to converge in cases where the current retrieval would not.

7.5.3 Validation

A full validation of the technique should be carried out. One method would be to place a large gas cell, containing a mixture of a known concentration of a pollutant in dry synthetic air (containing N_2 and O_2 only) at atmospheric pressure, in the optical path of the spectrometer such that it occupies the entire optical path (width and length), apart from that inside the spectrometer (which should be purged with, for example, N_2). Several spectra should be recorded and retrievals of the concentration of the pollutant gas carried out. This should be repeated for a range of different gaseous pollutants. The retrieved concentrations, together with their errors, could then be compared with the known concentrations placed in the cell.

7.5.4 Other work

Investigate why the measurements made with the DTGS detector give substantially (usually lower) concentrations than those made with the MCT detector.

Investigate the effects of using a lower resolution, e.g. 0.5 cm^{-1}. This would increase the signal-to-noise ratio, but by reducing the ability to distinguish between adjacent spectral lines it make actually make certain gases harder to detect (i.e. need a longer pathlength, or higher concentration of the gas).

Develop a solution to the problem of channelling. This may be to replace the tilted, parallel-sided KBr windows currently used to seal the optical module of the spectrometer with wedged and tilted KBr windows. Other solutions may be to use a more sophisticated method of correcting the interferogram than that investigated in section 3.3, or to model the channelling in spectral space.

Compare results of measurements with the predictions of one or more models, such as box or street canyon models, of air pollution.

Determine whether it might be possible to retrieve the particulate content of the atmosphere, in particular focusing on on particles with a median aerodynamic diameter of less than 10 μm, the PM_{10} fraction. PM_{10}s are one of the eight pollutants included in the UK Government's National Air Quality Strategy, and as such it would be useful to be able to measure the mass per m^3 of particulates present in the area of atmosphere being measured. Work carried out at Reading (Hilton & Black 1998) indicates that it might be possible to measure PM_{10}s.

References

Abrams M. C., Toon G. C., Schindler R. A., 1994. Practical Example of the Correction of Fourier-Transform Spectra for Detector Nonlinearity. *Applied Optics*, 33(27):6307–6314.

Ballard J., Johnston W. B., Moffat P. H., Llewellyn-Jones D. T., 1985. Experimental Determination of the Temperature Dependence of Nitrogen-Broadened Line Widths in the $1 \leftarrow 0$ Band of HCl. *Journal of Quantum Spectroscopy and Radiative Transfer*, 33(4):365–371.

Ballard J., Remedios J. J., Roscoe H. K., 1992. The Effect of Sample Emission on Measurements of Spectral Parameters Using a Fourier Transform Absorption Spectrometer. *Journal of Quantum Spectroscopy and Radiative Transfer*, 48(5/6):733–741.

Bartoli F., Allen R., Esterowitz L., Kruer M., 1974. Auger-Limited Carrier Lifetimes in HgCdTe at High Excess Carrier Concentrations. *J. Applied Physics*, 45:2150–2154.

Becker K. H., 1996. Design and Technical Development of the European Photoreactor and First Experimental Results. Final Report of the EUPHORE EC-Project EV5V-CT92-0059, University of Wuppertal. Also to be found at: http://www.physchem.uni-wuppertal.de/PC-WWW_Site/Wir_ueber_Uns/EUPHORE/EUPHORE_Report/00_Deckblatt.html.

Beer R., 1992. *Chemical Analysis*, *Remote Sensing by Fourier Transform Spectrometry*, John Wiley & Sons.

Bell R. J., 1972. *Introductory Fourier Transform Spectroscopy*, Academic Press.

Bennett V., Dudhia A., Rodgers C., 1999. Microwindow Selection for MIPAS using Informa-

tion Content. In: *Proceedings European Symposium on Atmospheric Measurements from Space*, pages 265–270, ed. Readings C., ESA.

Bingham E. O., 1974. *The Fast Fourier Transform*, Prentice-Hall.

Bishop G. A., Stedman D. H., 1996. Measuring the Emissions of Passing Cars. *Accounts of Chemical Research*, 29:489–495.

Boas M. L., 1983. *Mathematical Methods in the Physical Sciences*, John Wiley & Sons, 2 edition.

Borrello S. R., Kinch M. A., Lamont D., 1977. Photoconductive HgCdTe Detector Performance with Background Variations. *Infrared Physics*, 17:121–125.

Bower J., Broughton G., Willis P., 1995. *Air Pollution in the UK: 1993/4*. Department of the Environment and The National Environmental Technology Centre.

Bradley K. S., Brooks K. B., Hubbard L. K., Popp P. J., Stedman D. H., 2000. Motor Vehicle Fleet Emissions by OP-FTIR. *Environmental Science and Technology*, 34(5):897–899.

Carlson R. C., Hayden A. F., Telfair W. B., 1988. Remote observations of effluents from small building smokestacks using FTIR spectroscopy. *Applied Optics*, 27(23):4952–4959.

Carter III R. O., Lindsay N. E., Beduhn D., 1990. A Solution to Baseline Uncertainty Due to MCT Detector Nonlinearity in FT-IR. *Applied Spectroscopy*, 44(7):1147–1151.

Chaffin C. T., Marshall T., Fateley W., Hammaker R., 1995. Infrared analysis of volcanic plumes: A case study in the application of open-path FT-IR monitoring techniques. *Spectroscopy Europe*, 7(3):18–24.

Chamberlain J., 1979. *The Principles of Interferometric Spectroscopy*, John Wiley & Sons.

Chase D. B., 1984. Nonlinear Detector Response in FT-IR. *Applied Spectroscopy*, 38(4):491–494.

Curbelo R., 1993. *Techniques for Correcting Non-Linearity in a Photodetector Using Predefined Calibration Information, U.S. Patent Number 5,262,635.*

Davies N., Bell W., Vance A., Hilton M., 1998. Measurement of Fourier Transform Infrared

Spectrometer Instrument Lineshape. In: *Spectroscopic Atmospheric Environmental Monitoring Techniques*, pages 79–87, ed. Schäfer K., Volume 3493 of *Proceedings of SPIE EUROPTO Series*, SPIE.

Davies N. M., Hilton M., Lettington A. H., 1997. Vehicle exhaust gas monitoring by remote FT-IR spectroscopy. *Mikrochimica Acta [Supplements]*, 14:551–553.

Davies N. M., Lettington A. H., Hilton M., 1997. Superresolution and other mathematical techinques for quantitative analysis of infrared absorption and emission spectra of gases. *SPIE*, 3106.

de Castro A. J., Meneses J., Briz S., López F., 1999. Nondispersive infrared monitoring of NO emissions in exhaust gases of vehicles. *Review of Scientific Instruments*, 70(7):3156–3159.

Department of the Environment, Welsh Office, Scottish Office, 1997. *The United Kingdom Air Quality Strategy*, The Stationery Office. Also to be found at http://www.environment.detr.gov.uk/epsim/digest19/dig19-2.htm paragraphs 2.13 and 2.14.

Smog Information Made Clear. DETR Press Release 463, 1997.

Department of the Environment, Transport and the Regions, Executive S., for Wales T. N. A., of the Environment for Northern Ireland D., 2000. *The Air Quality Strategy for England, Scotland, Wales and Northern Ireland*, The Stationery Office. Also to be found at http://www.environment.detr.gov.uk/airquality/index.htm.

Dudhia A., 1997. Reference Forward Model - Software User's Manual. Technical Report PO-MA-OXF-GS-0003, AOPP, Oxford University. Also to be found at: http://www.atm.ox.ac.uk/RFM/.

Edwards D. P., 1992. *GENLN2: A General Line-by-Line Atmospheric Transmittance and Radiance Model (v3.0).* NCAR Technical Note TN-367+STR.

Geyer T. J., Plummer G. M., Dunder T. A., 1992. FTIR Technology Development. Technical Report, U. S. Environmental Protection Agency. EPA Contract Number 68D90055, Work Assignment Number 2.107. Also to be found at

http://www.epa.gov/ttn/emc/ftir/reports/entrop01.html.

Goldman A., 2000. *Highlights of IR Data Updates for HITRAN 2000, Distributed at the TES meeting, 13-15 Sept. 2000, at NASA Langley, VA.*

Goldman A., Paton-Walsh C., Bell W. et al., 1999. Network for the detection of stratospheric change Fourier transform infrared intercomparison at Table Mountain Facility, November 1996. *Journal of Geophysical Reasearch - Atmospheres*, 104(D23):30481–30503.

Griffiths P. R., de Haseth J. A., 1986. *Fourier Transform Infrared Spectrometry*, John Wiley and Sons.

Gronholz J., Herres W., Understanding FT-IR Data Processing. Combined reprint of Dr. Alfred Huethig Publishers (obtainable from Bruker, Karlsruhe), Instruments and Computers, Vols. 1 (1984) and 3 (1985).

Hanst P. L., Lefohn A. S., Gay, Jr B. W., 1973. Detection of Atmospheric Pollutants at Parts-per-Billion Levels by Infrared Spectroscopy. *Applied Spectroscopy*, 27(3):188–198.

Hanst P. L., Wong N. W., Bragin J., 1982. A long-path infra-red study of Los Angeles Smog. *Atmospheric Environment*, 16(5):969–981.

Hardin R. W., 1998. Eco-Optics: Remote Sensing Keeps Industry Clean. *Photonics Spectra*, 32(4):104–105.

Hardin R. W., 1998. Diode Lasers Pinpoint Pollutants. *Photonics Spectra*, 32(4):110–114.

Haus R., Schäfer K., Bautzer W., Heland J., Mosebach H., Bittner H., Eisenmann T., 1994. Mobine Fourier-transform infrared spectroscopy monitoring of air pollution. *Applied Optics*, 33(24):5682–5689.

Herget W. F., Brasher J. D., 1979. Remote measurement of gaseous pollutant concentrations using a mobile Fourier transfer interferometer system. *Applied Optics*, 18(20):2404–3420.

Herget W. F., 1982. Remote and cross-stack measurement of stack gas concentrations using a mobile FT-IR system. *Applied Optics*, 21(4):635–641.

Hilton M., Lettington A., 1997. Application of FTIR spectroscopy to measurement of gas turbine engine exhaust emissions. In: *proc. NATO-AGARD meeting on Non intrusive measurement techniques for propulsion engines.*

Hilton M., Black J. D., 1998. Detection of soot particles in gas turbine engine combustion gases using non intrusive FTIR spectroscopy. In: *Spectroscopic Atmospheric Environmental Monitoring Techniques*, pages 20–31, ed. Schäfer K., Volume 3493 of *Proceedings of SPIE EUROPTO Series.*

Hirst B., Gillespie S., Padgett M., Sibbett W., Lenney J., Hedges N., 1998. Optical sensors: a path to better gas detection. *Physics World*, 11(8):37–40.

Horrocks L., Burton M., Francis P., Oppenheimer C., 1999. Stable Gas Plume Composition Measured by OP-FTIR Spectroscopy at Masaya Volcano, Nicaragua, 1998-1999. *Geophys. Res. Letters*, 26(23):3497–3500.

Kaye G. W. C., Laby T. H., 1973. *Tables of Physical and Chemical Constants*, Longman Group Limited, Fourteenth edition.

Keens A., Simon A., 1990. *Correction of Non-Linearities in Detectors in Fourier Transform Spectroscopy, U.S. Patent Number 4,927,269.*

Kinch M. A., Borrello S. R., 1975. 0.1 eV HgCdTe Photoconductors. *Infrared Physics*, 15:111–124.

Knzli N., Kaiser R., Medina S., Studnicka M., Chanel O., Filliger P., Herry M., Horak Jr F., Puybonnieux-Texier V., Qunel P., Schneider J., Seethaler R., Vergnaud J.-C., Sommer H., 2000. Public-health impact of outdoor and traffic-related air pollution: a European assessment. *The Lancet*, 356(9232).

Leonelli J., 1995. LIDAR technology Measuring the Atmosphere. *Photonics Spectra*, 29(6):97–106.

Lindermeir E., Haschberger P., Geatches R. M., 1998. Evaluation procedure for non-intrusive exhaust gas analysis of jet engines using FTIR spectroscopy. In: *Spectroscopic Atmospheric Environmental Monitoring Techniques*, pages 44–55, ed. Schäfer K., Volume 3493 of *Proceedings of SPIE EUROPTO Series*, SPIE.

Marks C. J., Rodgers C. D., 1993. A Retrieval Method for Atmospheric Composition From Limb Emission Measurements. *Journal of Geophysical Research*, 98(D8):14939–14953.

Marshall T. L., Chaffin C. T., Hammaker R. M., Fateley W. G., 1994. An Introduction to Open-Path FT-IR Atmospheric Monitoring. *Environmental Science and Technology*, 28(5):224 A–232A.

Mertz L., 1965. *Transformations in Optics*, John Wiley & Sons.

Mertz L., 1967. *Infrared Physics*, 7(17).

Moody S. E., 1999. From Earth to Space, Lasers Take on Pollution. *Photonics Spectra*, 33(10):96–103.

Newnham D., Ballard J., 1995. Fourier Transform Infrared Spectroscopy of HCFC-142b Vapour. *Journal of Quantum Spectroscopy and Radiative Transfer*, 53(5):471–479.

Norton R. H., Beer R., 1976. New Apodizing Functions for Fourier Spectrometry. *Journal of the Optical Society of America*, 66(3):259–264. Errratum - J. Opt. Soc. Am., vol. 67, no. 3, page 419 (1976).

Ramelow K., 1997. Electronic Influences on an Infrared Detector Signal: Nonlinearity and Amplification. *Applied Optics*, 36(10):2123–2132.

Reisinger A., Fraser G., Johnston P., McKenzie R., Matthews W., 1998. Slow-scanning DOAS system for urban air pollution monitoring. In: *Proceedings of the XVIII Quadriennial Ozone Symposium 1996*, page 932, eds Bojkov R., Visconti G.

Richardson Jr R. L., Yang H., Griffiths P. R., 1998. Evaluation of a Correction for Photometric Errors in FT-IR Spectrometery Introduced by a Nonlinear Detector Response. *Applied Spectroscopy*, 52(4):565–571.

Rodgers C. D., 1976. Retrieval of Atmospheric Temperature and Compositions from Remote Measurements of Thermal Radiation. *Reviews of Geophysics and Space Physics*, 14(4):609–624.

Rodgers C. D., 2000. *Atmospheric, Oceanic and Planetary Physics*, *Inverse Methods for Atmospheric Sounding: Theory and Practice*, World Scientific Publishing Company.

Rothman L. S., Gamache R. R., Tipping R. H., Rinsland C., Smith M., Benner D., Devi V. M., J.-M.Flaud, C.Camy-Peyret, Perrin A., Goldman A., Massie S., Brown L., R.A.Toth, 1992. The HITRAN Molecular Database: Editions of 1991 and 1992. *Journal of Quantum Spectroscopy and Radiative Transfer*, 48(5/6):469–507.

Rothman L. S., Rinsland C., Goldman A., Massie S., Edwards D., J.-M.Flaud, Perrin A., Camy-Peyret C., Dana V., Mandin J., Schroeder J., McCann A., Gamache R., Wattson R., Yoshino K., Chance K., Jucks K., Brown L., Nemtchinov V., Varanasi P., 1998. The HITRAN molecular spectroscopic database and HAWKS (HITRAN Atmospheric Workstation): 1996 edition. *Journal of Quantum Spectroscopy and Radiative Transfer*, 60(5):665–710.

Russwurm G. M., 1997. *Compendium Method TO-16: Long-Path Open-Path Fourier Transform Infrared Monitoring of Atmospheric Gases*. U.S. Environmental Protection Agency.

Sandridge R. L., Peterson B. H., 1995. Using beam-steering mirrors and long-distance sources to extend coverage of Long-Path FTIRs. In: *Optical Instrumentation for Gas Emissions Monitoring and Atmospheric Measurements*, pages 194–202, eds Leonelli J., Killinger D. K., Vaughan W., Yost M. G., Volume 2366 of *SPIE Proceedings Series*.

Schäfer K., Haus R., Heland J., Haak A., 1995. Measurements of Atmospheric Trace Gases by Emission and Absorption Spectroscopy with FTIR. *Berichte der Bunsen-Gesellschaft-Physical Chemistry Chemical Physics*, 99(3):405–411.

Schindler R. A., 1986. Nonlinearity Correction Circuit for Photoconductive Detector. Technical Brief 2, NASA. Item 52.

Spellicy R. L., LaCosse J. P., Hull D. M., Cain S. J., Pophal J. C., 1995. Application of FTIR to Semiconductor Emissions Monitoring. In: *Optical Instrumentation for Gas Emissions Monitoring and Atmospheric Measurements*, pages 213–222, eds Leonelli J., Killinger D. K., Vaughan W., Yost M. G., Volume 2366 of *SPIE Proceedings Series*.

Steel W. H., 1964. Interferometers without Collimation for Fourier Spectroscopy. *Journal of the Optical Society of America*, 54(2):151–156.

Tuazon E. C., Graham R. A., Winer A. M., Easton R. R., 1978. A 1km Pathlength FTIR for the Study of Trace Pollutants in Ambient and Synthetic Atmospheres. *Atmospheric Environment*, 12:865–875.

White J. U., 1942. Long optical paths of large aperture. *Journal of the Optical Society of America*, 32:285–288.

Yokelson R. J., Griffith D. W. T., Ward D. E., 1996. Open-path Fourier transform infrared studies of large-scale laboratory biomass fires. *Journal of Geophysical Research*, 101(D15):21067–21080.

Yokelson R. J., Susott R., Ward D. E., Reardon J., Griffith D. W. T., 1997. Emissions from smoldering combustion of biomass measured by open-path Fourier transform infrared spectroscoy. *Journal of Geophysical Research*, 102(D15):18865–18877.